UNIVERSITY
OF OSLO

Eli Bæverfjord Rye

Searching for chargino–neutralino pair production in $\sqrt{s}$ = 13 TeV pp collisions with the ATLAS detector

And telling people about it

Thesis submitted for the degree of Philosophiae Doctor

Department of Physics
Faculty of Mathematics and Natural Sciences

2023

Series of dissertations submitted to the
Faculty of Mathematics and Natural Sciences, University of Oslo
No. 2657

ISSN 1501-7710

Cover: UiO.
Print production: Graphic center, University of Oslo.

Abstract

The Standard Model of particle physics is undoubtedly one of the greatest triumphs of modern physics. However, the Standard Model is not believed to be the final theory of particle physics. Supersymmetry is a popular proposed extension of the Standard Model, predicting the existence of many new particles. No experimental signs of supersymmetry have yet been observed, but the search continues. The topic of this thesis is the search for chargino–neutralino ($\tilde{\chi}_1^{\pm}\tilde{\chi}_2^0$) pair production using the full Run 2 dataset of $\sqrt{s} = 13$ TeV proton–proton collisions collected by the ATLAS detector at the Large Hadron Collider (LHC) between 2015 and 2018. This dataset corresponds to an integrated luminosity of 139 fb^{-1}.

A search for $\tilde{\chi}_1^{\pm}\tilde{\chi}_2^0$ pair production in final states with three leptons and missing transverse momentum is presented. No significant excess above the Standard Model predictions is found in the data. The results are interpreted in simplified models of supersymmetry, and statistically combined with results from a previous ATLAS search for compressed mass spectra in two-lepton final states. Various scenarios for the production and decay of $\tilde{\chi}_1^{\pm}$ and $\tilde{\chi}_2^0$ are considered. For a pure higgsino $\tilde{\chi}_1^{\pm}\tilde{\chi}_2^0$ scenario, exclusion limits at 95% confidence level are set on $\tilde{\chi}_2^0$ masses up to 210 GeV. For a pure wino $\tilde{\chi}_1^{\pm}\tilde{\chi}_2^0$ scenario, limits are set on $\tilde{\chi}_2^0$ masses up to 640 GeV for decays via on-shell W and Z bosons, up to 300 GeV for decays via off-shell W and Z bosons, and up to 190 GeV for decays via W and Standard Model Higgs bosons.

Also two studies based on the three-lepton search conducted in preparation for future runs of the LHC are presented. The first study concerns the final decision on the ATLAS hardware trigger architecture for the High-Luminosity LHC, where one of the options could allow for lowering the offline $E_{\mathrm{T}}^{\mathrm{miss}}$ trigger threshold from 200–210 GeV to 160 GeV. The three-lepton search would benefit materially from such a lowering, in particular in the especially intriguing low-$\Delta m(\tilde{\chi}_2^0, \tilde{\chi}_1^0)$ region predicting a relic density of dark matter consistent with current observations. The second study considers the new Run 3 derivation data format, DAOD_PHYS. By comparing this format to the Run 2 DAOD_SUSY2 format, an inconsistency in the trigger-matching procedure between the two formats is found, affecting low-p_{T} muons.

Further, a statistical combination of results for the simplified-model scenario of pure wino $\tilde{\chi}_1^{\pm}\tilde{\chi}_2^0$ decaying via W and Higgs bosons is presented, for which results from five different searches targeting different final states are combined. Projected onto the $m(\tilde{\chi}_1^{\pm}/\tilde{\chi}_2^0)$ vs. $m(\tilde{\chi}_1^0)$ plane, the observed combined 95% CL exclusion contour extends the contours for the individual searches in the area near the kinematic limit $\Delta m(\tilde{\chi}_2^0, \tilde{\chi}_1^0) = m_h$. For large $\tilde{\chi}_2^0$ masses, however, it falls within the contour of the best performing single search, due to one of the

other searches experiencing an excess.

A summary of various communication, outreach and recruitment activities are also reported. With the escalating need for persons educated in the natural sciences, and the decline in the number of applicants to science teacher programs and physics bachelor's programs in Norway in recents years, such activities are an important investment in the future.

Samandrag

Standardmodellen for partikkelfysikk er utvilsamt ein av dei største triumfane i moderne fysikk. Likevel er ikkje standardmodellen venta å vere den endelege teorien for partikkelfysikk. Supersymmetri er ei populær føreslått utviding av standardmodellen som spår eksistensen av mange nye partiklar. Ingen eksperimentelle teikn på supersymmetri har blitt observert enno, men søket held fram. Temaet for denne avhandlinga er søk etter parproduksjon av ladino og nøytralino[1] ($\tilde{\chi}_1^{\pm}\tilde{\chi}_2^0$) i datasettet av proton–proton-kollisjonar med ein kollisjonsenergi på 13 TeV samla inn med ATLAS-detektoren ved Large Hadron Collider (LHC) mellom 2015 og 2018. Dette datasettet svarar til ein integrert luminositet (datamengd) på 139 fb^{-1}.

Eit søk etter parproduksjon av $\tilde{\chi}_1^{\pm}\tilde{\chi}_2^0$ i sluttilstandar med tre lepton og manglande transvers rørslemengd $E_{\mathrm{T}}^{\mathrm{miss}}$ blir presentert. Ingen signifikante overskot samanlikna med standardmodellen sine prediksjonar blir funne i datasettet. Resultata tolkast ved hjelp av forenkla supersymmetri-modellar, og blir statistisk kombinert med resultata frå eit tidlegare ATLAS-søk etter komprimerte massespektrum i sluttilstandar med to lepton. Ulike scenario for produksjon og sundfall av $\tilde{\chi}_1^{\pm}$ og $\tilde{\chi}_2^0$ blir vurdert. For eit scenario med reint higgsino $\tilde{\chi}_1^{\pm}\tilde{\chi}_2^0$ blir grenser sett med 95% konfidensnivå på $\tilde{\chi}_2^0$-massar opp til 210 GeV. For eit scenario med reint wino $\tilde{\chi}_1^{\pm}\tilde{\chi}_2^0$ blir grenser sett på $\tilde{\chi}_2^0$-massar opp til 640 GeV for sundfall via W- og Z-boson på masseskala sine, opp til 300 GeV for sundfall via W- og Z-boson av masseskala sine, og opp til 190 GeV for sundfall via W- og Higgs-boson.

To studiar basert på tre-lepton-søket gjennomført som førebuingar til seinare datatakingsperiodar av LHC blir også presentert. Den første studien omhandlar den endelege avgjerda om kva trigger-arkitektur ATLAS-detektoren skal ha for High-Luminosity LHC (HL-LHC), kor eit av alternativa kan medføre ei senking av $E_{\mathrm{T}}^{\mathrm{miss}}$-trigger-terskelen frå 200–210 GeV til 160 GeV. Tre-lepton-søket vil ha nytte av ei slik senking, spesielt i området med låg $\Delta m(\tilde{\chi}_2^0, \tilde{\chi}_1^0)$, som er ekstra spanande fordi det spår den observerte rest-tettleiken av mørk materie. Den andre studien omhandlar det nye dataformatet DAOD_PHYS. Ved å samanlikne dette formatet med det tidlegare DAOD_SUSY2-formatet, fann vi eit avvik i prosedyren for såkalla trigger-matching mellom dei to formata, som påverkar myon med lav transvers rørslemengd.

Også ein statistisk kombinasjon av resultat frå fem ulike søk etter same forenkla supersymmetri-modell med reint wino $\tilde{\chi}_1^{\pm}\tilde{\chi}_2^0$ som sundfell via W- og Higgs-boson blir presentert, der dei ulike søka vurderer ulike sluttilstandar. Projisert ned på $m(\tilde{\chi}_1^{\pm}/\tilde{\chi}_2^0)$-$m(\tilde{\chi}_1^0)$-masseplanet ligg den observerte eksklusjon-

[1] Merk at det ikkje finst offisielle norske namn på dei supersymmetriske partiklane. Eg vel å bruke ladino og nøytralino for høvesvis chargino og neutralino.

skonturen for kombinasjonen utanfor konturane for dei individuelle søka i området nær den kinematiske grensa $\Delta m(\tilde{\chi}_2^0, \tilde{\chi}_1^0) = m_h$. For store $\tilde{\chi}_2^0$-massar ligg han derimot innanfor konturen for det best presterande søket, fordi eit av dei andre søka såg eit overskot samanlikna med standardmodellen sin prediksjon.

Ei oppsummering av ulike kommunikasjon-, formidling- og rekrutteringsaktivitetar blir også rapportert. Med det aukande behovet for folk utdanna innanfor naturvitskap, og nedgangen i søknadar til realfagslærarutdanningar og bachelorprogram i fysikk i Norge dei seinaste åra, er slike aktivitetar ei viktig investering i framtida.

Acknowledgements

First and foremost, I would like to thank my supervisors. Heidi Sandaker, my main supervisor and the constant in my supervision team, thank you for being so easy to talk to, supportive and positive. Eirik Gramstad and Sara Alderweireldt, thank you for taking me on as your student when I was lost, and for answering my many questions and helping me hands-on. This thesis would not have happened without the two of you. Thank you, Farid Ould-Saada, for taking the lead in getting me through my ATLAS authorship qualification task, and David Cameron, for supervising me on this task. I would also like to thank all the people I have had the pleasure to work with in the ATLAS Collaboration, in particular in the SUSY EWK 3L and the SUSY EWK combinations groups.

Twelwe years of studies at the Department of Physics is coming to an end, the last six with the HEP section, and it feels surreal. I have made many good friends over the years. Thank you all, for making these years so enjoyable. I have really appreciated our interesting conversations, endless quizzes, pub visits and soccer matches. A special thanks goes out to Knut Oddvar, Simen, Jeriek and Even: I am happy to be the "jenta gurl" to your "gutta boyz". I look back at many fond memories with you guys, traveling the world, enjoying Norway's winters on cross-country skis in Oslomarka, the tradition of celebrating May 17 together, and you guys visiting my summer-farm paradise. Another special thanks goes out to Gert, Oda, Even (again) and Alex, for all the mental support in the final stages of this endeavor.

Thank you, Hilde, for suggesting that I work on physics communication with you instead of the usual teaching duties. Not only has it been fun and rewarding, but you have also become a good friend that I truly appreciate. Thank you for encouraging me to do outreach myself, both inside and outside of university. I would never have ended up on Norway's biggest morning TV show (mostly talking about cows, but also some physics) or being interviewed for an hour on live radio (cows and physics is apparently a popular combination) if it wasn't for you. Thank you also to the departement's management for allowing me to spend my duty work like this.

Thank you, Are, for being my mentor and good friend, always with an open door. You help and support me, no matter the issue, and it has been reassuring to know you are just a staircase away. I probably wouldn't have participated in the abovementioned media madness if it wasn't for your peptalks in advance. Or started this Ph.D., for that matter. (Or finished it.)

Also some people and activities outside the university should be acknowledged for getting me through this Ph.D. Thank you to all the girls in my choir, TRILL. Pursuing a Ph.D. in physics can be an all-consuming exercise, and it has been healthy to have some good friends also outside of university. Some of you I have

met weekly for almost ten years now, and I have really enjoyed all the fun we have had, both when singing and otherwise. My summer-farm paradise also deserves some praise. When you spend most work days in front of a computer, searching for something that might not even exist, it is very refreshing to do some work showing immediate results from time to time, like chopping wood and milking cows. My hobby of knitting should also be mentioned. Again, actually creating something with my hands after a long day in front of the computer has been my meditation. And provided me with many warm sweaters, which is nice for Norwegian winters (and summers).

And of course, my family. Thank you, mamma, for teaching me to focus on one thing at a time when it all feels too overwhelming. And for constantly reminding me, from the very beginning of this Ph.D., that the goal is to get it done, not to make it perfect. Thank you, pappa, for passing down the gift of enjoying talking to everyone. And for teaching me that everyone is a "bra kar" (nice guy) — I'm grateful for growing up with that worldview. My sisters, Lisa and Nora, thank you for always being so supportive. I am very thankful for our friendship and close bond.

A big thanks also to other family and friends for all support and cheers along the way.

Lastly, I also found my special someone at the department. Thank you, Anders, for all your support, understanding and patience. Finally finishing this Ph.D. after six years is great, but the most important thing I take home is you.

Eli Bæverfjord Rye
Oslo, June 2023

Contents

Introduction

Our current best understanding of the universe is encapsulated in the Standard Model (SM) of particle physics [1–7]. The Standard Model describes the fundamental constituents, the matter particles, and their interactions, the forces. Over the years, the Standard Model has proven to be extremely successful at describing most features of nature that we have observed experimentally. The most prominent highlight came in 2012, when the ATLAS and CMS experiments at the Large Hadron Collider (LHC) discovered a particle consistent with the long-sought Higgs boson [8, 9]. The (Brout-Englert-)Higgs boson was first predicted theoretically in the 1960s [10–13], and its discovery marked the first observation of the full particle spectrum predicted by the Standard Model. However, despite its success, the Standard Model is not believed to be the final theory of particle physics. First and foremost, it does not include the force of gravity. Further, rather than coming from a higher theoretical principle, its parameters are chosen to match observations. More technical problems include the so-called hierarchy problem of the Higgs boson mass, and that it does not explain dark matter.

Supersymmetry (SUSY) [14–19] is a proposed extension of the Standard Model which introduces a fermion–boson symmetry, predicting the existence of many new particles. As supersymmetry can accomodate several of the shortcomings of the Standard Model simultaneously, it is one of the most popular theories for physics beyond the Standard Model (BSM). For instance, it offers a solution to the above-mentioned hierarchy problem, and the lightest supersymmetric particle is a candidate for dark matter. Great efforts have been put into searching for the hypothetical supersymmetric particles — both the ATLAS and CMS collaborations have separate working groups only occupied with this, each currently consisting of hundreds of people. No signs of supersymmetry have yet been observed, but the work continues.

Although production cross-sections are larger for strongly produced supersymmetric particles than for electroweakly produced supersymmetric particles, more and more eyes are now on electroweak (EWK) supersymmetry. Several hints that new physics might hide in the electroweak sector have emerged more or less recently. For instance, the so-called anomalous magnetic moment of the muon gives rise to the probably most clear discrepancy between the Standard Model and measurements today. The magnetic moment is usually expressed in terms of the so-called g-factor, which theoretically — without any quantum loop corrections — should equal exactly 2. However, quantum corrections increase this value, and the difference from the simple expectation of 2, $a_\mu \equiv (g-2)_\mu/2$, is commonly called the anomalous magnetic moment. The combined experimental average is currently $a_\mu^{\text{exp}} = 116592061(41) \times 10^{-11}$ [20], while the best Standard Model prediction is $a_\mu^{\text{SM}} = 116591810(43) \times 10^{-11}$ [21]. The difference between

these values corresponds to a significance of 4.2σ.

The topic of this thesis is the search for electroweak supersymmetry — more specifically, chargino–neutralino pair production — in 13 TeV proton–proton collisions with the ATLAS detector at the LHC. Simply put, charginos $\tilde{\chi}^{\pm}$ and neutralinos $\tilde{\chi}^{0}$, collectively referred to as electroweakinos, are the fermionic supersymmetric partners of the Standard Model W, Z and Higgs bosons. The dataset used throughout the thesis was collected with the ATLAS detector between 2015 and 2018, referred to as "Run 2" of the LHC. Most of the work presented in this thesis was performed as part of two different ATLAS SUSY analysis working groups. First, I was part of the ATLAS SUSY EWK 3L group, occupied with searching for chargino–neutralino pair production in final states with three leptons and missing transverse momentum, resulting in Ref. [22]. I contributed to the off-shell WZ part of the analysis, in particular aiding in the optimization of the signal regions and preparing necessary documentation for the HEPdata repository [23]. Later, I was part of the ATLAS SUSY EWK combinations group, engaged with statistically combining the results for multiple Run 2 electroweak SUSY searches, with a resulting paper in the pipeline. Results for searches targeting the same production and intermediate decay modes (i.e. the same simplified model) but different final states were combined. I was in charge of investigating and performing combinations for two different simplified models: higgsino $\tilde{\chi}_1^{\pm}\tilde{\chi}_2^{0}$ pair production decaying via W and Z bosons, and wino $\tilde{\chi}_1^{\pm}\tilde{\chi}_2^{0}$ pair production decaying via W and Higgs bosons.

In addition to analysis work, I have contributed to multiple communication, outreach and recruitment activities during the course of this Ph.D., both related to particle physics and physics in general. I did my ATLAS authorship qualification task on ATLAS@Home [24–26], part of the broader LHC@Home [27, 28], where volunteers can take part in high energy physics experiments by running Monte Carlo simulation on their private computers. My ATLAS authorship qualification task was on enhancing the ATLAS@Home graphical interface, showing some basic information on the physics relevant for ATLAS, as well as personalized information on the volunteer's contribution. Further, instead of the usual 25% teaching duties required for a four-year fellowship at the Department of Physics at the University of Oslo, I was allowed to work with the department's communications adviser 25% of my time. In this role, I contributed to the organization of the Norwegian media visit to CERN in October 2019, where I in addition to inviting journalists and setting up the program functioned as a tour guide and also got interviewed about my own research. Other examples include giving popular-science talks at different events, and guesting popular-science radio shows and podcasts.

I choose to include a description of these activities in this thesis because I believe they are very important. The research being carried out at CERN is at the mercy of funds and support from society, and with that comes the responsibility of disseminating the resulting knowledge to the general public. Further, continuous recruitment of good candidates is essential for CERN's success story to continue. Additionally, to keep up with technological development, and to solve today's imminent energy- and climate-related problems, society in general has an

escalating need for persons educated in the natural sciences — perhaps physics in particular. However, in Norway, the number of applications to science teacher education programs and physics bachelor's programs have been declining in recent years [29]. Outreach and recruitment activities are thus a good investment in the future, in many ways.

Thesis outline

This thesis consists of three parts, each containing two or more chapters. The first part introduces the foundations required to understand the work presented in this thesis. The second part describes the analysis work performed and the results obtained. In the third part, the topic shifts to communication, outreach and recruitment activities.

Part 1: Foundations

Chapter 1 gives an introduction to supersymmetry.

Chapter 2 gives an introduction to the experimental setup used to collect the data used in this thesis, namely the Large Hadron Collider and the ATLAS experiment.

Part 2: Searching for chargino–neutralino pair production

Chapters 3–6 describe the search for chargino–neutralino pair production in final states with three leptons and missing transverse momentum presented in Ref. [22]. Although I have only worked on parts of the search analysis, all relevant aspects of the analysis are introduced. Chapter 7 summarizes my contribution to the ATLAS SUSY EWK combinations effort.

Chapter 3 gives an introduction to the signals of chargino–neutralino pair production relevant for this thesis, and the corresponding backgrounds to the three-lepton final state.

Chapter 4 gives an introduction to some of the methodology used to analyze the vast amount of data collected with the ATLAS detector in the search for chargino–neutralino pair production in three-lepton final states.

Chapter 5 summarizes the three-lepton off-shell WZ analysis and presents the corresponding results.

Chapter 6 summarizes two studies based on the three-lepton off-shell WZ analysis, conducted in preparation for future runs of the Large Hadron Collider.

Chapter 7 summarizes my contribution to the ATLAS SUSY EWK combinations effort.

Part 3: Outreach and communication

Chapter 8 summarizes my ATLAS authorship qualification task on the ATLAS@Home project.

Chapter 9 summarizes the communication, outreach and recruitment activities I have contributed to during the course of this Ph.D., mostly as part of my duty work at the Department of Physics.

Part I

Foundations

Chapter 1

Supersymmetry

The Standard Model (SM) is undoubtedly one of the greatest triumphs of modern physics. However, as described in the Introduction, it is not believed to be the final theory of particle physics, and the topic of this thesis is the search for one of its most popular proposed extensions, namely supersymmetry (SUSY). In this chapter, a general introduction to supersymmetry will be given, mostly based on Refs. [30, 31]. More details on the specific supersymmetry model scenarios relevant for the work presented in this thesis will be given in Chapter 3.

To set the stage, a brief introduction to the Standard Model of particle physics will be given in Section 1.1, including an overview of some of its shortcomings. In Section 1.2, the concept of supersymmetry will be explained, before the Minimal Supersymmetric Standard Model (MSSM) is introduced in Section 1.3. Finally, in Section 1.4, two relevant theoretically motivated realizations of the MSSM are introduced.

1.1 The Standard Model of particle physics

The elementary particles of the Standard Model can be divided into two main categories. The *fermions* make up matter, while the *bosons* are force-mediating particles. Figure 1.1 shows an overview of the Standard Model. The three left-most columns list the fermions, divided into *quarks* and *leptons*. The lighter first-generation fermions make up all ordinary atomic matter, while the heavier fermions only appear as unstable products of particle interactions. The remaining particles in the overview are bosons, where the W and Z *bosons* mediate the weak nuclear force, the *gluon* g mediates the strong nuclear force, and the *photon* γ mediates the electromagnetic force. As gravity is not included in the Standard Model, the corresponding (hypothetical) force-mediating *graviton* is listed as being outside of the Standard Model. Finally, the Higgs boson is introduced as part of the so-called *Higgs mechanism*, in which the elementary particles acquire mass through *electroweak symmetry breaking*.

The elementary particles interact via some force if they carry the corresponding *charge*, which is conserved in the interaction. Only particles that are electrically charged interact via the electromagnetic force, only particles with *(weak) isospin* interact via the weak nuclear force, while only particles with *color charge*[1] interact via the strong nuclear force. Only quarks and gluons carry color charge. In addition, all elementary particles carry an intrinsic property referred to as *spin*, which can be seen as some type of internal angular momentum. Fermions carry half-integer spin, while bosons carry integer spin. Further, all

[1]There are three possible color charges: red, green and blue. Despite the naming, color charge has nothing to do with the visual perception of color.

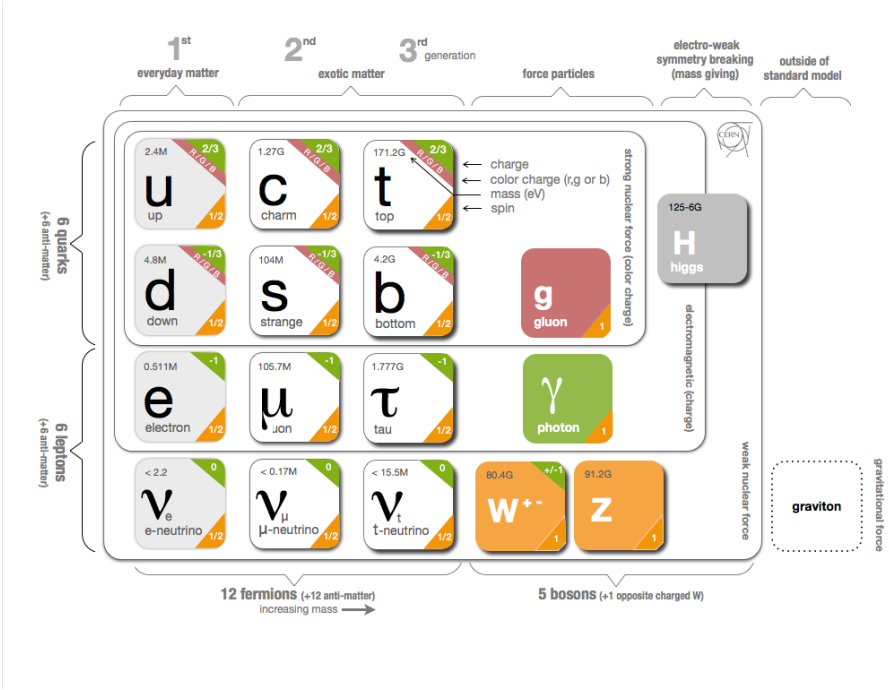

Figure 1.1: Overview of the elementary particles of the Standard Model [32]. The charge referred to in this overview is electric charge. In this overview created right after the Higgs boson discovery in 2012, the Higgs boson mass is listed to be 125-126 GeV. Since then, this mass has been measured more precisely, and the current value is 125.25 ± 0.17 GeV [33].

matter particles (fermions) have corresponding *antiparticles*. An antiparticle has the same mass and spin as its counterpart, but opposite charges. Some particles can be their own antiparticle, e.g. the neutrinos.

1.1.1 Lagrangian and symmetries

The above description of the Standard Model gave a somewhat superficial introduction to its ingredients. If we dive deeper, the fundamental constituents of the Standard Model are *quantum fields*, and particles are treated as excited states of these fields. This theoretical framework is called *quantum field theory* (QFT), which combines the theories of quantum mechanics, classical field theory and special relativity. The starting point of a quantum field theory is the *Lagrangian density* $\mathcal{L}$ (often simply referred to as the "Lagrangian"), which is a function of quantum fields and their derivatives. There is one quantum field per particle type in the theory, and interactions between different particle types are described by interaction terms involving the corresponding quantum fields. Such interactions can be visualized and "evaluated" using so-called *Feynman*

diagrams.

A transformation that leaves the Lagrangian invariant is referred to as a *symmetry*. There are two types of symmetries for quantum field theories. Invariance under transformations of spacetime, such as rotation and translation, are referred to as *external spacetime symmetries*. Invariance under transformations of the fields themselves are referred to as *internal gauge symmetries*. The term "gauge" refers to redundant degrees of freedom in the Lagrangian, meaning that they have no observational consequences. As will become clear in the following, the fundamental forces are closely related to such gauge symmetries.[2]

Symmetries are described in terms of mathematical groups. A set of gauge transformations that leaves the Lagrangian invariant form a *gauge group*. The Standard Model is based on invariance under three such groups, collectively known as the Standard Model gauge group, denoted $SU(3)_C \times SU(2)_L \times U(1)_Y$.[3] Here, $SU(3)_C$ is the symmetry group of *quantum chromodynamics* (QCD), which is the quantum field theory of the strong interaction. The subscript C refers to the color charge, which is the conserved charge in this interaction. Further, $SU(2)_L$ is the symmetry group of the weak force, for which weak isospin I is the conserved charge. In this case, the subscript L refers to that the weak force only acts on *left-chiral* particles (and antiparticles of *right-chiral* particles).[4] For the $U(1)_Y$ symmetry group, the conserved quantity is the *weak hypercharge* $Y = 2(Q - I_3)$, where Q is electric charge and I_3 is the third component of the weak isospin.

One important feature of the Standard Model is that the electromagnetic and weak interactions are unified into a more fundamental *electroweak interaction*, described by the combined gauge group $SU(2)_L \times U(1)_Y$. However, due to the electroweak symmetry breaking needed to give the particles their masses, this group is broken down to $U(1)_{\text{em}}$, so that the weak and electromagnetic interactions appear as two different forces at low energies. $U(1)_{\text{em}}$ is the symmetry group of *quantum electrodynamics* (QED), the quantum field theory of the electromagnetic interaction, conserving electric charge.

Fermions are represented by four-component *Dirac spinor fields*, describing both the particle and the antiparticle, with two possible spin states for each of them.[5] Fermions that are their own antiparticles are called *Majorana fermions*. In order to be acted upon by $SU(n)$ transformations, the fermion fields have to be put into vectors referred to as *gauge multiplets*. The $SU(2)$ and $SU(3)$ transformations are defined in terms of 2×2 and 3×3 matrices,[6] and they thus

[2] In fact, the force-mediating bosons are often referred to as *gauge bosons*.

[3] The "special unitary group" of degree n, $SU(n)$, is the Lie group (meaning that it describes a continuous symmetry) of $n \times n$ unitary matrices of determinant 1. The special unitary group is a subgroup of the more general unitary group $U(n)$, whose unitary matrices may have complex determinants with absolute value 1, rather than real 1 in the special case.

[4] In order to explain observations of parity symmetry (spatial inversion) violation of the weak interaction, it is defined as a *chiral* theory.

[5] All fermions have spin-1/2, but they exist in two different *spin states*, referred to as spin $+1/2$ and spin $-1/2$.

[6] These also form the fundamental representations acting on the fermions.

need two- and three-dimensional vectors to act upon, respectively, referred to as $SU(2)$ *doublets* and $SU(3)$ *triplets*. Fermions that are not charged under a particular force are referred to as *singlets* under the corresponding gauge group. For instance, leptons are $SU(3)$ singlets since they are not charged under the strong force.

The gauge bosons are described by vector (spin-1) fields, which appear when applying the so-called *gauge principle*. Simply put, we start out with a Lagrangian containing the free (non-interacting) fermion fields, identify *global* transformations of these fields that leave the Lagrangian unchanged, promote these transformations to *local* (or gauge) transformations and demand that the Lagrangian should still be invariant. This latter criterion forces the introduction of spin-1 vector fields, which are the vector bosons.

1.1.2 The need for new physics

Over the years, the Standard Model has shown to be in excellent agreement with experimental results across a range of observables. However, despite its success, the Standard Model is not believed to be the final theory of particle physics. For instance, as explained in the Introduction, the anomalous magnetic moment of the muon gives rise to the probably most clear discrepancy between the Standard Model and measurements today. There are also several other motivations for physics beyond the Standard Model. Some originate from unexplained observational phenomena, while others stem from a more theoretical perspective. Some of these motivations are explained below. Please note that this is not an exhaustive list.

Baryon asymmetry

The naive expectation is that equal amouts of matter and antimatter should have been produced in the Big Bang. However, the fact that the world around us is made up of baryonic[7] matter means that there is an imbalance of matter and antimatter in the observable universe. This is referred to as the *baryon asymmetry problem*, or simply the *matter asymmetry problem*, to which the Standard Model offers no explanation.

Neutrino masses

Neutrinos are assumed to be massless in the Standard Model. However, the observed *neutrino oscillations* [34, 35] are only possible for non-zero neutrino masses. The upper limit on their masses are very small, e.g. 0.8 eV in Ref. [36] published in 2023, and it is unknown whether they are Majorana or Dirac fermions.

[7] Baryons are composite subatomic particles containing three quarks, e.g. protons and neutrons.

Dark matter

The existence of *dark matter* is inferred from its gravitational effects on visible matter and gravitational lensing of background radiation. An example is the *galaxy rotation problem* [37]. Stars rotating in the periphery of spiral galaxies are rotating so fast that the galaxies would fly apart if the gravity of their constituent stars and gas is all that is holding them together. While "normal" baryonic matter makes up 5% of the total mass-energy content of the universe, dark matter is believed to make up 27% — i.e. five times more. Today, the most widely accepted explanation is that dark matter is composed of weakly interacting massive particles (WIMPs), that interact only through gravity and the weak force. The only such candidates in the Standard Model are the neutrinos, but they are very low in mass (see above) and cannot make up the total amount of dark matter.

Grand unification

The Standard Model is widely believed to be an effective low-energy model of a more fundamental high-energy model. In such a *Grand Unified Theory* (GUT) [38–41], the three interactions of the Standard Model should unite at a higher energy and act as a single interaction under some larger gauge group. In practice, this would mean that the three Standard Model *coupling constants* would unite at a high energy scale. However, by evolving the couplings to higher energies using so-called *renormalization group equations* (RGEs), they fail to intersect. Although this is not a direct problem with the Standard Model itself, it is often used as an argument for physics beyond the Standard Model.

Higgs mass hierarchy problem

The Higgs boson discovered in 2012 has a mass of 125.25±0.17 GeV [33]. However, the mass predicted by the Standard Model is much higher due to the divergence of *quantum loop corrections* to the "bare" Higgs mass. This divergence can be dealt with by introducing a cut-off scale Λ, above which the Standard Model in any case is not valid. The loop corrections at leading order in Λ are then [31]

$$\Delta m_h^2 = -\frac{|\lambda_f|^2}{8\pi^2}\Lambda^2 + \frac{\lambda_s}{16\pi^2}\Lambda^2 + ..., \tag{1.1}$$

where the first and second terms come from fermion and scalar loops, respectively, and λ_f and λ_s are their respective couplings to the Higgs boson.[8] The cut-off scale Λ is often taken to be the GUT scale ($\mathcal{O}(10^{16}$ GeV)) or the Planck scale ($\mathcal{O}(10^{19}$ GeV)), which makes it difficult to keep the Higgs mass at the electroweak scale of 10^2 GeV, as measured. This is referred to as the *Higgs hierarchy problem*.

[8] The terms left out are at most logarithmically dependent on the cut-off scale Λ.

1.2 Introducing supersymmetry

The need for physics beyond the Standard Model was argued above. One of the most popular extensions of the Standard Model is supersymmetry, which proposes a symmetry between fermions and bosons. In supersymmetry, each Standard Model particle has a *superpartner sparticle*, which only differs from the particle by half a unit of spin. If Q is a supersymmetry operator that alters the spin by 1/2, this can be illustrated schematically as

$$Q|\text{fermion}\rangle = |\text{boson}\rangle, \qquad Q|\text{boson}\rangle = |\text{fermion}\rangle. \tag{1.2}$$

The bosonic superpartners of the Standard Model fermions are called *sfermions*. The rule of thumb for individual sfermion names is also to add a prefix "s-" to the Standard Model fermion name, e.g. *selectron*. Further, the fermionic superpartners of the Standard Model gauge bosons are collectively referred to as *gauginos*. Also for the individual gauginos, the naming convention is to add a suffix "-ino" to the Standard Model boson name, e.g. *photino*. A tilde (~) is used to indicate supersymmetric particles. For instance, the above-mentioned selectron and photino are denoted $\tilde{e}$ and $\tilde{\gamma}$, respectively.

Just from this, some observations can be made. As no two Standard Model particles only differ by half a unit of spin, supersymmetry introduces many new particles. Further, as no supersymmetric particles have yet been observed, supersymmetry must be a broken symmetry if it exists. If it was unbroken, the sparticles would have had the same masses as their corresponding particles, meaning that we should have observed them already.

1.2.1 Extending the Poincaré group

The general concept of supersymmetry was introduced above, but what was its origin? Briefly, supersymmetry came about in the 1960s and 1970s as a result of an attempt at unifying internal gauge and external spacetime symmetries. More specifically, an attempt to extend the external spacetime symmetries to also include the internal gauge symmetries in a non-trivial way, i.e. without all the generators of the internal gauge symmetries commuting with the spacetime symmetry generators. When working with a mathematical group, it is often more instructive to look at the corresponding *algebra*, which is expressed in terms of the *generators* of the group. The group generators are group elements that can produce all the elements in the group by repeated application of the generators on themselves and each other.

The spacetime symmetry group which all physical objects obeying special relativity must be invariant under is the Poincaré group. This is the group of all Lorentz boosts and rotations, as well as translations. The corresponding generators must satisfy the Poincaré algebra:

$$[P_\mu, P_\nu] = 0, \tag{1.3}$$

$$[M_{\mu\nu}, P_\rho] = -i(g_{\mu\rho}P_\nu - g_{\nu\rho}P_\mu), \tag{1.4}$$

$$[M_{\mu\nu}, M_{\rho\sigma}] = -i(g_{\mu\rho}M_{\nu\sigma} - g_{\mu\sigma}M_{\nu\rho} - g_{\nu\rho}M_{\mu\sigma} + g_{\nu\sigma}M_{\mu\rho}), \tag{1.5}$$

where $M_{\mu\nu}$ are the generators of Lorentz boosts and rotations, P_μ are the generators of translations, and $g_{\mu\nu}$ are coefficients of the Minkowski metric tensor g. These generators commute with the generators B_i of the Standard Model gauge groups, i.e.

$$[P_\mu, B_i] = [M_{\mu\nu}, B_i] = 0. \tag{1.6}$$

In 1967, Coleman and Mandula showed that there exists no Lie-algebra-based[9] extension of the Poincaré algebra that fulfills the goal of unifying external and internal symmetries [42]. This is referred to as a *no-go theorem*. However, in 1975, Haag, Lopuszanski and Sohnius wanted to see if they could get around this no-go theorem by allowing anticommutators in Lie algebras, by introducing the concept of *graded Lie algebras*, also called *superalgebras* [43]. A superalgebra L is a direct sum of two Lie algebras L_0 and L_1, $L = L_0 \oplus L_1$, with a special binary operation called grading giving anticommutation relations for generators in L_1. By combining the Poincaré algebra with an algebra spanned by a set of four new generators Q_a, $a = 1, 2, 3, 4$, called *Majorana spinor charges*, Haag *et. al* came up with the supersymmetric extension of the Poincaré algebra — the super-Poincaré algebra.[10]

Instead of working with the four-component Majorana spinor charges, it is often useful to work with two-component *Weyl spinors* Q_A, related by

$$Q_a = \begin{pmatrix} Q_A \\ \bar{Q}^{\dot{A}} \end{pmatrix}, \tag{1.7}$$

where $\bar{Q}_{\dot{A}}$ is the hermitian conjugate of Q_A, and $A = 1, 2$ and $\dot{A} = 1, 2$ are distinct indices. The super-Poincaré algebra is then given by the Poincaré algebra, Equations (1.3)–(1.5), plus the (anti)commutation relations

$$\{Q_A, Q_B\} = \{\bar{Q}_{\dot{A}}, \bar{Q}_{\dot{B}}\} = 0, \tag{1.8}$$

$$\{Q_A, \bar{Q}_{\dot{B}}\} = 2\sigma^\mu_{A\dot{B}} P_\mu, \tag{1.9}$$

$$[Q_A, P_\mu] = [\bar{Q}_{\dot{A}}, P_\mu] = 0, \tag{1.10}$$

$$[Q_A, M^{\mu\nu}] = \sigma^{\mu\nu B}_A Q_B, \tag{1.11}$$

where $\sigma^{\mu\nu} = \frac{i}{4}(\sigma^\mu\bar{\sigma}^\nu - \sigma^\nu\bar{\sigma}^\mu)$, with $\sigma^\mu = (\mathbb{1}_{2\times2}, \sigma^i)$, and σ^i are the two-dimensional Pauli matrices. The transformations corresponding to this super-Poincaré algebra are called *supersymmetry transformations*, and the objects transforming under such transformations can be represented by so-called *superfields*.

Note that supersymmetry as defined in Equations (1.8)–(1.11) actually does not fulfill the original goal of unifying external and internal symmetries, since

[9] In physics, we are particularly interested in so-called Lie groups (named after the Norwegian mathematician Sophus Lie), which are used to describe continuous symmetries.

[10] The super-Poincaré algebra is often simply called the superalgebra, which can be a bit confusing.

no gauge generators B_i appear. The internal symmetries can appear for so-called $N > 1$ *supersymmetries*, where the super-Poincaré algebra is extended by introducing more Majorana spinor charges, labeled Q_a^α, where $\alpha = 1, ..., N$. However, such $N > 1$ supersymmetries introduce an extensive number of extra particles, and do not seem to be realized in nature. Nevertheless, as supersymmetry has some interesting features (such that it can be shown to be the largest possible extension of the Poincaré group), it ended up becoming a quite popular theory. In Section 1.2.3, we will see how supersymmetry can accomodate several of the shortcomings of the Standard Model described in Section 1.1.2. But first, we will see how the additional particles predicted by supersymmetry come into play.

1.2.2 Superfields and (s)particles

There are two different types of superfields, corresponding to the *irreducible representations* of the super-Poincaré algebra. The two types are referred to as scalar and vector superfields. The superfields do not correspond to individual particles directly, instead, they contain fermionic and scalar degrees of freedom related by supersymmetry transformations (Equation (1.2)).

After applying the equations of motion, a scalar superfield contains two scalar (bosonic) degrees of freedom and two fermionic degrees of freedom, where the former are contained in a complex scalar component field and the latter are contained in a two-component Weyl spinor. Note that scalar superfields and Weyl spinors are either left- or right-handed.[11] A vector superfield, after applying the equations of motion, contains a massless vector boson with two bosonic degrees of freedom and two Weyl spinors of opposite handedness with two fermionic degrees of freedom. The two Weyl spinors in a vector superfield are hermitian conjugates, and so they contain the same two degrees of freedom.

Fermions are constructed from scalar superfields. To construct a Dirac fermion and its antiparticle, four fermionic degrees of freedom are needed, or rather two different Weyl spinors of opposite handedness. As each scalar superfield contains two bosonic degrees of freedom in addition to a Weyl spinor, two scalar particle–antiparticle pairs are introduced when constructing a Dirac fermion. These are the sfermions, the bosonic superpartners of the Standard Model fermions.

Further, one vector superfield per Standard Model gauge boson is needed, each containing a massless vector boson with two bosonic degrees of freedom. The two "excessive" Weyl spinors in each superfield combine into the gauginos, the fermionic superpartners of the Standard Model gauge bosons.

1.2.3 Supersymmetry solutions

In this section, we will see why supersymmetry has become such a popular theory by briefly reviewing its solutions to some of the shortcomings of the Standard Model presented in Section 1.1.2.

[11] Corresponding to the two inequivalent fundamental representations of the $SL(2, \mathbb{C})$ group homomorphic to the Poincaré group.

Dark matter

As explained in Section 1.1.2, the only dark-matter candidates in the Standard Model are the neutrinos, which in any case cannot make up the total amount. Supersymmetry introduces many new particles, including some possible candidates for particle dark matter [44, 45]. In particular, the massive fermionic superpartners of the Standard Model gauge bosons can fulfill the criteria for being WIMPs.

Grand unification

As explained in Section 1.1.2, when evolving the Standard Model coupling constants to higher energies using RGEs, they fail to intersect. In supersymmetry, however, the evolution of the coupling constants is altered, and in some realizations they can indeed unify into a common coupling g_u at the GUT scale.

Higgs mass hierarchy problem

As supersymmetry introduces many new particles, the number of correction terms to the Higgs mass will in fact increase by introducing supersymmetry. However, there are exactly twice as many bosons as fermions in supersymmetry, and their couplings can be shown to satisfy the relation $|\lambda_f|^2 = \lambda_s$. This means that the correction terms from Standard Model fermions cancel out the correction terms from supersymmetry bosons in Equation (1.1), and vice versa. For unbroken supersymmetry, in which the Standard Model particles and their corresponding sparticles are mass degenerate, this cancellation is exact for all orders of Λ. This is currently one of the main motivations for supersymmetry.

For broken supersymmetry, however, the non-leading terms in Equation (1.1) become important, as they are mass-dependent. For so-called *softly* broken supersymmetry, the contributions to the Higgs mass is at most [31]

$$\Delta m_h^2 = -\frac{\lambda_s}{16\pi^2} m_s^2 \ln\left(\frac{\Lambda^2}{m_s^2}\right) + ..., \tag{1.12}$$

at leading order in Λ, where m_s is the mass scale of the soft-breaking terms, which can be seen as the "extra mass" of the supersymmetric particles compared to their corresponding Standard Model particles.[12] In order to keep the Higgs mass contributions in Equation (1.12) small, m_s cannot be too large. This is referred to as the *little hierarchy problem*, and is regarded as the main motivation for supersymmetry to be manifest at a relatively low energy scale.

[12] In fact, the label "soft term" refers to supersymmetry-breaking terms that at worst give mass corrections logarithmic in Λ.

1.3 The Minimal Supersymmetric Standard Model

The focus of this thesis will be on the Minimal Supersymmetric Standard Model (MSSM) [46, 47], which is the supersymmetric model with the smallest field content consistent with the Standard Model. The MSSM is based on the minimal extension of the Poincaré algebra, i.e. $N = 1$ supersymmetry. In the following, the superfields necessary to recover the Standard Model particles will be introduced, using notation conventional in phenomenology (as opposed to pure theory).

For the leptons, we introduce the left-handed scalar superfields

$$L_i = \begin{pmatrix} \nu_i \\ l_i \end{pmatrix} \quad \text{and} \quad \bar{E}_i, \tag{1.13}$$

where l_i and $\bar{E}_i$ are for the charged leptons, ν_i is for the (left-handed) neutrinos and the generation index i runs from 1 to 3. The $\bar{E}_i$ superfield contains the part of the (s)particles that do not couple to $SU(2)_L$, while l_i and ν_i are placed in $SU(2)_L$ doublets L_i. From these fields and their hermitian conjugates, all of the Standard Model leptons and their bosonic superpartners, collectively called *sleptons*, are constructed. Similarly, for up- and down-type quarks we introduce the scalar left-handed superfields

$$Q_i = \begin{pmatrix} u_i \\ d_i \end{pmatrix}, \quad \bar{U}_i \quad \text{and} \quad \bar{D}_i, \tag{1.14}$$

where again the generation index runs from 1 to 3, and u_i and d_i are placed in $SU(2)_L$ doublets Q_i.[13] From these fields and their hermitian conjugates, all of the Standard Model quarks as well as their bosonic superpartners, called *squarks*, are constructed.

For the gauge bosons, we need to introduce one vector superfield per generator of the Standard Model gauge groups, which is eight, three and one for $SU(3)_C$, $SU(2)_L$ and $U(1)_Y$, respectively.[14,15] The corresponding vector superfields are denoted

$$C^a, \quad W^a \quad \text{and} \quad B^0, \tag{1.15}$$

where a runs from 1 to 8 for C^a and from 1 to 3 for W^a. These altogether 12 vector superfields give the g (eight color combinations in total), $W^{1,2,3}$ and B^0 gauge bosons of the Standard Model,[16] as well as their fermionic superpartners referred to as gluino, wino and bino, respectively, denoted $\tilde{g}$, $\tilde{W}^a$ and $\tilde{B}^0$.

The only Standard Model particle then left to introduce is the Higgs boson. In the MSSM, two Higgs superfield $SU(2)_L$ doublets are needed in order to give masses to both up- and down-type quarks:

$$H_u = \begin{pmatrix} H_u^+ \\ H_u^0 \end{pmatrix} \quad \text{and} \quad H_d = \begin{pmatrix} H_d^0 \\ H_d^- \end{pmatrix}, \tag{1.16}$$

[13] Note that the color indices are omitted for simplicity.

[14] This requirement is needed to obey gauge invariance.

[15] The $SU(n)$ groups have $n^2 - 1$ generators.

[16] Before the electroweak symmetry breaking, in which $W^{1,2,3}$ and B^0 mix and form the physical (mass-eigenstate) bosons $W^{\pm}, Z^0$ and γ.

where the indices indicate which quarks they give mass to and the signs indicate the electric charge of the component superfields. These four left-handed scalar superfields introduce altogether four Weyl spinors, with two fermionic degrees of freedom each, and eight bosonic degrees of freedom. Three of the latter are absorbed into mass terms for the $W^{\pm}$ and Z^0 bosons through the Higgs mechanism (as in the Standard Model), while the remaining five form the physical mass eigenstates h^0, H^0, A^0 and $H^{\pm}$. The Weyl spinors combine into so-called *higgsinos*. In the next section, the Higgs sector of the MSSM will be discussed further, as it has some important features.

1.3.1 The MSSM Higgs sector

Compared to the Standard Model Lagrangian, the only new parameter in the (unbroken) MSSM Lagrangian is the Higgs superfield mass parameter, denoted μ. This parameter is introduced via a new mass term in the so-called superpotential of the MSSM,[17] which is quadratic in the Higgs doublets.[18] However, an additional 104 new parameters are introduced via the soft-breaking terms, which will be discussed in Section 1.3.3.

Further, in the MSSM, these soft-breaking terms are responsible for boosting the sparticle masses, but electroweak symmetry breaking is still needed for the Standard Model masses. The particles acquire their masses through the Higgs mechanism, in which a complex scalar field doublet with a non-vanishing vacuum expectation value is introduced, such that the electroweak $SU(2)_L \times U(1)_Y$ symmetry of the Standard Model is "spontaneously" broken down to the $U(1)_{\text{em}}$ symmetry of quantum electrodynamics. This means that the vacuum state breaks the symmetry that still exists in the Lagrangian. In the Standard Model, the Higgs mechanism is put in by hand through the choice of a potential for the Higgs fields. In the MSSM, however, so-called *radiative electroweak symmetry breaking* (REWSB) [48, 49] gives an explanation for the Higgs mechanism by creating a suitable Higgs potential. The term radiative refers to the fact that the symmetry breaking in this case is driven by quantum corrections from RGE running of the coupling constants and soft-masses of the model.

One of the desired results of the symmetry breaking is that the neutral components of the Higgs doublets acquire a non-vanishing vacuum expectation value, $v_u = \langle H_u^0 \rangle$ and $v_d = \langle H_d^0 \rangle$, respectively. To get the Standard Model boson masses, these must satisfy the experimental constraint

$$v_u^2 + v_d^2 \equiv v^2 = \frac{2m_Z^2}{g^2 + g'^2} \approx (174\,\text{GeV})^2, \tag{1.17}$$

where m_Z is the Z-boson mass, and g and g' are the $SU(2)_L$ and $U(1)_Y$ coupling constants, respectively. The remaining freedom in the ratio of the two vacuum

[17] Corresponding to the (non-gauge) interaction terms of an ordinary quantum field theory.

[18] The term is $\mu H_u^T i\sigma_2 H_d$, where σ_2 is the second Pauli matrix. The $i\sigma_2$ construction preserves $SU(2)_L$ invariance.

expectation values is usually parameterized as

$$\tan\beta \equiv \frac{v_u}{v_d}, \tag{1.18}$$

where by convention $0 < \beta < \pi/2$.

1.3.2 R-parity

In the Standard Model Lagrangian, there are no terms that violate conservation of baryon number B and lepton number L. And indeed, no processes violating B- and L-conservation have been observed experimentally. However, in the MSSM, some of the terms in the superpotential do not conserve B and L. As this leads to some unacceptable predictions, such as rapid proton decay, these terms need to be suppressed. This is done by introducing a new symmetry. In the MSSM, all interactions are required to conserve the discrete and multiplicative R-parity P_R [50], defined as

$$P_R = (-1)^{3(B-L)+2s}, \tag{1.19}$$

where s is spin. With this definition, all Standard Model particles and the additional Higgs bosons of the MSSM have $P_R = +1$, while all sparticles have $P_R = -1$.

In addition to suppressing the MSSM superpotential terms violating B- and L-conservation, conservation of R-parity leads to three very important phenomenological consequences:

1. When produced from Standard Model particles, sparticles can only occur in pairs.
2. Sparticles decay into an odd number of lighter sparticles.
3. All sparticle decay chains end with the lightest supersymmetric particle (LSP), which has to be absolutely stable.

As the LSP has not yet been observed experimentally, it has to be invisible to detectors if it exists. This means that it should be at most weakly interacting, i.e. both color and electrically neutral. It is therefore a good candidate for particle dark matter, mentioned in Section 1.2.3.

1.3.3 Supersymmetry breaking

As discussed in Section 1.2, supersymmetry must be a broken symmetry in order to produce the mass differences between the supersymmetric particles and their corresponding Standard Model particles required by experimental results. However, the underlying symmetry-breaking mechanism is unknown. In such cases, it is common to use an effective phenomenological theory constructed from an originally symmetric (non-broken) theory by adding terms that explicitly breaks the symmetry. This is referred to as *explicit symmetry breaking*, and is done in the MSSM.

All viable supersymmetry-breaking terms that satisfy a few phenomenologically motivated constraints must be included. First, only terms that break

supersymmetry softly are allowed. As explained in Section 1.2.3, one of the advantages of supersymmetry is that the quadratically divergent loop corrections to the Higgs boson mass are canceled out. Soft supersymmetry-breaking terms preserve this cancellation. Second, the full MSSM Lagrangian must remain invariant under the Standard Model gauge group, $SU(3)_C \times SU(2)_L \times U(1)_Y$. Finally, only terms conserving R-parity are allowed, as discussed in the previous section. Altogether 104 new parameters are added to the MSSM Lagrangian via such soft-breaking terms. The two that will become the most relevant in the following are M_1 and M_2, which are the bino and wino soft-mass parameters, respectively, breaking the mass degeneracy between the Standard Model gauge bosons and their superpartners.

1.3.4 Particle phenomenology of the MSSM

The field content of the MSSM was introduced at the very beginning of Section 1.3, together with some information on which (s)particles the different fields form. Here, some more details on the physical sparticles will be given. Due to electroweak symmetry breaking, the sparticle *mass eigenstates* are in general mixtures of the *gauge eigenstates*. An overview of the gauge and mass eigenstates of the MSSM sparticles are listed in Table 1.1.

As described in Section 1.2.2, two superpartner scalar particles are introduced with each Standard Model fermion. For instance, the scalar superpartners of the up-quark u are labeled $\tilde{u}_R$ and $\tilde{u}_L$. Note that scalars do not have any notion of handedness, and that the indices R and L are just part of the conventional name. For the sfermions, the amount of mixing is usually assumed to be proportional to the masses of the corresponding Standard Model fermions.[19] The mixing is thus negligible for the two first generations of squarks and sleptons. All mixed mass eigenstates are numbered according to increasing mass. For instance, $\tilde{t}_1$ is the lighter of the two stops.

The mixing of the MSSM Higgs fields was already briefly discussed when introducing them. In conclusion, there are five Higgs bosons in the MSSM after the Higgs mechanism. The h^0 and H^0 are neutral scalars, where the former is the lighter of the two and said to be "Standard Model-like". The $H^\pm$ are charged scalars, while the A^0 is a so-called pseudo-scalar, meaning that it changes sign under a parity inversion (which true scalars do not).

Of the gauginos, the fermionic superpartners of the Standard Model gauge bosons, only the gluino $\tilde{g}$ has identical gauge and mass eigenstates. As the gluino is a color-octet Majorana fermion, it has nothing to mix with in the MSSM. The bino $\tilde{B}^0$ and winos $\tilde{W}^0$ and $\tilde{W}^\pm$ mix with the higgsinos $\tilde{H}_u^+$, $\tilde{H}_u^0$, $\tilde{H}_d^0$ and $\tilde{H}_d^-$ and form the so-called *neutralinos* and *charginos*. The neutralinos are four neutral Majorana fermions, labeled $\tilde{\chi}_i^0$, $i = 1, 2, 3, 4$. The charginos are two charged fermion–antifermion pairs, labeled $\tilde{\chi}_i^\pm$, $i = 1, 2$. The neutralinos and charginos are collectively referred to as *electroweakinos*. The lightest neutralino $\tilde{\chi}_1^0$ is often assumed to be the lightest supersymmetric particle, and is considered

[19] Or more precisely the Yukawa coupling strengths of the fermions to the Higgs boson.

Table 1.1: The particle spectrum of the MSSM. The Standard Model fermions and gauge bosons are not included.

Name	Spin	P_R	Gauge eigenstates	Mass eigenstates
Higgs bosons	0	+1	$H_u^0\ H_d^0\ H_u^+\ H_d^-$	$h^0\ H^0\ A^0\ H^\pm$
squarks	0	−1	$\tilde{u}_L\ \tilde{u}_R\ \tilde{d}_L\ \tilde{d}_R$	(same)
			$\tilde{s}_L\ \tilde{s}_R\ \tilde{c}_L\ \tilde{c}_R$	(same)
			$\tilde{t}_L\ \tilde{t}_R\ \tilde{b}_L\ \tilde{b}_R$	$\tilde{t}_1\ \tilde{t}_2\ \tilde{b}_1\ \tilde{b}_2$
sleptons	0	−1	$\tilde{e}_L\ \tilde{e}_R\ \tilde{\nu}_e$	(same)
			$\tilde{\mu}_L\ \tilde{\mu}_R\ \tilde{\nu}_\mu$	(same)
			$\tilde{\tau}_L\ \tilde{\tau}_R\ \tilde{\nu}_\tau$	$\tilde{\tau}_1\ \tilde{\tau}_2\ \tilde{\nu}_\tau$
neutralinos	1/2	−1	$\tilde{B}^0\ \tilde{W}^0\ \tilde{H}_u^0\ \tilde{H}_d^0$	$\tilde{\chi}_1^0\ \tilde{\chi}_2^0\ \tilde{\chi}_3^0\ \tilde{\chi}_4^0$
charginos	1/2	−1	$\tilde{W}^\pm\ \tilde{H}_u^+\ \tilde{H}_d^-$	$\tilde{\chi}_1^\pm\ \tilde{\chi}_2^\pm$
gluino	1/2	−1	$\tilde{g}$	(same)

to be a viable dark-matter candidate. As the search for charginos and neutralinos is the topic of this thesis, we will review these particles in a bit more detail in the following.

Neutralinos and charginos

In the gauge eigenstate basis

$$(\tilde{\psi}^0)^T = \left(\tilde{B}^0, \tilde{W}^0, \tilde{H}_d^0, \tilde{H}_u^0\right), \tag{1.20}$$

the neutralinos can be expressed as

$$\tilde{\chi}_i^0 = N_{i1}\tilde{B}^0 + N_{i2}\tilde{W}^0 + N_{i3}\tilde{H}_d^0 + N_{i4}\tilde{H}_u^0 \tag{1.21}$$

where the coefficients N_{ij} indicate the size of the component of each field in the basis. Further, in this basis, the neutralino mass term can be written as

$$\mathcal{L}_{m_{\tilde{\chi}^0}} = -\frac{1}{2}(\tilde{\psi}^0)^T M_{\tilde{\chi}^0}\tilde{\psi}^0 + \text{c.c.}, \tag{1.22}$$

where the mass matrix is found from the Lagrangian to be

$$M_{\tilde{\chi}^0} = \begin{bmatrix} M_1 & 0 & -c_\beta s_{\theta_W} m_Z & s_\beta s_{\theta_W} m_Z \\ 0 & M_2 & c_\beta c_{\theta_W} m_Z & -s_\beta c_{\theta_W} m_Z \\ -c_\beta s_{\theta_W} m_Z & c_\beta c_{\theta_W} m_Z & 0 & -\mu \\ s_\beta s_{\theta_W} m_Z & -s_\beta c_{\theta_W} m_Z & -\mu & 0 \end{bmatrix}. \tag{1.23}$$

Here, $c_x = \cos x$ and $s_x = \sin x$, m_Z is the Z-boson mass, θ_W is the so-called *weak mixing angle* (also called the *Weinberg angle*), and β was defined in Equation (1.18). Further, we recognize the bino soft-mass parameter M_1, the wino soft-mass parameter M_2, as well as the supersymmetric mass parameter μ giving mass to the higgsinos. The neutralino masses can be found by diagonalizing this matrix.

Similarly, in the gauge eigenstate basis

$$(\tilde{\psi}^\pm)^T = \left(\tilde{W}^+, \tilde{H}_u^+, \tilde{W}^-, \tilde{H}_d^-\right), \tag{1.24}$$

the chargino mass matrix can be written as

$$M_{\tilde{\chi}^\pm} = \begin{bmatrix} 0 & 0 & M_2 & \sqrt{2} c_\beta m_W \\ 0 & 0 & \sqrt{2} s_\beta m_W & \mu \\ M_2 & \sqrt{2} s_\beta m_W & 0 & 0 \\ \sqrt{2} c_\beta m_W & \mu & 0 & 0 \end{bmatrix}, \tag{1.25}$$

where m_W is the W-boson mass. As for the neutralinos, the chargino masses can be found by diagonalizing this matrix.

1.4 Theoretically motivated models

As explained in Section 1.3.3, explicit symmetry breaking introduces more than 100 new parameters in the MSSM. To improve predictability, it is common to work with realizations of the MSSM involving a smaller number of parameters. Two such theoretically motivated realizations are introduced below.

1.4.1 The constrained MSSM

In the *constrained MSSM* (CMSSM), also known as *minimal supergravity* (mSUGRA) [51–53], so-called Planck-scale Mediated Supersymmetry Breaking (PMSB) is assumed. A common assumption is that the supersymmetry breaking takes place in a hidden sector[20] at some inaccessible, high energy scale, and that the effects of the breaking in this hidden sector are mediated down to the visible sector through some interaction that is common to both sectors. In PMSB, some gravity mechanism at the Planck scale ($\mathcal{O}(10^{19}$ GeV)) is assumed to mediate the supersymmetry breaking from the hidden to the visible sector.

[20] Consisting of superfields that do not couple directly to the superfields containing the Standard Model particles.

Further, motivated by the wish for gauge unification, a minimal form for the parameters at the GUT scale is assumed, resulting in a highly predictive theory parameterized by only four free parameters and a sign:

$$m_{1/2}, \quad m_0, \quad A_0, \quad \tan\beta \quad \text{and} \quad \text{sign}(\mu). \tag{1.26}$$

Here, m_0 is the common (GUT scale) scalar mass, $m_{1/2}$ is the common gaugino soft-mass, while A_0 is the common coupling for trilinear soft-breaking terms. Further, $\tan\beta$ was introduced in Equation (1.18), while $\text{sign}(\mu)$ is the sign of the by now well-known higgsino mass parameter. By choosing these input parameters at the GUT scale and then evolving the mass parameters m_0 and $m_{1/2}$ down to a lower scale, mass splittings between the individual sparticles appear. Because of this running, the model predicts $M_1 < M_2$ and typically has, with some exceptions, $M_1, M_2 \ll |\mu|$. Then $\tilde{\chi}_1^0$ is mostly bino, $\tilde{\chi}_2^0$ is mostly wino, and $\tilde{\chi}_3^0$ and $\tilde{\chi}_4^0$ are mostly higgsino. Further, $\tilde{\chi}_1^\pm$ is mostly wino, $\tilde{\chi}_2^\pm$ is mostly higgsino, and $m_{\tilde{\chi}_2^0} \simeq m_{\tilde{\chi}_1^\pm}$.

1.4.2 Natural supersymmetry

Theories that require fine-tuned cancellations of parameters in order to explain results are often considered to be theoretically unsatisfactory, or rather unnatural. This has led to the concept of *naturalness*, which can be interpreted as the heuristic rule that parameters in a fundamental physical theory should not be too fine-tuned. Note that this is an aesthetic criterion, not a physical one. However, it has shown to be a powerful guiding principle in physics.

Instead of evaluating the naturalness score of already existing supersymmetry models, so-called *natural supersymmetry models* [54, 55] are based on the criterion that the amount of fine-tuning should be kept as low as possible. In such models, $|\mu|$ is typically near the weak scale, predicting light higgsinos. Unless also M_1 and M_2 are relatively small, $\tilde{\chi}_1^0$, $\tilde{\chi}_2^0$ and $\tilde{\chi}_1^\pm$ are all mostly higgsino and have similar masses: $m_{\tilde{\chi}_1^0} \simeq m_{\tilde{\chi}_2^0} \simeq m_{\tilde{\chi}_1^\pm} \sim |\mu|$.

1.5 Summary

This chapter gave a general introduction to supersymmetry. We began by giving a short review of the Standard Model of particle physics and its shortcomings, before introducing the concept of supersymmetry and its origin. After explaining how supersymmetry can solve many of the Standard Model problems, we moved to introducing the Minimal Supersymmetric Standard Model, which is the supersymmetric model with the smallest field content consistent with the Standard Model. Here, the charginos and neutralinos were introduced as the fermionic superpartners of the Standard Model gauge bosons. Finally, two theoretically motivated realizations of the MSSM relevant to this thesis were introduced, namely the CMSSM and natural supersymmetry.

In the next chapter, the experimental setup used to collect the dataset used in this thesis will be introduced, namely the Large Hadron Collider and the ATLAS experiment.

Chapter 2

The Large Hadron Collider and the ATLAS experiment

To search for supersymmetry, an experimental setup is needed. The experimental data used in this thesis was collected with the ATLAS experiment, one of the four big experiments located along the Large Hadron Collider ring at CERN. In this chapter, CERN, the Large Hadron Collider and the ATLAS experiment will be introduced in Section 2.1, Section 2.2 and Section 2.3, respectively.

2.1 CERN

The European Organization for Nuclear Research, known as CERN (from French: Conseil Européen pour la Recherche Nucléaire), is a European research organization that operates the largest particle physics laboratory in the world. The organization, located on the Swiss-Franco border outside Geneva, was established in 1954 by 12 founding states, including Norway.[1] There are currently 23 member states — the latest addition was Serbia in 2019.[2] In addition to contributing to the capital and operating costs of CERN's programs, the member states are represented in the Council, where all important decisions about the organization and its activities are being made. Further, so-called observer status is given to states that have made significant contributions to the CERN infrastructure, and to international organizations that are linked to CERN, such as the European Union (EU) and UNESCO. These observers do not have any voting rights in the Council. CERN also has cooperation agreements and scientific contracts with even more countries. In 2021, more than 11,000 users of 115 different nationalities from institutes in 77 countries contributed to CERN's scientific mission [56]. Figure 2.1 shows a map of the world showing the CERN membership status of countries as of 2018 in shades of blue, where the darkest blue represent member states.

[1] The others were Belgium, Denmark, France, the Federal Republic of Germany, Greece, Italy, the Netherlands, Sweden, Switzerland, the United Kingdom and Yugoslavia.

[2] After its establishment, CERN was subsequently joined by Austria, Spain, Portugal, Finland, Poland, Czechoslovak Republic, Hungary, Bulgaria, Israel, Romania and Serbia. After their mutual independence in 1993, the Czech Republic and the Slovak Republic rejoined CERN. Yugoslavia, one of the founding states, left CERN in 1961.

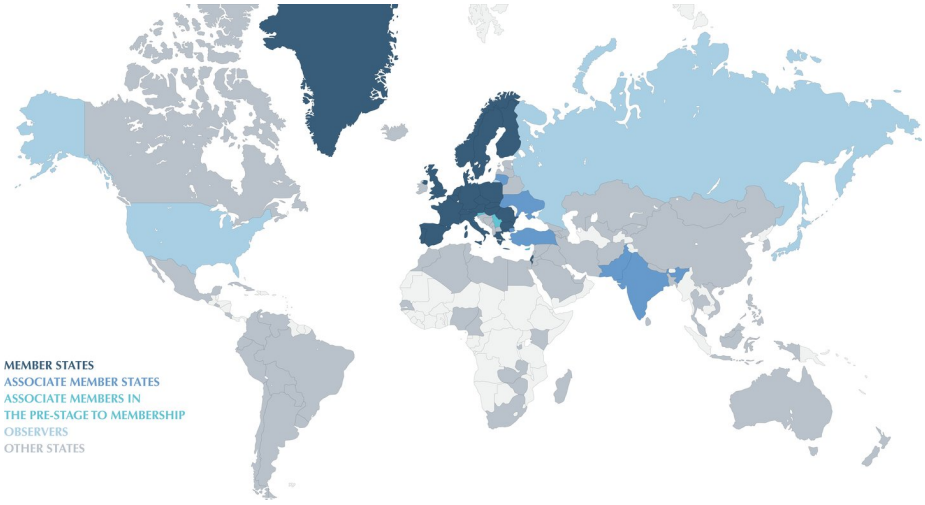

Figure 2.1: Map of the world showing the CERN membership status of countries in shades of blue, where the darkest blue represent member states [57]. Note that this overview shows the status in 2018, i.e. before Serbia became a full member in 2019.

2.2 The Large Hadron Collider

The Large Hadron Collider (LHC) [58, 59], located at CERN, is the world's largest and most powerful particle accelerator to date.[3] Located in a tunnel underground, the LHC consists of a 27-kilometer double ring of superconducting magnets with a number of accelerating structures to boost the particles along the way. The mean depth of the tunnel is 100 m, with a maximum depth of 175 m under the Jura mountains, and a minimum depth of 50 m towards Lake Geneva. Beams of proton bunches, traveling close to the speed of light, circulate in opposite directions inside the two rings.[4] The two beams are made to collide at four different locations along the double ring, around which big experiments have been built: ATLAS and CMS are multi-purpose experiments, while ALICE and LHCb are more specialized.

The LHC was first turned on in 2008. The dataset used in this thesis was collected with the ATLAS experiment between 2015 and 2018, referred to as "Run 2" of the LHC.[5] During this run, the proton bunches containing of order

[3]Hadrons are composite particles consisting of two or more quarks held together by the strong interaction.

[4]The LHC can also accelerate and collide heavy ions, but as only proton–proton collisions are relevant for this thesis, the LHC will be referred to as a proton–proton collider.

[5]Run 1 was between 2009 and 2013, followed by a two-year long shutdown referred to as "Long Shutdown 1" (LS1) for maintenance and upgrades before the start of Run 2 in 2015. After Run 2 came the second long shutdown (LS2), lasting from 2018 to 2022. Run 3 is currently ongoing, and will last until the end of 2025. The full LHC schedule will be discussed in Section 2.4.

10^{11} protons each had a bunch-spacing of 25 ns, corresponding to 7 m. Further, each beam was accelerated up to 6.5 TeV, giving a center-of-mass collision energy ($\sqrt{s}$) of 13 TeV.[6]

2.2.1 The LHC accelerator complex

The LHC is actually the last step in a long and complex chain of accelerators, as illustrated in Figure 2.2. During Run 2, the source of the proton beams for the CERN accelerator complex was Linac2 (Linear accelerator 2), later replaced by Linac4 in 2020. From a bottle of hydrogen gas, hydrogen was passed through an electric field to strip off the electrons, leaving only protons to enter the accelerator. In linear accelerators, cylindrical conductors are charged using radiofrequency cavities. The conductors are alternately positively and negatively charged, such that charged particles passing through are pushed by the conductor behind them and pulled by the conductor ahead of them, causing the particles to accelerate. Further, small quadrupole magnets are used to focus the beam, i.e. making sure the particles remain in a tight beam. At the end of Linac2, the protons had reached an energy of 50 MeV and gained 5% in mass.

The next accelerator in the chain is the Proton Synchrotron Booster (PSB), which consists of four superimposed synchrotron rings. A synchrotron is a cyclical accelerator, in which charged particles are accelerated while moving in a fixed, circular path. As the particles gain energy, the magnetic field which ensures the particles' circular motion is increased to maintain the fixed path. During Run 2, the 50 MeV protons from Linac2 were accelerated up to 1.4 GeV in the PSB, before entering the Proton Synchrotron (PS). The PS was CERN's first synchrotron, and with its circumference of 627 m, it was CERN's flagship accelerator when built in the 1950s. In the PS, the protons are accelerated up to 25 GeV. Further, in the last step before the LHC, the protons are accelerated up to 450 GeV in the Super Proton Synchrotron (SPS), which measures nearly 7 km in circumference. The Standard Model W and Z bosons were discovered using the SPS in 1983.

Finally, the proton beams are injected into the LHC, which is also a synchrotron. Here, acceleration is ensured via 16 radiofrequency cavities. Inside each of these cavities, an oscillating electromagnetic field results in standing waves, creating an electric field along the beams' directions. By careful timing of their arrival, each proton bunch experiences an accelerating field when passing through a cavity. On average, the protons gain 485 keV of energy with each lap around the LHC ring. The beams are guided around the accelerator ring by a

[6]The center-of-mass energy $\sqrt{s}$ is given by the square root of the Lorentz invariant quantity s formed from the total energy E and momentum $\boldsymbol{p}$ of the two initial-state particles, which in natural units with $c = 1$ is [60]

$$s = \left(\sum_{i=1}^{2} E_i\right)^2 - \left(\sum_{i=1}^{2} \boldsymbol{p}_i\right)^2 . \tag{2.1}$$

The center-of-mass energy is typically given in units of *electron volts*, eV.

strong magnetic field maintained by thousands of superconducting electromagnets of different types and sizes. These include 1,232 15 m long dipole magnets which bend the beams, and 392 5–7 m long quadrupole magnets which focus the beams.

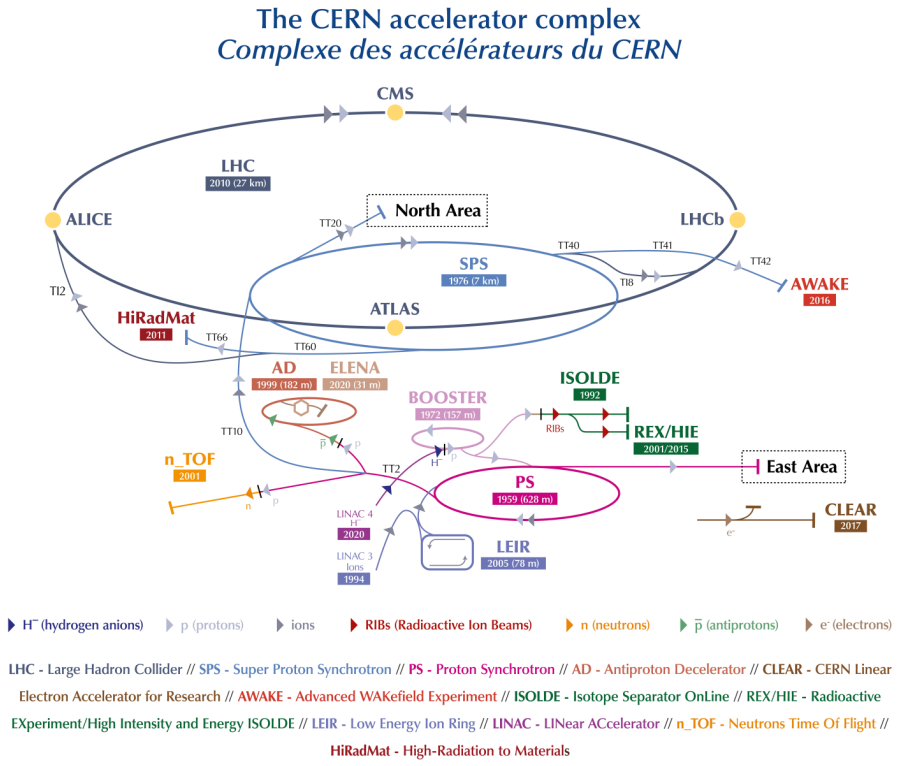

Figure 2.2: An overview of the CERN accelerator complex [61]. The LHC is the last ring (dark blue line) in a chain of particle accelerators. The smaller machines are used to boost the particles to their final energies and provide beams to a whole set of smaller experiments, which also aim to uncover the mysteries of the universe. The ATLAS, CMS, ALICE and LHCb detectors are shown as yellow dots along the LHC ring.

2.2.2 Luminosity

When the two beams of proton bunches are steered towards each other, only a few protons from each bunch end up interacting with protons coming in from the opposite direction. The *instantaneous luminosity* $\mathcal{L}$ is a measure of the expected number of interactions per time per area. In the case of the LHC, assuming that the beams have a Gaussian profile and collide head-on, the instantaneous

luminosity is given by [60]

$$\mathcal{L} = f \frac{n_1 n_2}{4\pi\sigma_x\sigma_y}, \tag{2.2}$$

where n_1 and n_2 are the number of protons in the colliding bunches, f is the frequency at which the bunches collide, and σ_x and σ_y are the root-mean-square (rms) horizontal and vertical beam sizes. The nominal LHC beam parameters relevant for the peak instantaneous luminosity are listed in Table 2.1.

Further, the *integrated luminosity* L is a measure of the total number of interactions over a period of time:

$$L = \int \mathcal{L}\, dt. \tag{2.3}$$

The integrated luminosity has unit inverse area, often given in inverse *barn* (b), where $1\,\mathrm{b} \equiv 10^{-28}\,\mathrm{m}^2$.

2.2.3 Cross-sections

In short, the *cross-section* is a measure of the probability that a given process will occur in a particle collision. In the early days of particle physics, particles were thought to be tiny, indestructible balls. In that case, the probability for such balls to collide would be proportional to their size (unless they were precisely aimed). We have later learned that this is the wrong mental image. Instead, elementary particles behave as tiny waves of probability, which can also interact at a distance. However, the term "cross-section" stuck. The cross-section is defined as having unit area, usually given in barns as introduced above.

Figure 2.3 shows a summary of production cross-sections for a few selected Standard Model processes as measured with the ATLAS experiment (to be introduced in Section 2.3), as a function of center-of-mass energy $\sqrt{s}$. The cross-section values span several orders of magnitude, from order 1 pb (picobarn) for diboson production to order 10^5 pb for production of single bosons. In

Table 2.1: Nominal LHC beam parameters relevant for the peak instantaneous luminosity [62].

Parameter	Value	Description
N	2,808	Number of bunches
n	1.15×10^{11}	Number of protons per bunch
f	40 MHz	Bunch-crossing frequency
σ	16.7 μm	Transverse beam size ($\sigma_x = \sigma_y$)
$\mathcal{L}_{\mathrm{peak}}$	$1.0 \times 10^{34}\,\mathrm{cm}^{-2}\mathrm{s}^{-1}$	Peak instantaneous luminosity

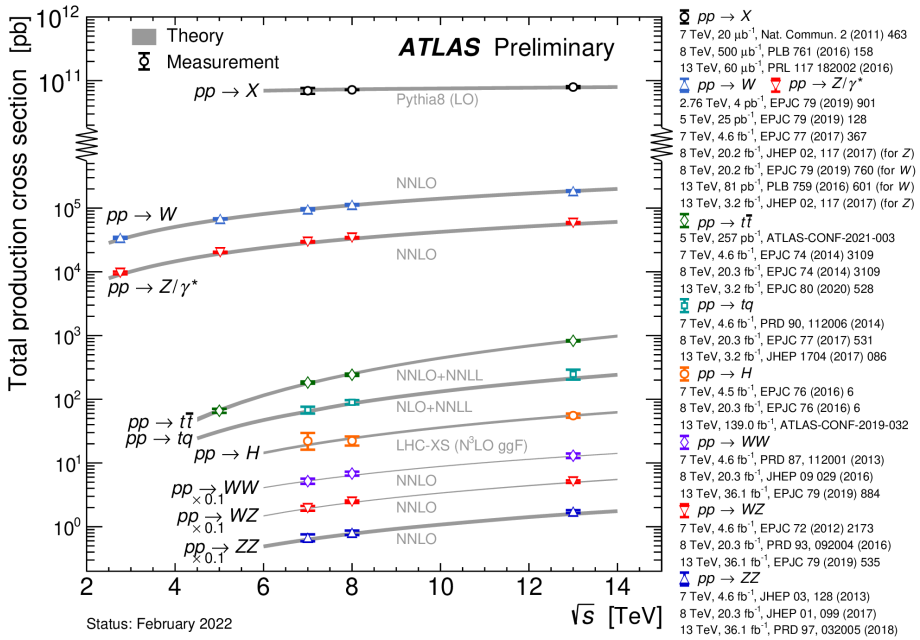

Figure 2.3: Summary of production cross-sections for a few selected Standard Model processes as a function of center-of-mass energy $\sqrt{s}$, measured with the ATLAS experiment [63]. The measurements have been performed at LHC collision energies of 2.76 TeV, 5 TeV, 7 TeV, 8 TeV and 13 TeV, shown as colored markers. The gray lines show theoretical predictions, where the gray text indicates the precision level of the prediction.

comparison, the inclusive (total) cross-section for proton–proton collisions at the LHC is of order 10^{11} pb.

Further, Figure 2.4 shows predicted cross-sections for sparticle pair production in proton–proton collisions at $\sqrt{s} = 13$ TeV, as a function of sparticle mass. The cross-sections fall exponentially with increasing sparticle mass. Moreover, they are larger for colored sparticles (squarks and gluinos) than for non-colored sparticles (sleptons and electroweakinos) for similar masses.

Expected number of events

Knowing the cross-section σ_X for a given process X, we can calculate the event rate R_X (the expected number of events per second) as

$$R_X = \frac{dN_X}{dt} = \mathcal{L}\sigma_X, \tag{2.4}$$

and the total number of expected events N_X during a given data-taking period as

$$N_X = L\sigma_X, \tag{2.5}$$

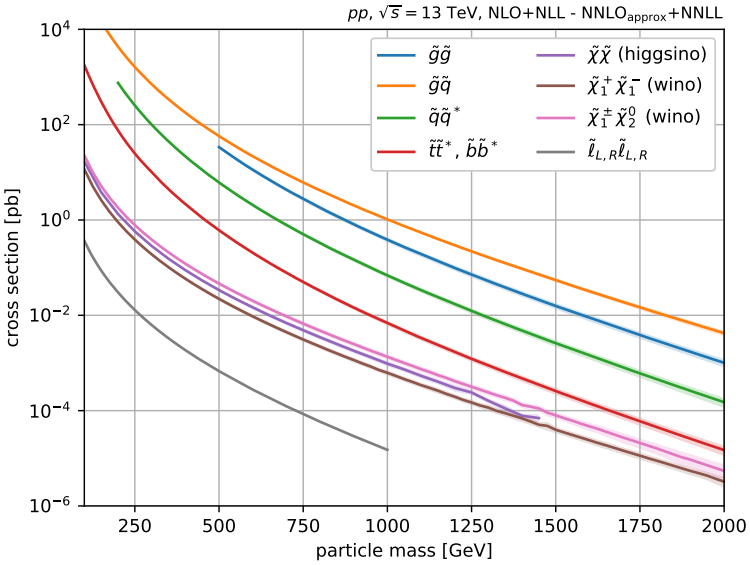

Figure 2.4: Predicted cross-sections for sparticle pair production in proton–proton collision at $\sqrt{s} = 13$ TeV as a function of sparticle mass [64]. The production cross-sections are larger for colored sparticles (squarks and gluinos — blue, orange, green and red lines) than for non-colored sparticles (sleptons and electroweakinos — purple, brown, pink and gray lines) for similar masses.

where $\mathcal{L}$ and L are instantaneous and integrated luminosity, respectively.

2.3 The ATLAS experiment

The ATLAS (short for "A Toroidal LHC ApparatuS") experiment [65–67] is one of the two multi-purpose detectors at the LHC. With its length of 46 m and diameter of 25 m, ATLAS is the detector with the largest volume ever constructed for a particle collider. Further, ATLAS weighs 7,000 tonnes, similar to the weight of the Eiffel tower. The detector consists of different layers of detecting subsystems, wrapped concentrically around the collision point to record the trajectory, momentum and energy of particles. This way, the particles traveling through the detector can be individually identified and measured. Figure 2.5 shows a computer-generated image of the whole ATLAS detector, also listing the different detector layers.[7]

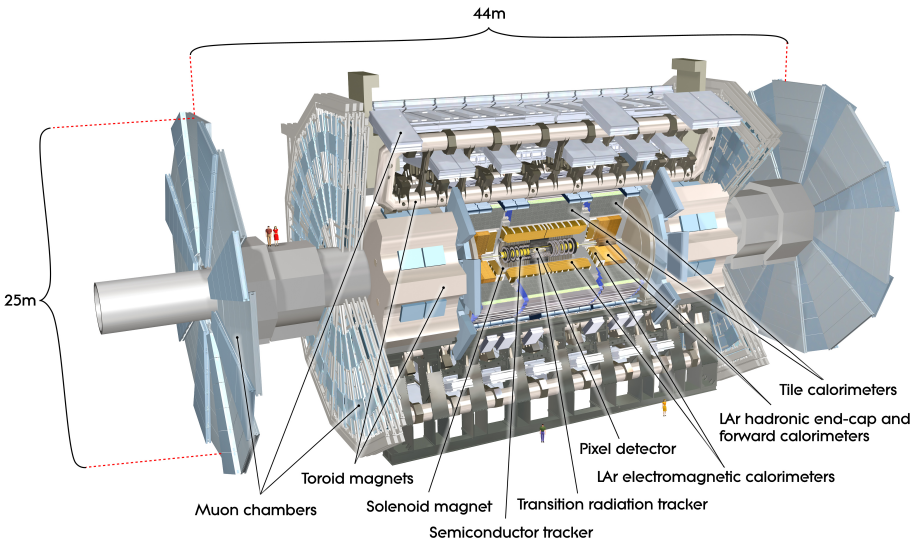

Figure 2.5: A computer-generated image of the whole ATLAS detector, indicating the different detector layers [68].

2.3.1 Coordinate system

The collision point, or interaction point, around which the detector is built, is the origin of the ATLAS coordinate system. In standard Cartesian coordinates (x, y, z), the positive x-axis is defined as pointing towards the center of the LHC ring, the positive y-axis is defined as pointing upwards, while the beam direction defines the z-axis. Spherical coordinates (r, θ, ϕ) are also used, where r is the radial distance from the origin ($r = \sqrt{x^2 + y^2}$), the azimuthal angle ϕ lies in the

[7] Note that in this image produced in 2008, the length of ATLAS is listed as 44 m instead of 46 m.

x-y plane, and the polar angle θ lies in the y-z plane. In practice, it is common to refer to the so-called *pseudorapidity* η instead of the polar angle, defined as

$$\eta = -\ln \tan \frac{\theta}{2}. \tag{2.6}$$

As the polar angle approaches zero, the pseudorapidity tends towards infinity. Particles with high pseudorapidity values are generally lost, as they escape the detector along the beamline. One reason for using pseudorapidity is that for ultra-relativistic particles, differences in this variable ($\Delta\eta = eta_2 - \eta_1$) are approximately invariant under Lorentz boosts along the beam direction. Another commonly used parameter is the *angular distance* ΔR in the η-ϕ plane, defined as

$$\Delta R = \sqrt{(\Delta\eta)^2 + (\Delta\phi)^2}. \tag{2.7}$$

Importance of the transverse plane

In collider experiments, the so-called *transverse plane* is important. In ATLAS, this is the x-y plane — any vector in this plane is perpendicular to the LHC beamline. In proton–proton collisions, it is not the protons themselves that collide, but rather the partons (quarks and gluons) that make up the protons. As each parton carries an unknown fraction of the total proton momentum, we do not know the momenta of the particles that actually collide. What we do know, however, is that most of the momentum of the partons point in the z-direction, such that the total incoming momentum in the transverse plane can be approximated to be zero. Further, as the ATLAS detector is approximately hermetic in the transverse plane, most of the outgoing momentum in this plane is accounted for. This means that we can use conservation of energy and momentum in this plane, which is why transverse energy E_{T} and transverse momentum $\mathbf{p}_{\mathrm{T}}$ have central roles at collider experiments.

In particular, the so-called *missing transverse momentum* plays an important role in searches for new physics. "Invisible" particles, such as the neutrino and the lightest supersymmetric particle (if it exists), escape the detector without leaving a trace. However, their presence can be inferred from momentum conservation, as will be explained in more detail in Section 2.3.4.

2.3.2 Detector layout

Figure 2.6 shows an illustration of a slice of the ATLAS detector, depicting the detector layers. The different layers will be briefly introduced in the following.

Inner detector

The ATLAS inner detector has a length of 6.2 m and a diameter of 2.1 m. Despite its relatively small size, it is highly sensitive. The main purpose of the inner detector is to track the paths of electrically charged particles produced in the proton–proton collisions. Further, based on these *tracks*, the *vertices*

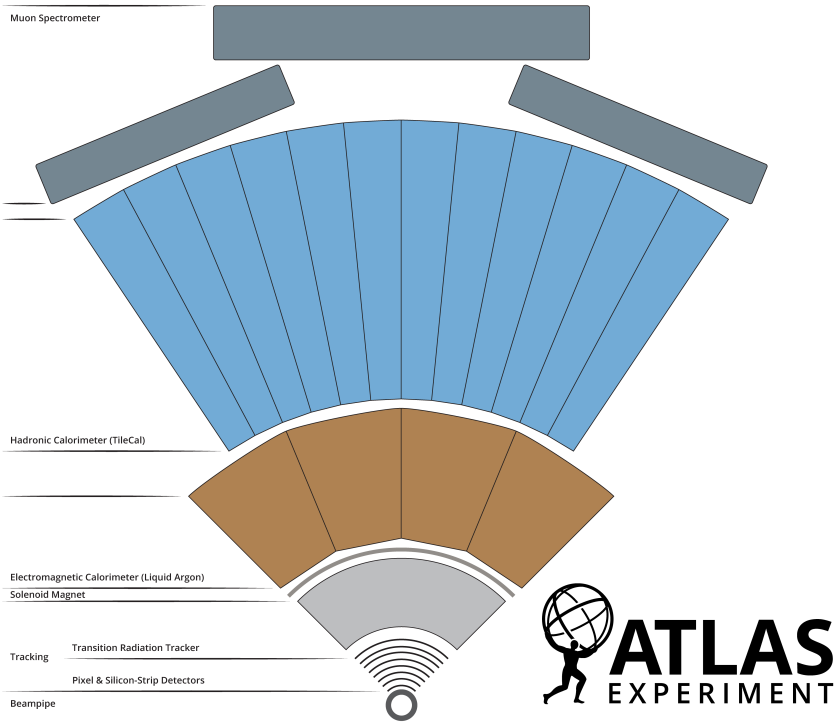

Figure 2.6: Illustration of a slice of the ATLAS detector, showing the different detector layers [69].

of a collision can be determined. The primary vertex is the actual collision point, while secondary vertices arise from subsequent decays of the particles produced in the collision. The inner detector itself consists of three layers: the pixel detector, the semiconductor tracker (SCT) and the transition radiation tracker (TRT). Figure 2.7 shows a computer-generated image of the ATLAS inner detector.

The innermost layer is the pixel detector, which is located just 3.3 cm from the LHC beampipe. It consists of four layers of silicon pixels with over 92 million pixels in total, each being smaller than a grain of sand. Silicon pixels give excellent spatial resolution, but they are very costly, which is why they are only used in the innermost part of ATLAS. As charged particles burst out from the collision point, they leave behind small energy deposits, or *hits*, in the pixel detector.

Surrounding the pixel detector is the semiconductor tracker. Like the pixel detector, the SCT is a silicon-based semiconductor detector. But instead of pixels, the SCT sensors are shaped like long, thin “micro-strips”. With over

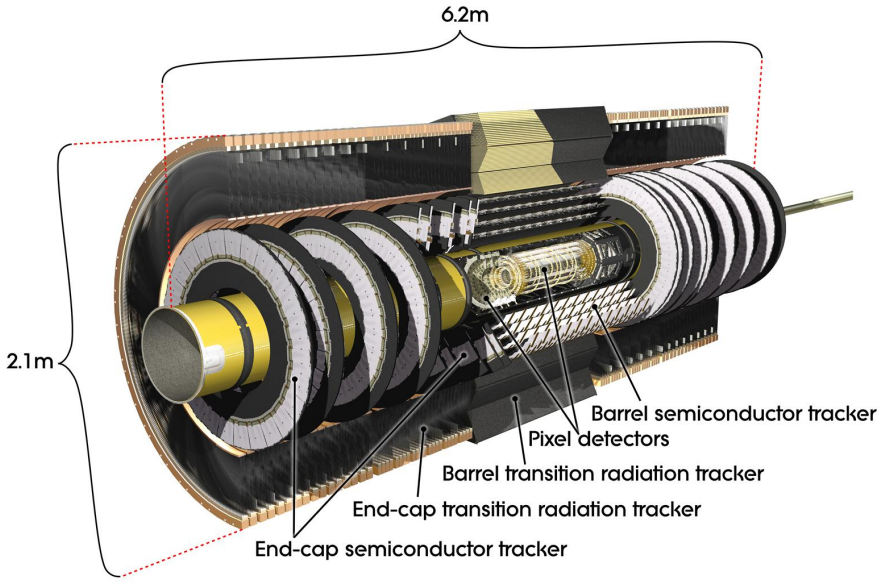

Figure 2.7: Computer-generated image of the ATLAS inner detector [70].

4,000 modules with more than six million micro-strips in total, the SCT allows for measuring particle tracks with a precision of up to 25 nm, which is less than half the width of a human hair.

The third and final layer of the ATLAS inner detector is the transition radiation tracker. The TRT is made up of 300,000 thin-walled drift tubes, or "straws", with a diameter of 4 mm. The straws are filled with a gas mixture, which is ionized by charged particles passing through, resulting in detectable electric signals. In addition to detecting particle tracks, the TRT provides information on the particle type through *transition radiation*.

Magnet system

The purpose of the magnets in the ATLAS detector is to bend the trajectories of charged particles, allowing for measurement of their momenta. Due to the Lorentz force, the trajectory of a charged particle moving through a magnetic field will be curved.[8] Knowing the strength of the magnetic field, the momentum of the particle can be inferred from the radius of its trajectory. ATLAS has two different types of magnets: solenoidal and toroidal. The main sections are the central solenoid magnet, the barrel toroid magnet and the end-cap toroid magnets. In order to provide the necessary magnetic field strengths, the magnets are superconducting, with an operating temperature of about 4.5 K.

[8]This is the principle behind circular accelerators like the LHC.

The central solenoid magnet surrounds the inner detector. With a length of 5.6 m, a diameter of 2.56 m and a weight of more than 5 tonnes, this powerful magnet consists of more than 9 km of superconducting wire, providing a 2 tesla magnetic field in just 4.5 cm thickness. As seen in Figure 2.8, the field lines of the solenoidal magnetic field are parallel to the beam axis.

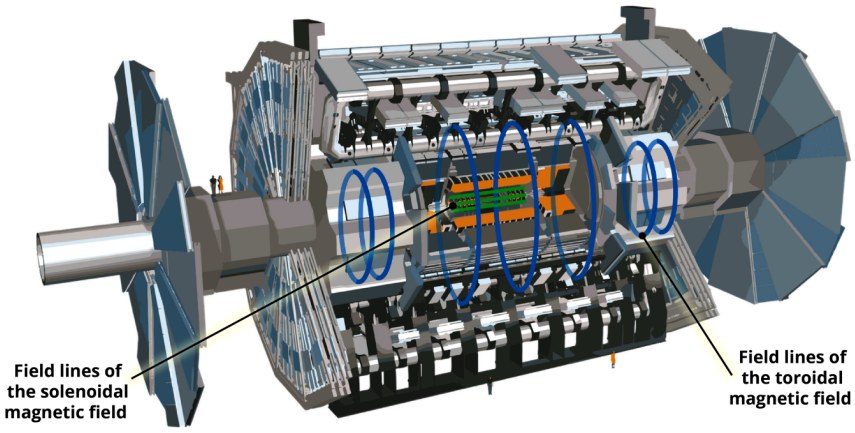

Figure 2.8: Illustration of the ATLAS detector magnetic fields [71].

The toroidal magnets are located further out. Their specific purpose is to bend muon trajectories. Each of them consists of a series of eight coils, providing a magnetic field of up to 3.5 tesla. The configuration of the coils results in circular magnetic field lines around the beam axis, as illustrated in Figure 2.8. The barrel toroid magnet is the largest toroidal magnet ever constructed, with a length of 25.3 m and an outer diameter of 20.1 m. It is made with more than 56 km of superconducting wire and weighs about 830 tonnes. The end-cap toroid magnets extend the magnetic field so that the momenta of particles leaving the detector close to the beampipe can also be measured. Each of these end-cap toroids is made with around 13 km of superconducting wire, has an outer diameter of 10.7 m and weighs about 240 tonnes.

Calorimeters

Calorimeters are used to measure particle energies, by forcing them to deposit all of their energy and stop within the detector. All known particles except muons and neutrinos can be stopped in calorimeters.[9] The ATLAS calorimeters are *sampling* calorimeters, meaning that they consist of layers of an "absorbing"

[9]Muons are measured using muon spectrometers (to be introduced in the next subsection), while neutrinos escape detection completely and appear as missing transverse momentum (introduced in Section 2.3.1).

high-density material that stops the incoming particles, interleaved with layers of an "active" medium that measures their energy.[10] More specifically, when an incoming particle hits the absorbing layers, it is converted into a "shower" of new, lower-energy particles whose energies are measured in the active layers. The energy of the original particle hitting the detector can be determined by combining the measured energies of all particles in the shower.

Calorimeters are often separated into two main classes: electromagnetic calorimeters (ECALs) and hadronic calorimeters (HCALs). As the name implies, electromagnetic calorimeters measure the energy of particles that lose most of their energy through the electromagnetic interaction, i.e. mainly electrons and photons. Due to different mechanisms for energy loss, hadronic showers usually take longer to develop than electromagnetic showers. Hadronic calorimeters, typically made of denser and thicker material than electromagnetic calorimeters, are thus usually placed outside of electromagnetic calorimeters.

Figure 2.9 shows a computer-generated image of the ATLAS calorimetry system, located just outside the inner detector and the central solenoid magnet. The electromagnetic calorimeter has one barrel segment and two end-cap segments. All three segments are made up of absorbing lead plates interleaved with volumes of liquid argon (LAr) acting as the active medium. The shower particles ionize the liquid argon and produce electric currents that are measured.

The hadronic calorimeter measures the energy of hadronic particles that did not deposit all of their energy in the LAr electromagnetic calorimeter. In the barrel and extended barrel regions, the hadronic calorimeter is made up of layers of absorbing steel plates and plastic scintillating tiles. In the end-cap and forward regions, liquid argon is used as the active medium also for the hadronic calorimeter. The absorbing layers consists of copper in the end-cap regions, and a combination of copper and tungsten in the forward regions.

Muon spectrometer

As muons are over 200 times heavier than electrons, they lose much less energy from interactions with detector material, e.g. through *bremsstrahlung*. Muons are thus not stopped by the ATLAS calorimeters. Instead, the outermost layer of the ATLAS detector is the muon spectrometer, dedicated to identifying and tracking muons and measuring their momenta. Figure 2.10 shows a computer-generated image of the ATLAS muon spectrometer, which is made up of 4,000 individual *muon chambers*, using four different technologies. Thin-gap chambers (TGCs) and resistive-plate chambers (RPCs) are used for triggering muon events (see Section 2.3.3), while cathode strip chambers (CSCs) and monitored drift tubes (MDTs) are used for precision position measurements and track curvature

[10] Homogeneous calorimeters, on the other hand, only consists of active materials. Such calorimeters provide excellent energy resolution, but are not so easily segmented, making position measurements and particle identification harder. Further, due to the detector thickness required to measure hadron showers (with large interaction lengths), homogeneous calorimeters are rarely used in accelerator experiments. More information on calorimetry for particle physics can be found in Ref. [72].

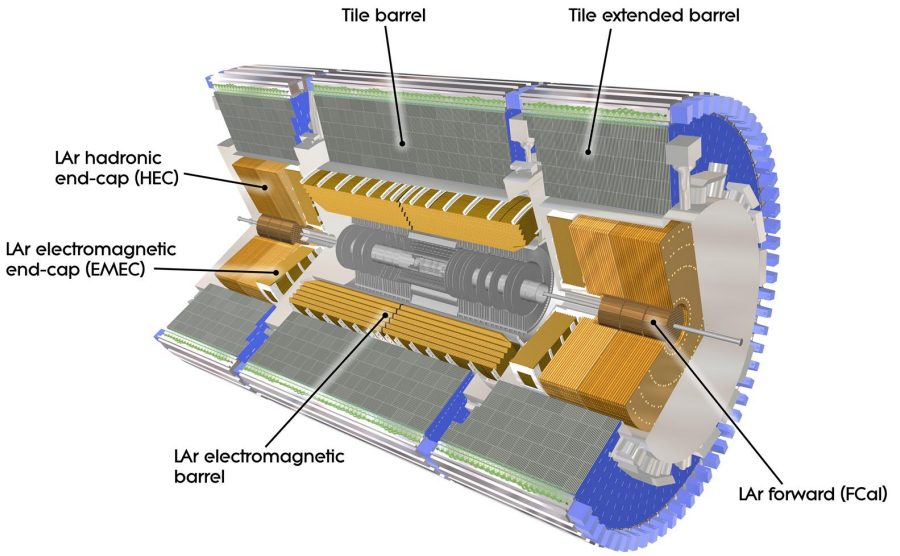

Figure 2.9: Computer-generated image of the ATLAS calorimetry system [73].

measurements, respectively. As seen in the image, the muon chambers are embedded in the toroidal magnet system (yellow), with the specific purpose to bend muon trajectories. In addition, two large muon-detector "wheels" are located outside the end-caps.

2.3.3 Trigger and data acquisition

With a proton bunch-spacing of 25 ns, the LHC has a peak bunch-crossing frequency of 40 MHz, as listed in Table 2.1. The probability of two individual particles colliding in a bunch-crossing is extremely low. However, as the number of protons in each bunch is so large, each bunch-crossing typically sees a few tens of *hard collisions*. For Run 2 of the LHC, the mean number of interactions per crossing registered by ATLAS was 34. Having multiple concurrent interactions per bunch-crossing is referred to as *pile-up*, denoted μ. With this pile-up, more than one billion collisions took place in the ATLAS detector every second during Run 2. It would be physically impossible to record and store the data from all these collision events. In addition, only a few of the events actually contain interesting characteristics hinting at new physics. This is where the ATLAS trigger and data acquisition (TDAQ) system [75] comes into play. This system performs *online* (real-time) processing of detector measurements, identifying and storing the most interesting events for *offline* analysis. Figure 2.11 shows an overview of the ATLAS TDAQ system in Run 2 of the LHC.

The ATLAS trigger system has two steps, or levels. The *Level 1 (L1) trigger*

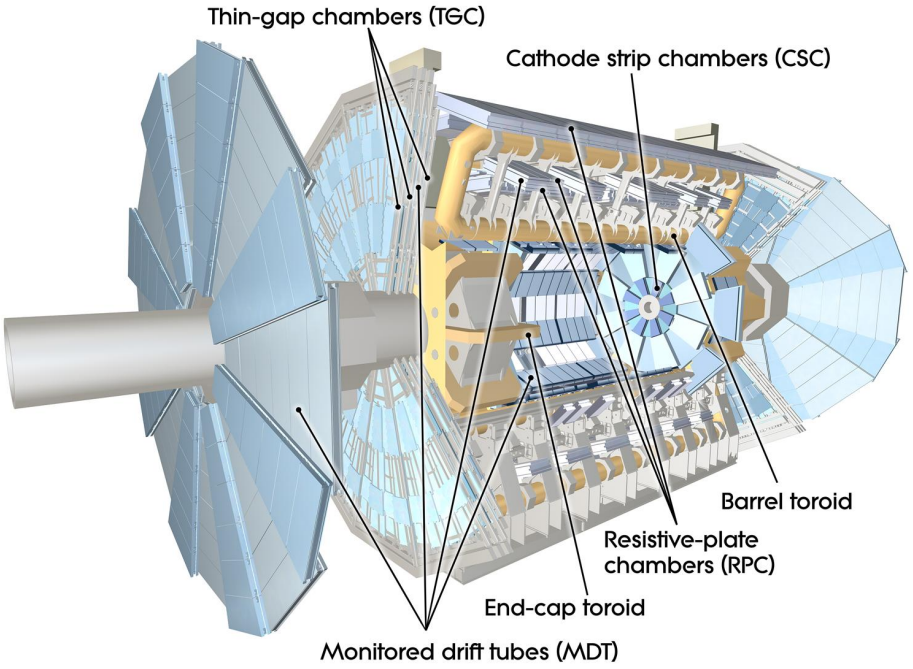

Figure 2.10: Computer-generated image of the ATLAS muon spectrometer system [74].

is hardware-based, constructed with custom-made electronics located on the detector. The L1 trigger uses information from the calorimeters (L1Calo) and the muon spectrometer (L1Muon). The L1 trigger decision is made by the Central Trigger Processor (CTP), which in addition to L1Calo and L1Muon (through the L1Muon Central Trigger Processor Interface (MUCTPI)) takes input from L1Topo, applying topological requirements to geometric or kinematic combinations between trigger objects received from L1Calo and L1Muon. The decision to keep or discard the data from an event is made in less than 2.5 µs after the event occurs. During this time, the data is kept in storage buffers. The maximum event rate from the L1 trigger is 100 kHz.

Events kept by the L1 trigger are passed to the *high-level trigger* (HLT). The HLT is software-based, making use of so-called regions of interest (RoIs) in η and ϕ identified by the L1 trigger. The HLT conducts detailed analyses of each collision event in just 200 µs, deciding if an event should be passed to the data storage system for offline analysis. About 1,000 events are stored per second.

The ATLAS trigger system is restricted in both bandwidth and CPU cost, and careful considerations must be made when deciding on which *trigger chains* to include in the *trigger menu*. Each chain defines specific selection criteria at L1 and HLT. To accomodate the large variety of physics analyses, a typical trigger menu contains several hundreds of chains. The ATLAS trigger menu

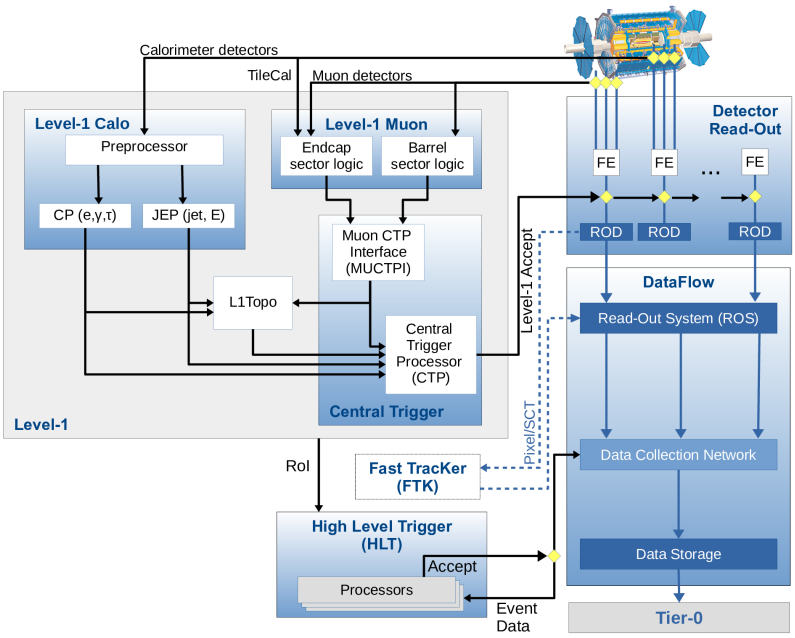

Figure 2.11: The ATLAS TDAQ system in Run 2 of the LHC, showing the components relevant for triggering as well as the detector read-out and data flow [75].

is optimized such that a large part of the bandwidth and CPU cost budget is allocated to primary object trigger chains relevant to most. The aim is to create a menu where these primary triggers are unprescaled[11] and mostly constant over the data-taking period, and distributed fairly among the objects. This leads to the concept of *lowest unprescaled* triggers for objects such as leptons, jets and $E_{\mathrm{T}}^{\mathrm{miss}}$, and some combinations of them (e.g. multi-lepton). In addition to the primary trigger chains, some dedicated analysis trigger chains are included in the trigger menu to target specific signatures, often using tighter thresholds.

2.3.4 Event reconstruction and particle identification

The different layers of the ATLAS detector were reviewed in Section 2.3.2. Particles are not measured directly in the detector. Instead, specialized

[11] If the threshold of a trigger (often p_{T}-regulated) is set too low, such that it would fire too often for the bandwidth capacity, a prescale factor must be applied. For instance, a trigger with a prescale factor of 5 only accepts every fifth event that fires the trigger. If such a prescale factor is applied, the resulting event rate must be multiplied with the factor in order to obtain the actual number of events that fired the trigger. However, this comes with the cost of increased statistical uncertainty, and such prescale factors are therefore usually avoided, if possible.

reconstruction software links together the signals registered in the different detector layers, and constructs objects such as *vertices*, *tracks* and *energy clusters*. Further, based on these objects, the software constructs physical objects such as particles and jets (to be introduced) which are usually the starting point when analyzing collision data.

Figure 2.12 shows a visualization of how different particle types interact with the different layers of the ATLAS detector, illustrating how they can be told apart. Solid (dashed) lines indicate that the particle type does (does not) interact with a given detector layer. Electrically charged particles such as electrons, muons and protons leave hits in the inner detector, and their trajectories are bent due to the magnetic fields provided by the magnet system. Their momentum can be determined from the curvature of their reconstructed track, and the sign of their electric charge can be determined from the direction of their deflection. Further, most particles deposit energy in the calorimeters. Photons and electrons deposit their energy in the electromagnetic calorimeter, while hadrons such as protons and neutrons deposit their energy in the hadronic calorimeter.[12] Muons interact with all the detector layers, but they traverse the whole detector without being stopped. Instead, they are identified and measured in the muon spectrometer, as explained in Section 2.3.2. Lastly (in this illustration), neutrinos are so weakly interacting that they travel through the whole detector without leaving a trace, but their presence can be inferred from missing transverse momentum, introduced in Section 2.3.1. Note that the reconstruction procedure is not without flaws, and that misidentification of objects does occur. This is often taken into account when analyzing the data.

As will become clear in the next chapter, electrons, muons, jets and missing transverse momentum are the most important objects in the work presented in this thesis. The reconstruction and identification of these objects will thus be briefly explained in the following. Note that also τ-leptons and photons are typically reconstructed in ATLAS.

Electrons

The reconstruction and identification of electrons in ATLAS are explained in detail in e.g. Ref. [77]. Briefly summarized, electrons are reconstructed by matching clusters of energy deposited in the electromagnetic calorimeter with tracks in the inner detector. Further, they are identified using a likelihood-based identification method, where a *likelihood discriminator* is formed for each electron candidate. Four fixed values of this discriminant are used to define four *working points* (WPs), referred to as "VeryLoose", "Loose", "Medium" and "Tight", with increasing discriminant thresholds. Looser working points accept more electron candidates, but at the cost of higher probability for misidentifying other objects as electrons. The efficiencies for identifying a *prompt* electron[13] with a transverse

[12] An exception is pions. They are very light hadrons that deposit their energy in the electromagnetic calorimeter.

[13] A prompt lepton originates from the hard collision, i.e. it is not a later decay product or a misidentified different object.

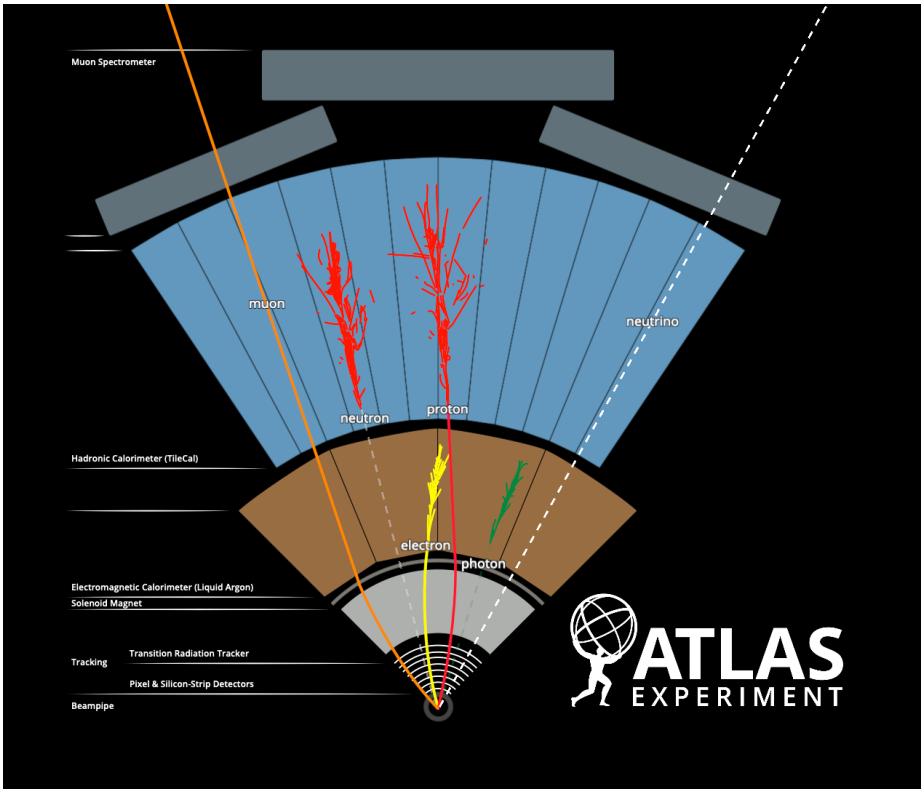

Figure 2.12: Visualization of how different particle types interact with the different layers of the ATLAS detector [76]. Solid (dashed) lines indicate that the particle type does (does not) interact with a given detector layer.

energy of 40 GeV are 93%, 88% and 80% for the Loose, Medium and Tight working points, respectively.

Muons

Thorough introductions to muon reconstruction and identification in ATLAS can be found in e.g. Refs. [78, 79]. Although the muon spectrometer is specifically designed to detect muons, muons interact with all the detector layers. For the reconstruction of muons, four different muon types are defined, depending on which subdetector(s) the information used stems from. Simply explained, *standalone* muons are reconstructed using only information from the muon spectrometer. *Combined* muons are reconstructed using information from both the inner detector and the muon spectrometer. *Segment-tagged* muons are like combined muons, but only requiring a "partial track" in the muon spectrometer. Finally, *calorimeter-tagged* muons are reconstructed using information from the inner detector and the calorimeters. A reconstructed muon belongs to exactly

one of the four types.

After reconstruction, different quality requirements are applied to the muon candidates. For muons, a given set of such requirements is referred to as an identification working point. Five working points have been defined to suit the needs of the wide variety of physics analyses involving muons. These five working points are referred to as "Loose", "Medium", "Tight", "Low-p_{T}" and "High-p_{T}". The efficiencies for identifying a prompt muon with transverse momentum between 20 GeV and 100 GeV are 99%, 97%, 93%, 97% and 80% for the Loose, Medium, Tight, Low-p_{T} and High-p_{T} working points, respectively.

Jets

Because of the nature of quantum chromodynamics, quarks are never observed as free particles — they are always found confined within hadrons. Quarks and gluons thus form showers of hadrons called *jets*, which is what we observe in a detector. In ATLAS, the signature of a jet is a large energy deposit in the calorimeters together with collimated charged-particle tracks in the inner detector. For the work presented in this thesis, jet candidates are reconstructed from topological energy clusters in the electromagnetic and hadronic calorimeters [80], grouped using the anti-k_t algorithm [81] implemented in the FastJet package [82].[14] The radius parameter defining the size of the jet cone is set to $R = 0.4$.

Missing transverse momentum

The concept of missing transverse momentum was introduced in Section 2.3.1. A detailed introduction to the reconstruction of missing transverse momentum in ATLAS can be found in e.g. Ref. [84]. Based on momentum conservation, the missing transverse momentum is reconstructed as the negative vector sum of the transverse momenta of the visible particles and objects in a collision. This sum has two types of contributions: *hard terms* and *soft terms*. The hard terms stem from so-called hard objects, meaning fully reconstructed particles (electrons, photons, τ-leptons and muons) and jets. The soft terms stem from so-called soft signals, meaning reconstructed tracks and energy clusters associated with the primary vertex but not with any of the hard objects.

From the components $p_{x(y)}$ of the transverse momentum vectors $\mathbf{p}_{\mathrm{T}}$ of the various contributions, the missing transverse momentum components $E^{\mathrm{miss}}_{x(y)}$ are given as

$$E^{\mathrm{miss}}_{x(y)} = -\sum_{\text{hard objects}} p_{x(y)} - \sum_{\text{soft signals}} p_{x(y)}. \tag{2.8}$$

[14] In the last years, particle-flow (PFlow) jets [83], exploiting also tracking information, have been increasingly used.

The set of observables constructed from $E^{\text{miss}}_{x(y)}$ are then

$$\mathbf{E}^{\text{miss}}_{\text{T}} = (E^{\text{miss}}_x, E^{\text{miss}}_y), \tag{2.9}$$

$$E^{\text{miss}}_{\text{T}} = |\mathbf{E}^{\text{miss}}_{\text{T}}| = \sqrt{(E^{\text{miss}}_x)^2 + (E^{\text{miss}}_y)^2}, \tag{2.10}$$

$$\phi^{\text{miss}} = \tan^{-1}(E^{\text{miss}}_y / E^{\text{miss}}_x), \tag{2.11}$$

i.e. the vector $\mathbf{E}^{\text{miss}}_{\text{T}}$ with magnitude $E^{\text{miss}}_{\text{T}}$ and direction in the transverse plane ϕ^{miss}. Note that $E^{\text{miss}}_{\text{T}}$ is often referred to as missing transverse *energy*. For relativistic particles, energies and momenta are approximately equal.

2.4 Summary and outlook

This chapter gave an introduction to the experimental setup used to collect the dataset used in this thesis. We began by briefly introducing CERN and the Large Hadron Collider. We moved on to introducing the ATLAS experiment, including a description of the different detector layers, before explaining how the ATLAS trigger and data acquisition system works. Finally, we reviewed how the different objects are reconstructed and identified in ATLAS.

Note that the perspective of this chapter was Run 2 of the LHC. Figure 2.13 shows the full LHC schedule, updated in February 2022. During the second long shutdown (LS2) after Run 2, both the LHC and its experiments underwent upgrades. In ATLAS, the muon system got some additions — for instance, the New Small Wheel (NSW) system was installed. Further, the ATLAS TDAQ system and the LAr calorimeter front-end electronics were upgraded. Run 3 started in 2022 and will last until the end of 2025. From 2026 to 2028, the third long shutdown (LS3) is planned. During this shutdown, the LHC and its experiments will be heavily upgraded to enter into the era of the High-Luminosity LHC (HL-LHC) [85]. The objective of the HL-LHC is to increase the integrated luminosity by a factor 10 compared to LHC's design luminosity. During LS3, ATLAS will get a new all-silicon Inner Tracker (ITk) system, aiming to reach equal or even better performance than the current inner detector in the new conditions. In addition, the LAr and tile calorimeters will be upgraded, and both the muon and TDAQ systems will get further upgrades. The HL-LHC will operate until around 2040.

The particle physics community is currently discussing post-LHC collider projects. By the recommendation of the European Strategy for particle physics [87], mandated by the CERN council, the Future Circular Collider (FCC) [88] feasibility study is underway. If built, the circumference of the FCC would be between 80 and 100 km, with a collision energy of around 350 GeV for

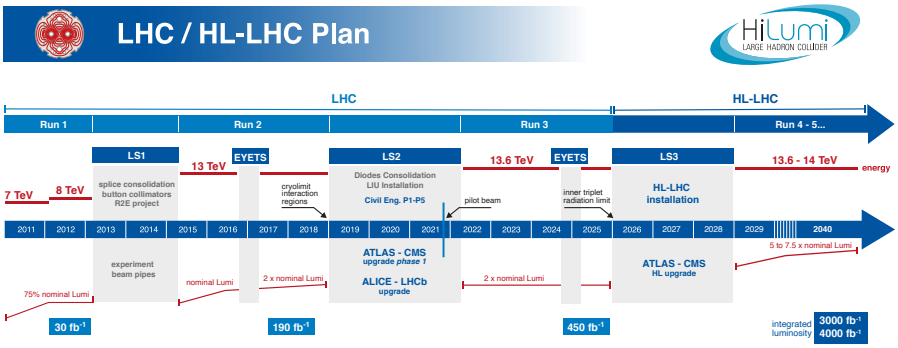

Figure 2.13: The Large Hadron Collider schedule, including the High-Luminosity era, updated in February 2022 [86].

electron–positron collisions and around 100 TeV for proton–proton collisions.[15] The FCC feasibility study investigates the technical and financial viability of such a facility at CERN. If the FCC is finally approved, the first step will probably be an electron–positron collider (FCC-ee) starting operation around 2045, before a proton–proton collider (FCC-hh) is built in the same tunnel, operating from around 2070 to the end of the century. In addition to the FCC, several other proposals for future colliders are discussed. In the category of linear electron–positron colliders, which can achieve higher collision energies than circular lepton colliders, the two most noteworthy proposals are probably the Compact Linear Collider (CLIC) and the International Linear Collider (ILC).

In Part II of this thesis, the topic shifts to analysis work, starting with an introduction to the relevant signals and corresponding Standard Model backgrounds of chargino–neutralino pair production in the next chapter.

[15] Hadrons can more easily be accelerated to very high energies than leptons, but the energy is distributed among the constituent quarks and gluons of the hadron, making the initial state of a hadron–hadron collision process ambiguous. Lepton colliders, on the other hand, offer a well-defined initial state. The collision energy is then known and tuneable, allowing the choice of the best suited center-of-mass energy, e.g. thresholds for particle pair production. Hadron and lepton colliders are complementary to each other, where the former are often referred to as discovery machines, and the latter are referred to as precision machines.

Part II

Searching for chargino–neutralino pair production

Chapter 3

Signals and backgrounds

An introduction to supersymmetry was given in Chapter 1. If supersymmetry is realized in nature, it introduces multiple new supersymmetric particles, or sparticles. The LHC collides protons — or rather partons, the quarks and gluons inside the proton. Since the strong coupling is large, the production cross-sections for colored sparticles (squarks and gluinos) are in general larger than for non-colored sparticles (sleptons and electroweakinos) for similar masses, as seen in Figure 2.4. However, colored sparticles are expected to be heavier than non-colored sparticles, and if they are too heavy to be produced with the current LHC energy, the first signs of supersymmetry at the LHC could be through direct production of sleptons and electroweakinos. And as explained in the Introduction, the anomalous magnetic moment of the muon might indicate that new physics is indeed hiding in the electroweak sector.

The topic of this thesis is the search for chargino–neutralino pair production with the ATLAS detector at the LHC. The main focus is Ref. [22], which presents a search for said production in final states with three leptons and missing transverse momentum.[1] This search will be discussed in the current and the three following chapters. In this chapter, the signals and corresponding backgrounds of chargino–neutralino pair production relevant to the search will be introduced.

In Section 3.1, some relevant jargon used in searches for new physics will be introduced. Section 3.2 will present the target signal model scenarios, before the concept of simplified models is introduced in Section 3.3, including previous results for the models in question. Finally, Section 3.4 will briefly summarize the most important Standard Model backgrounds to the three-lepton final state.

3.1 Relevant jargon when searching for new physics

When searching for a new physics process with a particle collider experiment, the first step is to identify the *experimental signature* of the process. Such experimental signatures are often given as *final states* with given numbers/amounts of different objects, such as leptons, jets and missing transverse momentum. Events with the target final state are then selected for the search analysis. However, when considering a single particle collision event on its own, one can never know whether the observed particles stem from the proposed new physics process (*the signal*), from a known Standard Model interaction, or simply from measurement errors. Events that mimic the signal being searched for in an analysis are called *background events*. Such events can be the result of Standard Model processes giving rise to the same final state as the signal, or detector effects such as particle

[1] In the following, "leptons" will refer to electrons and muons only.

misidentification. To increase the chance of discovering the potential signal, events are selected such that the signal-to-background ratio of the analysis is maximized. Backgrounds that can be removed or reduced by making clever cuts and selections are called *reducible backgrounds*. *Irreducible backgrounds*, on the other hand, are background processes that have the exact same experimental signature as the signal and cannot be told apart from it. More information on analysis methodology will be given in the next chapters.

3.2 Target signal-model scenarios

The Minimal Supersymmetric Standard Model (MSSM), the supersymmetric model with the smallest field content consistent with the Standard Model, was introduced in Section 1.3. In this model, the bino, the winos and the higgsinos are the superpartners of the $U(1)_Y$ gauge field, the $SU(2)_L$ gauge fields and the Higgs fields, respectively. These superpartners mix and form chargino and neutralino mass eigenstates, collectively referred to as electroweakinos. The lightest neutralino $\tilde{\chi}_1^0$ is the lightest supersymmetric particle (LSP) in many of the most popular realizations of the MSSM, and is considered to be a viable dark-matter candidate.

The mass parameters for the bino, wino and higgsino states are M_1, M_2 and μ, respectively. In Ref. [22], two different physics scenarios are considered: the *wino/bino* scenario and the *higgsino* scenario. In the wino/bino scenario, the hierarchy of the mass parameters is assumed to be $|M_1| < |M_2| \ll |\mu|$, so that the $\tilde{\chi}_1^0$ LSP is bino-dominated, and the $\tilde{\chi}_1^\pm$ and $\tilde{\chi}_2^0$ are wino-dominated. Such a hierarchy is typically predicted in models motivated by gauge coupling unification, such as the CMSSM introduced in Section 1.4.1, and also in a MSSM parameter space where the discrepancy between the measured muon anomalous magnetic moment and its Standard Model prediction can be explained [89–91].

The higgsino scenario, on the other hand, is motivated by naturalness arguments (see Section 1.4.2 on Natural SUSY), with $|\mu|$ near the weak scale, while M_1 and/or M_2 can be larger. In this scenario, $\tilde{\chi}_1^\pm$, $\tilde{\chi}_2^0$ and $\tilde{\chi}_1^0$ are all higgsino-like and considered to be the lightest supersymmetric particles. The magnitude of M_1 and M_2 relative to $|\mu|$ determines the mass splittings between the higgsino states. In Ref. [22], the mass splitting between $\tilde{\chi}_2^0$ and $\tilde{\chi}_1^0$ is about 5–60 GeV, corresponding to moderately decoupled bino and wino states ($M_1, M_2 > 0.5$ TeV).

3.3 Simplified models and experimental signature

A model of new physics is defined by a TeV-scale effective Lagrangian describing its particle content and interactions. There are many proposed extensions of the Standard Model, and some of them have qualitatively similar phenomenology, depending on a large number of free parameters. Even within the MSSM, the experimental signatures that are commonly searched for can usually be produced in multiple ways, and if a signal is seen, it is not necessarily immediately clear

what particles are producing it. It can thus be useful to step back from detailed predictions of any one model or region of parameter space, and rather focus on a small set of unambiguous parameters based on typical supersymmetry phenomenology by constructing *simplified models* [92–94].Despite their small size, specifically designed to involve only a few particles and decay modes, such simplified models can give useful coarse descriptions of SUSY-like physics, and also allow for comparison to other models. Using simplified models, limits can be set on production cross-sections and branching fractions[2], or directly on sparticle masses.

Although using simplified models seems like a sensible approach when searching for new physics of unknown origin, the interpretation can be challenging. A point in a simplified model parameter space does not necessarily correspond to a point in a physical model parameter space. However, simplified models are used in numerous analyses, as it is considered a straightforward and minimal approach to obtain first hints of physics beyond the Standard Model, in particular supersymmetry.

The two physics scenarios considered in Ref. [22] were presented in Section 3.2. For optimization of the selections and interpretation of the results, simplified SUSY models are considered for both scenarios. For the wino/bino scenario, the $\tilde{\chi}_1^0$ is assumed to be purely bino, while the $\tilde{\chi}_1^\pm$ and $\tilde{\chi}_2^0$ are assumed to be purely wino and mass degenerate. Further, the product of the two signed neutralino eigenmass parameters, $m_{\text{eig}}(\tilde{\chi}_2^0) \times m_{\text{eig}}(\tilde{\chi}_1^0)$, can be either positive or negative.[3] The two cases are referred to as the wino/bino '$(+)$' and wino/bino '$(-)$' scenarios, respectively. For the higgsino scenario, $\tilde{\chi}_1^\pm$, $\tilde{\chi}_2^0$ and $\tilde{\chi}_1^0$ are all assumed to be purely higgsino, and the mass of $\tilde{\chi}_1^\pm$ is taken to be the mean of the $\tilde{\chi}_2^0$ and $\tilde{\chi}_1^0$ masses. All other sparticles are assumed to be much heavier in both the wino/bino and higgsino scenarios, so that they do not affect the production and decay of the $\tilde{\chi}_1^\pm$ and $\tilde{\chi}_2^0$.

The search presented in Ref. [22] targets direct pair production of the lightest chargino and the next-to-lightest neutralino, $\tilde{\chi}_1^\pm\tilde{\chi}_2^0$, decaying into a pair of $\tilde{\chi}_1^0$ LSPs via an intermediate state with a W boson and a Z boson (WZ-mediated) or with a W boson and a Standard Model Higgs boson (Wh-mediated). In both cases, the final state of interest contains three leptons ℓ (electrons or muons) and missing transverse momentum $E_{\text{T}}^{\text{miss}}$. One lepton originates from a leptonic decay of the W boson, while the other two come from a direct leptonic decay of the Z boson or an indirect decay of the Higgs boson. The missing transverse momentum originates from the LSPs, and might be enhanced if hadronic *initial-state radiation* (ISR) is present, due to recoil between the $\tilde{\chi}_1^\pm\tilde{\chi}_2^0$ system and the jets.

[2]A given particle has more than one decay mode in general. The percentage chance that it decays via a given decay mode is referred to as the *branching fraction*, or *branching ratio*, for that decay.

[3]As explained in the footnote on page 3 of Ref. [22]: "The mixing matrix used to diagonalise the neutral electroweakino states can be complex, even in the absence of CP violation, but can be made real at the cost of introducing negative mass eigenstates. The sign will affect the couplings and thus the distributions in the decay under consideration."

Three simplified-model scenarios of $\tilde{\chi}_1^\pm\tilde{\chi}_2^0$ pair production are considered with dedicated selections:

- **On-shell *WZ***: $\tilde{\chi}_2^0 \to Z\tilde{\chi}_1^0$ with 100% branching ratio, where $\Delta m(\tilde{\chi}_2^0, \tilde{\chi}_1^0) \gtrsim m_Z$, for the wino/bino (+) scenario.
- **Off-shell *WZ***: $\tilde{\chi}_2^0 \to Z^{(*)}\tilde{\chi}_1^0$ with 100% branching ratio, where $\Delta m(\tilde{\chi}_2^0, \tilde{\chi}_1^0) < m_Z$, for the wino/bino (+), the wino/bino (−), and the higgsino scenarios.
- ***Wh***: $\tilde{\chi}_2^0 \to h\tilde{\chi}_1^0$ with 100% branching ratio, where $\Delta m(\tilde{\chi}_2^0, \tilde{\chi}_1^0) > m_h$, for the wino/bino (+) scenario.

The terms *on-shell* and *off-shell* refer to the fact that *virtual*, intermediate-state particles can have any mass — they do not to have lie on their "mass shell". An asterisk (*) is used to denote off-shell particles. In this case, where a $\tilde{\chi}_2^0$ decays into a $\tilde{\chi}_1^0$ and a Z boson, and the Z boson subsequently decays into two leptons, the Z boson is virtual. The mass difference between the $\tilde{\chi}_2^0$ and the $\tilde{\chi}_1^0$ then determines whether the Z boson is on-shell or not. The energy (momentum) available for the final-state leptons decreases with decreasing $\Delta m(\tilde{\chi}_2^0, \tilde{\chi}_1^0)$. Leptons with low p_T are often referred to as *soft leptons*, and are typically harder to reconstruct than high-p_T leptons.

A 100% branching ratio is assumed for $\tilde{\chi}_1^\pm \to W^{(*)}\tilde{\chi}_1^0$ for all models. Further, the Higgs boson in the Wh-mediated model has Standard Model properties and branching ratios, such that three-lepton final states are expected when the Higgs boson decays into WW, ZZ or $\tau\tau$, and each W boson, Z boson or τ-lepton decays leptonically. Figure 3.1 shows Feynman diagrams of the targeted simplified models.

The three simplified-model scenarios introduced above are analyzed separately, in the following referred to as the (three-lepton) on-shell WZ analysis, the (three-lepton) off-shell WZ analysis and the (three-lepton) Wh analysis individually, and simply the three-lepton analysis collectively. I was part of the analysis team for the off-shell WZ analysis, which will be the main focus of the coming chapters. Further, the results of the Wh analysis are used in a statistical combination of search results that will be presented in Chapter 7.

3.3.1 Previous results

Previous searches for chargino–neutralino pair production have not found evidence for the existence of any supersymmetric particles. Instead, lower limits on the sparticle masses have been set, summarized below. An explanation on how such limits are set will be given in Section 5.5.

For the wino/bino (+) scenario, limits for $\tilde{\chi}_1^\pm\tilde{\chi}_2^0$ pair production with decays via WZ to three-lepton final states have been set by the CMS Collaboration for $\tilde{\chi}_1^\pm/\tilde{\chi}_2^0$ masses up to 500 GeV for massless $\tilde{\chi}_1^0$, up to 200 GeV for $\Delta m(\tilde{\chi}_2^0, \tilde{\chi}_1^0) \sim$

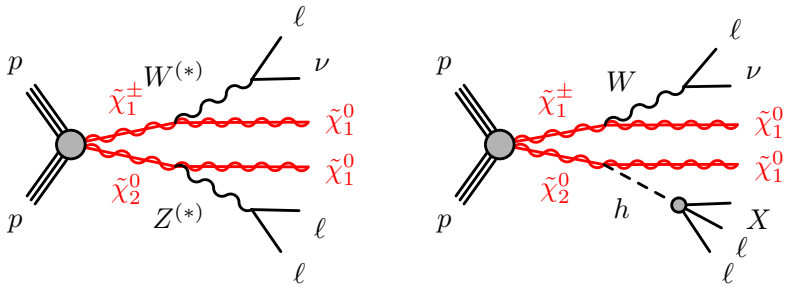

Figure 3.1: Feynman diagrams of the targeted simplified models: $\tilde{\chi}_1^{\pm}\tilde{\chi}_2^0$ pair production with subsequent decays into two $\tilde{\chi}_1^0$ and two Standard Model bosons. The left diagram (a) shows intermediate WZ (W^*Z^*) bosons, where both bosons decay leptonically. The right diagram (b) shows intermediate Wh bosons, with W decaying leptonically and the Higgs boson decaying indirectly into leptons+X (where X denotes additional decay products) via WW, ZZ, or $\tau\tau$. In both cases, the resulting final state contains three leptons ℓ and missing transverse momentum $E_{\mathrm{T}}^{\mathrm{miss}}$.

m_Z, and up to 240 GeV for Δm between 50 GeV and m_Z [95].[4] For Δm below 50 GeV, limits have been set in two-lepton final states by the ATLAS Collaboration for $\tilde{\chi}_1^{\pm}/\tilde{\chi}_2^0$ masses up to 250 GeV [96]. For decays via Wh to three-lepton final states (including hadronically decaying τ-leptons), limits have been set by the ATLAS Collaboration for $\tilde{\chi}_1^{\pm}/\tilde{\chi}_2^0$ masses up to 150 GeV for massless $\tilde{\chi}_1^0$, and up to 145 GeV for a $\tilde{\chi}_1^0$ mass of 20 GeV [97].

For the higgsino scenario, the most stringent limits for Δm between 5 GeV and 55 GeV have been set in two-lepton final states by the ATLAS Collaboration, excluding $\tilde{\chi}_2^0$ masses up to 130–190 GeV, depending on Δm [96]. For mass splittings greater than 55 GeV, $\tilde{\chi}_1^{\pm}$ masses up to 103.5 GeV were excluded by LEP [98–107].

3.4 Backgrounds to the three-lepton final state

As became clear in the previous section, the final state of interest for the search presented in Ref. [22] contains three leptons and missing transverse momentum. As explained in Section 3.1, background events are events that mimic the signal being searched for in an analysis, either as a result of Standard Model processes with the same final state as the signal, or due to detector effects such as particle misidentification. In this section, the most important backgrounds to the three-lepton final state will be introduced briefly.

The dominant background is not surprisingly from Standard Model WZ events with only leptonic decays. This process leads to three real and prompt

[4] Unless stated otherwise, Δm will refer to $\Delta m(\tilde{\chi}_2^0, \tilde{\chi}_1^0)$ in the following.

leptons, where the latter means that they originate from the prompt decay of heavy particles produced in the main collision of the event. Further, missing transverse momentum arise from the neutrino of the W boson decay.

Another important background is $t\bar{t}$. The only known decay of the top quark is through the weak interaction, producing a W boson and a bottom quark. Subsequent leptonic decays of both W bosons result in two leptons, and an additional non-prompt lepton can originate from the decay of a b- or c-hadron. Electrons from photon conversion, semileptonic decays of heavy-flavored hadrons, and hadrons and jets wrongly identified as leptons are collectively referred to as *fake or non-prompt* (FNP) leptons.

Further, the set of $(Z/\gamma^* \to \ell\ell) + (\text{jets}/\gamma)$ processes, collectively referred to as "Z+jets", is also a substantial background, due to their relatively large cross-sections at the LHC. They result in two prompt leptons, and an additional FNP lepton can arise from jets or photons. There are no invisible particles in these processes at tree-level (i.e. not including quantum corrections). However, missing transverse momentum can arise from mismeasured leptons and/or jets, or due to the $E_{\mathrm{T}}^{\mathrm{miss}}$ soft term.

There are many other processes in addition to the ones mentioned above that can result in final states with three leptons. For some processes that in theory should lead to fewer final-state leptons, FNP leptons can add to the count, as seen above. For other processes that should lead to more final-state leptons, not all of them are always reconstructed. In order to get the total background estimate right, all relevant processes should be taken into account, albeit some are more negligible than others. More information on the backgrounds considered in the search presented in Ref. [22], including technical details, will be given in the following chapters.

3.5 Summary

In this chapter, it became clear the main focus of this thesis is Ref. [22], which presents a search for chargino–neutralino pair production in final states with three leptons and missing transverse momentum. This chapter gave an introduction to the relevant signals and most important backgrounds for the search. We began by reviewing some relevant jargon when searching for new physics, before introducing the target signal-model scenarios, referred to as higgsino, wino/bino (+) and wino/bino (−). We moved on to introducing the concept of simplified models, and discussed three relevant simplified-model scenarios of $\tilde{\chi}_1^{\pm}\tilde{\chi}_2^0$ pair production, all resulting in final states with three leptons and missing transverse momentum. These three scenarios are analyzed separately — in the following referred to as the (three-lepton) on-shell WZ analysis, the (three-lepton) off-shell WZ analysis and the (three-lepton) Wh analysis individually, and simply the three-lepton analysis collectively. I was part of the analysis team for the off-shell WZ analysis, which will be the focus in the coming chapters. Finally, the most important backgrounds to the three-lepton final state were discussed, namely WZ, $t\bar{t}$ and Z+jets.

In the next chapter, we will review some of the methodology used to analyze the data collected with the ATLAS detector in the search for chargino–neutralino pair production in three-lepton final states, before moving to summarizing the off-shell WZ analysis in the subsequent chapter.

Chapter 4

Analysis methodology

The theory behind what we are searching for — supersymmetry, charginos and neutralinos in particular — and the experimental setup used to search for it — the Large Hadron Collider and the ATLAS detector — were described in the previous chapters. This chapter will introduce some of the methodology used to analyze the vast amount of data collected with the ATLAS detector in the search for chargino–neutralino pair production in three-lepton final states.

In Section 4.1, the concept of simulated events will be introduced, followed by information on the simulated event samples used in the three-lepton analysis introduced in the previous chapter. In Section 4.2, some details on the dataset used in the analysis will be given. Finally, Section 4.3 covers event reconstruction and preselection used in the analysis.

4.1 Simulated events

In order to be able to discover potential new physics in actual data, we need to know what to expect if new physics is *not* present. Thus, the Standard Model background must be modeled as accurately as possible. For this, we use *simulated data*, which is an intergral part of any ATLAS analysis. We also need simulated data for the beyond Standard Model (BSM) physics process(es) we are searching for, in order to tell if potential deviations from the Standard Model actually stem from this process — or something else.

4.1.1 Producing simulated events

This section will briefly describe the different steps of producing simulated particle collision events.[1] The first step is to generate such events using *Monte Carlo event generators*.

Event generation

A stochastic process is a process determined by the laws of probability. Particle scattering processes like the ones at the LHC are inherently stochastic: it is not possible to exactly calculate properties of final-state particles of single particle interactions, such as scattering angles and momenta. Instead, we have to work with probability distributions for such properties. Thus, in order to simulate particle collision events, so-called Monte Carlo (MC) algorithms must be used. A MC algorithm is per definition any mathematical method that relies on random number sampling to solve a problem. Using MC event generators, large sets of

[1] For a more thorough introduction, the reader is referred to e.g. Refs. [108–111].

simulated particle collision events can be produced — referred to as MC samples. The input to such generators is the *differential cross-section* of the process in question to some order of *perturbation theory*, usually leading order (LO) or next-to-leading order (NLO).

Figure 4.1 shows a sketch of a hadron–hadron collision as simulated by a MC event generator. In a real hadron–hadron collision, there is a lot going on in addition to the *hard scattering process*, i.e. the one we are interested in. There are many scattering and rescattering effects, which must be taken into account by MC generators in order to reflect the full complexity of the event structure. First, the colored partons from the hard interaction radiate gluons as they separate, commonly referred to as *parton showering*. This effect is merely a product of quantum chromodynamics, and is thus model independent. Often specialized event-generator software is used to model the parton showering. Then follows *hadronization*, in which the parton-shower constituents hadronize to form colorless hadrons, and ultimately particles that can be detected. In addition, there is an *underlying event*, meaning the interactions of the remaining partons of the original interacting protons.

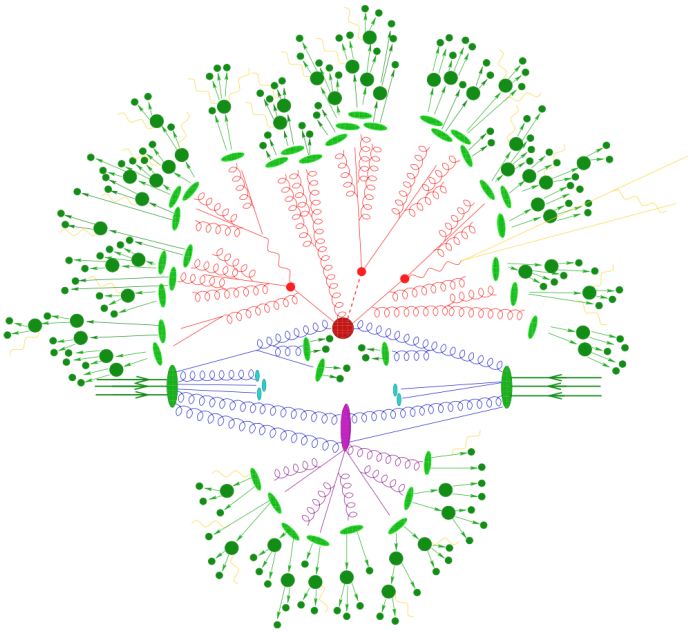

Figure 4.1: Sketch of a hadron–hadron collision as simulated by a Monte Carlo event generator [112]. The red blob in the middle represents the hard collision, surrounded by parton showers. The hadronization is represented by light green blobs, while dark green blobs indicate hadron decays. The purple blob indicates the underlying event. The yellow lines signal soft photon radiation.

All stages described above need to be implemented in order to simulate a

complete collision event. There are several different MC generators available, with different strengths and weaknesses. General-purpose generators like Pythia [113], Herwig [114, 115] and Sherpa [116] can be used to simulate any or all of the stages. Other generators are dedicated to specific stages, like MadGraph [117] for hard scattering and EvtGen [118] for decays of heavy-flavor particles. It is common to interface dedicated generators with a general-purpose one in order to get a full event simulation. Details on which generators are used to produce the MC samples used in the three-lepton analysis will be given in Section 4.1.2.

As described above, the goal of this exercise is to compare sets of simulated events with real data, to see if the data contains an excess compared to the Standard Model expectation. However, as real data has been measured in a detector, the MC-generated events must go through *detector simulation* before comparison with data, modeling how the generated particles interact with the detector material.

Detector simulation

A complete computer-simulated model of the ATLAS detector has been constructed [111] using the Geant4 simulation software toolkit [119–121]. This model includes misalignments and dead material (e.g. cables and supporting pillars), and is kept up to date by adding information on e.g. dead modules. It describes how particles interact with matter and how they propagate through the detector. Each particle created by a MC generator is propagated through this detector model, which then models desired particle–detector interactions such as calorimeter showers and hits in the semiconductor detector material, but also undesired effects and inefficiencies such as particles being deflected or absorbed by passive detector material.

A full Geant4 detector simulation is complex, and requires a lot of time and computing resources. Modeling calorimeter response is particularly time consuming — about 80% of the simulation time is spent on simulating particle showers in the calorimeters, in particular the electromagnetic calorimeter. This might limit the number of events that can be produced to model a background process, increasing the statistical fluctuations of background samples. Different methods and software packages have been created to bypass this limitation. One of them is AtlFast-II [111], which models tracking in the inner detector and muon spectrometer using Geant4, while using a parametric description of calorimeter responses (FastCaloSim [122]). Using this method cuts the simulation time with more than 90%. The accuracy of AtlFast-II is slightly worse than for full simulation, but has been deemed good enough in many cases.

After detector simulation, the simulated events go through *digitization* and *reconstruction* in order to end up in the same format as real data, to enable direct comparison.

Digitization and reconstruction

In the digitization step, the energy deposits from the GEANT4 simulation are converted into detector response information, in the same form as the raw data from the real detector. After this, the process of reconstruction is the same for both simulated and real events. In the reconstruction step, the identity and kinematics of physical objects such as leptons and jets are inferred from the detector response information, as explained in Section 2.3.4. Some information on the event reconstruction used in the three-lepton analysis will be given in Section 4.3.

Data formats

Figure 4.2 shows the ATLAS data-processing chain, also indicating the corresponding data format for each step. The right-hand side shows the different steps for MC-simulated data as described in this section, while the left-hand side shows the steps for real data. We see that the steps and formats are the same for real and simulated data from the reconstruction step onwards.

Not mentioned above is the step of derivation. The AOD files produced in the reconstruction step are generally very large, as they contain "everything". However, the majority of the content is usually not relevant for a particular analysis. *Derived AODs* (DAODs) are therefore prepared, containing only a subset of the events ("skimmed"), only a subset of the analysis objects ("thinned"), or only a subset of the information about particular analysis objects ("slimmed"). DAODs with different subsets of the data are produced "centrally" in the ATLAS Collaboration, where each type is often used by multiple, similar analyses. The different analysis teams in turn use these DAODs as input when they produce so-called *ntuples*, which is an even more specialized data format used for "offline" analysis.

4.1.2 Relevant Monte Carlo samples

The signals and backgrounds of chargino–neutralino pair production relevant for the three-lepton analysis were reviewed in Chapter 3. In this section, some information on the production of MC samples for these processes will be given. As producing simulated events is a complicated task, ATLAS has formed the ATLAS MC Production Group to take care of this. In addition to MC samples for common processes relevant to many searches, this group produces samples on request by different analysis teams. The information below briefly summarizes which software and settings have been used to produce the MC samples used in the three-lepton analysis. Further details can be found in Section 4 of Ref. [22].

Some details are common for all samples. First, the detector simulation was done as described in the previous section, either using a full GEANT4 simulation of the ATLAS detector, or using ATLFAST-II for a faster simulation. Further, EVTGEN 1.6.0 and 1.2.0 were used for the modeling of b- and c-hadrons, except those generated using SHERPA. Finally, pile-up was simulated using PYTHIA 8.2. All MC-predicted event yields are used directly in the SM background

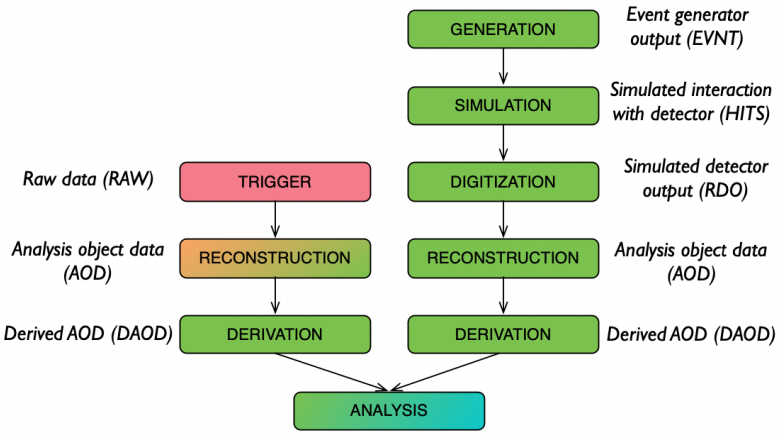

Figure 4.2: The ATLAS data processing chain, also indicating the corresponding data format for each step [123]. The right- and left-hand sides show the steps for MC-simulated and real data, respectively. From the reconstruction step onwards, the steps are the same for both types of data. The background colors of the different steps indicate "where" the steps are executed: "online" (real-time) in the ATLAS detector (pink), at the CERN data centre (orange), on the Worldwide LHC Computing Grid (green) [124, 125], or locally on the analyzer's computer (blue).

estimation, except for the most important backgrounds (details will be given in Section 5.3).

Signal samples

The $\tilde{\chi}_1^\pm\tilde{\chi}_2^0 \to WZ/Wh \to 3\ell$ signal samples were generated from leading-order matrix elements with up to two additional partons using MadGraph 2.6 and Pythia 8.2, for both the wino/bino and the higgsino scenarios. Off-shell WZ decays were modeled using MadSpin [126]. Samples were generated for $\tilde{\chi}_1^\pm/\tilde{\chi}_2^0$ masses between 100 GeV and 850 GeV, and mass splittings Δm between 5 GeV and 850 GeV. The only decays considered for $\tilde{\chi}_1^\pm/\tilde{\chi}_2^0$ were via bosons, with subsequent leptonic decays according to Standard Model branching fractions. Only Higgs-boson decays via WW, ZZ and $\tau\tau$ were generated for the Wh samples. For the on-shell WZ samples, the generated signal events were required to have at least two leptons.[2] For the off-shell WZ and the Wh samples, they were required to have at least three leptons.

All signal samples with decays via WZ were generated for the wino/bino $(+)$ scenario. To simulate the wino/bino $(-)$ scenario relevant for the off-shell WZ

[2]The concept of MC event generator filters will be explained in Section 5.7.1.

analysis, a reweighting in $m_{Z^{(*)}}$ was added,[3] as the only difference between the two scenarios is the mass lineshape of the Z boson from the $\tilde{\chi}_2^0$ decay.

Inclusive production cross-sections were computed at next-to-leading order (NLO) plus next-to-leading-log (NLL) precision [128–133]. For wino production, the computation was performed in the limit of mass-degenerate $\tilde{\chi}_1^\pm$ and $\tilde{\chi}_2^0$, with light $\tilde{\chi}_1^0$. For higgsino production, a partially degenerate case was considered, with the $\tilde{\chi}_1^\pm$ mass equal to the mean of the $\tilde{\chi}_1^0$ and $\tilde{\chi}_2^0$ masses. For both productions, all other supersymmetric particles were assumed to be heavy and decoupled. For production at a center-of-mass energy of $\sqrt{s} = 13$ TeV, the wino $\tilde{\chi}_1^\pm\tilde{\chi}_2^0$ cross-section ranges between 22.67 ± 0.97 pb and 3.42 ± 0.41 fb for $\tilde{\chi}_2^0$ masses between 100 GeV and 850 GeV. For higgsino $\tilde{\chi}_1^\pm\tilde{\chi}_2^0$, the cross-section depends on Δm, and ranges between 12.22 ± 0.26 pb ($\Delta m = 80$ GeV) and 87.2 ± 3.2 fb ($\Delta m = 20$ GeV) for $\tilde{\chi}_2^0$ masses between 100 GeV and 350 GeV.

Background samples

As stated in Section 3.4, there are many Standard Model processes that can result in final states with three leptons. All processes considered in the three-lepton analysis are listed in Table 4.1, together with information on which MC generators have been used to simulate them.

[3] Based on an analytic function presented in Ref. [127].

Table 4.1: Event generators used to simulate the different background processes considered in three-lepton analysis. The middle column lists the generator used for the matrix element calculations, while the right-most column lists the generator used for parton showering and hadronization. "V" denotes a W or Z boson, while the "ggF" and "VBF" acronyms for Higgs stands for "gluon–gluon fusion" and "vector boson fusion", respectively.

Process	Matrix element	Parton showering & hadronization
Diboson [134], triboson [134]	Sherpa 2.2.2	same
Triboson (alternative) [134]	Sherpa 2.2.1	same
Z+jets [135]	Sherpa 2.2.1	Sherpa 2.2.2
$t\bar{t}$ [136], tW [137], single-t [138, 139], $t\bar{t}h$ [140]	Powheg Box 2	Pythia 8.2
$t\bar{t}V$, tZ, tWZ, $t\bar{t}\ell\ell(t \to Wb + (\gamma^*/Z \to \ell\ell))$ [141]	MadGraph5_aMC@NLO 2.3	Pythia 8.2
$t\bar{t}VV$, 3-top, 4-top	MadGraph5_aMC@NLO 2.2	Pythia 8.1
Higgs (ggF, VBF, Vh)	Powheg Box 2	Pythia 8.2

4.2 13 TeV proton–proton collision data

The three-lepton analysis uses the full Run 2 dataset of $\sqrt{s} = 13$ TeV proton–proton collisions recorded by the ATLAS detector between 2015 and 2018. During this run, the LHC collided bunches of protons with bunch-crossing intervals of 25 ns, with an average number of interactions per crossing $\langle\mu\rangle = 34$, see Figure 4.3. The total integrated luminosity delivered by the LHC during the run was 156 fb^{-1}. However, only 147 fb^{-1} was recorded by the ATLAS detector, and after applying quality requirements for the beams, all detector systems and the data itself, the dataset certified for physics-analysis usage corresponds to a total integrated luminosity of 139.0 ± 2.4 fb^{-1}, see Figure 4.4.[4] Table 4.2 shows a breakdown of the total integrated luminosity per year.

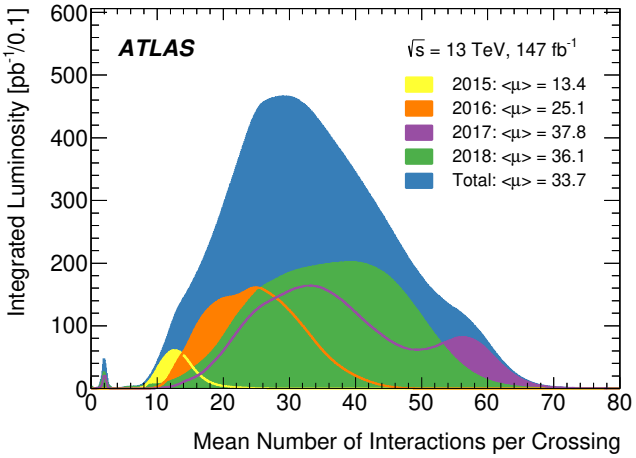

Figure 4.3: Luminosity-weighted distributions of the mean number of interactions per bunch crossing μ for the full Run 2 proton–proton collision dataset at $\sqrt{s} = 13$ TeV [143]. Also shown is the integrated luminosity and the mean μ-value per year.

[4] ATLAS luminosity measurements are obtained using the ATLAS luminosity monitor, LUCID-2 [142].

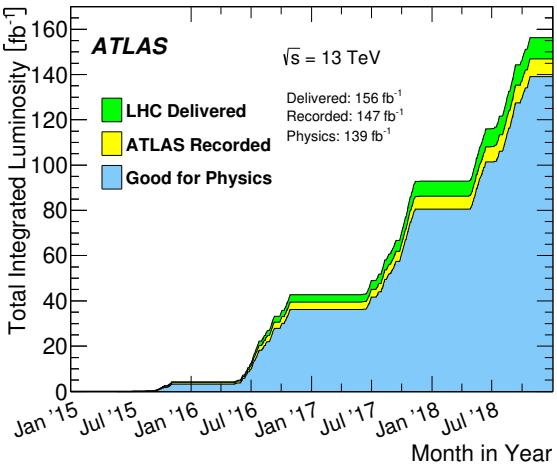

Figure 4.4: Cumulative integrated luminosity delivered to (green) and recorded by (yellow) the ATLAS detector between 2015 and 2018 during stable-beam proton–proton collision data-taking at $\sqrt{s} = 13$ TeV [143]. Also shown is the cumulative integrated luminosity certified for physics-analysis usage (blue).

Table 4.2: Summary of the integrated luminosities recorded by ATLAS (after applying quality requirements) during Run 2, per year and combined [144].

Year	Int. lumi. [fb^{-1}]	Tot. unc. [fb^{-1}]	Rel. unc. [%]
2015 + 2016	36.2	0.8	2.1
2017	44.3	1.0	2.4
2018	58.5	1.2	2.0
Combined	139.0	2.4	1.7

4.3 Event reconstruction and preselection

The concept of event reconstruction was discussed in Sections 2.3.4 and 4.1.1. As explained in the latter, the reconstruction process is the same for both simulated data (after digitization) and real data (after triggering). In this section, a brief summary of the event reconstruction and common preselection used in the three-lepton analysis will be given, including information on the triggers used for the real data. Further details can be found in Section 5 of Ref. [22].

For the Wh and on-shell WZ analyses, events are chosen using dilepton triggers [145, 146]. For the off-shell WZ analysis, events are selected using single-lepton, dilepton and trilepton triggers. Further, the off-shell WZ selection is complemented at high $E_{\mathrm{T}}^{\mathrm{miss}}$ with events with softer leptons using $E_{\mathrm{T}}^{\mathrm{miss}}$

triggers [147]. The p_{T} thresholds used for the lepton triggers depend on the lepton type, their quality and multiplicity. In order to ensure that the trigger efficiencies are well understood in the analysis phase space, tighter requirements on quality and p_{T} are applied to fully reconstructed signal leptons (to be introduced in the following). For the same reason, an offline requirement of $E_{\mathrm{T}}^{\mathrm{miss}} > 200$ GeV is imposed on events selected by a $E_{\mathrm{T}}^{\mathrm{miss}}$ trigger.

In order to be considered, reconstructed objects must satisfy a set of loose, *baseline* criteria. To be selected for the analysis, they also have to pass a second, tigther set of *signal* criteria. The most important objects in the three-lepton analysis are electrons, muons and jets. The baseline and signal selection criteria used for leptons and jets are shown in Tables 4.3 and 4.4, respectively, and briefly discussed below.

Baseline electrons (muons) must satisfy $p_{\mathrm{T}} > 4.5$ (3) GeV and $|\eta| < 2.47$ (2.5). The different identification working points (ID WPs) for electrons and muons were introduced in 2.3.4. Baseline muons must satisfy the "Medium" ID WP. In addition to satisfying the "Loose" ID WP, baseline electrons must produce a "hit" in the innermost pixel-detector layer (referred to as the *B-layer*) [148]. Signal muons must also satisfy the "Medium" ID WP.[5] Further, in order to suppress pile-up, all baseline leptons are required to have a trajectory consistent with the primary vertex of the collision by setting an upper limit on the *longitudinal impact parameter* z_0, $|z_0 \sin\theta| < 0.5$ mm.[6] For signal leptons, an additional requirement on the significance of the *transverse impact parameter* d_0, $|d_0/\sigma(d_0)|$, is imposed, where $\sigma(d_0)$ is the resolution of d_0. Signal electrons and muons must satisfy $|d_0/\sigma(d_0)| < 5$ and < 3, respectively. Finally, in order to reduce contributions from fake or non-prompt (FNP) leptons, the signal leptons are required to be sufficiently isolated from other objects. Simply put, this is achieved by setting an upper limit on the amount of activity near the lepton candidate. The isolation working points (ISO WPs) used in this analysis are described in Refs. [148] and [149] for electrons and muons, respectively. In the off-shell WZ analysis, signal electrons must satisfy the "Gradient" ISO WP, while muons must satisfy the "Loose" ISO WP.[7] Further, as the lepton with the lowest p_{T} of the three (ℓ_3) is commonly the most FNP-like, a dedicated multivariate discriminant "non-prompt lepton BDT" [150] is used to tighten the requirements on this lepton. The "PLVTight" working point for this discriminator is used.

Baseline jets must satisfy $p_{\mathrm{T}} > 20$ GeV and fall within the full calorimeter acceptance, i.e. $|\eta| < 4.5$. Signal jets must satisfy $|\eta| < 2.8$, and satisfy the "Loose" quality requirement described in Ref. [151]. Further, in order to suppress jets originating from pile-up, signal jet candidates with $p_{\mathrm{T}} > 120$ GeV and

[5] Although some of the electron and muon identification working points are called the same, they have different definitions.

[6] The distance of closest approach in the transverse plane between a track and the beamline is referred to as the transverse impact parameter d_0. The longitudinal impact parameter z_0 corresponds to the z-coordinate distance between the primary vertex and the point along the track defining the impact parameter.

[7] Note that the on-shell WZ and Wh analyses use the "Tight" ISO WP for all signal leptons. The different WP choices reflect the different levels of contribution from the FNP lepton background in the analyses.

Table 4.3: Summary of the lepton selection criteria used in the three-lepton analysis. The signal requirements are applied on top of the baseline requirements.

	Baseline electron	Baseline muon
p_{T} [GeV]	> 4.5	> 3
$\lvert\eta\rvert$ [-]	< 2.47	< 2.5
ID WP	Loose and B-layer	Medium
$\lvert z_0 \sin\theta\rvert$ [mm]	< 0.5	
	Signal electron	**Signal muon**
ID WP	Medium	-
$\lvert d_0/\sigma(d_0)\rvert$ [-]	< 5	< 3
ISO WP	Gradient	Loose
	+ PLVTight for ℓ_3	

$|\eta| < 2.5$ (i.e. falling within the inner-detector acceptance) must satisfy the "Medium" working point of the track-based jet vertex tagger (JVT) [152, 153]. Additionally, for signal jets with $|\eta| < 2.5$, the MV2c10 b-tagging algorithm [154] is used to identify if they contain b-hadrons. The working point of this algorithm is chosen such that *b-jets* from simulated $t\bar{t}$ events are identified with 85% efficiency.

Not mentioned above is *overlap removal*. In order to prevent that single tracks and calorimeter deposits are identified as or assigned to multiple objects, an overlap-removal procedure is applied to baseline leptons and jets. First, all electrons sharing an inner-detector track with a muon are discarded. Second, all jets separated from remaining electrons by less than $\Delta R = 0.2$ are removed. Third, all jets associated with fewer than three tracks with $p_{\mathrm{T}} \geq 500$ MeV and within $\Delta R = 0.4$ of a muon are removed. Finally, electrons or muons separated from surviving jets by less than $\Delta R = 0.4$ are discarded.

In order to account for small differences in efficiency between simulated and real data, the simulated events are corrected with scale factors often referred to as "weights". Some examples include weights for efficiencies for trigger and flavor-tagging.

A common preselection of exactly three signal leptons is applied for all three simplified-model scenarios. In addition, events are required to have exactly three baseline leptons to ensure *orthogonality* with other ATLAS supersymmetry searches, to allow for statistical combination of analysis results. Two such statistical combinations will be presented in Chapter 7. More detailed search regions for the off-shell WZ analysis will be defined in the next chapter.

Table 4.4: Summary of the jet selection criteria used in the three-lepton analysis. The signal requirements are applied on top of the baseline requirements.

	Baseline jet
p_{T} [GeV]	> 20
$\lvert\eta\rvert$ [-]	< 4.5
	Signal jet
$\lvert\eta\rvert$ [-]	< 2.8
JVT WP	Medium (if $p_{\mathrm{T}} < 120$ GeV and $\lvert\eta\rvert < 2.5$)
	Signal b-jet
$\lvert\eta\rvert$ [-]	< 2.5
b-tagging algorithm	MV2c10
Efficiency WP	85%

4.4 Summary and outlook

This chapter gave an introduction to some of the methodology used to analyze the data collected with the ATLAS detector in the search for chargino–neutralino pair production in three-lepton final states. We started by arguing the need for simulated data when searching for new physics processes, before explaining how simulated events are generated using Monte Carlo event generators, as well as how such simulated events must go through detector simulation and digitization in order to end up in the same format as the real data collected with the ATLAS detector. We then moved on to giving some information on the Monte Carlo samples used in the three-lepton analysis, before describing the Run 2 dataset of $\sqrt{s} = 13$ TeV proton–proton collisions recorded by ATLAS. Finally, we reviewed the event reconstruction and preselection used in the analysis.

Note that all software and data formats mentioned in this chapter were described in the context of Run 2 of the LHC. These are constantly being improved. For instance, the AtlFast-II package, using a parametric description of calorimeter responses to speed up ATLAS detector simulation for simulated events, has been replaced by the AtlFast3 package [155] for Run 3, which has better accuracy in reproducing Geant4. Further, in Section 6.2, we will learn that a new analysis model has been deployed for Run 3, where as many analyses as possible will use the same DAOD format.

In the next chapter, the three-lepton off-shell WZ analysis will be summarized.

Chapter 5

A three-lepton off-shell WZ analysis

The three simplified-model scenarios of chargino–neutralino pair production considered in the three-lepton analysis were presented in Chapter 3: on-shell WZ, off-shell WZ and Wh. I worked on the off-shell WZ analysis, which will be summarized in this chapter. My contributions were aiding in the optimization of the high-$E_{\mathrm{T}}^{\mathrm{miss}}$ signal regions and preparing input to enable reinterpretation of the analysis. For completeness, the final results for the on-shell WZ and Wh analyses will also be presented, as the on-shell WZ results are statistically combined with the off-shell WZ results, while the Wh results will be used in a statistical combination to be presented in Chapter 7.

An overview of the variables used in the off-shell WZ analysis will be given in Section 5.1. In Section 5.2, the analysis search regions will be presented, including an explanation on how these are optimized, before the estimation of the most important backgrounds will be explained in Section 5.3. Section 5.4 will give a summary of the systematic uncertainties considered in the analysis. Further, Section 5.5 will introduce the statistical procedures for discovery and exclusion, before the results will be presented in Section 5.6. Finally, Section 5.7 will summarize my contribution to preparing input to enable reinterpretation of the analysis.

5.1 Overview of variables

In this section, an overview of the variables used in the off-shell WZ analysis will be given. Note that these variables are considered/constructed after applying the preselection of exactly three baseline and signal leptons as explained in Section 4.3.

$\boldsymbol{n_{\mathbf{jets}}^{30\ \mathrm{GeV}}}$ The number of jets with $p_{\mathrm{T}} > 30$ GeV.

$\boldsymbol{n_{\text{b-jets}}}$ The number of b-jets with $p_{\mathrm{T}} > 20$ GeV.

$\boldsymbol{n_{\mathrm{SFOS}}}$ The number of *same-flavor opposite-sign* (SFOS) lepton pairs. A SFOS lepton pair is expected from the leptonic decay of the Z boson.

$\boldsymbol{m_{\ell\ell}}$ The *invariant mass* of the SFOS lepton pair. From the enegy–momentum relation $m^2 = E^2 - |\mathbf{p}|^2$,[1] where m is mass, E is energy, and $\mathbf{p}$ is momentum,

[1] When using natural units where the speed of light $c = 1$.

the invariant mass of a two-particle decay is defined as

$$\begin{aligned} m_0^2 &= (E_1 + E_2)^2 - |\mathbf{p_1} + \mathbf{p_2}|^2 \\ &= m_1^2 + m_2^2 + 2(E_1 E_2 - \mathbf{p_1} \cdot \mathbf{p_2}), \end{aligned} \tag{5.1}$$

where m_0 is the rest mass of the mother particle, and the subscripts 1 and 2 refer to the two daughter particles.

If there are more than one SFOS pair, there are multiple ways to assign leptons to the Z boson:

1. $m_{\ell\ell}$: assign the SFOS lepton pair with invariant mass closest to the Z-boson mass to the Z boson (traditional assignment),
2. $m_{\ell\ell}^{\text{min}}$: assign the SFOS lepton pair with the smallest invariant mass to the Z boson,
3. $m_{\ell\ell}^{\text{max}}$: assign the SFOS lepton pair with the largest invariant mass to the Z boson.

In all three cases, the remaining lepton is assigned to the W boson and is referred to as the W lepton, denoted ℓ_W. For the off-shell WZ analysis, the $m_{\ell\ell}^{\text{min}}$ assignment is used.

$m_{3\ell}$ The invariant mass of the three-lepton system.

m_{T} The *transverse mass* of the W boson. For a two-particle decay into one visible and one invisible particle, the equivalent of the invariant mass defined in Equation (5.1) is the transverse mass, denoted m_T. For events with at least one SFOS lepton pair, the transverse mass is constructed using the W lepton and the $E_{\text{T}}^{\text{miss}}$ as

$$m_T = \sqrt{2 p_{\text{T}}^{\ell_W} E_{\text{T}}^{\text{miss}} (1 - \cos(\Delta\theta))}, \tag{5.2}$$

where $\Delta\theta$ is the separation between the lepton and $E_{\text{T}}^{\text{miss}}$ in the transverse plane. This exploits the difference between Standard Model WZ, which has a Jacobian peak with a sharp cut-off at $m_{\text{T}} \sim m_W$, and the targeted signals, which have relatively flat m_{T} distributions.

Two different versions of this variable are used in the off-shell WZ analysis. In the following, m_{T} denotes the scenario where the W lepton is assigned according to $m_{\ell\ell}$, while $m_{\text{T}}^{\text{mllmin}}$ denotes the scenario where the W lepton is assigned according to $m_{\ell\ell}^{\text{min}}$, as described above.

m_{T2} The *stransverse mass* m_{T2} [156, 157] is an extension of the transverse mass. It was introduced to measure the masses of pair-produced particles at hadron colliders, where both decay into one visible and one invisible particle. This is the case for our supersymmetric signal, as illustrated in Figure 3.1. For such cases, two transverse masses can be defined, one for each branch. However, only the total transverse momentum of all invisible particles in the event is measured, and so the fraction belonging to each branch is unknown. Instead, the m_{T2} variable gives a lower bound on the maximum of the transverse mass.

For the off-shell WZ analysis, the two visible particles are considered to be the Z system (comprised of both Z leptons, $\ell_1\ell_2$, assigned according to $m_{\ell\ell}^{\text{min}}$), and the W lepton (ℓ_3). The invisible particles making up the total missing transverse momentum $\mathbf{E}_{\text{T}}^{\text{miss}}$ are the two LSPs and the W neutrino. This gives

$$m_{\text{T2}}^{m_\chi}\left(\mathbf{p}_{\text{T}}^{\ell_1\ell_2}, \mathbf{p}_{\text{T}}^{\ell_3}, \mathbf{E}_{\text{T}}^{\text{miss}}\right) = \min_{\mathbf{q}_{\text{T}}}\left(\max\left[m_{\text{T}}\left(\mathbf{p}_{\text{T}}^{\ell_1\ell_2}, \mathbf{q}_{\text{T}}, m_\chi\right), m_{\text{T}}\left(\mathbf{p}_{\text{T}}^{\ell_3}, \mathbf{E}_{\text{T}}^{\text{miss}} - \mathbf{q}_{\text{T}}, m_\chi\right)\right]\right), \quad (5.3)$$

where the transverse mass m_{T} in this m_{T2} formula is defined as

$$m_{\text{T}}\left(\mathbf{p}_{\text{T}}^{\ell}, \mathbf{q}_{\text{T}}, m_\chi\right) = \sqrt{m_\ell^2 + m_\chi^2 + 2\left(\sqrt{(p_{\text{T}}^\ell)^2 + m_\ell^2}\sqrt{q_{\text{T}}^2 + m_\chi^2} - \mathbf{p}_{\text{T}}^\ell \cdot \mathbf{q}_{\text{T}}\right)}. \quad (5.4)$$

Note that a hypothesized mass m_χ is assigned to each invisible particle leg, corresponding to the LSP $\tilde{\chi}_1^0$ mass. However, studies have shown that the dependency on this choice is generally small, except when assuming $m_\chi \sim 0$ GeV for signals with finite $\tilde{\chi}_1^0$ mass. Thus, a sufficiently high m_χ mass of 100 GeV is chosen, and the correponding variable is labeled m_{T2}^{100}.

min $\Delta R_{3\ell}$ The minimum angular distance between all lepton pairs: $\min \Delta R_{3\ell} = \min[\Delta R(\ell_i, \ell_j)$; for all lepton pairs $(\ell_i, \ell_j)]$.

min ΔR_{SFOS} The minimum angular distance between all SFOS lepton pairs: $\min \Delta R_{\text{SFOS}} = \min[\Delta R(\ell_i, \ell_j)$; for all SFOS lepton pairs $(\ell_i, \ell_j)]$.

$E_{\text{T}}^{\text{miss}}$ significance In an ideal detector, a non-zero $E_{\text{T}}^{\text{miss}}$ value indicates the presence of non-interacting particles. However, experimental effects such as the energy resolution of the reconstructed objects the $E_{\text{T}}^{\text{miss}}$ calculation is based on, and instrumental effects such as e.g. broken cells, can lead to artificial or fake $E_{\text{T}}^{\text{miss}}$. The so-called $E_{\text{T}}^{\text{miss}}$ *significance* is introduced to discriminate events where the $E_{\text{T}}^{\text{miss}}$ actually arises from undetected particles in the final state from events where the $E_{\text{T}}^{\text{miss}}$ arises from poorly measured particles and jets.

An "object-based $E_{\text{T}}^{\text{miss}}$ significance" [158] is defined as

$$E_{\text{T}}^{\text{miss}}\text{ significance} = \sqrt{\frac{|\mathbf{E}_{\text{T}}^{\text{miss}}|^2}{\sigma_{\text{L}}^2(1-\rho_{\text{LT}}^2)}}, \quad (5.5)$$

where the quantity σ_{L} denotes the p_{T} resolution of the system, and ρ_{LT} is a correlation factor between the resolutions of the p_{T} components parallel (L) and perpendicular (T) to $\mathbf{E}_{\text{T}}^{\text{miss}}$. A high $E_{\text{T}}^{\text{miss}}$-significance value indicates that the observed $E_{\text{T}}^{\text{miss}}$ is more likely to be the result of undetected particles rather than experimental effects.

$|\mathbf{p}_{\mathrm{T}}^{\mathbf{lep}}|/E_{\mathrm{T}}^{\mathbf{miss}}$ The ratio of the magnitude of a vectorial p_{T} sum of the three leptons, $|\mathbf{p}_{\mathrm{T}}^{\mathrm{lep}}|$, to $E_{\mathrm{T}}^{\mathrm{miss}}$. This ratio represents the extent to which the transverse momentum of the $\tilde{\chi}_1^{\pm}\tilde{\chi}_2^0$ system, recoiling against initial state radiation (ISR) jets, is converted into leptons as opposed to $E_{\mathrm{T}}^{\mathrm{miss}}$. As the massive $\tilde{\chi}_1^0$ contributes to the $E_{\mathrm{T}}^{\mathrm{miss}}$, signals tend to populate lower parts of the $|\mathbf{p}_{\mathrm{T}}^{\mathrm{lep}}|/E_{\mathrm{T}}^{\mathrm{miss}}$ distribution than Standard Model backgrounds.

5.2 Search regions

To search for a possible signal, selection criteria are defined to enhance the expected signal yield relative to the background. Signal regions (SRs) are designed using the MC simulation of SUSY signal and corresponding SM background processes, by setting upper and/or lower limits (cuts) on discriminant variables for which signal and background distributions look different. This design procedure will be explained in the following section, while the off-shell WZ signal regions will be presented in Section 5.2.2.

5.2.1 Signal region optimization

When designing signal regions, the figure of merit that we want to optimize is the expected signal sensitivity, or the *expected significance* of measuring a signal-induced excess of events on top of the background. Given expected numbers of background events b and signal events s, the significance Z is a measure of how (in)consistent a measurement of $s + b$ is with the background-only expectation. The significance is expressed in units of sigma (σ), i.e. the number of standard deviations of the unit Gaussian.

In this signal-region design process, we want to find the set of cuts that maximizes the expected significance. The final statistical procedure will be explained in Section 5.5. However, it can be overly time-consuming and computationally expensive to rerun the full statistical calculation for different cut alternatives when searching for the optimal one. Instead, it is often found satisfactory to estimate the approximate significance in the optimization process.[2] In the ATLAS Collaboration, this is usually done using the function

[2]For some analyses a reoptimization using the full statistical analysis is performed at a later stage. However, one should be cautious to reoptimize too much, as we do not want to base our choices too much on specific signal hypotheses. In addition, at least some background should be kept in order for the statistical analysis to be meaningful.

BinomialExpZ [159, 160] implemented in the RooStats package [161].[3,4] This function takes three input arguments: the expected number of signal events (s), the expected number of background events (b) and the relative background uncertainty ($\Delta b/b$) in the signal region. A Gaussian (normal) background uncertainty distribution is assumed, and the resulting significance is thus often referred to as Z_N. As a rough, conservative estimate, we use a flat (constant) 30% systematic uncertainty, i.e. $\Delta b/b = 0.30$. Note that using this simpler Z_N calculation typically gives slightly stronger results (higher Z-values) compared to doing a full statistical analysis.

In practice, cuts are chosen by looking by eye at so-called *N-1 distributions* like the one in Figure 5.1. In such plots, all already defined cuts for the selection/region have been applied, but no cut value has yet been applied for the variable the distribution is plotted for (so all N cuts applied minus one, hence N-1). The lower panel shows the expected significance Z_N for a relevant selection of signal hypotheses (signal mass points $(m(\tilde{\chi}_2^0), m(\tilde{\chi}_1^0))$ with different Δm), as a function of lower-cut value. Namely, each bin in the lower panel shows the expected significance for when all events to the left of the bin in the upper panel are rejected, and all events to the right (including the bin in question) are used as input to the Z_N calculation. The significance distributions in the lower panel can thus guide our choice on where to place a potential lower cut. In this particular example, a lower cut of 25 GeV is chosen for the leading lepton p_{T}, as indicated by the orange arrow in the upper panel. We see that this choice is a nice compromise for the four signal hypotheses with positive Z_N.[5]

Note that the choice of benchmark signal hypotheses to consider in the optimization process described above is important, as the expected significance can peak for different cut values for different hypotheses. We must therefore check a selection of hypotheses, to see how they behave under different cuts. In the final analysis, however, there are many more signal hypotheses that will be evaluated using the resulting signal region. Hence, we must make sure to find a compromise between maximizing the expected significance for a specific signal hypothesis and having good coverage for an assortment of hypotheses. Also note that for the example in Figure 5.1, the Z_N distributions in the lower panel should only be used to decide on a potential *lower* cut. Corresponding distributions can be made for the upper-cut case.

[3]This function calculates the significance Z from a *likelihood* L describing a main measurement x distributed as a Poisson around $s+b$ and an auxiliary measurement y distributed as a Poisson around τb:

$$L(x, y|s, b, \tau) = P(x|s + b) \times P(y|\tau b), \tag{5.6}$$

where P denotes a Poisson distribution, and the expected background in the auxiliary measurement is a factor τ larger than in the main measurement. More details on the relation between likelihoods and significances will be given in Section 5.5.

[4]In 2020, the ATLAS Collaboration published a public note, Ref. [162], comparing several methods for estimating the significance of an observation of a number of events given a predicted rate with some uncertainty. The resulting recommended method is based on the same likelihood as the BinomialExpZ function, as can be seen in Section 4.4 of the note.

[5]Negative expected significance is an artefact of the BinomialExpZ function, occuring in cases with very few signal events in combination with a large relative background uncertainty.

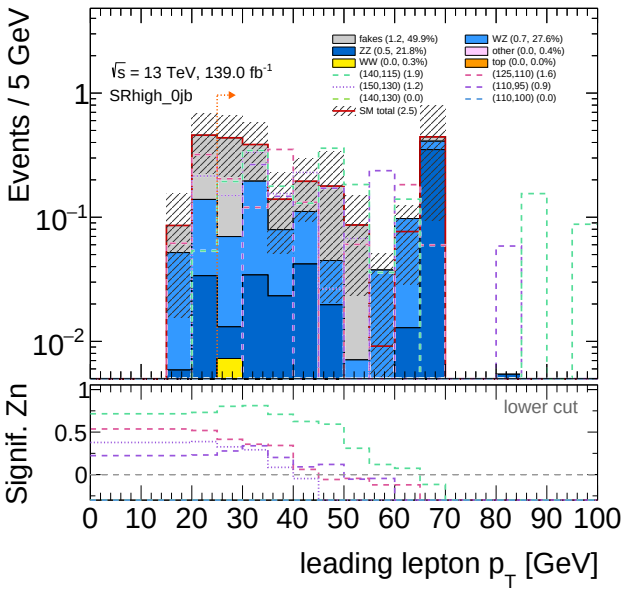

Figure 5.1: Example distribution used to explain the signal-region design process. In this so-called N-1 distribution, all already defined cuts for the selection/region have been applied, and the goal is to find the optimal cut for the variable shown in the distribution. The lower panel shows the expected significance Z_N for a relevant selection of signal hypotheses as a function of lower-cut value. In this particular example, a lower cut of 25 GeV is chosen for the leading lepton p_{T}, as indicated by the orange arrow in the upper panel.

I contributed to the optimization of the high-$E_{\mathrm{T}}^{\mathrm{miss}}$ signal regions of the off-shell WZ analysis, which will be summarized in the next section (together with the low-$E_{\mathrm{T}}^{\mathrm{miss}}$ ones, division to be explained). Due to the large number of relevant N-1 distributions (more than 160 altogether), for which each cut choice was made manually, and the fact that several people were involved in this work, I will not attempt to provide a full justification for each cut value. Only a few example distributions for some of the more high-level variables will be shown. Note that all signal regions in the three-lepton analysis are optimized to the wino/bino (+) interpretation.

5.2.2 Signal region definitions

In addition to the common preselection of exactly three baseline and exactly three signal leptons mentioned in Section 4.3, further preselection requirements for the off-shell WZ selection are given in the upper part of Table 5.1. First, at least one same-flavor opposite-sign (SFOS) lepton pair is required, assigned to the Z boson. The remaining lepton is assigned to the W boson. If more than

one SFOS lepton pair is present in the event, the pair with the smallest invariant mass is assigned to the Z boson, as explained in Section 5.1. A requirement $m_{\ell\ell}^{\min} < 75$ GeV is introduced to select *off-shell Z* events. Also requiring $m_{\ell\ell}^{\max} < 75$ GeV reduces on-shell Z contamination from Standard Model WZ background. The lower bound on $m_{\ell\ell}^{\min}$ of 1 GeV is set to remove events with collimated leptons, for which estimating FNP lepton background is challenging. Further, events with b-jets are vetoed to reduce contamination from $t\bar{t}$, and the three leptons are required to be well separated by setting min $\Delta R_{3\ell} > 0.4$. Finally, $m_{\ell\ell}^{\min}$ mass ranges of $[3, 3.2]$ and $[9, 12]$ GeV are vetoed to avoid contributions from the low-mass J/ψ and Υ resonances, except in the phase space with high $E_{\mathrm{T}}^{\mathrm{miss}}$ and at least one jet, where this contribution is negligible.

These preselected events are then further divided into four categories based on $E_{\mathrm{T}}^{\mathrm{miss}}$ and the multiplicity of jets with $p_{\mathrm{T}} > 30$ GeV. An overview of these categories, or inclusive regions, referred to as $\mathtt{SR}^{\mathtt{offWZ}}_{\mathtt{low}E_{\mathrm{T}}}\mathtt{-0j}$, $\mathtt{SR}^{\mathtt{offWZ}}_{\mathtt{low}E_{\mathrm{T}}}\mathtt{-nj}$, $\mathtt{SR}^{\mathtt{offWZ}}_{\mathtt{high}E_{\mathrm{T}}}\mathtt{-0j}$ and $\mathtt{SR}^{\mathtt{offWZ}}_{\mathtt{high}E_{\mathrm{T}}}\mathtt{-nj}$, are shown in Figure 5.2. Due to the recoil between the $\tilde{\chi}_1^{\pm}\tilde{\chi}_2^0$ system and the jet(s) in the jet-inclusive regions, the boundary between low and high $E_{\mathrm{T}}^{\mathrm{miss}}$ is set higher in these regions than in the jet-veto regions (200 GeV vs. 50 GeV). Regions $\mathtt{SR}^{\mathtt{offWZ}}_{\mathtt{low}E_{\mathrm{T}}}\mathtt{-0j}$, $\mathtt{SR}^{\mathtt{offWZ}}_{\mathtt{low}E_{\mathrm{T}}}\mathtt{-nj}$ and $\mathtt{SR}^{\mathtt{offWZ}}_{\mathtt{high}E_{\mathrm{T}}}\mathtt{-0j}$ primarily target signals with moderate mass splitting, $\Delta m(\tilde{\chi}_2^0, \tilde{\chi}_1^0) \sim [40, 90]$ GeV, and mostly rely on moderate kinematics and lepton triggers. The $\mathtt{SR}^{\mathtt{offWZ}}_{\mathtt{high}E_{\mathrm{T}}}\mathtt{-nj}$ region also target signals with highly compressed mass spectra, $\Delta m \lesssim 40$ GeV, resulting in events with very soft leptons. These events are selected using $E_{\mathrm{T}}^{\mathrm{miss}}$ triggers, by exploiting the high $E_{\mathrm{T}}^{\mathrm{miss}}$ recoiling against the hadronic activity. The initial lepton p_{T} requirements are kept as low as possible: $p_{\mathrm{T}} > 10$ GeV for $\mathtt{SR}^{\mathtt{offWZ}}_{\mathtt{low}E_{\mathrm{T}}}\mathtt{-0j}$, $\mathtt{SR}^{\mathtt{offWZ}}_{\mathtt{low}E_{\mathrm{T}}}\mathtt{-nj}$

Table 5.1: Summary of the preselection requirements applied in the inclusive signal regions of the off-shell WZ selection [22]. In rows where only one value is given it applies to all regions. "-" indicates no requirement is applied for a given variable/region.

	Preselection requirements			
Variable	$\mathtt{SR}^{\mathtt{offWZ}}_{\mathtt{low}E_{\mathrm{T}}}\mathtt{-0j}$	$\mathtt{SR}^{\mathtt{offWZ}}_{\mathtt{low}E_{\mathrm{T}}}\mathtt{-nj}$	$\mathtt{SR}^{\mathtt{offWZ}}_{\mathtt{high}E_{\mathrm{T}}}\mathtt{-0j}$	$\mathtt{SR}^{\mathtt{offWZ}}_{\mathtt{high}E_{\mathrm{T}}}\mathtt{-nj}$
$n_{\mathrm{lep}}^{\mathrm{baseline}}$, $n_{\mathrm{lep}}^{\mathrm{signal}}$	= 3			
n_{SFOS}	≥ 1			
$m_{\ell\ell}^{\max}$ [GeV]	< 75			
$m_{\ell\ell}^{\min}$ [GeV]	∈ [1, 75]			
$n_{b\text{-jets}}$	= 0			
min $\Delta R_{3\ell}$	> 0.4			
Resonance veto $m_{\ell\ell}^{\min}$ [GeV]	∉ [3, 3.2], ∉ [9, 12]			-
Trigger	(multi-)lepton		((multi-)lepton ‖ $E_{\mathrm{T}}^{\mathrm{miss}}$)	
$n_{\mathrm{jets}}^{30\ \mathrm{GeV}}$	= 0	≥ 1	= 0	≥ 1
$E_{\mathrm{T}}^{\mathrm{miss}}$ [GeV]	< 50	< 200	> 50	> 200
$E_{\mathrm{T}}^{\mathrm{miss}}$ significance	> 1.5	> 3.0	> 3.0	> 3.0
$p_{\mathrm{T}}^{\ell_1}$, $p_{\mathrm{T}}^{\ell_2}$, $p_{\mathrm{T}}^{\ell_3}$ [GeV]	> 10			> 4.5(3.0) for $e(\mu)$
$\lvert m_{3\ell} - m_Z \rvert$ [GeV]	> 20 ($\ell_{\mathrm{W}} = e$ only)		-	
min ΔR_{SFOS}	[0.6, 2.4] ($\ell_{\mathrm{W}} = e$ only)		-	

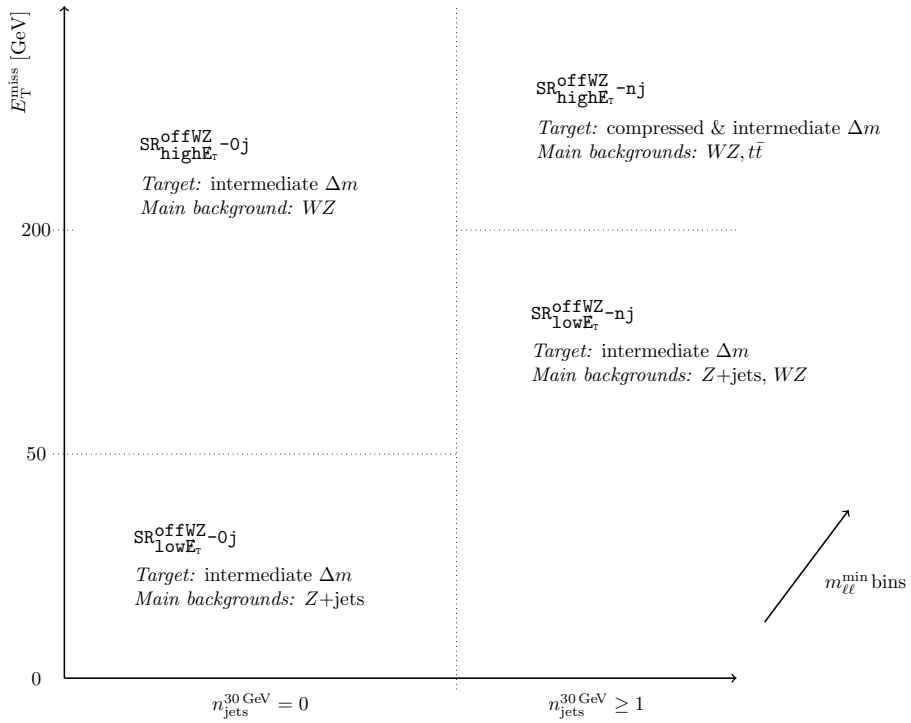

Figure 5.2: Overview of the four inclusive signal regions $\mathtt{SR}^{\mathtt{offWZ}}_{\mathtt{lowE_T}}$-0j, $\mathtt{SR}^{\mathtt{offWZ}}_{\mathtt{lowE_T}}$-nj, $\mathtt{SR}^{\mathtt{offWZ}}_{\mathtt{highE_T}}$-0j and $\mathtt{SR}^{\mathtt{offWZ}}_{\mathtt{highE_T}}$-nj for the off-shell WZ analysis, in terms of $E_{\mathrm{T}}^{\mathrm{miss}}$ and the number of jets with $p_{\mathrm{T}} > 30$. Each of these four regions are further divided into bins in the primary discrimant variable for the off-shell WZ selection, namely $m_{\ell\ell}^{\mathrm{min}}$.

and $\mathtt{SR}^{\mathtt{offWZ}}_{\mathtt{highE_T}}$-0j, and $p_{\mathrm{T}} > 4.5$ (3.0) GeV for electrons (muons) in $\mathtt{SR}^{\mathtt{offWZ}}_{\mathtt{highE_T}}$-nj. However, the selection is restricted by the trigger p_{T} requirements, and some further p_{T} requirements are applied in the bin-by-bin SR optimization that will be discussed in the following.

Further preselection requirements are added to suppress the Z+jets background. A lower bound on the $E_{\mathrm{T}}^{\mathrm{miss}}$ significance is set: 1.5 for $\mathtt{SR}^{\mathtt{offWZ}}_{\mathtt{lowE_T}}$-0j, and 3.0 for the three other regions. To suppress fake electrons due to photon-conversion, some additional requirements are applied for $\mathtt{SR}^{\mathtt{offWZ}}_{\mathtt{lowE_T}}$if the W lepton — in this case selected using the traditional $m_{\ell\ell}$ lepton assignment defined in Section 5.1, to best capture the SM background topology for rejection — is an electron: then the three-lepton invariant mass $m_{3\ell}$ is required to be off the Z-boson peak ($|m_{3\ell} - m_Z| > 20$ GeV), and the minimum angular distance between all SFOS lepton pairs must be within $\min \Delta R_{\mathrm{SFOS}} \in [0.6, 2.4]$.

The primary discriminant variable for the off-shell WZ selection is $m_{\ell\ell}^{\mathrm{min}}$. As the electroweakino signal decays via off-shell W and Z bosons, the invariant mass of the SFOS lepton pair is kinematically bound by the signal mass splitting

$\Delta m(\tilde{\chi}_2^0, \tilde{\chi}_1^0)$. This can be seen in the left plot of Figure 5.3, where the signals demonstrate a cut-off in $m_{\ell\ell}^{\text{min}}$ matching the mass splitting, while backgrounds do not. To take advantage of this signal feature, the signal region phase space is further divided into $m_{\ell\ell}^{\text{min}}$ bins targeting signals with different mass splittings. Seven $m_{\ell\ell}^{\text{min}}$ bins, labeled "a" to "g", are defined with boundaries at 1, 12, 15, 20, 30, 40, 60 and 75 GeV. The "a" bin is only considered for $\text{SR}^{\text{offWZ}}_{\text{high}\not{E}_{\text{T}}}\text{-nj}$, to avoid low-mass resonance backgrounds, as discussed above.

Also the stransverse mass m_{T2}^{100} shows a kinematic edge for the signal, see right plot of Figure 5.3. This cut-off reflects the kinematic constraint originating from the $\tilde{\chi}_1^{\pm} \to W^* \tilde{\chi}_1^0$ decay chain. The kinematic edge appears at $m_{\text{T2}}^{100} = \Delta m(\tilde{\chi}_2^0, \tilde{\chi}_1^0) + 100$ GeV. To take advantage of this feature, a sliding cut is applied per $m_{\ell\ell}^{\text{min}}$ bin, requiring m_{T2}^{100} to be smaller than the upper edge of the $m_{\ell\ell}^{\text{min}}$ bin + 100 GeV. This cut is particularly effective in the lowest $m_{\ell\ell}^{\text{min}}$ bins, targeting the smallest mass splittings. Figure 5.4(a) shows the N-1 distribution for m_{T2}^{100} for region $\text{SR}^{\text{offWZ}}_{\text{high}\not{E}_{\text{T}}}\text{-njd}$, for which an upper cut value of 130 GeV is applied.

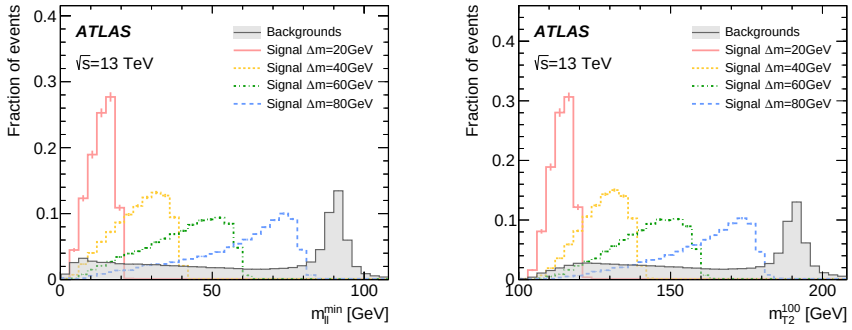

(a) (b)

Figure 5.3: Distributions of (a) $m_{\ell\ell}^{\text{min}}$ and (b) m_{T2}^{100} showing the expected Standard Model background as well as signals with various mass splittings $\Delta m(\tilde{\chi}_2^0, \tilde{\chi}_1^0)$, for a selection of exactly three baseline and signal leptons [22]. The distributions are normalized to unity. Signals demonstrate a cut-off in both variables matching the mass splitting, while backgrounds do not. The dominant background in this selection is WZ, with the Z-boson mass peak visible in both distributions.

Additional cuts on discriminating variables are applied per $m_{\ell\ell}^{\text{min}}$ bin, to further suppress the SM backgrounds. Different background processes are dominant for the different inclusive regions, as indicated in Figure 5.2. All cuts are summarized in Table 5.2. In $\text{SR}^{\text{offWZ}}_{\text{low}\not{E}_{\text{T}}}\text{-0j}$, $\text{SR}^{\text{offWZ}}_{\text{low}\not{E}_{\text{T}}}\text{-nj}$ and $\text{SR}^{\text{offWZ}}_{\text{high}\not{E}_{\text{T}}}\text{-0j}$, the lepton p_{T} thresholds are raised to reduce the FNP lepton background contributions from Z+jets and $t\bar{t}$. Further, to suppress contributions from the SM WZ background, the signal regions target phase space either below or above the Standard Model W boson Jacobian peak present at $m_{\text{T}}^{\text{mllmin}} \sim m_W$ as described in Section 5.1. For the low $m_{\ell\ell}^{\text{min}}$ bins, an upper bound $m_{\text{T}}^{\text{mllmin}} < 50 - 70$ GeV is applied, while the "f" and "g" bins are split into two parts — below ("f1",

Table 5.2: Summary of the selection requirements applied in the signal regions of the off-shell WZ selection [22]. These requirements are applied on top of the preselection requirements summarized in Table 5.1. "-" indicates no requirement is applied for a given variable/region, while × is marked for regions that are not considered.

	Selection requirements								
Variable	a	b	c	d	e	f1	f2	g1	g2
$m_{\ell\ell}^{\text{min}}$ [GeV]	[1, 12]	[12, 15]	[15, 20]	[20, 30]	[30, 40]	[40, 60]		[60, 75]	
	$\text{SR}_{\text{low}\not{E}_{\text{T}}}^{\text{offWZ}}$ common								
$m_{\ell\ell}^{\text{max}}$ [GeV]	×	< 60	< 60	< 60	< 60	-	-	-	-
$m_{\text{T}}^{\text{mllmin}}$ [GeV]	×	< 50	< 50	< 50	< 60	< 60	> 90	< 60	> 90
m_{T2}^{100} [GeV]	×	< 115	< 120	< 130	-	-	-	-	-
min ΔR_{SFOS}	×	< 1.6	< 1.6	< 1.6	-	-	-	-	-
$p_{\text{T}}^{\ell_1}, p_{\text{T}}^{\ell_2}, p_{\text{T}}^{\ell_3}$ [GeV]	×	> 10	> 10	> 10	> 10	> 15	> 15	> 15	> 15
	$\text{SR}_{\text{low}\not{E}_{\text{T}}}^{\text{offWZ}}$-0j								
$\lvert\mathbf{p}_{\text{T}}^{\text{lep}}\rvert / E_{\text{T}}^{\text{miss}}$	×	< 1.1	< 1.1	< 1.1	< 1.3	< 1.4	< 1.4	< 1.4	< 1.4
$m_{3\ell}$ [GeV]	×	-	-	-	-	> 100	> 100	> 100	> 100
	$\text{SR}_{\text{low}\not{E}_{\text{T}}}^{\text{offWZ}}$-nj								
$\lvert\mathbf{p}_{\text{T}}^{\text{lep}}\rvert / E_{\text{T}}^{\text{miss}}$	×	< 1.0	< 1.0	< 1.0	< 1.0	< 1.2	< 1.2	< 1.2	< 1.2
	$\text{SR}_{\text{high}\not{E}_{\text{T}}}^{\text{offWZ}}$ common								
m_{T2}^{100} [GeV]	< 112	< 115	< 120	< 130	< 140	< 160	< 160	< 175	< 175
	$\text{SR}_{\text{high}\not{E}_{\text{T}}}^{\text{offWZ}}$-0j								
$p_{\text{T}}^{\ell_1}, p_{\text{T}}^{\ell_2}, p_{\text{T}}^{\ell_3}$ [GeV]	×	> 25, > 15, > 10							
$m_{\text{T}}^{\text{mllmin}}$ [GeV]	×	< 50	< 50	< 60	< 60	< 70	> 90	< 70	> 90
	$\text{SR}_{\text{high}\not{E}_{\text{T}}}^{\text{offWZ}}$-nj								
						f		g	
$p_{\text{T}}^{\ell_1}, p_{\text{T}}^{\ell_2}, p_{\text{T}}^{\ell_3}$ [GeV]	> 4.5 (3.0) for e (μ)								
$\lvert\mathbf{p}_{\text{T}}^{\text{lep}}\rvert / E_{\text{T}}^{\text{miss}}$	< 0.2	< 0.2	< 0.3	< 0.3	< 0.3	< 1.0		< 1.0	

"g1", $m_{\text{T}}^{\text{mllmin}} < 60/70$ GeV) and above ("f2", "g2", $m_{\text{T}}^{\text{mllmin}} > 90$ GeV) the SM peak. Figure 5.4(b) shows the N-1 distribution for $m_{\text{T}}^{\text{mllmin}}$ for region $\text{SR}_{\text{high}\not{E}_{\text{T}}}^{\text{offWZ}}$-0jc, for which an upper cut value of 50 GeV is applied. In $\text{SR}_{\text{low}\not{E}_{\text{T}}}^{\text{offWZ}}$-0j, a lower bound on $m_{3\ell}$ is applied for the high $m_{\ell\ell}^{\text{min}}$ bins to reject the background of Standard Model Z decaying into four leptons, which peaks at $m_{3\ell} \sim m_Z$. Figure 5.4(c) shows the N-1 distribution for $m_{3\ell}$ for region $\text{SR}_{\text{low}\not{E}_{\text{T}}}^{\text{offWZ}}$-0jf1, for which a lower cut value of 100 GeV is applied. Also, the min $\Delta\ R_{\text{SFOS}}$ requirement is tightened in the low $m_{\ell\ell}^{\text{min}}$ bins of $\text{SR}_{\text{low}\not{E}_{\text{T}}}^{\text{offWZ}}$to exploit the topology with a relatively boosted Z^* in the target signatures. Lastly, upper bounds are set on $|\mathbf{p}_{\text{T}}^{\text{lep}}|/E_{\text{T}}^{\text{miss}}$, as signals tend to populate lower parts of the spectrum for this variable than Standard Model backgrounds. This effect is particularly prominent for compressed signals in the high-$E_{\text{T}}^{\text{miss}}$ regions, where the $E_{\text{T}}^{\text{miss}}$ is almost fully generated by the ISR jet(s). Thus, even tighter upper bounds are set on this variable for the low $m_{\ell\ell}^{\text{min}}$ bins of $\text{SR}_{\text{high}\not{E}_{\text{T}}}^{\text{offWZ}}$-nj. Figure 5.4(d) shows the N-1 distribution for $|\mathbf{p}_{\text{T}}^{\text{lep}}|/E_{\text{T}}^{\text{miss}}$ for region $\text{SR}_{\text{high}\not{E}_{\text{T}}}^{\text{offWZ}}$-nje, for which an upper cut value of 0.3 is applied.

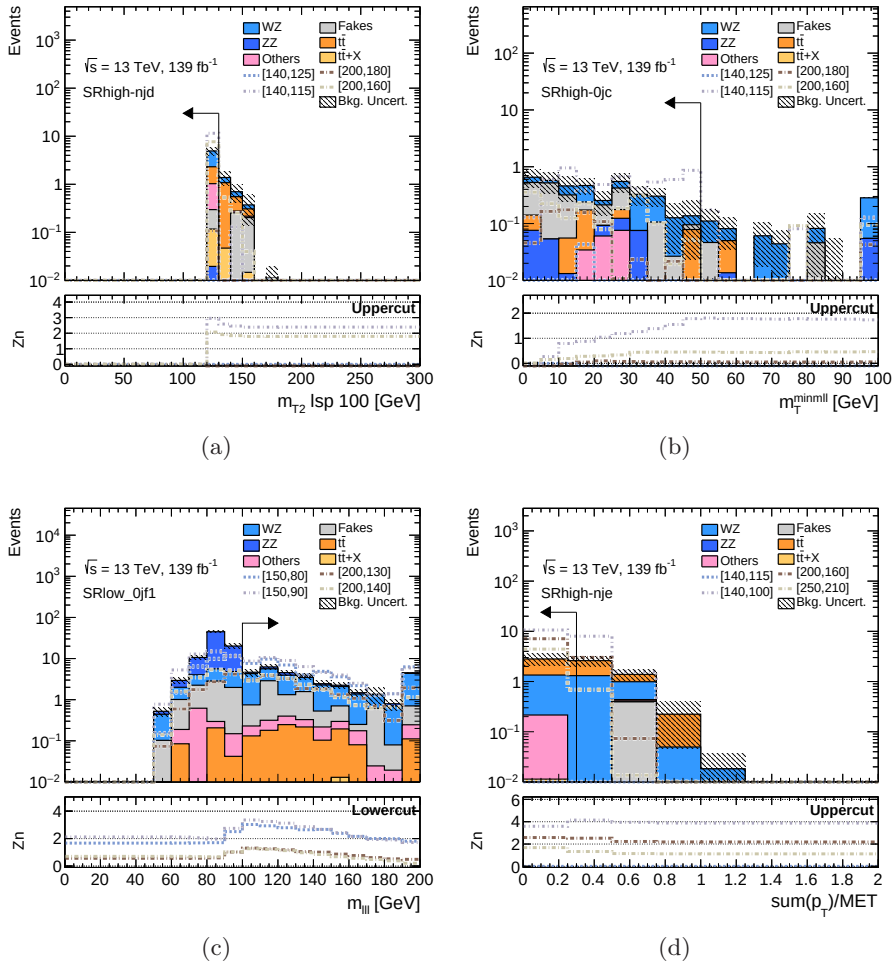

Figure 5.4: N-1 distributions for (a) m_{T2}^{100} in $\mathtt{SR}^{\mathtt{offWZ}}_{\mathtt{high}\not{E}_{\mathrm{T}}}\mathtt{-njd}$, (b) $m_{\mathrm{T}}^{\mathrm{mllmin}}$ in $\mathtt{SR}^{\mathtt{offWZ}}_{\mathtt{high}\not{E}_{\mathrm{T}}}\mathtt{-0jc}$, (c) $m_{3\ell}$ in $\mathtt{SR}^{\mathtt{offWZ}}_{\mathtt{low}\not{E}_{\mathrm{T}}}\mathtt{-0jf1}$ and (d) $|\mathbf{p}_{\mathrm{T}}^{\mathrm{lep}}|/E_{\mathrm{T}}^{\mathrm{miss}}$ in $\mathtt{SR}^{\mathtt{offWZ}}_{\mathtt{high}\not{E}_{\mathrm{T}}}\mathtt{-nje}$, indicating the lower/upper cut values applied.

5.3 Background estimation

In Section 3.4, the most important backgrounds to the three-lepton final state were introduced, namely Standard Model WZ, $t\bar{t}$ and Z+jets. In this section, brief explanations on how these backgrounds are estimated will be given. Further details can be found in Sections 6.2 and 8.2 of Ref. [22]. For all other backgrounds, the MC-predicted yields are used directly.

In order to estimate the most important SM backgrounds in an accurate and robust fashion, a partially data-driven method is often used, where the MC predictions are normalized to data in dedicated *control regions* (CRs). Such

control regions should be both similar and orthogonal to the signal regions, and have as little signal contamination as possible. This is usually achieved by taking the signal region definitions and inverting some of the selection requirements. To assess the quality of the resulting background estimation and its extrapolation to the signal regions, dedicated *validation regions* (VRs) are used. Such validation regions are designed to be kinematically in between the control and signal regions, and should also have low expected signal contamination. For some backgrounds, it is sufficient to check the background estimation using only validation regions. The final estimation of the background yields and uncertainties is performed with a simultaneous fit to the control and signal regions. The validation regions are not used in this fit.

5.3.1 WZ

The dominant Standard Model WZ background, producing three real and prompt leptons, is estimated using the partially data-driven method described above. Two CRs are defined to retrieve separate normalization factors for WZ events with and without hard ISR jets. The selection critera for these CRs, $\texttt{CRWZ}^{\texttt{offWZ}}_{\texttt{0j}}$ and $\texttt{CRWZ}^{\texttt{offWZ}}_{\texttt{nj}}$, are given in the second and third columns of Table 5.3. From the simultaneous fit to the CRs and SRs, the normalization factors are determined to be 1.06 ± 0.03 for $\texttt{CRWZ}^{\texttt{offWZ}}_{\texttt{0j}}$ and 0.93 ± 0.03 for $\texttt{CRWZ}^{\texttt{offWZ}}_{\texttt{nj}}$.

Further, three separate VRs are defined to validate the SM WZ estimation — $\texttt{VRWZ}^{\texttt{offWZ}}_{\texttt{0j}}$ and $\texttt{VRWZ}^{\texttt{offWZ}}_{\texttt{nj}}$ are designed to validate the estimation in the $\texttt{SR}^{\texttt{offWZ}}_{\texttt{low}E_{\mathrm{T}}}$ phase space, while $\texttt{VRWZ}^{\texttt{offWZ}}_{\texttt{nj-lowm}_{\ell\ell}}$ is used to validate the estimation in the $\texttt{SR}^{\texttt{offWZ}}_{\texttt{high}E_{\mathrm{T}}}$ phase

Table 5.3: Summary of the selection criteria for the CRs and VRs for the WZ and $t\bar{t}$ backgrounds [22]. In rows where only one value is given it applies to all regions. "-" indicates no requirement is applied for a given variable/region.

Variable	$\texttt{CRWZ}^{\texttt{offWZ}}_{\texttt{0j}}$	$\texttt{CRWZ}^{\texttt{offWZ}}_{\texttt{nj}}$	$\texttt{VRWZ}^{\texttt{offWZ}}_{\texttt{0j}}$	$\texttt{VRWZ}^{\texttt{offWZ}}_{\texttt{nj}}$	$\texttt{VRWZ}^{\texttt{offWZ}}_{\texttt{nj-lowm}_{\ell\ell}}$	$\texttt{VRt}\bar{\texttt{t}}^{\texttt{offWZ}}$
$n_{\text{lep}}^{\text{baseline}}$, $n_{\text{lep}}^{\text{signal}}$			= 3			
n_{SFOS}			≥ 1			
Trigger			((multi-)lepton ∥ $E_{\mathrm{T}}^{\text{miss}}$)			
min $\Delta R_{3\ell}$			> 0.4			
$n_{b\text{-jets}}$	= 0		= 0			≥ 1
$m_{\ell\ell}$ [GeV]	∈ [81, 101]		< 75			< 75
$n_{\text{jets}}^{30\text{ GeV}}$	= 0	≥ 1	= 0	≥ 1	≥ 1	-
$E_{\mathrm{T}}^{\text{miss}}$ [GeV]	< 50	< 50	< 50	< 80	> 80	> 50
$E_{\mathrm{T}}^{\text{miss}}$ significance	-		> 1.5	> 1.5	> 1.5	-
m_{T} [GeV]	> 50	> 50	∈ [60, 90]		> 30	-
$m_{\ell\ell}^{\text{min}}$ [GeV]	-		∈ [12, 75]		∈ [1, 12]	∈ [1, 75]
Resonance veto $m_{\ell\ell}^{\text{min}}$ [GeV]	-		-	-	∉ [3, 3.2], ∉ [9, 12]	∉ [3, 3.2], ∉ [9, 12]
$p_{\mathrm{T}}^{\ell_1}$, $p_{\mathrm{T}}^{\ell_2}$, $p_{\mathrm{T}}^{\ell_3}$ [GeV]	> 10		> 10	> 10	-	-
min ΔR	-		[0.6, 2.4] ($\ell_{\mathrm{W}} = e$ only)		-	-
$\lvert m_{3\ell} - m_Z \rvert$ [GeV]	-		> 20 ($\ell_{\mathrm{W}} = e$ only)		-	-
$m_{\mathrm{W}}^{\text{reco WZ}}$ [GeV]	-		> 75	-	-	-
$\Delta R(\ell_{\mathrm{W}}, E_{\mathrm{T}}^{\text{miss}})$	-		> 2.6	-	-	-
$\lvert \mathbf{p}_{\mathrm{T}}^{\text{lep}} \rvert / E_{\mathrm{T}}^{\text{miss}}$	-		-	-	> 0.3	-

space. The selection criteria for these three VRs are given in the middle columns of Table 5.3.

5.3.2 $t\bar{t}$

For the $t\bar{t}$ background, dominated by decays with a dileptonic final state and an additional non-prompt lepton from a b- or c-hadron decay, the MC-predicted yield is only validated in a dedicated VR. The selection criteria for this VR, called $\texttt{VRtt}^{\texttt{offWZ}}$, are given in the right-most column of Table 5.3. As the MC modeling is found to be satisfactory, no additional corrections are applied to the $t\bar{t}$ MC events.

5.3.3 Z+jets

The Z+jets processes result in two prompt leptons and one FNP lepton from jets or photons. As can be seen in Figure 5.2, this is the dominant background in the inclusive $\texttt{SR}^{\texttt{offWZ}}_{\text{low}E_{\text{T}}}\texttt{-0j}$ region, and it must thus be estimated carefully. However, as FNP leptons are hard to model with MC simulation, a fully data-driven method referred to as the "fake-factor method" [163, 164] is used to estimate this background. A brief explanation of this method will be given in the following.

The fake-factor method uses two sets of lepton identification criteria. The first set is the same criteria used to identify signal leptons in the analysis, referred to as "ID" lepton criteria. In the second set, referred to as "anti-ID", one or more of the lepton identification criteria are relaxed or inverted to enrich in fake leptons. The fake factor F is defined as the ratio of the probability for a given lepton candidate to pass the ID lepton criteria to the probability for it to pass the anti-ID criteria. This ratio is measured using data in a control region designed to target Z+jets events with FNP leptons whose sources are representative of those expected in the signal regions. In the three-lepton analysis, exactly three baseline leptons are required in the fake-factor control region, including at least one SFOS lepton pair assigned to the Z boson. If more than one, the SFOS pair with invariant mass closest to the Z-boson mass is assigned to the Z boson. The remaining lepton is the FNP lepton candidate. The Z+jets prediction in a given region is then obtained by applying the fake factors to events in its corresponding "anti-ID region", defined by the same selection criteria as the nominal region with three signal leptons, except that at least one of the leptons is anti-ID instead of ID. Each event in the anti-ID region is scaled by a weight based on the fake factor assigned to each anti-ID lepton in the region. In the off-shell WZ analysis, fake factors are derived separately per lepton flavor, and parameterized as a function of lepton p_{T} and $E_{\text{T}}^{\text{miss}}$ in the event. In both the fake-factor measurement and application procedure, contributions from processes other than Z+jets are subtracted using MC-simulated samples.

The selection criteria used for the fake-factor control region $\texttt{CRFF}^{\texttt{offWZ}}$ is

summarized in the second column of Table 5.4.[6] The yields predicted by the fake-factor method are cross-checked in three dedicated valdation regions enriched in FNP leptons. The selection criteria for these VRs are listed in the three rightmost columns of Table 5.4, where $\texttt{VRFF}^{\texttt{offWZ}}_{\texttt{0j}}$ and $\texttt{VRFF}^{\texttt{offWZ}}_{\texttt{nj}}$ are designed to validate the yields in $\texttt{SR}^{\texttt{offWZ}}_{\texttt{low}E_{\mathrm{T}}}\texttt{-0j}$ and $\texttt{SR}^{\texttt{offWZ}}_{\texttt{low}E_{\mathrm{T}}}\texttt{-nj}$, respectively, and $\texttt{VRFF}^{\texttt{offWZ}}_{\texttt{nj-low}p_{\mathrm{T}}}$ is designed to specifically cross-check the modeling of FNP leptons with $p_{\mathrm{T}} < 10$ GeV.

5.3.4 Summary

Figure 5.5 shows example kinematic distributions in the CRs and VRs after the background-only fit, demonstrating good agreement. Further, Figure 5.6 summarizes the expected and observed yields for all CRs and VRs used in the off-shell WZ analysis. Note that the hatched bands in these figures indicate the combined theoretical, experimental and MC-statistical uncertainties. The distinction between these uncertainty categories will be explained in the next section.

[6] Note that in the subtraction of non-Z+jets processes, a small normalization factor is applied to the $t\bar{t}$ events in the anti-ID region to account for different anti-ID lepton efficiencies in data and MC simulation, derived using the $\texttt{CRtt}^{\texttt{offWZ}}_{\text{anti-ID}}$ region defined in the third column of Table 5.4.

Table 5.4: Summary of the selection criteria for the CRs and VRs for the Z+jets background [22]. The corresponding anti-ID regions used for the Z+jets prediction follow the same selection criteria, except that at least one of the leptons is anti-ID instead of signal. "-" indicates no requirement is applied for a given variable/region.

Variable	$\texttt{CRFF}^{\texttt{offWZ}}$	$\texttt{CRtt}^{\texttt{offWZ}}_{\text{anti-ID}}$	$\texttt{VRFF}^{\texttt{offWZ}}_{\texttt{0j}}$	$\texttt{VRFF}^{\texttt{offWZ}}_{\texttt{nj}}$	$\texttt{VRFF}^{\texttt{offWZ}}_{\texttt{nj-low}p_{\mathrm{T}}}$
$n_{\text{lep}}^{\text{baseline}}, n_{\text{lep}}^{\text{signal}}$	= 3				
min $\Delta R_{3\ell}$	> 0.4				
Trigger	dilepton	((multi-)lepton ∥ $E_{\mathrm{T}}^{\text{miss}}$)			
n_{SFOS}	≥ 1	= 0	≥ 1		
$n_{b\text{-jets}}$	= 0	= 0 or ≥ 1	= 0		
$m_{\ell\ell}$ [GeV]	∈ $[m_Z - 15, m_Z + 15]$	-	< 75		
$n_{\text{jets}}^{30\text{ GeV}}$	≤ 1 if $p_{\mathrm{T}}^{\ell_{\mathrm{W}}=\mu} > 30$ GeV = 0 otherwise	-	= 0	≥ 1	≥ 1
$E_{\mathrm{T}}^{\text{miss}}$ [GeV]	< 40	> 50	< 50	< 200	∈ [50, 200]
$E_{\mathrm{T}}^{\text{miss}}$ significance	-	-	∈ [0.5, 1.5]	∈ [0.5, 3.0]	∈ [0.5, 3.0]
$p_{\mathrm{T}}^{\ell_1}, p_{\mathrm{T}}^{\ell_2}, p_{\mathrm{T}}^{\ell_3}$ [GeV]	-	> 10	> 10	> 10	< 10
$m_{\ell\ell}^{\text{min}}$ [GeV]	-	-	∈ [12, 75]	∈ [12, 75]	∈ [1, 75]
m_{T} [GeV]	< 30	-	< 50		
min ΔR	-	-	[0.6, 2.4] ($\ell_{\mathrm{W}} = e$ only)		
$m_{3\ell}$ [GeV]	> 105	-	[81.2, 101.2] ($\ell_{\mathrm{W}} = e$ only)		

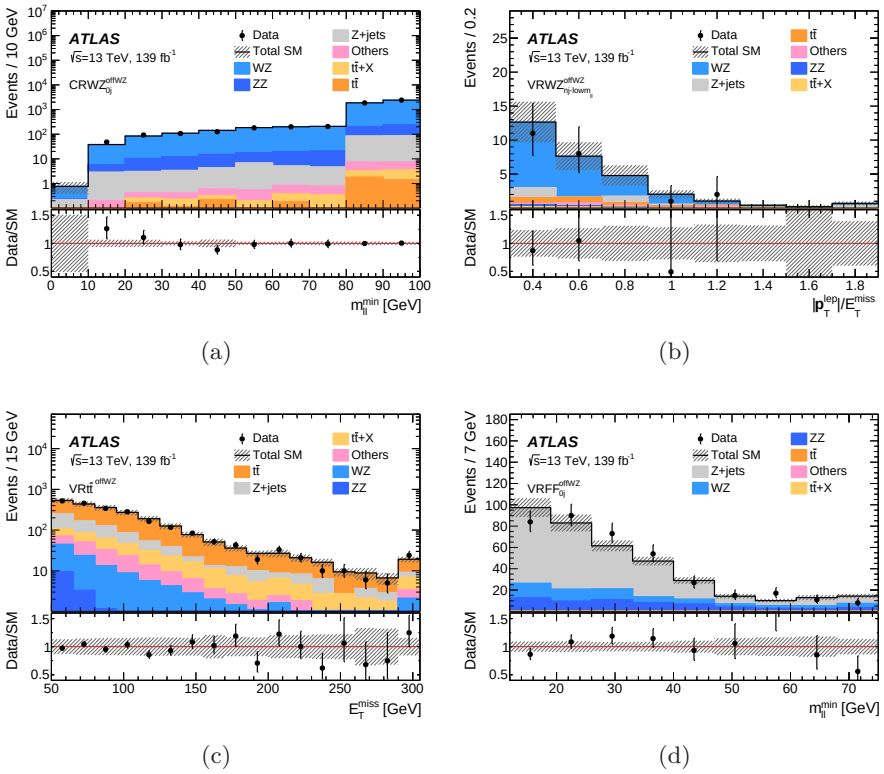

Figure 5.5: Example kinematic distributions after the background-only fit, showing the data and the post-fit expected background, in regions of the off-shell WZ selection [22]. The figure shows (a) the $m_{\ell\ell}^{\text{min}}$ distribution in $\texttt{CRWZ}_{0j}^{\texttt{offWZ}}$, (b) the $|\mathbf{p}_{\text{T}}^{\text{lep}}|/E_{\text{T}}^{\text{miss}}$ distribution in $\texttt{VRWZ}_{\texttt{nj-lowm}_{\ell\ell}}^{\texttt{offWZ}}$, (c) the $E_{\text{T}}^{\text{miss}}$ distribution in $\texttt{VRt}\bar{\texttt{t}}^{\texttt{offWZ}}$, and (d) the $m_{\ell\ell}^{\text{min}}$ distribution in $\texttt{VRFF}_{0j}^{\texttt{offWZ}}$. The last bin includes overflow. The "Others" category contains backgrounds from single-top, WW, triboson, Higgs and rare top processes. The bottom panel shows the ratio of the observed data to the predicted yields. The hatched bands indicate the combined theoretical, experimental, and MC-statistical uncertainties. The slope change in the $E_{\text{T}}^{\text{miss}}$ distribution in (c) illustrates the selection extension with $E_{\text{T}}^{\text{miss}}$-triggered events, which start contributing at $E_{\text{T}}^{\text{miss}} \gtrsim 200$ GeV.

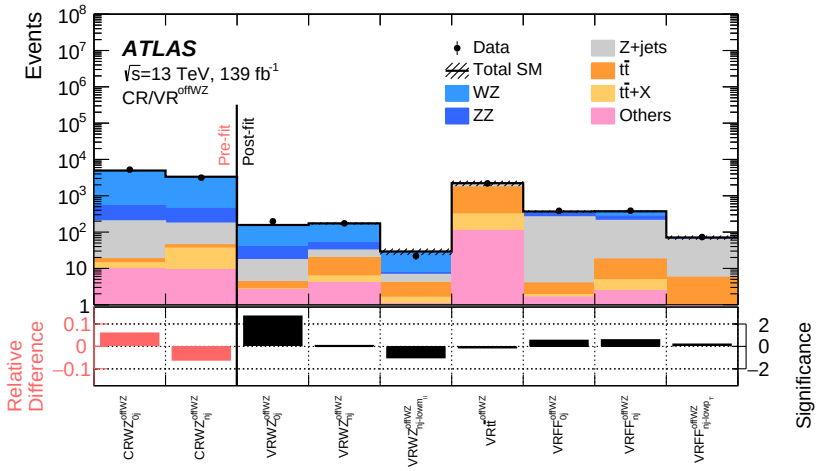

Figure 5.6: Comparison of the observed data and expected SM background yields in the CRs and VRs of the off-shell WZ selection [22]. The SM prediction is taken from the background-only fit. The "Others" category contains backgrounds from single-top, WW, triboson, Higgs and rare top processes. The hatched bands indicate the combined theoretical, experimental, and MC-statistical uncertainties. The bottom panel shows the significance of the difference between the observed and expected yields, calculated with the profile-likelihood method from Ref. [165], adding a minus sign if the yield is below the prediction.

5.4 Systematic uncertainties

Two different types of uncertainties are considered in particle physics analyses. Statistical (random) uncertainties are uncertainties that can be reliably estimated by repeating measurements. They follow a known distribution, such as the Gaussian or Poisson distributions, or are determined empirically from the distribution of an unbiased, sufficiently large sample. The relative statistical uncertainty reduces as $1/\sqrt{N}$, where N is the sample size.

Systematic uncertainties, on the other hand, are uncertainties that cannot be calculated solely from sampling fluctuations. Even with infinite statistics, a systematic uncertainty will never become zero. Systematic uncertainties are generally divided into three categories: (i) instrumental uncertainties from experimental conditions and reconstructed objects, (ii) theoretical uncertainties on parameters that enter the Monte Carlo simulations, and (iii) uncertainties on data-driven background estimates. Systematic uncertainties also often become smaller with larger sample sizes, but not as $1/\sqrt{N}$ in most cases. Finding and estimating systematic uncertainties are complicated, and often ends up being a large fraction of the work in an analysis. In most cases, one finds independent sources of systematic uncertainties, meaning that they can be added in quadrature. A few sources often dominate the total systematic uncertainty, meaning that not too much effort should be put into correctly estimating the smaller ones.

Both statistical and systematic uncertainties are assigned to the predicted event yields of signal and background processes in each region. Information on how the uncertainties are statistically implemented will be given in Section 5.5. First, the remainder of this section will give a brief summary of the systematic uncertainties considered in the off-shell WZ analysis. Further details can be found in Sections 6.3 and 8.2 of Ref. [22].

5.4.1 Instrumental uncertainties

Instrumental uncertainties can arise from a number of sources. For instance, both the ATLAS luminosity and pile-up measurements have corresponding systematic uncertainties. Other examples include resolution effects in the various sub-detector systems, reconstruction of the momenta of particle tracks from hits in multiple detector layers, and the assignment of energy deposits in the calorimeters to different reconstructed objects. Instrumental uncertainties affect all MC samples used to model the background and signal processes (except data-driven samples, like the Z+jets sample for the off-shell WZ analysis).

In the off-shell WZ analysis, the dominant instrumental uncertainties are the so-called jet-energy scale (JES) and resolution (JER). Also significant is the uncertainty in the modeling of $E_{\mathrm{T}}^{\mathrm{miss}}$. Other instrumental uncertainties concerning the efficiency of the trigger selection, flavor-tagging and the jet vertex tagger (JVT), as well as reconstruction, identification, impact-parameter selection and isolation for leptons, are found to have minor impact. Each instrumental

uncertainty is treated as fully correlated across the analysis regions and physics processes considered.

5.4.2 Theoretical uncertainties

For the processes estimated using MC simulation, the predicted yield is also affected by different sources of theoretical modeling uncertainties. Several choices must be made when simulating events using event generators, such as which generator and parton distribution function (PDF) set to use, and to which accuracy the matrix element of the process is calculated. All such choices have corresponding uncertainties that need to be taken into account in the statistical analysis.

In the off-shell WZ analysis, a theoretical uncertainty accounting for the uncertainty in the cross-section of the process is considered for each background. Further, for the important WZ, ZZ and $t\bar{t}$ backgrounds, also other sources of theoretical uncertainties on the modeling are considered, which will be listed in the following. For the diboson backgrounds, the leading modeling uncertainties arise from variations in the QCD renormalization and factorization scales. Also considered is the impact of the choice of parton distribution function set and the value of the strong coupling constant α_s, scales for resummation and merging between matrix element and parton-showering calculations, and the parton-showering recoil scheme. For WZ, which is normalized to data in control regions, the uncertainties are implemented as transfer-factor uncertainties that reflect differences in the SR-to-CR and VR-to-CR ratio of yields, and therefore provide an uncertainty in the assumed shape of MC distributions across analysis regions. For the $t\bar{t}$ background, several sources of theoretical uncertainties are considered: choice of matrix element generator, choice of parton distribution function set and the value of α_s, parton-shower scales for initial-state and final-state radiation, and choice of generator for parton-showering and hadronization.

Theoretical uncertainties in the expected yields for the SUSY signals are also estimated. Considered sources are scales for QCD renormalization and factorization as well as jet-parton matching, and settings used for the parton showering with Pythia.

5.4.3 Uncertainties on data-driven Z+jets background estimate

The data-driven Z+jets estimation, carried out with the fake factor method as described in Section 5.3.3, is subject to a number of systematic uncertainties. The uncertainties are evaluated by considering the variation in the fake factor F, and propagating the effects to the estimated yields.

First, the limited number of ID and anti-ID events in the control region leads to a statistical uncertainty on the measurement of the fake factor F, which is accounted for with a systematic uncertainty. Further, the fake factor F depends on the composition of fake lepton sources (light-flavor jets, heavy-flavor jets and photon-conversion), and thus the composition in the control region should be as close to the composition in the signal region as possible. This composition

is expected to vary with p_{T}, $E_{\mathrm{T}}^{\mathrm{miss}}$ and η. As stated in Section 5.3.3, the fake factors are parameterized as a function of lepton p_{T} and $E_{\mathrm{T}}^{\mathrm{miss}}$ in the off-shell WZ analysis, but an alternative parameterization could also include lepton η. This ambiguity is translated into a systematic uncertainty. Also the choice of binning for the $E_{\mathrm{T}}^{\mathrm{miss}}$ parameterization leads to a systematic uncertainty. In addition, the cross-section uncertainty on the dominant WZ background, substracted in the determination of F, is also translated into a systematic uncertainty. Finally, to increase the number of FNP lepton candidates at high p_{T}, muons overlapping with jets are kept in the control region (as opposed to what is done in the actual analysis). However, this leads to some discrepancies with the results for the other regions, and is thus treated as a systematic uncertainty.

5.4.4 Summary

Figure 5.7 shows a breakdown of the total uncertainties in the background prediction for the signal regions of the off-shell WZ analysis. In this plot, the uncertainties related to experimental (instrumental) effects are grouped and shown as "Experimental" uncertainty. Theoretical uncertainties, including the WZ transfer-factor uncertainties, are grouped and shown as "Modeling" uncertainty. Further, the uncertainties related to the data-driven Z+jets background estimation are represented by the "FNP" uncertainty, while statistical uncertainties of the simulated event samples are shown as "MC Stats". Finally, the uncertainties related to the normalization factors derived from the CRs are described by the "Normalization" uncertainty.

We see that the total uncertainty vary considerably from signal region to signal region. As the expected yields themselves vary a lot, both the statistical and experimental uncertainties are also expected to fluctuate from region to region, and these uncertainties are often dominant in regions with limited MC statistics in the phase space of the region selection. Further, the FNP lepton uncertainty is naturally more important in regions with larger FNP lepton background contributions. Also, the modeling uncertainty is larger for regions with one or more ISR jets, and high $E_{\mathrm{T}}^{\mathrm{miss}}$.

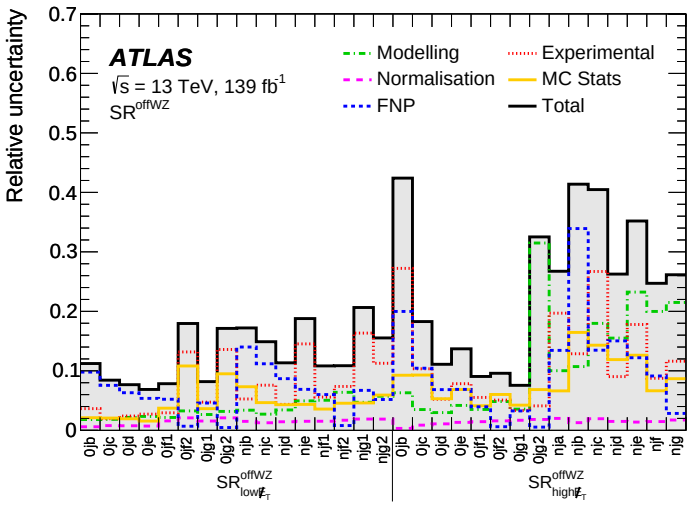

Figure 5.7: Breakdown of the total uncertainties in the background prediction for the SRs of the off-shell WZ selection [22].

5.5 Statistical procedure

Since 2012, the HistFitter framework [166] has been the primary tool for statistical analysis in ATLAS supersymmetry searches. This framework is built on top of the HistFactory [167] and RooFit [168] packages for parametric model construction, and RooStats [161] for statistical tests of the data. One of the main developments of HistFitter compared to RooFit/RooStats alone is that the concepts of control, validation and signal regions are incorporated into the design of the framework. Together with all analysis ntuples (data and MC), the input to HistFitter is a single configuration file containing the region definitions, information on the systematic uncertainties to be considered, and one or more fit configuration objects describing the fit(s) to be performed.

Roughly speaking, the steps of the HistFitter processing sequence are as follows. Based on the input ntuples and configurations, HistFitter produces ROOT [169, 170] histograms for each of the regions. According to each specified fit configuration, HistFactory then constructs a corresponding probability density function (PDF) by combining the relevant histograms. These combined PDFs are stored in a so-called RooWorkspace, together with the dataset and the model configuration. These PDFs and workspaces are subsequently used to perform fits of the data with RooFit, statistical tests with RooStats, and producing plots and tables with HistFitter itself. The processing chain is illustrated in Figure 5.8. All these steps require a substantial bookkeeping and configuration machinery, which is provided by HistFitter.

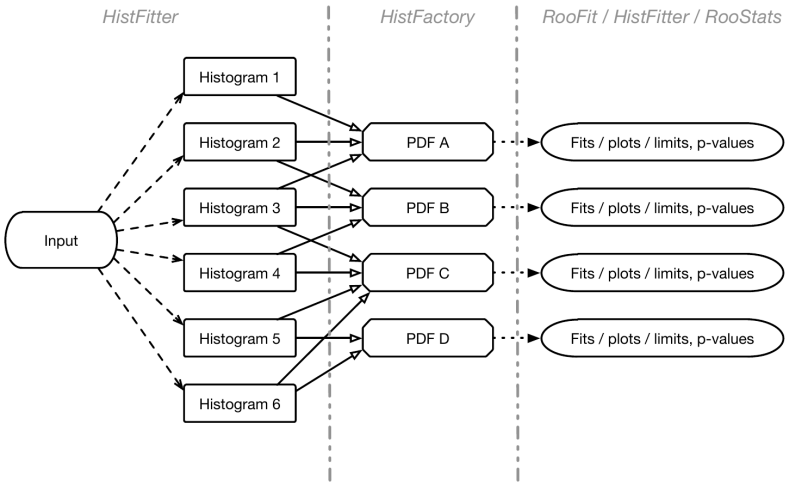

Figure 5.8: Overview of the HistFitter processing sequence [166]. In the first step (left), HistFitter creates histograms for all control, validation and signal regions. In the second step (middle), HistFactory constructs a probability density function (PDF) for each of the fit configurations. In the third step (right), these PDFs are used to perform fits of the data with RooFit, perform statistical tests with RooStats and producing plots and tables with HistFitter itself.

5.5.1 The likelihood function

To summarize, HistFitter uses the HistFactory package to construct a parametric model describing the data, based on provided input histograms. After looking at the data, the actual number of events in each region is known. The so-called *likelihood function* L then gives a measure of the probability for the observed data as a function of the model parameters. Although constructed from PDF(s), the likelihood function is not a PDF itself.

In HistFitter, the general likelihood is the product of Poisson distributions of event counts in the SR(s) and/or CR(s),[7] and of additional distributions that implement constraints on the systematic uncertainties (parameterized by *nuisance parameters*):

$$\begin{aligned} L(\mathbf{n}|\mu_s,\boldsymbol{\theta}) &= P_{\mathrm{SR}} \times P_{\mathrm{CR}} \times C_{\mathrm{syst}} \\ &= \prod_{i\in\mathrm{SR}} P\big(n_i|N_i(\mu_s,\boldsymbol{\theta})\big) \times \prod_{j\in\mathrm{CR}} P\big(n_j|N_j(\mu_s,\boldsymbol{\theta})\big) \times C_{\mathrm{syst}}(\boldsymbol{\theta}), \end{aligned} \quad (5.7)$$

where P denotes a Poisson distribution; the vector $\mathbf{n}$ holds the observed number of events in each CR and SR — n_i for region i; $N_i(\mu_s,\boldsymbol{\theta})$ is the expected number

[7] In a counting experiment like this (either we keep an event or we discard it), where the total number of events is very large, the probability of keeping an event is low, and the expected number of kept events is constant, the actual number of kept events is said to follow a Poisson distribution.

of events for region i; and $C_{\text{syst}}(\boldsymbol{\theta})$ incorporates the distributions constraining the systematic uncertainties $\boldsymbol{\theta}$. The expected number of events for region i is given as

$$N_i(\mu_s, \boldsymbol{\theta}) = \mu_s s_i(\boldsymbol{\theta}) + b_i(\boldsymbol{\theta}), \tag{5.8}$$

where s_i is the number of signal events, b_i is the total number of background events, and μ_s is the so-called *signal strength*. For $\mu_s = 0$, the signal component is turned off, and for $\mu_s = 1$, the signal expectation equals the nominal value of the model under consideration. Further, the nuisance parameters $\boldsymbol{\theta}$ are typically considered to be Gaussian distributed around their expectation values. In the case where all nuisance parameters are taken to be independent, $C_{\text{syst}}(\boldsymbol{\theta})$ is simply the product of Gaussian distributions for each systematic uncertainty.

The *maximum likelihood estimates* (MLEs) of the parameters $(\mu_s, \boldsymbol{\theta})$ are the values for which the likelihood function $L(\mu_s, \boldsymbol{\theta})$ has its global maximum. These can be found by performing a *maximum likelihood fit*. In practice, however, it is often more convenient to work with the logarithm of the likelihood function, called the *log-likelihood*, and rather search for the minimum of the negative log-likelihood function, $-\ln L(\mu_s, \boldsymbol{\theta})$.

5.5.2 Hypothesis testing

As mentioned above, HistFitter makes use of RooStats to perform statistical tests. An example is hypothesis testing. In LHC searches for supersymmetry, the first step is to check the compatibility of the data with the so-called *background-only (b-only) hypothesis*, to see if there is any excess. If so, the size of the excess determines if it can be classified as evidence for the supersymmetry signal, or even a disovery. If no significant excess is observed, the next step is to set limits on the signal model in question by considering the *signal+background (s+b) hypothesis*.

Test statistic and p-value

To determine the level of agreement between a hypothesis and an observation, it is common to use a *test statistic*. A test statistic is a function of the data that characterizes the full dataset in a single number. For searches, the test statistic should be constructed such that its distributions for the background-only and signal+background hypotheses are maximally separated.

The standard test statistic used by the LHC collaborations is the *profile likelihood ratio* q_{μ_s}, defined as

$$q_{\mu_s} = -2\ln\left(\frac{L(\mu_s, \hat{\hat{\boldsymbol{\theta}}})}{L(\hat{\mu}_s, \hat{\boldsymbol{\theta}})}\right), \tag{5.9}$$

where a single hat corresponds to the values that maximize the likelihood overall, and a double hat corresponds to values that maximize the likelihood for a fixed μ_s. So in order to calculate the value of this test statistic, two separate maximum likelihood fits must be performed. To obtain the denominator, $L(\hat{\mu}_s, \hat{\boldsymbol{\theta}})$,

all model parameters are allowed to float in order to obtain the maximum likelihood estimates $\hat{\mu}_s$ and $\hat{\boldsymbol{\theta}}$, given the data. For the numerator, $L(\mu_s, \hat{\hat{\boldsymbol{\theta}}})$, the signal strength μ_s is fixed at a value depending on the type of fit while the remaining parameters are allowed to float, in order to obtain the *profiled* maximum likelihood estimates $\hat{\hat{\boldsymbol{\theta}}}$ for the nuisance parameters, given the data and the specific μ_s value. The test statistic in Equation (5.9) has the advantage that its true distribution can be approximated — in the asymptotic limit, it will follow a χ^2 distribution [171]. Another option is to use toy experiments to obtain the test-statistic distribution.

The figure of merit to decide if a hypothesis can be rejected is the *p-value*. The p-value is the probability of obtaining results at least as extreme as the observed results of a statistical hypothesis test, assuming that the so-called *null hypothesis* is correct. The lower the p-value, the stronger the evidence that you should reject the null hypothesis. Before doing the test, you need to decide on which *confidence level* (CL) you want to use for rejection, i.e. how willing you are to potentially be wrong.

In terms of the test statistic in Equation (5.9), the p-value is formulated mathematically as

$$p_{\mu_s} = \int_{q_{\mu_s}^{\text{obs}}}^{\infty} f(q_{\mu_s}|\mu_s)\, dq_{\mu_s}, \tag{5.10}$$

where $f(q_{\mu_s}|\mu_s)$ is the test-statistic distribution, and $q_{\mu_s}^{\text{obs}}$ is the observed test-statistic value. This expression then quantifies the probability of obtaining a test-statistic value at least as far away from the expectation value as what is observed, given the null hypothesis.

It is common to convert the p-value into an *observed significance* Z, corresponding to a unit Gaussian:

$$\int_Z^{\infty} \frac{1}{\sqrt{2\pi}} e^{-\frac{1}{2}t^2}\, dt = p. \tag{5.11}$$

The observed significance gives how far away from the expected value a measurement is, expressed in units of sigma (σ), i.e. the number of standard deviations of the unit Gaussian.

Test for discovery

When testing for discovery, we check if the background-only hypothesis can be rejected. The background-only hypothesis is then the null hypothesis.

In this case, the test statistic defined in Equation (5.9) takes the form

$$q_0 = -2 \ln\left(\frac{L(0, \hat{\hat{\boldsymbol{\theta}}})}{L(\hat{\mu}_s, \hat{\boldsymbol{\theta}})} \right), \tag{5.12}$$

where the signal-strength parameter in the numerator is fixed at zero, such that the signal component in the likelihood is turned off and only background

contributions are included. The corresponding p-value is

$$p_0 = \int_{q_0^{\text{obs}}}^{\infty} f(q_0|0)\, dq_0, \tag{5.13}$$

where $f(q_0|0)$ is the test-statistic distribution for the background-only hypothesis.

In high energy physics, the convention is to reject the background-only hypothesis and claim *discovery* for a new-physics signal if $p_0 < 2.87 \times 10^{-7}$, which corresponds to an at least 5σ one-sided Gaussian devation from the expectation of the background-only hypothesis ($Z > 5\sigma$). A looser requirement of $p_0 < 0.013$, or $Z > 3\sigma$, is used to claim *evidence* for the signal.

Test for exclusion

If discovery of a new signal cannot be claimed (the background-only hypothesis cannot be rejected), the next step is to set limits on the signal model in question. Such limits are often displayed as mass plots with contours indicating which parts of the model's parameter space are excluded. To obtain such contours, we check if the signal+background hypothesis can be rejected for different points in the parameter space of the signal model. For each signal point, the test statistic then takes the form

$$q_1 = -2 \ln\left(\frac{L(1, \hat{\hat{\boldsymbol{\theta}}})}{L(\hat{\mu}_s, \hat{\boldsymbol{\theta}})}\right), \tag{5.14}$$

where the signal-strength parameter in the numerator is fixed at 1, such that the signal expectation equals the nominal value for the given point. The corresponding p-value is

$$p_1 = \int_{q_1^{\text{obs}}}^{\infty} f(q_1|1)\, dq_1, \tag{5.15}$$

where $f(q_1|1)$ is the test-statistic distribution for the signal+background hypothesis.

The standard in high energy physics is to set exclusion limits at 95% confidence level (CL), which means that signal points with $p_1 < 0.05$, or equivalently, a deviation from the expectation of the signal+background hypothesis of at least 1.64σ, are excluded. However, there are some undesirable consequences associated with this choice. Near the sensitivity limit, where the test-statistic distributions for the background-only and signal+background hypotheses are not well separated (either because the signal is small or the analysis is not powerful enough to separate signal and background), a downward fluctuation in the data with respect to the background-only expectation will result in the exclusion of a signal while the analysis has no real sensitivity. One of the common solutions experiments invoke to address this issue is to correct for a downward fluctuation by using the so-called CL_s method [172], where a signal point is excluded at 95% CL if $\text{CL}_\text{s} < 0.05$, where

$$\text{CL}_\text{s} \equiv \frac{p_1}{1 - p_0}. \tag{5.16}$$

It is also common to scan a range of signal-strength values μ_s in order to find the specific value that gives $\mathrm{CL_s} = 0.05$. This is then the upper limit on the signal strength. All larger signal-strength values, for which $\mathrm{CL_s} < 0.05$, are excluded. Further, this upper limit on the signal strength can be converted into an upper limit on the production cross-section.

5.6 Results

After defining the signal regions (Section 5.2), validating the background estimates (Section 5.3), making sure all uncertainties are taken into account (Section 5.4), and deciding on the statistical procedure (Section 5.5), it is time to look at the data. This is done by *unblinding* the signal regions, and comparing the observed data in the signal regions with the background-only expectation.

The results for the $\mathtt{SR}^{\mathtt{offWZ}}_{\mathtt{low}\not{E}_{\mathrm{T}}}$ and $\mathtt{SR}^{\mathtt{offWZ}}_{\mathtt{high}\not{E}_{\mathrm{T}}}$ signal regions are summarized in Tables 5.5 and 5.6, respectively, and visualized in Figure 5.9. Representative signal MC predictions are overlaid on the figure to illustrate the sensitivity to various $\tilde{\chi}_1^{\pm}\tilde{\chi}_2^0$ signals throughout the regions. The sensitivity to signals with different mass splittings $\Delta m(\tilde{\chi}_2^0, \tilde{\chi}_1^0)$ depends on the $m_{\ell\ell}^{\mathrm{min}}$ range of the signal region bins, where the bins with smaller and larger $m_{\ell\ell}^{\mathrm{min}}$ values are sensitive to signals with smaller and larger mass splittings, respectively. For signals with the lowest mass splitting, only $\mathtt{SR}^{\mathtt{offWZ}}_{\mathtt{high}\not{E}_{\mathrm{T}}}\mathtt{-nja}$ has sensitivity. As seen in the tables and figure, no significant deviation from the SM background prediction is found in any of the signal regions. The maximum deviation of the data from the background expectation is in $\mathtt{SR}^{\mathtt{offWZ}}_{\mathtt{low}\not{E}_{\mathrm{T}}}\mathtt{-0jd}$ with a 2.3σ data excess, followed by a 2.1σ deficit in $\mathtt{SR}^{\mathtt{offWZ}}_{\mathtt{high}\not{E}_{\mathrm{T}}}\mathtt{-0jf2}$.

Since no significant excess above the SM prediction is observed, we move on to setting limits. Model-independent and model-dependent limits will be presented in Sections 5.6.1 and 5.6.2, respectively.

5.6.1 Model-independent limits

The nominal signal regions defined in Section 5.2.2 are model-dependent by definition. When deriving model-independent limits, single-bin *discovery regions* are used instead. These regions, constructed by combining nominal signal regions in order to be sensitive to different $m_{\ell\ell}^{\mathrm{min}}$ shapes, and thus also referred to as *inclusive regions*, are listed in Table 5.7. As the $m_{\ell\ell}^{\mathrm{min}}$ shape of a signal should not depend on the amount of initial-state radiation, the corresponding 0-jet and n-jet regions have have been united. Further, the high- and low-$E_{\mathrm{T}}^{\mathrm{miss}}$ regions are kept separate for regions with $m_{\ell\ell}^{\mathrm{min}} < 20$ GeV, as the sensitivity for the targeted simplified model decreases when joining them. The selection of the original low-$m_{\ell\ell}^{\mathrm{min}}$ $\mathtt{SR}^{\mathtt{offWZ}}_{\mathtt{high}\not{E}_{\mathrm{T}}}\mathtt{-nj}$ regions have the best sensitivity to models with small mass-splittings, and so these regions are kept as is.

Model-independent 95% CL upper limits for a generic beyond Standard Model (BSM) signal are calculated by performing a discovery fit for each target signal region and all control regions. The results are reported in Table 5.8.

Table 5.5: Observed and expected yields after the background-only fit in $\mathrm{SR}^{\mathrm{offWZ}}_{\mathrm{low}E_{\mathrm{T}}}$ [22]. The normalization factors of the WZ sample are extracted separately for 0j and nj, and are treated separately in the combined fit. The "Others" category contains backgrounds from single-top, WW, triboson, Higgs and rare top processes. Combined statistical and systematic uncertainties are presented.

Region	$\mathrm{SR}^{\mathrm{offWZ}}_{\mathrm{low}E_{\mathrm{T}}}$-0jb	$\mathrm{SR}^{\mathrm{offWZ}}_{\mathrm{low}E_{\mathrm{T}}}$-0jc	$\mathrm{SR}^{\mathrm{offWZ}}_{\mathrm{low}E_{\mathrm{T}}}$-0jd	$\mathrm{SR}^{\mathrm{offWZ}}_{\mathrm{low}E_{\mathrm{T}}}$-0je	$\mathrm{SR}^{\mathrm{offWZ}}_{\mathrm{low}E_{\mathrm{T}}}$-0jf1	$\mathrm{SR}^{\mathrm{offWZ}}_{\mathrm{low}E_{\mathrm{T}}}$-0jf2
Observed	25	42	77	101	33	7
Fitted SM events	32 ± 4	44 ± 4	54 ± 4	91 ± 6	32.2 ± 2.5	5.9 ± 1.1
WZ	7.6 ± 0.9	13.8 ± 1.3	16.3 ± 1.9	25.6 ± 1.8	20.1 ± 1.5	4.9 ± 1.0
ZZ	5.5 ± 1.3	7.4 ± 1.2	9.6 ± 1.6	21.8 ± 3.2	2.7 ± 1.1	0.43 ± 0.14
Z+jets	19.1 ± 3.2	22.7 ± 3.4	26.5 ± 3.5	40 ± 5	7.2 ± 1.7	$0.00 \pm {}^{0.04}_{0.00}$
$t\bar{t}$	$0.05 \pm {}^{0.18}_{0.05}$	$0.11 \pm {}^{0.17}_{0.11}$	0.38 ± 0.22	1.1 ± 0.4	0.78 ± 0.29	$0.08 \pm {}^{0.10}_{0.08}$
$t\bar{t}$+X	$0.007 \pm {}^{0.019}_{0.007}$	$0.002 \pm {}^{0.008}_{0.002}$	$0.009 \pm {}^{0.019}_{0.009}$	$0.019 \pm {}^{0.026}_{0.019}$	0.026 ± 0.026	$0.010 \pm {}^{0.015}_{0.010}$
Others	0.045 ± 0.031	0.30 ± 0.12	1.3 ± 0.6	1.9 ± 0.6	1.4 ± 0.4	0.51 ± 0.18

Region	$\mathrm{SR}^{\mathrm{offWZ}}_{\mathrm{low}E_{\mathrm{T}}}$-0jg1	$\mathrm{SR}^{\mathrm{offWZ}}_{\mathrm{low}E_{\mathrm{T}}}$-0jg2	$\mathrm{SR}^{\mathrm{offWZ}}_{\mathrm{low}E_{\mathrm{T}}}$-njb	$\mathrm{SR}^{\mathrm{offWZ}}_{\mathrm{low}E_{\mathrm{T}}}$-njc	$\mathrm{SR}^{\mathrm{offWZ}}_{\mathrm{low}E_{\mathrm{T}}}$-njd	$\mathrm{SR}^{\mathrm{offWZ}}_{\mathrm{low}E_{\mathrm{T}}}$-nje
Observed	34	9	6	13	17	14
Fitted SM events	34.7 ± 2.8	6.3 ± 1.1	3.5 ± 0.6	8.0 ± 1.2	13.5 ± 1.5	18.2 ± 3.4
WZ	21.4 ± 2.1	5.2 ± 1.0	1.62 ± 0.30	3.2 ± 0.6	6.0 ± 0.8	8.6 ± 1.3
ZZ	4.7 ± 1.4	0.45 ± 0.14	0.45 ± 0.13	0.72 ± 0.22	1.00 ± 0.28	1.4 ± 0.9
Z+jets	6.6 ± 1.6	$0.001 \pm {}^{0.029}_{0.001}$	1.2 ± 0.5	3.7 ± 0.9	4.5 ± 1.2	3.3 ± 1.3
$t\bar{t}$	0.8 ± 0.4	0.36 ± 0.21	0.15 ± 0.13	0.28 ± 0.14	1.5 ± 0.4	3.3 ± 0.9
$t\bar{t}$+X	0.039 ± 0.025	$0.003 \pm {}^{0.008}_{0.003}$	0.030 ± 0.013	0.052 ± 0.019	0.24 ± 0.06	0.33 ± 0.07
Others	1.16 ± 0.27	0.27 ± 0.09	0.006 ± 0.004	$0.14 \pm {}^{0.34}_{0.14}$	0.21 ± 0.06	$1.3 \pm {}^{1.8}_{1.3}$

Region	$\mathrm{SR}^{\mathrm{offWZ}}_{\mathrm{low}E_{\mathrm{T}}}$-njf1	$\mathrm{SR}^{\mathrm{offWZ}}_{\mathrm{low}E_{\mathrm{T}}}$-njf2	$\mathrm{SR}^{\mathrm{offWZ}}_{\mathrm{low}E_{\mathrm{T}}}$-njg1	$\mathrm{SR}^{\mathrm{offWZ}}_{\mathrm{low}E_{\mathrm{T}}}$-njg2
Observed	25	20	22	12
Fitted SM events	23.4 ± 2.5	17.9 ± 1.9	17.0 ± 3.5	12.4 ± 1.9
WZ	11.1 ± 1.2	9.4 ± 1.1	10.0 ± 1.2	7.3 ± 1.3
ZZ	4.0 ± 1.6	0.66 ± 0.25	$1.1 \pm {}^{2.6}_{1.1}$	0.34 ± 0.11
Z+jets	2.2 ± 1.4	$0.00 \pm {}^{0.14}_{0.00}$	1.8 ± 1.1	$0.0 \pm {}^{0.6}_{0.0}$
$t\bar{t}$	4.6 ± 1.1	5.7 ± 1.2	3.0 ± 0.8	2.9 ± 0.7
$t\bar{t}$+X	0.44 ± 0.09	0.72 ± 0.11	0.36 ± 0.08	0.44 ± 0.09
Others	1.0 ± 0.4	1.4 ± 0.9	0.71 ± 0.21	1.4 ± 0.6

The two first columns list the observed (N_{obs}) and expected (N_{exp}) yields in the inclusive discovery regions. The third column lists the upper limits on the visible cross-section, reflecting the product of the production cross-section, the acceptance and the selection efficiency for a BSM process.[8] The fourth and fifth columns list the upper limits on the observed (S^{95}_{obs}) and expected (S^{95}_{exp}) number of BSM events. The last two columns indicate the $\mathrm{CL_b}$ value, i.e. the confidence level observed for the background-only hypothesis, and the discovery p-value ($p(s=0)$) and correponding significance (Z). The maximum significance Z is 1.29σ, meaning that the background-only hypothesis cannot be rejected for any of the discovery regions.

[8]The concepts of acceptance and efficiency will be explained in Section 5.7.1.

Table 5.6: Observed and expected yields after the background-only fit in $\mathrm{SR}^{\mathrm{offWZ}}_{\mathrm{high}\not{E}_{\mathrm{T}}}$ [22]. The normalization factors of the WZ sample are extracted separately for 0j and nj, and are treated separately in the combined fit. The "Others" category contains backgrounds from single-top, WW, triboson, Higgs and rare top processes. Combined statistical and systematic uncertainties are presented.

Region	$\mathrm{SR}^{\mathrm{offWZ}}_{\mathrm{high}\not{E}_{\mathrm{T}}}$-0jb	$\mathrm{SR}^{\mathrm{offWZ}}_{\mathrm{high}\not{E}_{\mathrm{T}}}$-0jc	$\mathrm{SR}^{\mathrm{offWZ}}_{\mathrm{high}\not{E}_{\mathrm{T}}}$-0jd	$\mathrm{SR}^{\mathrm{offWZ}}_{\mathrm{high}\not{E}_{\mathrm{T}}}$-0je	$\mathrm{SR}^{\mathrm{offWZ}}_{\mathrm{high}\not{E}_{\mathrm{T}}}$-0jf1
Observed	1	4	11	13	37
Fitted SM events	1.5 ± 0.7	4.3 ± 0.8	14.0 ± 1.6	11.5 ± 1.6	35.7 ± 3.2
WZ	$0.20 \pm {}^{0.27}_{0.20}$	1.5 ± 0.5	6.0 ± 0.9	6.1 ± 1.1	20.5 ± 2.1
ZZ	0.5 ± 0.5	0.31 ± 0.12	1.8 ± 0.8	0.89 ± 0.24	3.1 ± 1.0
Z+jets	0.81 ± 0.31	1.7 ± 0.4	4.4 ± 1.0	1.1 ± 0.8	4.3 ± 1.4
$t\bar{t}$	0.05 ± 0.05	0.45 ± 0.17	0.64 ± 0.28	1.8 ± 0.6	4.4 ± 1.0
$t\bar{t}+X$	$0.003 \pm {}^{0.014}_{0.003}$	$0.009 \pm {}^{0.013}_{0.009}$	0.029 ± 0.015	0.08 ± 0.04	0.11 ± 0.05
Others	$0.014 \pm {}^{0.018}_{0.014}$	$0.3 \pm {}^{0.4}_{0.3}$	1.1 ± 0.4	1.6 ± 0.4	3.3 ± 0.8

Region	$\mathrm{SR}^{\mathrm{offWZ}}_{\mathrm{high}\not{E}_{\mathrm{T}}}$-0jf2	$\mathrm{SR}^{\mathrm{offWZ}}_{\mathrm{high}\not{E}_{\mathrm{T}}}$-0jg1	$\mathrm{SR}^{\mathrm{offWZ}}_{\mathrm{high}\not{E}_{\mathrm{T}}}$-0jg2	$\mathrm{SR}^{\mathrm{offWZ}}_{\mathrm{high}\not{E}_{\mathrm{T}}}$-nja	$\mathrm{SR}^{\mathrm{offWZ}}_{\mathrm{high}\not{E}_{\mathrm{T}}}$-njb
Observed	14	43	17	3	2
Fitted SM events	25.5 ± 2.4	39.5 ± 3.0	21 ± 7	6.0 ± 1.6	1.4 ± 0.6
WZ	16.0 ± 2.3	26.4 ± 2.2	15 ± 7	3.8 ± 1.2	0.57 ± 0.18
ZZ	0.95 ± 0.35	3.0 ± 0.9	0.58 ± 0.17	0.044 ± 0.023	0.009 ± 0.005
Z+jets	$0.00 \pm {}^{0.15}_{0.00}$	3.4 ± 1.3	$0.00 \pm {}^{0.11}_{0.00}$	1.5 ± 0.8	0.5 ± 0.5
$t\bar{t}$	4.4 ± 1.0	4.3 ± 0.9	3.1 ± 0.7	0.6 ± 0.5	$0.14 \pm {}^{0.15}_{0.14}$
$t\bar{t}+X$	0.109 ± 0.030	0.16 ± 0.05	0.09 ± 0.04	0.16 ± 0.06	$0.014 \pm {}^{0.025}_{0.014}$
Others	4.0 ± 1.0	2.3 ± 0.8	2.0 ± 0.5	0.038 ± 0.030	0.22 ± 0.22

Region	$\mathrm{SR}^{\mathrm{offWZ}}_{\mathrm{high}\not{E}_{\mathrm{T}}}$-njc	$\mathrm{SR}^{\mathrm{offWZ}}_{\mathrm{high}\not{E}_{\mathrm{T}}}$-njd	$\mathrm{SR}^{\mathrm{offWZ}}_{\mathrm{high}\not{E}_{\mathrm{T}}}$-nje	$\mathrm{SR}^{\mathrm{offWZ}}_{\mathrm{high}\not{E}_{\mathrm{T}}}$-njf	$\mathrm{SR}^{\mathrm{offWZ}}_{\mathrm{high}\not{E}_{\mathrm{T}}}$-njg
Observed	2	2	2	11	4
Fitted SM events	2.1 ± 0.8	5.4 ± 1.4	3.0 ± 1.1	9.9 ± 2.5	6.8 ± 1.8
WZ	1.25 ± 0.25	2.5 ± 0.4	1.31 ± 0.25	4.5 ± 0.7	3.7 ± 0.6
ZZ	0.020 ± 0.011	0.014 ± 0.013	0.029 ± 0.014	0.081 ± 0.033	0.050 ± 0.020
Z+jets	$0.04 \pm {}^{0.28}_{0.04}$	$0.7 \pm {}^{0.8}_{0.7}$	$0.0 \pm {}^{0.4}_{0.0}$	$0.6 \pm {}^{0.9}_{0.6}$	$0.00 \pm {}^{0.19}_{0.00}$
$t\bar{t}$	0.6 ± 0.5	1.3 ± 0.8	1.2 ± 1.0	3.4 ± 2.0	2.5 ± 1.6
$t\bar{t}+X$	0.027 ± 0.023	0.08 ± 0.08	0.09 ± 0.04	0.31 ± 0.08	0.21 ± 0.07
Others	$0.14 \pm {}^{0.36}_{0.14}$	0.8 ± 0.6	0.33 ± 0.21	1.0 ± 0.4	$0.3 \pm {}^{0.4}_{0.3}$

5.6.2 Model-dependent limits

When deriving model-dependent limits, the nominal signal regions defined in Section 5.2.2 are used. Model-dependent 95% CL exclusion limits are obtained by performing an exclusion fit for all signal regions and control region simultaneously for each signal point. The resulting exclusion contours for the off-shell WZ analysis are shown for the wino/bino (+), wino/bino (−) and higgsino interpretations in Figure 5.10. Individual limits for the inclusive $\mathrm{SR}^{\mathrm{offWZ}}_{\mathrm{low}\not{E}_{\mathrm{T}}}$-0j, $\mathrm{SR}^{\mathrm{offWZ}}_{\mathrm{low}\not{E}_{\mathrm{T}}}$-nj, $\mathrm{SR}^{\mathrm{offWZ}}_{\mathrm{high}\not{E}_{\mathrm{T}}}$-0j and $\mathrm{SR}^{\mathrm{offWZ}}_{\mathrm{high}\not{E}_{\mathrm{T}}}$-nj regions are shown together with combined

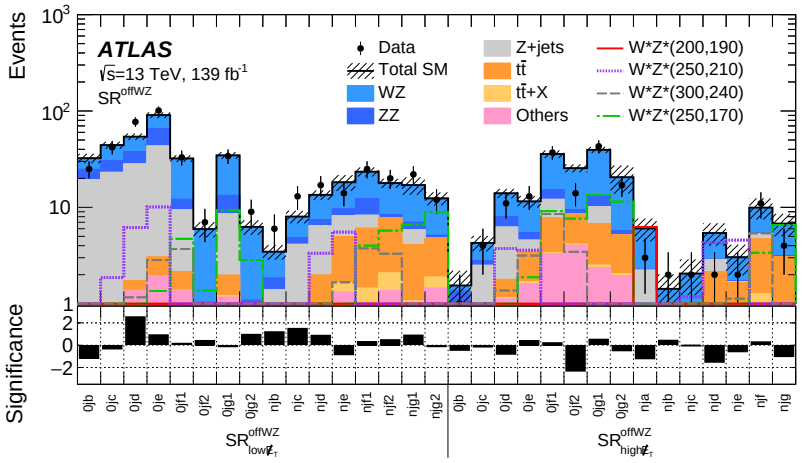

Figure 5.9: Comparison of the observed data and expected SM background yields in the SRs of the off-shell WZ selection [22]. The SM prediction is taken from the background-only fit. The "Others" category contains backgrounds from single-top, WW, triboson, Higgs and rare top processes. The hatched bands indicate the combined theoretical, experimental, and MC-statistical uncertainties. Distributions for wino/bino (+) $\tilde{\chi}_1^{\pm}\tilde{\chi}_2^0 \to W^*Z^*$ signals are overlaid, with mass values given as $(m(\tilde{\chi}_2^0), m(\tilde{\chi}_1^0))$ GeV. The bottom panel shows the signifcance of the difference between the observed and expected yields, calculated with the profile-likelihood method from Ref. [165], adding a minus sign if the yield is below the prediction.

limits. As expected, the $\mathrm{SR}^{\mathrm{offWZ}}_{\mathrm{high}\not{E}_{\mathrm{T}}}$-nj region is most sensitive at low Δm.

In Ref. [22], statistical combinations of the results for the three-lepton off-shell WZ analysis, the three-lepton on-shell WZ analysis (which also did not obtain any significant deviation from the background expectation), and the compressed two-lepton analysis presented in Ref. [173] are performed. Such combinations are performed to extend the results of each analysis alone. All regions of the above-mentioned analyses were designed to be statistically independent, allowing for combination. More information on statistical combinations and how they are performed will be given in Section 7.1. Here, only the resulting exclusion plots will be shown. For the wino/bino (+) interpretation, a combination of the results for all three analyses is performed. For the wino/bino (−) and higgsino interpretations, only the results for the three-lepton off-shell WZ and compressed two-lepton analyses are combined. See Section 9.2 of Ref. [22] for details on which regions and signal points are considered for the different combinations. Details on which regions and signal points are considered for the different combinations can be found in Section 9.2 of Ref. [22]. The 95% CL exclusion limits for all three combinations are shown in Figure 5.11. The combined results are shown together with the individual contributions.

Table 5.7: Summary of the selection criteria for the inclusive SRs in the off-shell WZ selection [22].

	$\text{incSR}^{\text{offWZ}}_{\text{high}E_T}\text{-nj}$			
	a	b	c1	c2
$m_{\ell\ell}^{\text{min}}$ [GeV]	[1, 12]	[12, 15]	[1, 20]	[15, 20]
	$\text{SR}^{\text{offWZ}}_{\text{high}E_T}\text{-nj[a]}$	$\text{SR}^{\text{offWZ}}_{\text{high}E_T}\text{-nj[b]}$	$\text{SR}^{\text{offWZ}}_{\text{high}E_T}\text{-nj[a-c]}$	$\text{SR}^{\text{offWZ}}_{\text{high}E_T}\text{-nj[c]}$

	$\text{incSR}^{\text{offWZ}}_{\text{low}E_T}$		$\text{incSR}^{\text{offWZ}}_{\text{high}E_T}$	
	b	c	b	c
$m_{\ell\ell}^{\text{min}}$ [GeV]	[12, 15]	[12, 20]	[12, 15]	[12, 20]
	$\text{SR}^{\text{offWZ}}_{\text{low}E_T}\text{-0j[b]}$, $\text{SR}^{\text{offWZ}}_{\text{low}E_T}\text{-nj[b]}$	$\text{SR}^{\text{offWZ}}_{\text{low}E_T}\text{-0j[b-c]}$, $\text{SR}^{\text{offWZ}}_{\text{low}E_T}\text{-nj[b-c]}$	$\text{SR}^{\text{offWZ}}_{\text{high}E_T}\text{-0j[b]}$, $\text{SR}^{\text{offWZ}}_{\text{high}E_T}\text{-nj[b]}$	$\text{SR}^{\text{offWZ}}_{\text{high}E_T}\text{-0j[b-c]}$, $\text{SR}^{\text{offWZ}}_{\text{high}E_T}\text{-nj[b-c]}$

	$\text{incSR}^{\text{offWZ}}$				
	d	e1	e2	f1	f2
$m_{\ell\ell}^{\text{min}}$ [GeV]	[12, 30]	[12, 40]	[20, 40]	[12, 60]	[30, 60]
	$\text{SR}^{\text{offWZ}}_{\text{low}E_T}\text{-0j[b-d]}$, $\text{SR}^{\text{offWZ}}_{\text{low}E_T}\text{-nj[b-d]}$, $\text{SR}^{\text{offWZ}}_{\text{high}E_T}\text{-0j[b-d]}$, $\text{SR}^{\text{offWZ}}_{\text{high}E_T}\text{-nj[b-d]}$	$\text{SR}^{\text{offWZ}}_{\text{low}E_T}\text{-0j[b-e]}$, $\text{SR}^{\text{offWZ}}_{\text{low}E_T}\text{-nj[b-e]}$, $\text{SR}^{\text{offWZ}}_{\text{high}E_T}\text{-0j[b-e]}$, $\text{SR}^{\text{offWZ}}_{\text{high}E_T}\text{-nj[b-e]}$	$\text{SR}^{\text{offWZ}}_{\text{low}E_T}\text{-0j[c-e]}$, $\text{SR}^{\text{offWZ}}_{\text{low}E_T}\text{-nj[c-e]}$, $\text{SR}^{\text{offWZ}}_{\text{high}E_T}\text{-0j[c-e]}$, $\text{SR}^{\text{offWZ}}_{\text{high}E_T}\text{-nj[c-e]}$	$\text{SR}^{\text{offWZ}}_{\text{low}E_T}\text{-0j[c-f2]}$, $\text{SR}^{\text{offWZ}}_{\text{low}E_T}\text{-nj[c-f2]}$, $\text{SR}^{\text{offWZ}}_{\text{high}E_T}\text{-0j[c-f2]}$, $\text{SR}^{\text{offWZ}}_{\text{high}E_T}\text{-nj[c-f]}$	$\text{SR}^{\text{offWZ}}_{\text{low}E_T}\text{-0j[e-f2]}$, $\text{SR}^{\text{offWZ}}_{\text{low}E_T}\text{-nj[e-f2]}$, $\text{SR}^{\text{offWZ}}_{\text{high}E_T}\text{-0j[e-f2]}$, $\text{SR}^{\text{offWZ}}_{\text{high}E_T}\text{-nj[e-f]}$

	$\text{incSR}^{\text{offWZ}}$			
	g1	g2	g3	g4
$m_{\ell\ell}^{\text{min}}$ [GeV]	[12, 75]	[30, 75]	[40, 75]	[60, 75]
	$\text{SR}^{\text{offWZ}}_{\text{low}E_T}\text{-0j[b-g2]}$, $\text{SR}^{\text{offWZ}}_{\text{low}E_T}\text{-nj[b-g2]}$, $\text{SR}^{\text{offWZ}}_{\text{high}E_T}\text{-0j[b-g2]}$, $\text{SR}^{\text{offWZ}}_{\text{high}E_T}\text{-nj[b-g]}$	$\text{SR}^{\text{offWZ}}_{\text{low}E_T}\text{-0j[e-g2]}$, $\text{SR}^{\text{offWZ}}_{\text{low}E_T}\text{-nj[e-g2]}$, $\text{SR}^{\text{offWZ}}_{\text{high}E_T}\text{-0j[e-g2]}$, $\text{SR}^{\text{offWZ}}_{\text{high}E_T}\text{-nj[e-g]}$	$\text{SR}^{\text{offWZ}}_{\text{low}E_T}\text{-0j[f1-g2]}$, $\text{SR}^{\text{offWZ}}_{\text{low}E_T}\text{-nj[f1-g2]}$, $\text{SR}^{\text{offWZ}}_{\text{high}E_T}\text{-0j[f1-g2]}$, $\text{SR}^{\text{offWZ}}_{\text{high}E_T}\text{-nj[f1-g]}$	$\text{SR}^{\text{offWZ}}_{\text{low}E_T}\text{-0j[g1-g2]}$, $\text{SR}^{\text{offWZ}}_{\text{low}E_T}\text{-nj[g1-g2]}$, $\text{SR}^{\text{offWZ}}_{\text{high}E_T}\text{-0j[g1-g2]}$, $\text{SR}^{\text{offWZ}}_{\text{high}E_T}\text{-nj[g]}$

For the wino/bino (+) interpretation, shown in (a-b) of Figure 5.11, observed (expected) lower limits for mass-degenerate $\tilde{\chi}_1^{\pm}/\tilde{\chi}_2^0$ are set at 640 (660) GeV for massless $\tilde{\chi}_1^0$, and up to 300 (300) GeV for scenarios with mass splittings close to the Z-boson mass, driven by the on-shell WZ selection. For mass splittings below the Z-boson mass, the exclusion is driven by the off-shell WZ selection, as expected. Here, observed and expected limits are set at values up to 300 GeV for $\Delta m > 35$ GeV, and up to 210–300 GeV for $\Delta m = 20$–35 GeV. For $\Delta m < 15$ GeV, the compressed analysis comes into play, and observed and expected limits are set at values up to 240 GeV for $\Delta m = 10$ GeV. For a $\tilde{\chi}_1^{\pm}/\tilde{\chi}_2^0$ mass of 100 GeV, limits are set down to as low as $\Delta m = 2$ GeV. Compared to the results of the corresponding Run 1 ATLAS search [97], shown as light gray in the plots, the obtained exclusion limits are greatly improved. This is attributed to a combination of increased production cross-section due to increased collision energy, larger data sample, and improved analysis techniques.

For the wino/bino (−) interpretation, shown in (c) of Figure 5.11, observed (expected) lower limits for mass-degenerate $\tilde{\chi}_1^{\pm}/\tilde{\chi}_2^0$ are set at 310 (300) GeV for mass splittings Δm around 80 GeV, and up to 250 (250) GeV for Δm around 40 GeV. The combination of the two analyses is most powerful for $\Delta m = 10$–20 GeV, where the expected limit is raised to 270 GeV, while the observed limit is not as strong due to a deficit seen by the compressed analysis. For a $\tilde{\chi}_1^{\pm}/\tilde{\chi}_2^0$ mass of 100 GeV, observed (expected) limits are set down to as low as $\Delta m = 1$ (1.5) GeV.

Table 5.8: Observed yields (N_{obs}) after the discovery fit and expected yields (N_{exp}) after the background-only fit, for the inclusive signal regions of the off-shell WZ selection [22]. The third and fourth columns list the 95% CL upper limits on the visible cross-section (σ^{95}_{vis}) and on the number of signal events (S^{95}_{obs}). The fifth column shows the 95% CL upper limit on the number of signal events, given the expected number of background events and $\pm 1\sigma$ excursions of the expectation (S^{95}_{exp}). The last two columns indicate the CL_b value, i.e. the confidence level observed for the background-only hypothesis, and the discovery p-value ($p(s=0)$). If the observed yield is below the expected yield, the p-value is capped at 0.5.

SR	N_{obs}	N_{exp}	σ^{95}_{vis} [fb]	S^{95}_{obs}	S^{95}_{exp}	CL_b	$p(s=0)$ (Z)
$\texttt{incSR}^{\texttt{offWZ}}_{\texttt{highE}_\tau}\texttt{-nja}$	3	6.0 ± 1.6	0.03	4.6	$6.3^{+2.4}_{-2.0}$	0.16	0.50 (0.00)
$\texttt{incSR}^{\texttt{offWZ}}_{\texttt{highE}_\tau}\texttt{-njb}$	2	1.4 ± 0.6	0.03	4.8	$4.0^{+1.6}_{-0.7}$	0.71	0.30 (0.53)
$\texttt{incSR}^{\texttt{offWZ}}_{\texttt{highE}_\tau}\texttt{-njc1}$	7	9.5 ± 2.2	0.05	7.0	$8.4^{+2.9}_{-2.2}$	0.28	0.50 (0.00)
$\texttt{incSR}^{\texttt{offWZ}}_{\texttt{highE}_\tau}\texttt{-njc2}$	2	2.1 ± 0.8	0.03	4.7	$4.6^{+1.8}_{-1.1}$	0.52	0.50 (0.00)
$\texttt{incSR}^{\texttt{offWZ}}_{\texttt{lowE}_\tau}\texttt{-b}$	31	36 ± 4	0.09	12	15^{+6}_{-4}	0.25	0.50 (0.00)
$\texttt{incSR}^{\texttt{offWZ}}_{\texttt{highE}_\tau}\texttt{-b}$	3	3.0 ± 0.9	0.04	5.4	$5.2^{+2.0}_{-1.3}$	0.53	0.50 (0.00)
$\texttt{incSR}^{\texttt{offWZ}}_{\texttt{lowE}_\tau}\texttt{-c}$	86	88 ± 7	0.17	23	24^{+9}_{-7}	0.44	0.50 (0.00)
$\texttt{incSR}^{\texttt{offWZ}}_{\texttt{highE}_\tau}\texttt{-c}$	9	9.3 ± 1.5	0.06	7.7	$7.7^{+3.4}_{-1.8}$	0.50	0.50 (0.00)
$\texttt{incSR}^{\texttt{offWZ}}\texttt{-d}$	202	184 ± 12	0.37	51	37^{+14}_{-11}	0.84	0.16 (0.99)
$\texttt{incSR}^{\texttt{offWZ}}\texttt{-e1}$	332	308 ± 17	0.49	68	49^{+19}_{-15}	0.84	0.16 (1.00)
$\texttt{incSR}^{\texttt{offWZ}}\texttt{-e2}$	298	269 ± 15	0.50	69	46^{+17}_{-14}	0.90	0.10 (1.29)
$\texttt{incSR}^{\texttt{offWZ}}\texttt{-f1}$	479	457 ± 22	0.56	78	63^{+22}_{-20}	0.77	0.23 (0.75)
$\texttt{incSR}^{\texttt{offWZ}}\texttt{-f2}$	277	272 ± 13	0.33	46	42^{+17}_{-12}	0.60	0.37 (0.34)
$\texttt{incSR}^{\texttt{offWZ}}\texttt{-g1}$	620	593 ± 28	0.69	96	74^{+29}_{-22}	0.77	0.21 (0.79)
$\texttt{incSR}^{\texttt{offWZ}}\texttt{-g2}$	418	408 ± 20	0.46	64	57^{+23}_{-15}	0.65	0.32 (0.47)
$\texttt{incSR}^{\texttt{offWZ}}\texttt{-g3}$	288	285 ± 16	0.35	48	47^{+19}_{-12}	0.55	0.38 (0.30)
$\texttt{incSR}^{\texttt{offWZ}}\texttt{-g4}$	141	136 ± 10	0.25	35	31^{+13}_{-8}	0.64	0.35 (0.39)

For the higgsino interpretation, shown in (d) of Figure 5.11, with the $\tilde{\chi}^{\pm}_1$ mass set to the mean of the $\tilde{\chi}^0_2$ and $\tilde{\chi}^0_1$ masses, observed (expected) limits extend to around 150–210 (160–215) GeV for mass splittings Δm between 30 and 60 GeV. The combination of the two analyses is most powerful for $\Delta m = 15$–30 GeV, improving on the limits for the individual analyses by up to 15 GeV. The combined results are dominated by the compressed analysis below $\Delta m = 20$ GeV, where limits extend down to $\Delta m = 2$ GeV.

The obtained results for the wino/bino (−) and higgsino interpretations complement the results of the previous compressed results for two-lepton final states as well. The new results make use of the larger data sample and target a novel phase space in the intermediately compressed $\Delta m(\tilde{\chi}^0_2, \tilde{\chi}^0_1)$ region, extending the exclusion by up to 100 GeV in $\tilde{\chi}^0_2$ mass.

For completeness, exclusion limits for the Wh analysis — which also did not obtain any significant deviation from the background expectation — are also

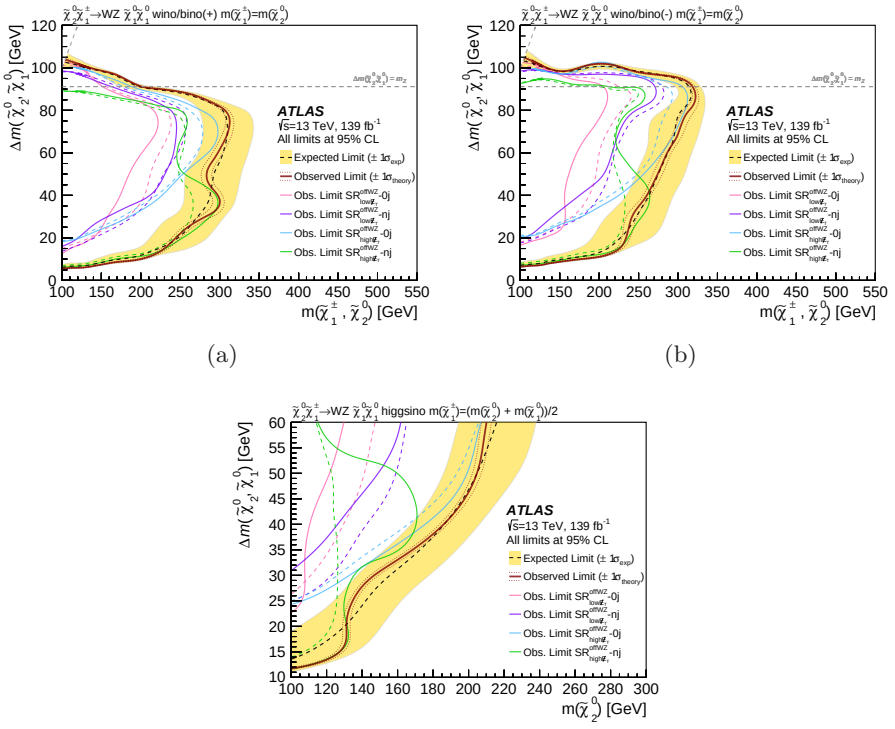

Figure 5.10: Exclusion limits obtained for the off-shell WZ analysis for (a) the wino/bino (+) interpretation, (b) the wino/bino (−) interpretation, and (c) the higgsino interpretation, projected onto the $m(\tilde{\chi}_2^0)$ vs. $\Delta m(\tilde{\chi}_2^0, \tilde{\chi}_1^0)$ plane [22]. The expected 95% CL sensitivity (dashed black line) is shown with $\pm 1\sigma_{\text{exp}}$ (yellow band) from experimental systematic uncertainties and statistical uncertainties on the data yields. The observed limit (red solid line) is shown with $\pm 1\sigma_{\text{theory}}$ (dotted red lines) from signal cross-section uncertainties. The main contours show the expected and observed limits using the full off-shell WZ selection. Individual results for the inclusive $\text{SR}^{\text{offWZ}}_{\text{low}E_{\text{T}}^{\text{miss}}}\text{-0j}$, $\text{SR}^{\text{offWZ}}_{\text{low}E_{\text{T}}^{\text{miss}}}\text{-nj}$, $\text{SR}^{\text{offWZ}}_{\text{high}E_{\text{T}}^{\text{miss}}}\text{-0j}$ and $\text{SR}^{\text{offWZ}}_{\text{high}E_{\text{T}}^{\text{miss}}}\text{-nj}$ regions are overlaid in pink, purple, blue and green, respectively.

presented. These results will be used in a statistical combination to be presented in Section 7.3. Figure 5.12 shows the 95% CL exclusion limits obtained for this analysis, only considering the wino/bino (+) interpretation. For $\tilde{\chi}_1^0$ masses below 20 GeV, observed and expected lower mass limits for $\tilde{\chi}_1^{\pm}/\tilde{\chi}_2^0$ are set at values up to 190 GeV and 240 GeV, respectively. That the observed exclusion is weaker than the expected exclusion is due to a mild excess found in one of the signal regions. However, the limits are compatible within 2σ. Compared to the 8 TeV Run 1 ATLAS search presented in Ref. [97], the observed (expected) limits are improved by up to 40 (80) GeV.

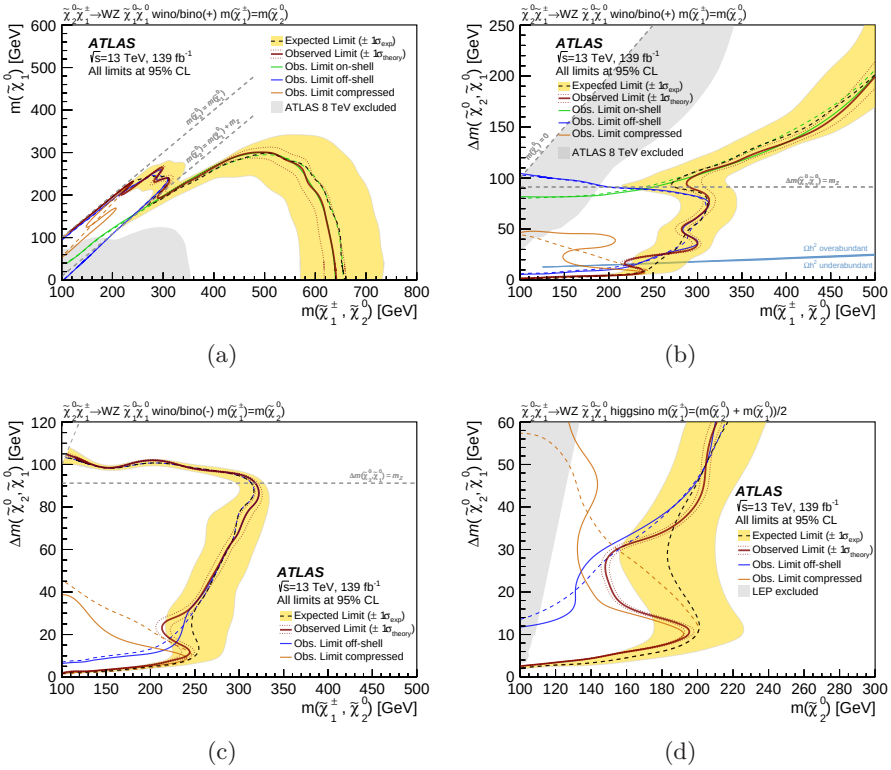

Figure 5.11: Exclusion limits obtained for the WZ-mediated models for (a-b) the wino/bino (+) interpretation, (c) the wino/bino (−) interpretation, and (d) the higgsino interpretation [22]. The expected 95% CL sensitivity (dashed black line) is shown with $\pm 1\sigma_{\text{exp}}$ from experimental systematic uncertainties and statistical uncertainties in the data yields, and the observed limit (red solid line) is shown with $\pm 1\sigma_{\text{theory}}$ (red dotted lines) from signal cross-section uncertainties. The statistical combination of the on-shell WZ, off-shell WZ, and compressed two-lepton results is shown as the main contour, while the observed (expected) limits for each individual selection are overlaid in green, blue and orange solid (dashed) lines, respectively. The exclusion is shown projected onto the $m(\tilde{\chi}_1^{\pm}/\tilde{\chi}_2^0)$ vs. $m(\tilde{\chi}_1^0)$ plane in (a), and onto the $m(\tilde{\chi}_2^0)$ vs. Δm plane in (b-d). The light gray area denotes (a-b) the constraints obtained by the previous equivalent analysis in ATLAS using the 8 TeV 20.3 fb^{-1} dataset [97], and (c) the LEP lower $\tilde{\chi}_1^{\pm}$ mass limit [98]. The pale blue line in (b) represents the mass-splitting range that yields a dark-matter relic density equal to the observed relic density, $\Omega h^2 = 0.1186 \pm 0.0020$ [174], when the mass parameters of all the decoupled SUSY partners are set to 5 TeV and $\tan\beta$ is chosen such that the lightest Higgs boson's mass is consistent with the observed value of the SM Higgs [175]. The area above (below) the blue line represents a dark-matter relic density larger (smaller) than the observed.

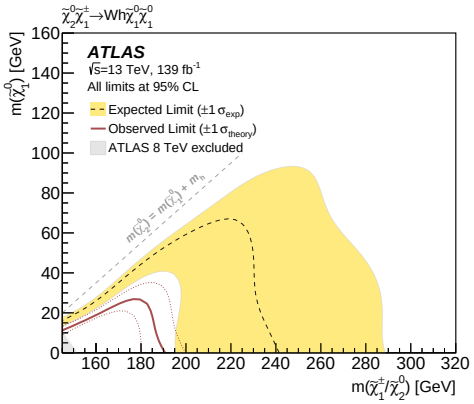

Figure 5.12: Exclusion limits obtained for the Wh-mediated model for the wino/bino (+) interpretation, calculated using the Wh SRs and projected onto the $m(\tilde{\chi}_1^\pm, \tilde{\chi}_2^0)$ vs. $m(\tilde{\chi}_1^0)$ plane. The expected 95% CL sensitivity (dashed black line) is shown with $\pm 1\sigma_{\text{exp}}$ (yellow band) from experimental systematic uncertainties and statistical uncertainties in the data yields, and the observed limit (red solid line) is shown with $\pm 1\sigma_{\text{theory}}$ (dotted red lines) from signal cross-section uncertainties. The light gray area denotes the constraints obtained by the previous equivalent analysis in ATLAS using the 8 TeV 20.3 fb^{-1} dataset [97].

5.7 Preparing for reinterpretation

The Durham High-Energy Physics Database (HEPData) [23] is an open-access repository for scattering data from experimental particle physics. It contains data points from plots and tables related to several thousand publications, including LHC ones. Public access to such data is important because it allows for reinterpretation of the results by people not involved in the original analyses.

Reinterpretation should be enabled to maximize the scientific impact of the data obtained and the analyses performed. Any supersymmetry analysis can constrain a much wider range of theories than considered in the original, published analysis. And as SUSY is much richer than the MSSM, there are many theoretical ideas that cannot all be tested by the experimental collaboration alone. Further, it can be favorable to go beyond an analysis-by-analysis approach and rather take on a global view. We also need large-scale exploration of the complementarities between LHC results and other experimental results. Additionally, reinterpretation allows phenomenologists to give detailed feedback on the original analyses and suggest promising new avenues.

Preparing input for HEPData is a mandatory step in the ATLAS collaboration's publication process. My main contribution to Ref. [22] was preparing some of the HEPData input for the off-shell WZ analysis, namely signal acceptance and efficiency plots and cutflows for the signal regions. This work will be summarized in this section, together with some examples on how this information is used by different reinterpretation tools.

5.7.1 Acceptance and efficiency plots

The *acceptance* A is defined as the fraction of signal events passing the selection of a given signal region at generator-level, and is thus often referred to as *truth-level acceptance*. It is given by

$$A = \frac{n_{\text{accept}}^{\text{generator}}}{n_{\text{total}}^{\text{generator}}}, \tag{5.17}$$

where $n_{\text{accept}}^{\text{generator}}$ is the number of generated events passing the selection, and $n_{\text{total}}^{\text{generator}}$ is the total number of generated events. The acceptance is highly dependent on the final-state particles and kinematics of the signal model in question. In ATLAS, the analysis framework SimpleAnalysis [176, 177] is used to calculate such truth-level acceptances. This framework is designed to run on the output of event generators (generator-level information, or just *truth*), and has been used in most ATLAS supersymmetry results since 2016.[9]

As explained in Section 4.1.1, all simulated events must go through detector simulation and reconstruction after generation. Not all signal events accepted at generator-level will survive these subsequent steps. The ATLAS detector sensors are not perfectly efficient, and also ATLAS' systems for particle reconstruction

[9]Note that a more widely used toolkit with for the same purpose is Rivet (Robust Independent Validation of Experiment and Theory) [178]. However, SimpleAnalysis is the preferred tool for ATLAS supersymmetry searches for historical reasons.

and identificaton can be inefficient. These inefficiencies are encapsulated in the *reconstruction efficiency* ε, which is calculated from the "acceptance times efficiency", $A \otimes \varepsilon$, as

$$A \otimes \varepsilon = \frac{n_{\text{accept}}^{\text{reco}}}{n_{\text{total}}^{\text{reco}}} \quad \Rightarrow \quad \varepsilon = \frac{A \otimes \varepsilon}{A}, \tag{5.18}$$

where $n_{\text{accept}}^{\text{reco}}$ is the number of reconstructed events passing the selection, and $n_{\text{total}}^{\text{reco}}$ is the total number of reconstructed events. The acceptance times efficiency is the full event selection efficiency at reconstruction level, and is calculated with the actual analysis framework using fully reconstructed quantities. Armed with background estimates per signal region, usually listed in the publication, theorists can probe their favorite models by first validating their implementation of the signal-region selections and detector simulation against the provided acceptance and efficiency numbers, respectively.

Calculating the acceptance

For the off-shell WZ analysis, a total of 125 and 53 signal points $(m(\tilde{\chi}_2^0), m(\tilde{\chi}_1^0))$ are considered for the wino/bino and higgsino scenarios, respectively. After implementing all regions of the off-shell WZ analysis at generator-level,[10] SimpleAnalysis is run on so-called *MC truth samples* for all signal points. The output of SimpleAnalysis is a text file with acceptances per region. However, these "raw" SimpleAnalysis acceptances must be multiplied with a couple of factors in order to arrive at the relevant numbers: the *generator filter efficiency*, and the branching ratio for WZ decaying into a three-lepton final state.

In order to increase statistics in a particular region of phase space, it is common to apply a filter during MC event generation, such that the generator will only generate events that pass some selection. For the off-shell signal samples, a filter requiring that all events contain at least three leptons with a transverse momentum of 3 GeV or more was applied during generation. If this filter was not applied, many of the generated events would not have been useful to the off-shell WZ analysis, which would have been a waste of computing resources. However, if such a filter is applied, it must be accounted for in the analysis by multiplying with a single factor taking into account that you are not generating the full cross-section of that process. For instance, a filter efficiency of 0.30 indicates that 30% of the total number of generated events passed the filter and were actually stored in the sample. The filter efficiency is part of the output from the event generator, and varies from signal sample to signal sample. It is typically larger for samples for heavier sparticles, as their decay products are more energetic and thus more easily pass a filter.

Further, the branching fraction (BF) has to be multiplied in to take into account that we are only interested in leptonic decays of W and Z, in order to end up with a three-lepton final state. For the two wino/bino

[10] I did not do this implementation myself, but contributed to the validation of it.

scenarios, the branching ratio is the same regardless of sparticle masses, namely $3 \times \mathrm{BF}(W \to \ell\nu) \times 3 \times \mathrm{BF}(Z \to \ell\ell) = 0.032716$. For the higgsino scenario — for which the $\tilde{\chi}_1^{\pm}$ and $\tilde{\chi}_2^0$ are not mass-degenerate — the branching ratio depends on $\Delta m(\tilde{\chi}_2^0, \tilde{\chi}_1^0)$, and is calculated using the SUSY-HIT package [179].

There is an extra level of complication for off-shell signal points compared to on-shell ones. Due to technical problems with the matching between software tools used for their production, MC samples are produced separately for chargino decays via W^+ and W^- for off-shell signal points. The acceptances for the two different signs thus need to be combined to get the "total" acceptance for these points.

Calculating the efficiency

In practice, the reconstruction efficiency for a given signal region as defined in Equation (5.18) is calculated by

$$\varepsilon = \frac{n/\mathcal{L}}{A\sigma}, \tag{5.19}$$

where n is the signal event yield given by the analysis, $\mathcal{L}$ is the integrated luminosity of the full Run 2 dataset (139 fb^{-1}), A is the acceptance and σ is the production cross-section for the signal point. Rearranging this expression gives $n = A\varepsilon\sigma\mathcal{L}$, which is the standard event-rate expression $\sigma\mathcal{L}$ multiplied with a total "MC factor" $A\varepsilon$.

Resulting plots

As there are 31 signal regions in total for the off-shell WZ analysis, the results are simplified by only quoting the numbers for the four inclusive regions $\mathtt{SR}^{\mathtt{offWZ}}_{\mathtt{low}E_{\mathrm{T}}}\mathtt{-0j}$, $\mathtt{SR}^{\mathtt{offWZ}}_{\mathtt{low}E_{\mathrm{T}}}\mathtt{-nj}$, $\mathtt{SR}^{\mathtt{offWZ}}_{\mathtt{high}E_{\mathrm{T}}}\mathtt{-0j}$ and $\mathtt{SR}^{\mathtt{offWZ}}_{\mathtt{high}E_{\mathrm{T}}}\mathtt{-nj}$. Figures 5.13 and 5.14 show the truth-level accceptances and reconstruction efficiencies, respectively, for these regions for the wino/bino (+) scenario. Corresponding plots for the wino/bino (−) and higgsino scenarios can be found in Appendix A.

5.7.2 Cutflows

Also so-called *cutflows* are important tools for validating an analysis implementation for reinterpretation. As explained in Section 5.2.1, signal regions are constructed by applying cuts on different discriminant variables. The cuts are chosen so that as many signal events and as few background events as possible pass the selection, to maximize the signal-to-background ratio. A cutflow is a table showing how many of the events pass each cut, when applying the cuts one by one. The last line in a cutflow then shows the final event yield of the region, after all cuts have been applied.

Tables 5.9, 5.10 and 5.11 show cutflows for three representative signal points — with different mass splittings, well inside and close to the exclusion contour in Figure 5.10(a) — for the wino/bino (+) scenario. Corresponding tables for the wino/bino (−) and higgsino scenarios can be found in Appendix A.

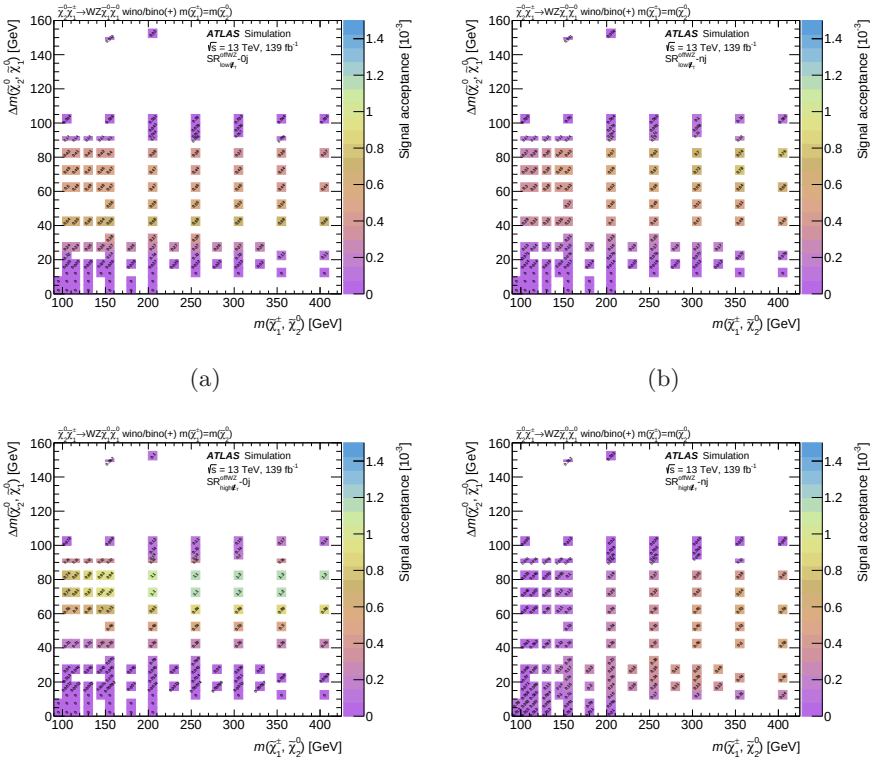

(a) (b)

(c) (d)

Figure 5.13: Truth-level acceptances for the four inclusive off-shell WZ signal regions (a) $\mathtt{SR}^{\mathtt{offWZ}}_{\mathtt{low}E_{\mathrm{T}}}\mathtt{-0j}$, (b) $\mathtt{SR}^{\mathtt{offWZ}}_{\mathtt{low}E_{\mathrm{T}}}\mathtt{-nj}$, (c) $\mathtt{SR}^{\mathtt{offWZ}}_{\mathtt{high}E_{\mathrm{T}}}\mathtt{-0j}$ and (d) $\mathtt{SR}^{\mathtt{offWZ}}_{\mathtt{high}E_{\mathrm{T}}}\mathtt{-nj}$ for the wino/bino (+) scenario.

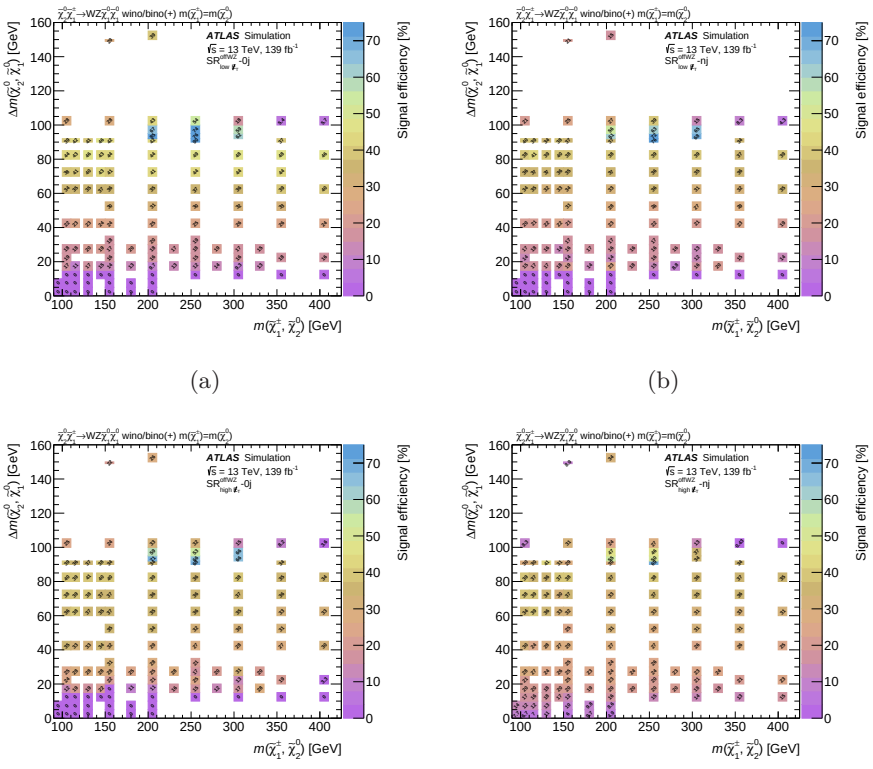

Figure 5.14: Reconstruction efficiencies for the four inclusive off-shell WZ signal regions (a) $\mathtt{SR}^{\mathtt{offWZ}}_{\mathtt{low}E_{\mathrm{T}}}\mathtt{-0j}$, (b) $\mathtt{SR}^{\mathtt{offWZ}}_{\mathtt{low}E_{\mathrm{T}}}\mathtt{-nj}$, (c) $\mathtt{SR}^{\mathtt{offWZ}}_{\mathtt{high}E_{\mathrm{T}}}\mathtt{-0j}$ and (d) $\mathtt{SR}^{\mathtt{offWZ}}_{\mathtt{high}E_{\mathrm{T}}}\mathtt{-nj}$ for the wino/bino (+) scenario.

Table 5.9: Cutflow for the off-shell WZ event selection for the $(m(\tilde{\chi}_2^0), m(\tilde{\chi}_1^0)) =$ (125,85) GeV signal point for the wino/bino (+) scenario. The yields are normalized to a luminosity $\mathcal{L}$ of 139 fb^{-1}. MC-to-data efficiency weights from triggering and from the reconstruction and identification of individual physics objects are applied to the final yields in each signal region. After the initial selections, the table is split in row blocks for the inclusive $\mathtt{SR}^{\mathtt{offWZ}}_{\mathtt{low}\not{E}_{\mathrm{T}}}\mathtt{\text{-}0j}$, $\mathtt{SR}^{\mathtt{offWZ}}_{\mathtt{low}\not{E}_{\mathrm{T}}}\mathtt{\text{-}nj}$, $\mathtt{SR}^{\mathtt{offWZ}}_{\mathtt{high}\not{E}_{\mathrm{T}}}\mathtt{\text{-}0j}$, $\mathtt{SR}^{\mathtt{offWZ}}_{\mathtt{high}\not{E}_{\mathrm{T}}}\mathtt{\text{-}nj}$ regions, with the individual signal region yields in columns. The inclusive OR of regions a through g2 is given in the last column. Selection details per bin are indicated in bracketed blue as relevant, and the final yields for each signal region is highlighted in bold green at the end of each block. The "3 isolated lepton selection" includes the preselection as described in Section 4.3 and the initial SFOS lepton pair selection.

$\tilde{\chi}_1^\pm\tilde{\chi}_2^0 \to WZ\tilde{\chi}_1^0\tilde{\chi}_1^0$ wino/bino (+)					m($\tilde{\chi}_2^0$,$\tilde{\chi}_1^0$) = (125, 85) GeV					
	a	**b**	**c**	**d**	**e**	**f1**	**f2**	**g1**	**g2**	**a through g2**
Common cuts										
$\mathcal{L} \times \sigma$					1394866					1394866
$\mathcal{L} \times \sigma \times$ BF					45634					45634
$\mathcal{L} \times \sigma \times$ BF $\times$ filt. eff.					16811					16811
3 isolated lepton selection					2.66e+03					2.66e+03
b-veto					2.55e+03					2.55e+03
Trigger selection					1.81e+03					1.81e+03
$m_{\ell\ell}, m_{\ell\ell}^{\max}$ [GeV]					[< 75] 1.79e+03					1.79e+03
Common cuts $\mathtt{SR}^{\mathtt{offWZ}}_{\mathtt{low}\not{E}_{\mathrm{T}}}$										
$m_{\ell\ell}^{\min}$ [GeV]	-		[∈ [12, 40]] 1.70e+03				[∈ [40, 75]] 14.6			1.71e+03
lepton $p_{\mathrm{T}}^{1,2,3}$ [GeV]	-		[> 10] 1.44e+03				[> 15] 7.74			1.45e+03
FNP lepton cleaning (conversions)	-		1.12e+03				5.92			1.12e+03
$m_{\ell\ell}^{\max}$ [GeV]	-		[< 60] 1.02e+03				5.92			1.03e+03
$m_{\ell\ell}^{\min}$ [GeV]	-	[∈ [12, 15]] 47.0	[∈ [15, 20]] 119	[∈ [20, 30]] 406	[∈ [30, 40]] 452	[∈ [40, 60]] 5.92		[∈ [60, 75]] 0		1.03e+03
m_{T2}^{100} [GeV]	-	[< 115] 19.4	[< 120] 74.7	[< 130] 374	452	5.92		0		926
minΔR	-	[< 1.6] 19.4	[< 1.6] 73.2	[< 1.6] 295	452	5.92		0		846
Cuts $\mathtt{SR}^{\mathtt{offWZ}}_{\mathtt{low}\not{E}_{\mathrm{T}}}\mathtt{\text{-}0j}$										
$n_{\mathrm{jets}}^{p_{\mathrm{T}}>30\,\mathrm{GeV}}$	-	[= 0] 12.2	[= 0] 49.5	[= 0] 186	[= 0] 291	[= 0] 3.28		[= 0] 0		542
$E_{\mathrm{T}}^{\mathrm{miss}}$ [GeV]	-	[< 50] 11.2	[< 50] 42.9	[< 50] 147	[< 50] 242	[< 50] 2.62		[< 50] 0		446
$E_{\mathrm{T}}^{\mathrm{miss}}$ signif.	-	[> 1.5] 8.57	[> 1.5] 34.7	[> 1.5] 123	[> 1.5] 182	[> 1.5] 1.91		[> 1.5] 0		350
$m_{3\ell}$ [GeV]	-	8.57	34.7	123	182	[> 100] 0.656		[> 100] 0		349
$m_{\mathrm{T}}^{\mathrm{minmll}}$ [GeV]	-	[< 50] 8.16	[< 50] 32.6	[< 50] 97.8	[< 60] 158	[< 60] 0.560	[> 90] 0	[< 60] 0	[> 90] 0	297
$p_{\mathrm{T}}^{\mathrm{lep}}/E_{\mathrm{T}}^{\mathrm{miss}}$	-	[< 1.1] 5.27	[< 1.1] 22.7	[< 1.1] 64.3	[< 1.3] 138	[< 1.4] 0.560	[< 1.4] 0	[< 1.4] 0	[< 1.4] 0	231
MC-to-data eff. weights	**-**	**4.77**	**20.2**	**59.3**	**126**	**0.525**	**0**	**0**	**0**	**211**
Cuts $\mathtt{SR}^{\mathtt{offWZ}}_{\mathtt{low}\not{E}_{\mathrm{T}}}\mathtt{\text{-}nj}$										
$n_{\mathrm{jets}}^{p_{\mathrm{T}}>30\,\mathrm{GeV}}$	-	[> 0] 7.20	[> 0] 23.8	[> 0] 110	[> 0] 161	[> 0] 2.64		[> 0] 0		304
$E_{\mathrm{T}}^{\mathrm{miss}}$ [GeV]	-	[< 200] 6.52	[< 200] 21.3	[< 200] 102	[< 200] 150	[< 200] 2.64		[< 200] 0		282
$E_{\mathrm{T}}^{\mathrm{miss}}$ signif.	-	[> 3.0] 4.72	[> 3.0] 16.1	[> 3.0] 76.3	[> 3.0] 106	[> 3.0] 1.70		[> 3.0] 0		205
$m_{\mathrm{T}}^{\mathrm{minmll}}$ [GeV]	-	[< 50] 2.85	[< 50] 10.7	[< 50] 42.9	[< 60] 65.7	[< 60] 1.41	[> 90] 0	[< 60] 0	[> 90] 0	124
$p_{\mathrm{T}}^{\mathrm{lep}}/E_{\mathrm{T}}^{\mathrm{miss}}$	-	[< 1.0] 2.54	[< 1.0] 10.6	[< 1.0] 36.5	[< 1.0] 59.9	[< 1.2] 1.34	[< 1.2] 0	[< 1.2] 0	[< 1.2] 0	111
MC-to-data eff. weights	**-**	**2.31**	**9.82**	**33.7**	**53.0**	**1.25**	**0**	**0**	**0**	**100**
Cuts $\mathtt{SR}^{\mathtt{offWZ}}_{\mathtt{high}\not{E}_{\mathrm{T}}}\mathtt{\text{-}0j}$										
lepton $p_{\mathrm{T}}^{1,2,3}$ [GeV]					[> 25, 15, 10] 1.17e+03					1.17e+03
$m_{\ell\ell}^{\min}$ [GeV]	-	[∈ [12, 15]] 44.0	[∈ [15, 20]] 120	[∈ [20, 30]] 422	[∈ [30, 40]] 541	[∈ [40, 60]] 11.1		[∈ [60, 75]] 0.148		1.14e+03
m_{T2}^{100} [GeV]	-	[< 115] 19.1	[< 120] 76.3	[< 130] 388	[< 140] 540	[< 160] 11.1		[< 175] 0.148		1.03e+03
$n_{\mathrm{jets}}^{p_{\mathrm{T}}>30\,\mathrm{GeV}}$	-	[= 0] 11.6	[= 0] 49.6	[= 0] 239	[= 0] 341	[= 0] 7.28		[= 0] 0.148		649
$E_{\mathrm{T}}^{\mathrm{miss}}$ [GeV]	-	[> 50] 2.05	[> 50] 10.3	[> 50] 50.8	[> 50] 67.0	[> 50] 1.08		[> 50] 0		131
$E_{\mathrm{T}}^{\mathrm{miss}}$ signif.	-	[> 3.0] 1.80	[> 3.0] 9.37	[> 3.0] 46.1	[> 3.0] 60.5	[> 3.0] 0.805		[> 3.0] 0		119
$m_{\mathrm{T}}^{\mathrm{minmll}}$ [GeV]	-	[< 50] 1.74	[< 50] 8.84	[< 60] 43.3	[< 60] 52.4	[< 70] 0.805	[> 90] 0	[< 70] 0	[> 90] 0	107
MC-to-data eff. weights	**-**	**1.84**	**8.03**	**40.2**	**48.6**	**0.760**	**0**	**0**	**0**	**99.5**
Cuts $\mathtt{SR}^{\mathtt{offWZ}}_{\mathtt{high}\not{E}_{\mathrm{T}}}\mathtt{\text{-}nj}$										
lepton $p_{\mathrm{T}}^{1,2,3}$ [GeV]					[>4.5,3] 1.79e+03					1.79e+03
						f		**g**		
$m_{\ell\ell}^{\min}$ [GeV]	[∈ [1, 12]] 78.4	[∈ [12, 15]] 83.5	[∈ [15, 20]] 207	[∈ [20, 30]] 661	[∈ [30, 40]] 746	[∈ [40, 60]] 14.5		[∈ [60, 75]] 0.148		1.79e+03
m_{T2}^{100} [GeV]	[< 112] 25.2	[< 115] 34.8	[< 120] 131	[< 130] 607	[< 140] 744	[< 160] 14.5		[< 175] 0.148		1.56e+03
$n_{\mathrm{jets}}^{p_{\mathrm{T}}>30\,\mathrm{GeV}}$	[> 0] 9.71	[> 0] 15.8	[> 0] 52.7	[> 0] 252	[> 0] 287	[> 0] 5.24		[> 0] 0		622
$E_{\mathrm{T}}^{\mathrm{miss}}$ [GeV]	[> 200] 0.713	[> 200] 2.09	[> 200] 5.85	[> 200] 22.3	[> 200] 24.1	[> 200] 7.10e-02		[> 200] 0		55.1
$E_{\mathrm{T}}^{\mathrm{miss}}$ signif.	[> 3.0] 0.713	[> 3.0] 2.09	[> 3.0] 5.85	[> 3.0] 22.3	[> 3.0] 24.1	[> 3.0] 7.10e-02		[> 3.0] 0		55.1
$p_{\mathrm{T}}^{\mathrm{lep}}/E_{\mathrm{T}}^{\mathrm{miss}}$	[< 0.2] 0.611	[< 0.2] 1.99	[< 0.3] 5.39	[< 0.3] 14.6	[< 0.3] 13.8	[< 1.0] 7.10e-02		[< 1.0] 0		36.4
MC-to-data eff. weights	**0.594**	**1.92**	**4.94**	**13.4**	**12.6**	**7.20e-02**		**0**		**33.5**

Table 5.10: Cutflow for the off-shell WZ event selection for the $(m(\tilde{\chi}_2^0), m(\tilde{\chi}_1^0)) = (250,170)$ GeV signal point for the wino/bino (+) scenario. The yields are normalized to a luminosity $\mathcal{L}$ of 139 fb^{-1}. MC-to-data efficiency weights from triggering and from the reconstruction and identification of individual physics objects are applied to the final yields in each signal region. After the initial selections, the table is split in row blocks for the inclusive $\mathsf{SR}^{\mathsf{offWZ}}_{\mathsf{low}E_{\mathrm{T}}}$-0j, $\mathsf{SR}^{\mathsf{offWZ}}_{\mathsf{low}E_{\mathrm{T}}}$-nj, $\mathsf{SR}^{\mathsf{offWZ}}_{\mathsf{high}E_{\mathrm{T}}}$-0j, $\mathsf{SR}^{\mathsf{offWZ}}_{\mathsf{high}E_{\mathrm{T}}}$-nj regions, with the individual signal region yields in columns. The inclusive OR of regions a through g2 is given in the last column. Selection details per bin are indicated in bracketed blue as relevant, and the final yields for each signal region is highlighted in bold green at the end of each block. The "3 isolated lepton selection" includes the preselection as described in Section 4.3 and the initial SFOS lepton pair selection.

$\tilde{\chi}_1^\pm\tilde{\chi}_2^0 \to WZ\tilde{\chi}_1^0\tilde{\chi}_1^0$ wino/bino (+)										m($\tilde{\chi}_2^0$,$\tilde{\chi}_1^0$) = (250, 170) GeV										
	a		**b**		**c**		**d**		**e**		**f1**		**f2**		**g1**		**g2**		**a through g2**
Common cuts																				
$\mathcal{L} \times \sigma$									108769										108769	
$\mathcal{L} \times \sigma \times$ BF									3559										3559	
$\mathcal{L} \times \sigma \times$ BF $\times$ filt. eff.									1638										1638	
3 isolated lepton selection									384										384	
b-veto									367										367	
Trigger selection									307										307	
$m_{\ell\ell}$, $m_{\ell\ell}^{\mathrm{min}}$ [GeV]									[< 75]	299									299	
Common cuts $\mathsf{SR}^{\mathsf{offWZ}}_{\mathsf{low}E_{\mathrm{T}}}$																				
$m_{\ell\ell}^{\mathrm{min}}$ [GeV]	-					[∈ [12, 40]]	58.8							[∈ [40, 75]]	239				298	
lepton $p_{\mathrm{T}}^{\ell,2,3}$ [GeV]	-					[> 10]	51.1							[> 15]	189				240	
FNP lepton cleaning (conversions)	-						38.0								146				184	
$m_{\ell\ell}^{\mathrm{sfos}}$ [GeV]	-					[< 60]	23.9								146				170	
$m_{\ell\ell}^{\mathrm{min}}$ [GeV]	-	[∈ [12, 15]]	0.738	[∈ [15, 20]]	1.99	[∈ [20, 30]]	7.44	[∈ [30, 40]]	13.7		[∈ [40, 60]]	58.2				[∈ [60, 75]]	87.6		170	
m_{T2}^{100} [GeV]	-	[< 115]	4.80e-02	[< 120]	0.566	[< 130]	3.17		13.7			58.2					87.6		163	
minΔR	-	[< 1.6]	4.80e-02	[< 1.6]	0.560	[< 1.6]	2.83		13.7			58.2					87.6		163	
Cuts $\mathsf{SR}^{\mathsf{offWZ}}_{\mathsf{low}E_{\mathrm{T}}}$-0j																				
$p_{\mathrm{T}}^{\ell_3 > 30\mathrm{GeV}}$	-	[= 0]	2.20e-02	[= 0]	0.395	[= 0]	1.75	[= 0]	8.35		[= 0]	34.4				[= 0]	52.1		97.0	
$E_{\mathrm{T}}^{\mathrm{miss}}$ [GeV]	-	[< 50]	1.60e-02	[< 50]	0.239	[< 50]	1.10	[< 50]	3.51		[< 50]	15.8				[< 50]	26.6		47.3	
$E_{\mathrm{T}}^{\mathrm{miss}}$ signif.	-	[> 1.5]	6.00e-03	[> 1.5]	0.239	[> 1.5]	0.977	[> 1.5]	3.04		[> 1.5]	13.5				[> 1.5]	22.6		40.4	
$m_{3\ell}$ [GeV]	-		6.00e-03		0.239		0.977		3.04		[> 100]	10.5				[> 100]	21.0		35.8	
$m_{\ell\ell}^{\mathrm{minOS}}$ [GeV]	-	[< 50]	6.00e-03	[< 50]	0.223	[< 50]	0.517	[< 60]	1.74	[< 60]	5.92	[> 90]	1.57	[< 60]	11.3	[> 90]	3.14		24.5	
$p_{\mathrm{T}}^{\mathrm{jet}}/E_{\mathrm{T}}^{\mathrm{miss}}$	-	[< 1.1]	6.00e-03	[< 1.1]	0.150	[< 1.1]	0.268	[< 1.3]	1.38	[< 1.4]	5.11	[< 1.4]	1.44	[< 1.4]	9.87	[< 1.4]	2.99		21.2	
MC-to-data eff. weights	-		**6.00e-03**		**0.171**		**0.241**		**1.36**		**4.72**		**1.37**		**9.32**		**2.84**		**20.0**	
Cuts $\mathsf{SR}^{\mathsf{offWZ}}_{\mathsf{low}E_{\mathrm{T}}}$-nj																				
$p_{\mathrm{T}}^{\ell_3 > 30\mathrm{GeV}}$	-	[> 0]	2.70e-02	[> 0]	0.165	[> 0]	1.08	[> 0]	5.33		[> 0]	23.7				[> 0]	35.4		65.8	
$E_{\mathrm{T}}^{\mathrm{miss}}$ [GeV]	-	[< 200]	2.70e-02	[< 200]	0.165	[< 200]	0.953	[< 200]	4.66		[< 200]	21.2				[< 200]	31.0		58.0	
$E_{\mathrm{T}}^{\mathrm{miss}}$ signif.	-	[> 3.0]	1.60e-02	[> 3.0]	0.165	[> 3.0]	0.806	[> 3.0]	3.77		[> 3.0]	17.9				[> 3.0]	25.2		47.8	
$m_{\ell\ell}^{\mathrm{minOS}}$ [GeV]	-	[< 50]	6.00e-03	[< 50]	0.136	[< 50]	0.470	[< 60]	1.20	[< 60]	5.88	[> 90]	7.08	[< 60]	8.86	[> 90]	10.3		33.9	
$p_{\mathrm{T}}^{\mathrm{jet}}/E_{\mathrm{T}}^{\mathrm{miss}}$	-	[< 1.0]	6.00e-03	[< 1.0]	0.136	[< 1.0]	0.433	[< 1.0]	0.666	[< 1.2]	4.35	[< 1.2]	6.17	[< 1.2]	7.15	[< 1.2]	9.47		28.4	
MC-to-data eff. weights	-		**5.00e-03**		**0.125**		**0.404**		**0.624**		**4.01**		**5.74**		**6.62**		**8.89**		**26.4**	
Cuts $\mathsf{SR}^{\mathsf{offWZ}}_{\mathsf{high}E_{\mathrm{T}}}$-0j																				
lepton $p_{\mathrm{T}}^{\ell,2,3}$ [GeV]								[> 25, 15, 10]	274										274	
$m_{\ell\ell}^{\mathrm{min}}$ [GeV]	-	[∈ [12, 15]]	1.74	[∈ [15, 20]]	4.67	[∈ [20, 30]]	15.7	[∈ [30, 40]]	27.2		[∈ [40, 60]]	91.8				[∈ [60, 75]]	132		273	
m_{T2}^{100} [GeV]	-	[< 115]	0.380	[< 120]	1.25	[< 130]	7.51	[< 140]	16.7		[< 160]	81.8				[< 175]	131		239	
$p_{\mathrm{T}}^{\ell_3 > 30\mathrm{GeV}}$	-	[= 0]	0.264	[= 0]	0.865	[= 0]	4.35	[= 0]	9.91		[= 0]	49.6				[= 0]	77.9		143	
$E_{\mathrm{T}}^{\mathrm{miss}}$ [GeV]	-	[> 50]	5.20e-02	[> 50]	0.214	[> 50]	1.28	[> 50]	3.51		[> 50]	24.5				[> 50]	37.1		66.6	
$E_{\mathrm{T}}^{\mathrm{miss}}$ signif.	-	[> 3.0]	5.20e-02	[> 3.0]	0.193	[> 3.0]	1.13	[> 3.0]	3.35		[> 3.0]	23.4				[> 3.0]	35.5		63.7	
$m_{\ell\ell}^{\mathrm{minOS}}$ [GeV]	-	[< 50]	6.00e-03	[< 50]	0.131	[< 60]	0.812	[< 60]	2.10	[< 70]	9.62	[> 90]	8.00	[< 70]	14.9	[> 90]	12.1		47.6	
MC-to-data eff. weights	-		**5.00e-03**		**0.115**		**0.805**		**1.88**		**9.13**		**7.64**		**13.5**		**11.5**		**44.5**	
Cuts $\mathsf{SR}^{\mathsf{offWZ}}_{\mathsf{high}E_{\mathrm{T}}}$-nj																				
lepton $p_{\mathrm{T}}^{\ell,2,3}$ [GeV]								[>4.5,3]	299										299	
											f				**g**					
$m_{\ell\ell}^{\mathrm{min}}$ [GeV]	[∈ [1, 12]]	1.68	[∈ [12, 15]]	2.44	[∈ [15, 20]]	6.18	[∈ [20, 30]]	19.3	[∈ [30, 40]]	30.8		[∈ [40, 60]]	100			[∈ [60, 75]]	139		299	
m_{T2}^{100} [GeV]	[< 112]	0.253	[< 115]	0.435	[< 120]	1.57	[< 130]	8.73	[< 140]	18.7		[< 160]	89.2			[< 175]	138		257	
$p_{\mathrm{T}}^{\ell_3 > 30\mathrm{GeV}}$	[> 0]	0.203	[> 0]	0.155	[> 0]	0.609	[> 0]	3.84	[> 0]	7.86		[> 0]	35.6			[> 0]	56.7		105	
$E_{\mathrm{T}}^{\mathrm{miss}}$ [GeV]	[> 200]	0.119	[> 200]	7.00e-03	[> 200]	7.40e-02	[> 200]	0.600	[> 200]	0.932		[> 200]	3.78			[> 200]	7.48		13.0	
$E_{\mathrm{T}}^{\mathrm{miss}}$ signif.	[> 3.0]	0.119	[> 3.0]	7.00e-03	[> 3.0]	7.40e-02	[> 3.0]	0.600	[> 3.0]	0.932		[> 3.0]	3.78			[> 3.0]	7.35		12.9	
$p_{\mathrm{T}}^{\mathrm{jet}}/E_{\mathrm{T}}^{\mathrm{miss}}$	[< 0.2]	4.90e-02	[< 0.2]	7.00e-03	[< 0.3]	7.40e-02	[< 0.3]	0.458	[< 0.3]	0.624		[< 1.0]	3.67			[< 1.0]	7.22		12.1	
MC-to-data eff. weights		**4.30e-02**		**8.00e-03**		**8.30e-02**		**0.421**		**0.580**			**3.38**				**6.57**		**11.1**	

Table 5.11: Cutflow for the off-shell WZ event selection for the $(m(\tilde{\chi}_2^0), m(\tilde{\chi}_1^0)) = (250{,}235)$ GeV signal point for the wino/bino (+) scenario. The yields are normalized to a luminosity $\mathcal{L}$ of 139 fb^{-1}. MC-to-data efficiency weights from triggering and from the reconstruction and identification of individual physics objects are applied to the final yields in each signal region. After the initial selections, the table is split in row blocks for the inclusive $\texttt{SR}^{\texttt{offWZ}}_{\texttt{low}\not{E}_\texttt{T}}\texttt{-0j}$, $\texttt{SR}^{\texttt{offWZ}}_{\texttt{low}\not{E}_\texttt{T}}\texttt{-nj}$, $\texttt{SR}^{\texttt{offWZ}}_{\texttt{high}\not{E}_\texttt{T}}\texttt{-0j}$, $\texttt{SR}^{\texttt{offWZ}}_{\texttt{high}\not{E}_\texttt{T}}\texttt{-nj}$ regions, with the individual signal region yields in columns. The inclusive OR of regions a through g2 is given in the last column. Selection details per bin are indicated in bracketed blue as relevant, and the final yields for each signal region is highlighted in bold green at the end of each block. The “3 isolated lepton selection” includes the preselection as described in Section 4.3 and the initial SFOS lepton pair selection.

$\tilde{\chi}_1^\pm\tilde{\chi}_2^0 \to WZ\tilde{\chi}_1^0\tilde{\chi}_1^0$ wino/bino (+)									$m(\tilde{\chi}_2^0,\tilde{\chi}_1^0) = (250, 235)$ GeV										
		a		**b**		**c**		**d**		**e**		**f1**		**f2**		**g1**		**g2**	**a through g2**
Common cuts																			
$\mathcal{L}\times\sigma$										108769									108769
$\mathcal{L}\times\sigma\times$BF										3559									3559
$\mathcal{L}\times\sigma\times$BF $\times$ filt. eff.										992									992
3 isolated lepton selection										40.0									40.0
b-veto										37.4									37.4
Trigger selection										20.4									20.4
$m_{\ell\ell}, m_{\ell\ell}^{\max}$ [GeV]									[< 75]	20.3									20.3
Common cuts $\texttt{SR}^{\texttt{offWZ}}_{\texttt{low}\not{E}_\texttt{T}}$																			
$m_{\ell\ell}^{\min}$ [GeV]		-			[∈ [12, 40]]	7.28							[∈ [40, 75]]	0					7.28
lepton $p_\mathrm{T}^{1,2,3}$ [GeV]		-			[> 10]	2.43							[> 15]	0					2.43
FNP lepton cleaning (conversions)		-				2.22								0					2.22
$m_{\ell\ell}^{\max}$ [GeV]		-			[< 60]	2.06								0					2.06
$m_{\ell\ell}^{\min}$ [GeV]		-	[∈ [12, 15]]	2.04	[∈ [15, 20]]	2.20e-02	[∈ [20, 30]]	0	[∈ [30, 40]]	0	[∈ [40, 60]]	0			[∈ [60, 75]]	0			2.06
m_{T2}^{100} [GeV]		-	[< 115]	1.98	[< 120]	2.20e-02	[< 130]	0		0		0				0			2.00
minΔR		-	[< 1.6]	1.98	[< 1.6]	2.20e-02	[< 1.6]	0		0		0				0			2.00
Cuts $\texttt{SR}^{\texttt{offWZ}}_{\texttt{low}\not{E}_\texttt{T}}\texttt{-0j}$																			
$n_{\mathrm{jets}}^{p_\mathrm{T}>30\,\mathrm{GeV}}$		-	[= 0]	0.829	[= 0]	2.20e-02	[= 0]	0	[= 0]	0	[= 0]	0			[= 0]	0			0.851
$E_\mathrm{T}^{\mathrm{miss}}$ [GeV]		-	[< 50]	0.799	[< 50]	2.20e-02	[< 50]	0	[< 50]	0	[< 50]	0			[< 50]	0			0.821
$E_\mathrm{T}^{\mathrm{miss}}$ signif.		-	[> 1.5]	0.404	[> 1.5]	0	[> 1.5]	0	[> 1.5]	0	[> 1.5]	0			[> 1.5]	0			0.404
$m_{3\ell}$ [GeV]		-		0.404		0		0		0	[> 100]	0			[> 100]	0			0.404
$m_\mathrm{T}^{\mathrm{minmll}}$ [GeV]		-	[< 50]	0.404	[< 50]	0	[< 50]	0	[< 60]	0	[< 60]	0	[> 90]	0	[< 60]	0	[> 90]	0	0.404
$p_\mathrm{T}^{\mathrm{lep}}/E_\mathrm{T}^{\mathrm{miss}}$		-	[< 1.1]	0.321	[< 1.1]	0	[< 1.1]	0	[< 1.3]	0	[< 1.4]	0	[< 1.4]	0	[< 1.4]	0	[< 1.4]	0	0.321
MC-to-data eff. weights		**-**		**0.274**		**0**		**0**		**0**		**0**		**0**		**0**		**0**	**0.274**
Cuts $\texttt{SR}^{\texttt{offWZ}}_{\texttt{low}\not{E}_\texttt{T}}\texttt{-nj}$																			
$n_{\mathrm{jets}}^{p_\mathrm{T}>30\,\mathrm{GeV}}$		-	[> 0]	1.15	[> 0]	0	[> 0]	0	[> 0]	0	[> 0]	0			[> 0]	0			1.15
$E_\mathrm{T}^{\mathrm{miss}}$ [GeV]		-	[< 200]	0.895	[< 200]	0	[< 200]	0	[< 200]	0	[< 200]	0			[< 200]	0			0.895
$E_\mathrm{T}^{\mathrm{miss}}$ signif.		-	[> 3.0]	0.698	[> 3.0]	0	[> 3.0]	0	[> 3.0]	0	[> 3.0]	0			[> 3.0]	0			0.698
$m_\mathrm{T}^{\mathrm{minmll}}$ [GeV]		-	[< 50]	0.356	[< 50]	0	[< 50]	0	[< 60]	0	[< 60]	0	[> 90]	0	[< 60]	0	[> 90]	0	0.356
$p_\mathrm{T}^{\mathrm{lep}}/E_\mathrm{T}^{\mathrm{miss}}$		-	[< 1.0]	0.356	[< 1.0]	0	[< 1.0]	0	[< 1.0]	0	[< 1.2]	0	[< 1.2]	0	[< 1.2]	0	[< 1.2]	0	0.356
MC-to-data eff. weights		**-**		**0.299**		**0**		**0**		**0**		**0**		**0**		**0**		**0**	**0.299**
Cuts $\texttt{SR}^{\texttt{offWZ}}_{\texttt{high}\not{E}_\texttt{T}}\texttt{-0j}$																			
lepton $p_\mathrm{T}^{1,2,3}$ [GeV]									[> 25, 15, 10]	2.73									2.73
$m_{\ell\ell}^{\min}$ [GeV]		-	[∈ [12, 15]]	1.17	[∈ [15, 20]]	2.20e-02	[∈ [20, 30]]	0	[∈ [30, 40]]	0	[∈ [40, 60]]	0			[∈ [60, 75]]	0			1.19
m_{T2}^{100} [GeV]		-	[< 115]	1.16	[< 120]	2.20e-02	[< 130]	0	[< 140]	0	[< 160]	0			[< 175]	0			1.18
$n_{\mathrm{jets}}^{p_\mathrm{T}>30\,\mathrm{GeV}}$		-	[= 0]	0.583	[= 0]	2.20e-02	[= 0]	0	[= 0]	0	[= 0]	0			[= 0]	0			0.605
$E_\mathrm{T}^{\mathrm{miss}}$ [GeV]		-	[> 50]	5.50e-02	[> 50]	0	[> 50]	0	[> 50]	0	[> 50]	0			[> 50]	0			5.50e-02
$E_\mathrm{T}^{\mathrm{miss}}$ signif.		-	[> 3.0]	3.00e-02	[> 3.0]	0	[> 3.0]	0	[> 3.0]	0	[> 3.0]	0			[> 3.0]	0			3.00e-02
$m_\mathrm{T}^{\mathrm{minmll}}$ [GeV]		-	[< 50]	3.00e-02	[< 50]	0	[< 60]	0	[< 60]	0	[< 70]	0	[> 90]	0	[< 70]	0	[> 90]	0	3.00e-02
MC-to-data eff. weights		**-**		**1.20e-02**		**0**		**0**		**0**		**0**		**0**		**0**		**0**	**1.20e-02**
Cuts $\texttt{SR}^{\texttt{offWZ}}_{\texttt{high}\not{E}_\texttt{T}}\texttt{-nj}$																			
lepton $p_\mathrm{T}^{1,2,3}$ [GeV]									[>4.5,3]	20.3									20.3
												f				**g**			
$m_{\ell\ell}^{\min}$ [GeV]	[∈ [1, 12]]	13.0	[∈ [12, 15]]	7.17	[∈ [15, 20]]	0.103	[∈ [20, 30]]	0	[∈ [30, 40]]	0	[∈ [40, 60]]	0			[∈ [60, 75]]	0			20.3
m_{T2}^{100} [GeV]	[< 112]	12.2	[< 115]	6.87	[< 120]	0.103	[< 130]	0	[< 140]	0	[< 160]	0			[< 175]	0			19.1
$n_{\mathrm{jets}}^{p_\mathrm{T}>30\,\mathrm{GeV}}$	[> 0]	7.15	[> 0]	4.37	[> 0]	7.20e-02	[> 0]	0	[> 0]	0	[> 0]	0			[> 0]	0			11.6
$E_\mathrm{T}^{\mathrm{miss}}$ [GeV]	[> 200]	3.98	[> 200]	2.25	[> 200]	7.20e-02	[> 200]	0	[> 200]	0	[> 200]	0			[> 200]	0			6.30
$E_\mathrm{T}^{\mathrm{miss}}$ signif.	[> 3.0]	3.98	[> 3.0]	2.25	[> 3.0]	7.20e-02	[> 3.0]	0	[> 3.0]	0	[> 3.0]	0			[> 3.0]	0			6.30
$p_\mathrm{T}^{\mathrm{lep}}/E_\mathrm{T}^{\mathrm{miss}}$	[< 0.2]	3.95	[< 0.2]	2.22	[< 0.3]	7.20e-02	[< 0.3]	0	[< 0.3]	0	[< 1.0]	0			[< 1.0]	0			6.24
MC-to-data eff. weights		**3.88**		**2.30**		**7.80e-02**		**0**		**0**		**0**				**0**			**6.25**

5.7.3 Usage

In this section, some examples on how data uploaded to HEPData are used for reinterpreting LHC results in terms of new theories will be given. Some tools developed for such reinterpretations make use of simulated events, while others do not, and the two categories of tools use different input from the original analyses. To illustrate this, we will briefly describe one example from each category below.

SModelS

The SModelS Collaboration has developed the SModelS tool [180–182] for interpreting simplified-model results from the LHC. This tool will be briefly described in the following, as a specific example on how the signal acceptances and efficiencies we provide are used by others.

The concept of simplified models was introduced in Section 3.3. Both the ATLAS and CMS collaborations have adopted the approach of using simplified models in supersymmetry searches, and results for a large variety of such simplified models are available. However, how to make use of these results to constrain more complicated BSM theories, both supersymmetric and non-supersymmetric, is not straightforward. The SModelS tool was developed to tackle this challenge.

Figure 5.15 shows a schematic view of the working principle of SModelS. In short, SModelS uses a three-step procedure: First, for a given parameter point in the full BSM theory, the complete set of predicted signal topologies is computed, each with an associated $\sigma \times BR$ value and the set of particle masses involved. Next, this set of possible signals is matched to the set of simplified-model signal topologies that have actually been constrained by different ATLAS and CMS searches. The theory prediction for a given simplified model signal can now be obtained by taking the $\sigma \times BR$ for each contributing signal topology and multiply with its corresponding $A\epsilon$ value, taken from the given mass point in the $A\epsilon$ maps published by the experiments. Finally, this theory prediction can then be directly compared to the cross-section upper limits published by the experiments, to determine if the given parameter point in the full BSM theory has been excluded.

Mapping a complete theory onto the space of simplified-model predictions involves approximations, and the derived exclusions are typically conservative. However, the SModelS approach has the benefit of being computationally cheap, since it does not rely on the explict event generation to compute signal predictions from the BSM theory.

GAMBIT

The GAMBIT Collaboration has developed the GAMBIT software framework [183] for BSM *global fits*, i.e. large-scale BSM parameter-estimation studies which simultaneously subject a given BSM theory to all available experimental constraints. The approach taken in GAMBIT to reinterpret LHC searches is

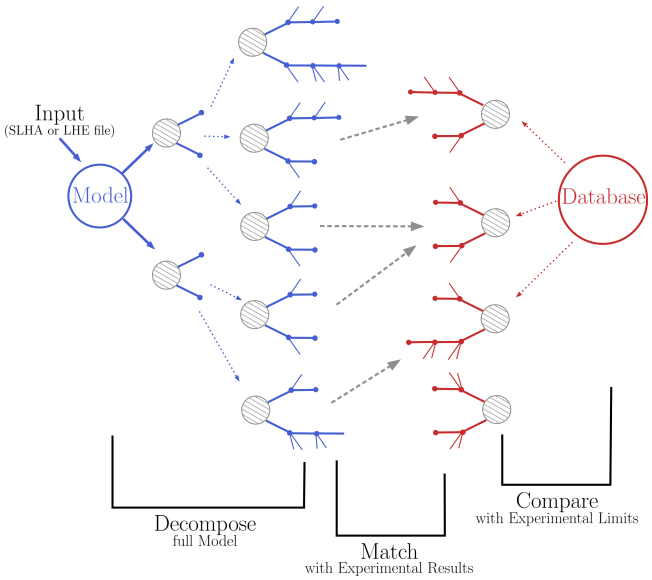

Figure 5.15: Schematic view of the working principle of SModelS [182].

based on direct MC simulations of signal events. At each tested parameter point in a given BSM theory, a set of MC signal events is generated and passed through the event selections of each ATLAS and CMS search that has been implemented in GAMBIT. For each signal region, the fraction of surviving MC signal events is scaled with the luminosity and the theory production cross-section to obtain the predicted number of signal events. This signal prediction is then combined with the background prediction taken from the ATLAS/CMS publication, to compute a likelihood value to be used in the global fit.

Compared to the method used in SModelS, the approach in GAMBIT involves fewer approximations but comes with a much higher computational cost. And since it is based on directly emulating the event selections of the ATLAS and CMS searches, each search implementation in GAMBIT must be validated by reproducing cutflows published by the experiment, using simulations of the same signal model as studied by the experiment. Such cutflows, along with the detailed description in the ATLAS/CMS publication of the event selection procedure, are therefore the key inputs needed to enable the simulation-based reinterpretation approach used in GAMBIT.

5.8 Summary and outlook

This chapter summarized the three-lepton off-shell WZ analysis. We began by introducing the relevant variables used to define the analysis signal regions, before explaining the signal-region design process and describing the final signal regions. I contributed to the optimization of the high-$E_{\mathrm{T}}^{\mathrm{miss}}$ signal regions.

We moved on to briefly describing how the most important backgrounds to the three-lepton final state were estimated, before introducing the concept of systematic uncertainties and briefly discussing the uncertainties considered in the analysis. We then explained the statistical procedure, before presenting the results. Finally, my contribution to preparing input for HEPData to enable reinterpretation of the analysis was summarized. I produced accceptance and efficiency plots, as well as cutflows, for the signal regions.

Since no significant deviation from the Standard Model prediction was found in any of the signal regions, we moved on to setting limits. Model-independent 95% CL upper limits for a generic BSM signal were calculated by testing for discovery, using inclusive discovery regions. The maximum significance Z found was 1.29σ, meaning that the background-only hypothesis could not be rejected for any of the discovery regions. Further, model-dependent 95% CL upper limits were calculated by testing for exclusion, using the nominal signal regions. Resulting exclusion limits were shown for the wino/bino (+), wino/bino (−) and higgsino interpretations for the three-lepton off-shell WZ analysis alone, and also for statistical combinations of the results for the three-lepton off-shell WZ, the three-lepton on-shell WZ analysis, and the compressed two-lepton analysis presented in Ref. [173]. The obtained exclusion limits extended previous results by a large margin. Figure 5.16 shows summary exclusion plots prepared by the ATLAS Collaboration for the wino/bino (+) interpretation, before and after the addition of the three-lepton analysis.

Note that the results of the three-lepton analysis could further evolve for different assumptions and/or analysis designs. For instance, the simplified-model scenarios used in the analysis assume specific gaugino mixes and 100% branching ratios. Using different assumptions would change the visible cross-sections for the processes in question and consequently also the results. Further, the conventional *cut-and-count* method is used in the three-lepton analysis. Instead using more novel analysis techniques, such as machine learning, could affect the results. A few more improvement examples specific to the off-shell WZ analysis will be mentioned in the following. First, as described in 5.3, the phase space of control and validation regions should be close to the phase space of the signal regions, but with as little signal contamination as possible. However, the control regions for the dominant Standard Model WZ background selects on-shell W and Z bosons, due to orthogonality restrictions and limited possibilities in terms of phase space. Designing new, off-shell control regions would probably improve the estimates for this background. Second, as described in Section 4.3, events are triggered mostly using lepton triggers. However, to target signals with more compressed mass spectra, the selection is complemented with events with softer leptons using $E_{\mathrm{T}}^{\mathrm{miss}}$ triggers in $\mathrm{SR}^{\mathrm{offWZ}}_{\mathrm{high}E_{\mathrm{T}}}$-nj. To increase the sensitivity for compressed signals also in the other signal regions, a specialized trigger could be developed.

In the next chapter, two different studies based on the three-lepton off-shell WZ analysis will be presented, conducted in preparation for future runs of the Large Hadron Collider.

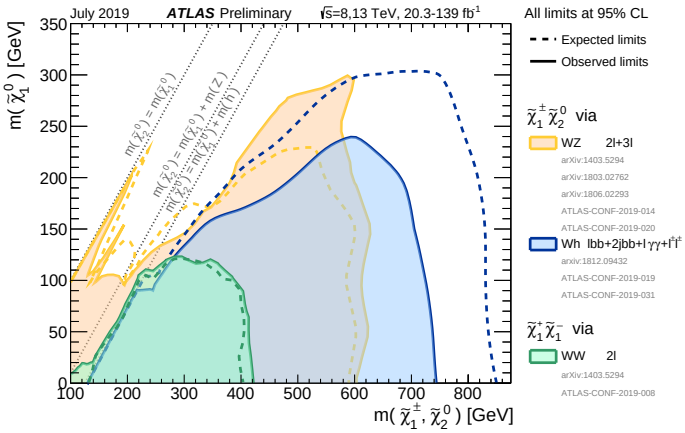

(a)

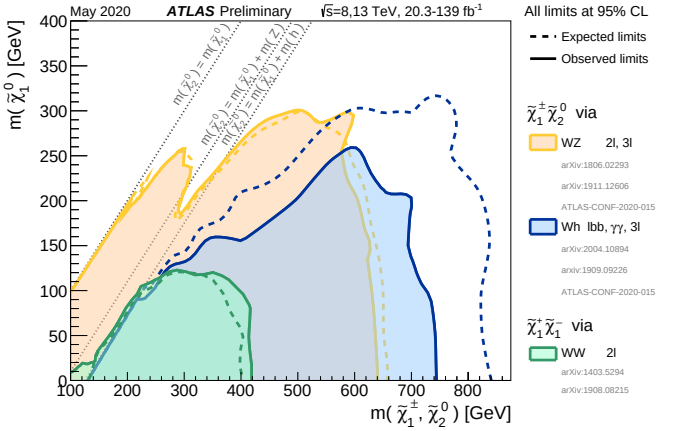

(b)

Figure 5.16: Summary exclusion plots prepared by the ATLAS Collaboration for the wino/bino (+) interpretation, (a) before and (b) after the addition of the three-lepton analysis (shown as "ATLAS-CONF-2020-015" in the lower plot).

Chapter 6

Preparing for future LHC runs

The three-lepton off-shell WZ analysis presented in the previous chapter also forms the basis for a couple of studies I have conducted in preparation for future runs of the Large Hadron Collider, which will be summarized in this chapter. First, Section 6.1 summarizes a study of the impact of reducing the $E_{\mathrm{T}}^{\mathrm{miss}}$ trigger threshold from 210 GeV to 160 GeV, considered for the High-Luminosity LHC.[1] Second, Section 6.2 summarizes a simple validation study of the new DAOD format prepared for Run 3 of the LHC.[2] Only the wino/bino (+) interpretation is considered for these studies.

6.1 $E_{\mathrm{T}}^{\mathrm{miss}}$ trigger threshold study for the HL-LHC

The LHC schedule was discussed in Section 2.4. During the third long shutdown, from 2026 until 2028, the LHC and its experiments will be heavily upgraded to enter into the era of the High-Luminosity LHC (HL-LHC). All aspects of this massive upgrade must be planned well ahead. In 2020, the ATLAS Collaboration set up a process to decide on the baseline configuration of the *trigger architecture* during the HL-LHC operations in Run 4 and beyond. This section will present a study concerning the decision on the final hardware architecture: either a single-level trigger configuration (similar to the Run 2 configuration, referred to as "L0-only"), or a two-level trigger configuration based on hardware tracking at level 1 (referred to as "L0/L1"). The decision between the two options relied on multiple factors: physics gain, technical feasibility and risk, human and financial resources, and commitments of funding agencies. Thus, the combined effort to reach a conclusion spanned across several ATLAS systems, upgrade projects and activities. Focusing on the physics, the L0/L1 option would enhance the acceptance of interesting physics signals. However, as this option would be more complex and expensive, the physics gain for key physics signatures had to be carefully scrutinized.

One of the advantages of choosing the L0/L1 option would be that the *offline* $E_{\mathrm{T}}^{\mathrm{miss}}$ *trigger threshold* could be lowered. Triggers have a turn-on curve before they reach a plateau at which they are 100% efficient. To ensure full efficiency, an offline trigger threshold (cut) is applied. For Run 2, the offline $E_{\mathrm{T}}^{\mathrm{miss}}$ trigger threshold was 200–210 GeV, depending on the period. For Run 4, the L0 option would give a similar threshold of 210 GeV. The L0/L1 option, on the other hand, would allow for lowering the threshold to 160 GeV.

As described in Section 4.3, the primary triggers used to select events for the three-lepton off-shell WZ analysis are single-, di- and tri-lepton triggers.

[1] This study was carried out together with Sara Alderweireldt.
[2] This study was carried out together with Eirik Gramstad.

However, for the high-$E_{\mathrm{T}}^{\mathrm{miss}}$ signal regions, the selection is complemented with events with softer leptons using $E_{\mathrm{T}}^{\mathrm{miss}}$ triggers, see Table 5.1. The $E_{\mathrm{T}}^{\mathrm{miss}}$ trigger threshold thus has an impact on the analysis results for these regions. In relation to the decision process described above, the analysis team for the three-lepton off-shell WZ analysis was contacted by the ATLAS SUSY upgrade contact[3] and TDAQ experts, who wanted to know if and how much the analysis would gain from lowering the $E_{\mathrm{T}}^{\mathrm{miss}}$ trigger threshold to 160 GeV. They were particularly interested in results for the compressed signal regions, where lepton triggers are harder to make use of due to soft leptons.

6.1.1 Impact of lowering the $E_{\mathrm{T}}^{\mathrm{miss}}$ trigger threshold for the three-lepton off-shell WZ analysis

To investigate the impact of lowering the $E_{\mathrm{T}}^{\mathrm{miss}}$ trigger threshold for the three-lepton off-shell WZ analysis, we perform a simple study not taking into account the extra luminosity of the HL-LHC. Only the inclusive $\mathtt{SR}^{\mathtt{offWZ}}_{\mathtt{high}\not{E}_{\mathrm{T}}}\mathtt{-nj}$ signal region is considered, as this is the only region targeting both highly and moderately compressed mass spectra ($\Delta m(\tilde{\chi}_2^0, \tilde{\chi}_1^0) \lesssim 40$ GeV). As seen in Table 5.2, the most compressed signal region, designed for signals with $\Delta m < 12$ GeV, is only covered by $\mathtt{SR}^{\mathtt{offWZ}}_{\mathtt{high}\not{E}_{\mathrm{T}}}\mathtt{-nj}$.

Five different variations of $\mathtt{SR}^{\mathtt{offWZ}}_{\mathtt{high}\not{E}_{\mathrm{T}}}\mathtt{-nj}$ are compared, summarized in Table 6.1. Variation I is the original $\mathtt{SR}^{\mathtt{offWZ}}_{\mathtt{high}\not{E}_{\mathrm{T}}}\mathtt{-nj}$ selection, with an $E_{\mathrm{T}}^{\mathrm{miss}}$ threshold of 200 GeV.[4] The only change for variation II is that the $E_{\mathrm{T}}^{\mathrm{miss}}$ threshold is lowered to 160 GeV. Variation IV is the same as variation II, but with an additional simple reoptimization of the $|\mathbf{p}_{\mathrm{T}}^{\mathrm{lep}}|/E_{\mathrm{T}}^{\mathrm{miss}}$ thresholds per $m_{\ell\ell}^{\mathrm{min}}$ bin. As explained in Section 5.2.1, upper bounds on the $|\mathbf{p}_{\mathrm{T}}^{\mathrm{lep}}|/E_{\mathrm{T}}^{\mathrm{miss}}$ variable are introduced as signals tend to populate lower parts of the spectrum for this variable than Standard Model backgrounds, in particular compressed signals in the high-$E_{\mathrm{T}}^{\mathrm{miss}}$ regions. In variation IV, these upper bounds are tightened for most $m_{\ell\ell}^{\mathrm{min}}$ bins of $\mathtt{SR}^{\mathtt{offWZ}}_{\mathtt{high}\not{E}_{\mathrm{T}}}\mathtt{-nj}$, to recover the signal-to-background ratio after lowering the $E_{\mathrm{T}}^{\mathrm{miss}}$ threshold (effectively increasing the total SM background yield). The reoptimized (original) upper bounds on $|\mathbf{p}_{\mathrm{T}}^{\mathrm{lep}}|/E_{\mathrm{T}}^{\mathrm{miss}}$ are 0.1 (0.2), 0.15 (0.2), 0.2 (0.3), 0.3 (0.3), 0.3 (0.3), 0.6 (1.0) and 0.8 (1.0) for $m_{\ell\ell}^{\mathrm{min}}$ bins a, b, c, d, e, f and g, respectively. Finally, variations III and V are the same as variations II and IV, respectively, but also removing the overlap with the lepton-triggered selection in the original $\mathtt{SR}^{\mathtt{offWZ}}_{\mathtt{low}\not{E}_{\mathrm{T}}}\mathtt{-nj}$ region, to assess the unique acceptance gain from the lowered $E_{\mathrm{T}}^{\mathrm{miss}}$ trigger threshold.[5]

[3] This contact is appointed to aid and coordinate the prospects of supersymmetry searches in future phases of LHC data-taking.

[4] At the time of the analysis, the recommended offline $E_{\mathrm{T}}^{\mathrm{miss}}$ trigger threshold was 210 GeV. However, after evaluating the $E_{\mathrm{T}}^{\mathrm{miss}}$ trigger turn-on for a relevant selection, the efficiencies were confirmed to reach the plateau for $E_{\mathrm{T}}^{\mathrm{miss}} > 200$ GeV, with excellent data/MC agreements.

[5] Note that the term "acceptance" here does not refer to the truth-level acceptance defined in Eq. (5.17).

Table 6.1: The five variations of the inclusive $\mathtt{SR}^{\mathtt{offWZ}}_{\mathtt{high}E_{\mathrm{T}}}\mathtt{-nj}$ signal region compared in this simple study assessing the impact of lowering the $E_{\mathrm{T}}^{\mathrm{miss}}$ trigger threshold to 160 GeV. The original selection criteria are listed in Table 5.2.

$\mathtt{SR}^{\mathtt{offWZ}}_{\mathtt{high}E_{\mathrm{T}}}\mathtt{-nj}$ variations	
I	original selection, with $E_{\mathrm{T}}^{\mathrm{miss}} > 200$ GeV
II	I, but lowering to $E_{\mathrm{T}}^{\mathrm{miss}} > 160$ GeV
III	II + removing overlap with original $\mathtt{SR}^{\mathtt{offWZ}}_{\mathtt{low}E_{\mathrm{T}}}\mathtt{-nj}$ (lepton trigger & $E_{\mathrm{T}}^{\mathrm{miss}} \in [160,200]$ GeV)
IV	II + simple reoptimization of $\lvert\mathbf{p}_{\mathrm{T}}^{\mathrm{lep}}\rvert/E_{\mathrm{T}}^{\mathrm{miss}}$ thresholds per $m_{\ell\ell}^{\mathrm{min}}$ bin
V	IV + removing overlap with original $\mathtt{SR}^{\mathtt{offWZ}}_{\mathtt{low}E_{\mathrm{T}}}\mathtt{-nj}$

Acceptance gain

Figure 6.1 shows the total background yield and the yield per background group for all five variations of the $\mathtt{SR}^{\mathtt{offWZ}}_{\mathtt{high}E_{\mathrm{T}}}\mathtt{-nj}$ region. The upper part of Table 6.2 lists the corresponding values including statistical uncertainties. We see that the acceptance gain from variation I to variation II is more than 90% for the total background. After also removing the overlap with the lepton-triggered selection in the original $\mathtt{SR}^{\mathtt{offWZ}}_{\mathtt{low}E_{\mathrm{T}}}\mathtt{-nj}$ region (variation III), there is still 50% unique acceptance gain. Further, we see that the acceptance increase is similar for all background groups. Note that we are using the MC-simulated Z+jets sample for this study, rather than the data-driven estimate used in the published analysis, overestimating this contribution. For single-top processes in the "Others" group, the increase is slightly larger, but this is not major a background.

Figure 6.2 shows signal yields for all variations. The lower part of Table 6.2 shows the corresponding values including statistical uncertainties for a selection of signal points. The $\mathtt{SR}^{\mathtt{offWZ}}_{\mathtt{high}E_{\mathrm{T}}}\mathtt{-nj}$ region contributes most for smaller Δm ($\Delta m < 20$ GeV). For larger Δm (harder leptons), the acceptance gain overlaps with lepton-triggered selection in the original $\mathtt{SR}^{\mathtt{offWZ}}_{\mathtt{low}E_{\mathrm{T}}}\mathtt{-nj}$ region (orange and purple lines in Figure 6.2). For smaller Δm, the acceptance gain is more unique (green and pink lines i Figure 6.2). This gain would probably increase with a dedicated reoptimization of the $\mathtt{SR}^{\mathtt{offWZ}}_{\mathtt{low}E_{\mathrm{T}}}\mathtt{-nj}$ and $\mathtt{SR}^{\mathtt{offWZ}}_{\mathtt{high}E_{\mathrm{T}}}\mathtt{-nj}$ selection criteria, and the $E_{\mathrm{T}}^{\mathrm{miss}}$ boundary between them.

Table 6.2: Background and signal yields for all five variations of the inclusive $\mathrm{SR}^{\mathrm{offWZ}}_{\mathrm{high}\not{E}_{\mathrm{T}}}$-nj region defined in Table 6.1. The "Others" group contains the single-top, WW, Higgs and rare top processes. The signal points in the lower part of the table are on the form $(m(\tilde{\chi}_2^0), m(\tilde{\chi}_1^0))$ GeV. All uncertainties are statistical only.

	$\mathrm{SR}^{\mathrm{offWZ}}_{\mathrm{high}\not{E}_{\mathrm{T}}}$-nj variation				
	I	II	III	IV	V
Z+jets	0.52 ± 0.21	1.17 ± 0.36	0.99 ± 0.30	0.94 ± 0.33	0.84 ± 0.28
WZ	18.75 ± 0.54	33.91 ± 0.75	26.31 ± 0.66	24.12 ± 0.61	18.23 ± 0.52
ZZ	0.24 ± 0.03	0.52 ± 0.05	0.39 ± 0.04	0.38 ± 0.04	0.28 ± 0.03
$t\bar{t}$	11.74 ± 1.15	23.21 ± 1.57	18.16 ± 1.41	20.83 ± 1.49	16.53 ± 1.36
$t\bar{t}$+X	1.10 ± 0.09	2.28 ± 0.14	1.66 ± 0.11	1.77 ± 0.12	1.24 ± 0.10
triboson	0.78 ± 0.10	1.15 ± 0.13	0.84 ± 0.11	0.97 ± 0.11	0.73 ± 0.10
Others	2.24 ± 0.42	5.24 ± 0.78	4.06 ± 0.69	4.63 ± 0.75	3.70 ± 0.68
Total bkg	35.35 ± 1.36	67.57 ± 1.94	52.39 ± 1.74	53.70 ± 1.82	41.54 ± 1.63
(150, 140)	10.07 ± 0.73	15.91 ± 0.94	15.74 ± 0.93	10.79 ± 0.77	10.66 ± 0.76
(150, 120)	32.48 ± 2.63	49.81 ± 3.27	40.55 ± 2.94	42.21 ± 3.02	34.47 ± 2.74
(150, 100)	24.76 ± 2.22	43.45 ± 2.99	31.37 ± 2.53	38.58 ± 2.81	28.11 ± 2.40
(150, 70)	27.34 ± 1.90	45.70 ± 2.49	31.79 ± 2.06	37.04 ± 2.24	26.58 ± 1.90
(250, 240)	2.84 ± 0.24	3.93 ± 0.27	3.82 ± 0.27	3.32 ± 0.26	3.23 ± 0.25
(250, 220)	10.57 ± 0.58	15.11 ± 0.71	13.46 ± 0.67	12.78 ± 0.65	11.34 ± 0.62
(250, 200)	10.59 ± 0.62	15.91 ± 0.77	12.23 ± 0.65	15.01 ± 0.74	11.43 ± 0.64
(250, 170)	11.49 ± 0.70	17.40 ± 0.86	12.50 ± 0.73	15.85 ± 0.84	11.71 ± 0.72
(100, 60)	42.89 ± 3.85	68.88 ± 4.84	54.04 ± 4.29	60.16 ± 4.54	46.13 ± 3.99
(200, 160)	18.21 ± 0.91	27.51 ± 1.12	21.96 ± 0.99	25.73 ± 1.09	20.44 ± 0.96
(300, 260)	6.39 ± 0.37	9.36 ± 0.46	7.73 ± 0.40	8.26 ± 0.42	6.90 ± 0.39
(400, 360)	2.44 ± 0.13	3.65 ± 0.17	3.04 ± 0.16	3.37 ± 0.17	2.73 ± 0.14
(100, 20)	37.36 ± 3.44	73.01 ± 4.69	46.03 ± 3.80	54.96 ± 4.03	34.38 ± 3.21
(200, 120)	18.01 ± 1.02	28.90 ± 1.29	19.74 ± 1.08	26.04 ± 1.25	18.20 ± 1.05
(300, 220)	6.84 ± 0.44	10.58 ± 0.56	7.39 ± 0.46	9.75 ± 0.53	6.89 ± 0.44
(400, 320)	2.65 ± 0.16	3.99 ± 0.20	2.84 ± 0.16	3.71 ± 0.18	2.73 ± 0.14

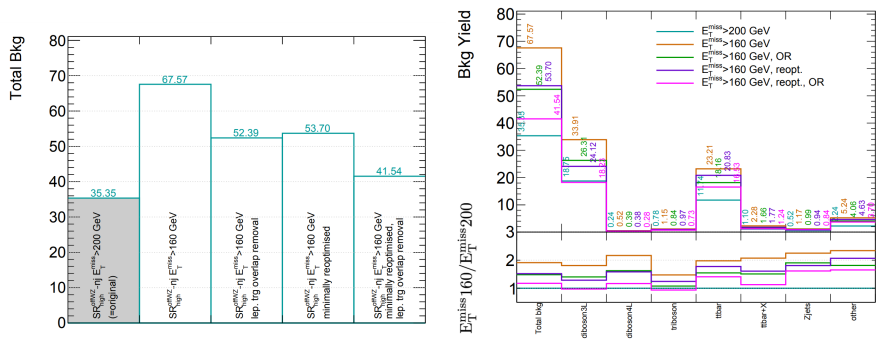

(a) (b)

Figure 6.1: The (a) total background yields and (b) yields per background group for all five variations of the $\mathtt{SR}^{\mathtt{offWZ}}_{\mathtt{high}E_{\mathrm{T}}}\mathtt{-nj}$ signal region listed in Table 6.1. The lower panel of (b) shows the yield ratio of variations II–V to the original selection with an $E_{\mathrm{T}}^{\mathrm{miss}}$ threshold of 200 GeV, i.e. variation I. The "diboson3L" and "diboson4L" entries correspond to WZ and ZZ, respectively, while the "other" group contains the single-top, WW, Higgs and rare top processes.

Significance gain

For this study, the expected significance is estimated using the heuristic BinomialExpZ function introduced in Section 5.2.1.[6] A flat (constant) 20% systematic background uncertainty is applied, i.e. $\Delta b/b = 0.20$. Figure 6.3 shows a direct comparison of the 95% CL exclusion limits based on Z_N for all five variations of the $\mathtt{SR}^{\mathtt{offWZ}}_{\mathtt{high}E_{\mathrm{T}}}\mathtt{-nj}$ region.[7] Comparing the exclusion limits for variations I (black line) and II (orange line), we see that there is no improvement in significance. The increased acceptance we saw includes events overlapping with the lepton-triggered $\mathtt{SR}^{\mathtt{offWZ}}_{\mathtt{low}E_{\mathrm{T}}}\mathtt{-nj}$ selection. For variation IV (purple line), still without overlap removal with the $\mathtt{SR}^{\mathtt{offWZ}}_{\mathtt{low}E_{\mathrm{T}}}\mathtt{-nj}$ selection, but with a minimal reoptimization of the $|\mathbf{p}_{\mathrm{T}}^{\mathrm{lep}}|/E_{\mathrm{T}}^{\mathrm{miss}}$ thresholds, we see an improvement at higher Δm. However, this is a migration from $\mathtt{SR}^{\mathtt{offWZ}}_{\mathtt{low}E_{\mathrm{T}}}\mathtt{-nj}$, and as stated above for the acceptance gain, the combined selection would need to be reoptimized. For variation III and V (green and pink lines), with overlap removal, we see an improvement at low Δm due to the new, unique events.

Further, Figure 6.4 shows heatmaps of significance values together with the exclusion limits for variations I, III and V. Comparing the plots for variations I and III, we see that there is a significance gain at low $m(\tilde{\chi}_2^0)$, but that it quickly drops with increasing $m(\tilde{\chi}_2^0)$. Instead comparing the plots for variations I and V, we see a small significance gain at lowest Δm. This is a promising result, as the

[6] Using this simple Z_N calculation typically gives slightly stronger exclusion limits compared to doing a full statistical analysis

[7] Where the significances obtained for each $m_{\ell\ell}^{\mathrm{min}}$ bin of $\mathtt{SR}^{\mathtt{offWZ}}_{\mathtt{high}E_{\mathrm{T}}}\mathtt{-nj}$ have been added in quadrature to obtain a total $\mathtt{SR}^{\mathtt{offWZ}}_{\mathtt{high}E_{\mathrm{T}}}\mathtt{-nj}$ significance for each signal point.

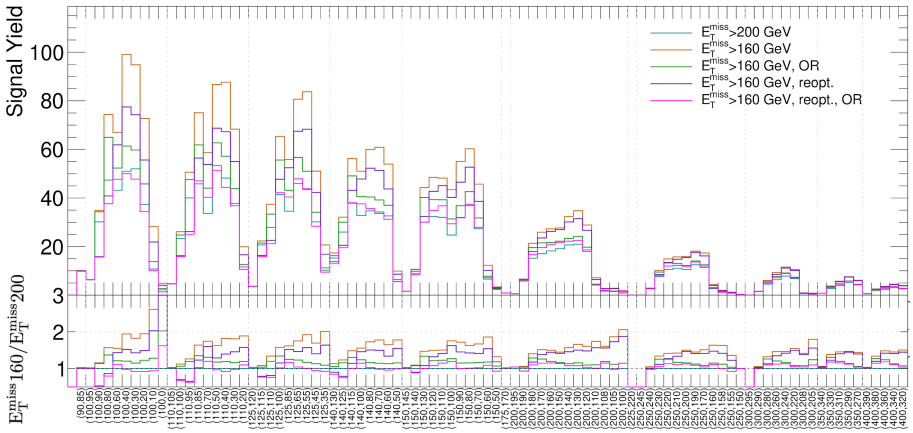

Figure 6.2: Yields per signal point $(m(\tilde{\chi}_2^0), m(\tilde{\chi}_1^0))$ GeV for all five variations of the $\mathtt{SR}^{\mathtt{offWZ}}_{\mathtt{high}\not{E}_{\mathrm{T}}}\mathtt{-nj}$ signal region listed in Table 6.1. The signal points are ordered by $m(\tilde{\chi}_2^0)$ and Δm. The lower panel shows the yield ratio of variations II–V to the original selection with an $E_{\mathrm{T}}^{\mathrm{miss}}$ threshold of 200 GeV, i.e. variation I.

$\Delta m = 5$–15 GeV region is where we would need improvement to "close the gap" between the three-lepton off-shell WZ analysis and the compressed two-lepton analysis presented in Ref. [173], see Figure 5.11(b).

Conclusion

We have studied the impact of lowering the $E_{\mathrm{T}}^{\mathrm{miss}}$ threshold from 200 GeV to 160 GeV for the inclusive $\mathtt{SR}^{\mathtt{offWZ}}_{\mathtt{high}\not{E}_{\mathrm{T}}}\mathtt{-nj}$ signal region of the three-lepton off-shell WZ analysis, without making any other major changes to the selection requirements. In conclusion, lowering the threshold gives significant acceptance gains for signal assuming Run 2 luminosity, but of course also increases the background. However, without dedicated reoptimization to make optimal use of the low-$E_{\mathrm{T}}^{\mathrm{miss}}$ events, and after accounting for overlap with other signal regions, the significance in the region with low Δm is improved by up to 30%, as can be seen in Figure 6.5. This region is of particular interest, as a mass difference of $\mathcal{O}(10$ GeV$)$ gives co-annihilation in the early universe and thus predicts the observed relic density of dark matter, and has not yet been excluded. Further, covering this region also allows closing the sensitivity gap in parameter space between the three-lepton off-shell WZ analysis and the compressed two-lepton analysis.[8]

[8]The effect of lowering the $E_{\mathrm{T}}^{\mathrm{miss}}$ trigger threshold has also been considered for the compressed two-lepton analysis, for which the assessment was that this analysis would not benefit from a lower $E_{\mathrm{T}}^{\mathrm{miss}}$ threshold out-of-the-box. Improving the combined exclusion contour from the three-lepton off-shell WZ analysis side thus becomes even more important.

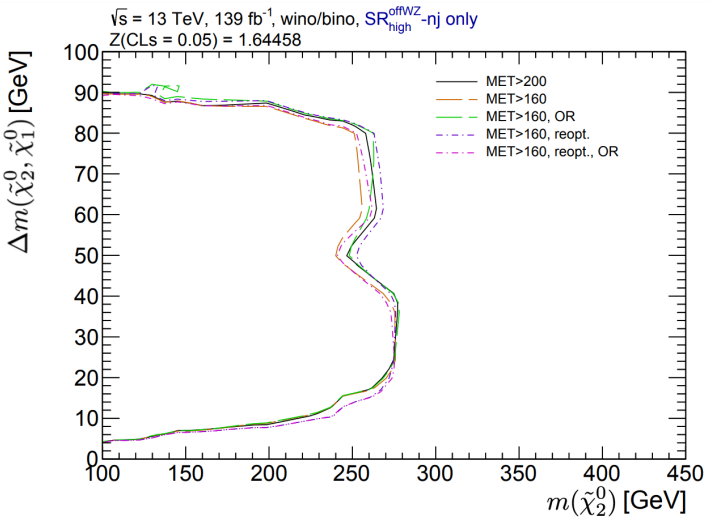

Figure 6.3: Direct comparison of 95% CL exclusion limits for all five variations of the $\mathrm{SR}^{\mathrm{offWZ}}_{\mathrm{high}E_{\mathrm{T}}}$-nj signal region listed in Table 6.1. "MET" in the legends refers to missing transverse momentum $E_{\mathrm{T}}^{\mathrm{miss}}$.

6.1.2 Final decision on the ATLAS trigger architecture for HL-LHC

The simple study presented here shows that the three-lepton off-shell WZ analysis would gain from lowering the $E_{\mathrm{T}}^{\mathrm{miss}}$ threshold to 160 GeV, which would be possible if choosing the L0/L1 option for the ATLAS hardware trigger architecture from Run 4 onwards. However, other studies of physics gains for this option did not show as promising results. Taking into account multiple other considerations such as cost and complexity, the final decision was to go for the L0-only option [184].

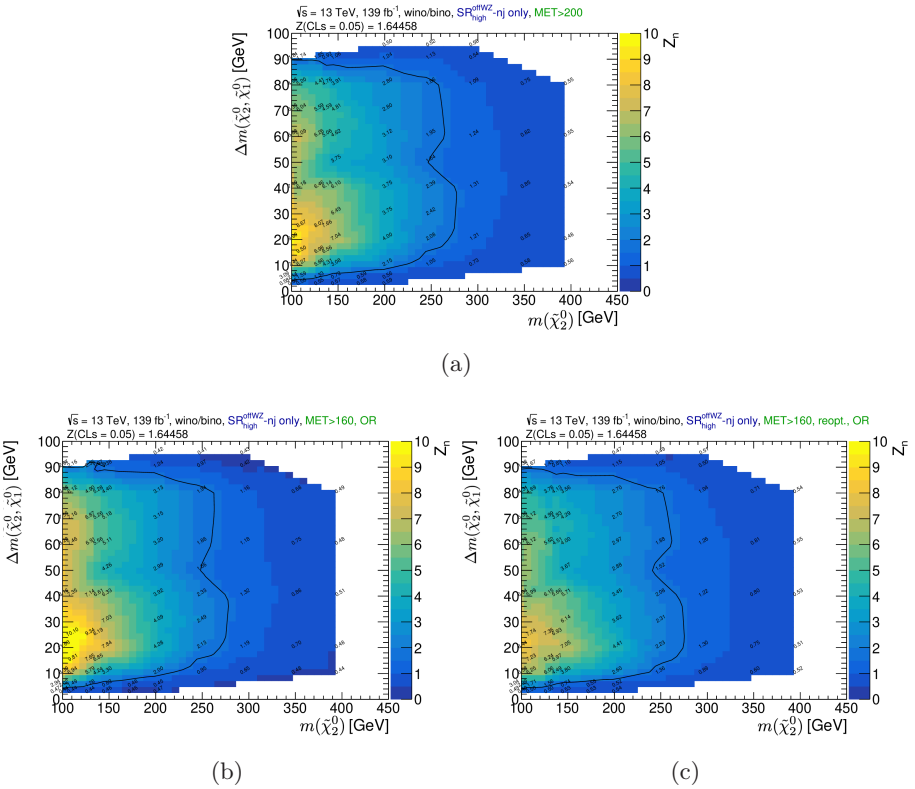

Figure 6.4: Heatmaps of significance values together with 95% CL exclusion limits for variations (a) I, (b) III, and (c) V of the $\mathtt{SR}^{\mathtt{offWZ}}_{\mathtt{high}\vec{E}_{\mathrm{T}}}\mathtt{-nj}$ signal region listed in Table 6.1. The "MET" in the plot titles refers to missing transverse momentum $E_{\mathrm{T}}^{\mathrm{miss}}$.

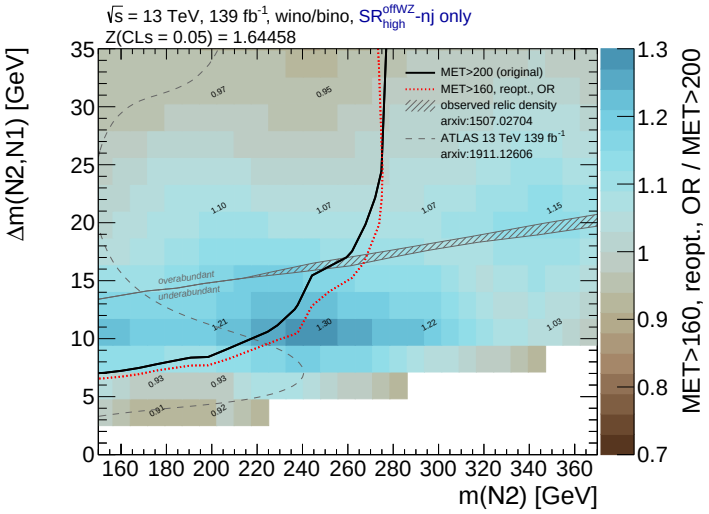

Figure 6.5: Impact of reduced $E_{\mathrm{T}}^{\mathrm{miss}}$ threshold on the significance for the inclusive $\mathrm{SR}^{\mathrm{offWZ}}_{\mathrm{high}E_{\mathrm{T}}}$-nj region of the three-lepton off-shell WZ analysis. The colorbar shows the relative impact on significance as function of $\Delta m(\tilde{\chi}_2^0, \tilde{\chi}_1^0)$ and $m(\tilde{\chi}_2^0)$. "MET" refers to missing transverse momentum $E_{\mathrm{T}}^{\mathrm{miss}}$, while "N2" and "N1" correspond to $\tilde{\chi}_2^0$ and $\tilde{\chi}_1^0$, respectively. The solid black and dotted red contours indicate the exclusion limits for the two $E_{\mathrm{T}}^{\mathrm{miss}}$ thresholds (variations I and V), but the analysis has not been reoptimized to make better use of the low-$E_{\mathrm{T}}^{\mathrm{miss}}$ events. The observed relic density of dark matter (hatched gray area) and the exclusion limit for the compressed two-lepton analysis (dashed gray line) are also shown.

6.2 Validation study of new Run 3 DAOD format

The concept of derived AODs, or DAODs, was introduced at the end of Section 4.1.1, where it was stated that DAOD formats with different subsets of the data (simulated and real) are produced centrally in the ATLAS Collaboration, and that each format is often used by multiple, similar analyses. This was the case for Run 2 of the LHC. More specifically, around 100 different DAOD formats, tailored to different analyses, were prepared in Run 2. Although this was a successful analysis model from the perspective of most analysts, the Run 2 model took up too much disk space. The total size of DAODs ended up being larger than originally planned, and many of the formats had very similar content on an event-by-event basis, as most analyses need the same subset of variables.

Thus, for Run 3, a new analysis model has been deployed. As many analyses as possible will use the same DAOD format, containing the subset of variables most analyses need. This baseline format has been named "DAOD_PHYS", and targets at least 80% of the analyses. It is unskimmed, meaning that no events have been fully removed. Further, it contains the full set of high-level objects and variables per event needed by all ATLAS analysis tools. Instead, by removing many of the collections and objects not needed by most, such as inner-detector tracks, trigger objects and (for MC) the full truth record, the final format size ends up being within the acceptable level of 50 kB per event.[9] For the analysts, the "look and feel" of DAOD_PHYS is the same as the Run 2 DAOD formats.

However, before moving to this new format, it must be carefully validated. In this section, a small validation study based on the three-lepton off-shell WZ analysis will be presented.

6.2.1 DAOD_PHYS and DAOD_SUSY2 comparison

For the original three-lepton off-shell WZ analysis, ntuples were made from a combination of the DAOD_SUSY2 and DAOD_SUSY16 formats.[10] The SUSY2 format, used in multiple electroweak SUSY analyses, contains events with at least two leptons with $p_{\mathrm{T}} > 9$ GeV, or at least one lepton with $p_{\mathrm{T}} > 25$ GeV and at least one photon with $p_{\mathrm{T}} > 40$ GeV. The SUSY16 format was added to also include softer leptons for the most compressed signal regions. This format, prepared for the compressed two-lepton analysis presented in Ref. [173], contains events with at least two leptons with $p_{\mathrm{T}} > 4$ GeV (2.5 GeV) for electrons (muons).

For the validation study presented here, we produced two sets of new ntuples using the ntuple production framework set up for the three-lepton off-shell WZ analysis. One set using the Run 2 SUSY2 format as input, and one set using the

[9] Some Run 2 DAOD formats will have to be retained for special analyses, such as those requiring additional tracking information (especially B-physics and long-lived particle searches), and for so-called *performance groups* who require additional variables for deriving calibrations and associated systematic uncertainties.

[10] For simplicity, the prefix "DAOD_" for the formats will be omitted in the following.

new PHYS format as input. For simplicity, we only produced ntuples for period K of the 2018 data,[11] some selected supersymmetry signal samples and the triboson Standard Model background sample. Since the SUSY2 format already apply a tighter event and object selection than the unskimmed PHYS format, the content of the ntuples cannot be compared directly. Instead, we compare the ntuples after applying a selection of exactly three baseline and exactly three signal leptons, using the lepton selection criteria listed in Table 4.3.

Figures 6.6, 6.7 and 6.8 show distributions for variables $p_{\mathrm{T}}^{\ell_1}$, $p_{\mathrm{T}}^{\ell_2}$ and $E_{\mathrm{T}}^{\mathrm{miss}}$, respectively, for period K of the 2018 data. The plots show direct comparisons of the distributions for the PHYS and SUSY2 ntuples, for electrons and muons separately. As seen in all three figures, the distributions for the two formats agree nicely for electrons. For muons, however, there is a discrepancy.[12] To investigate this difference, we carefully studied the "extra" SUSY2 events compared to PHYS, and realized that the discrepancy was due to a difference in the so-called *trigger-matching* of low-p_{T} muons for the two formats.

6.2.2 Trigger-matching in DAOD_PHYS

Trigger-matching means matching objects on trigger level, i.e. objects used by the trigger software, to "offline", reconstructed objects. In many cases, knowing the trigger decision itself is sufficient, i.e. knowing which trigger triggered a

[11] Events in a given data period share common data-taking conditions, like *trigger menu*, LHC conditions, etc.

[12] The same is seen in corresponding comparison plots for the MC ntuples, but the discrepancy is most prominent for data.

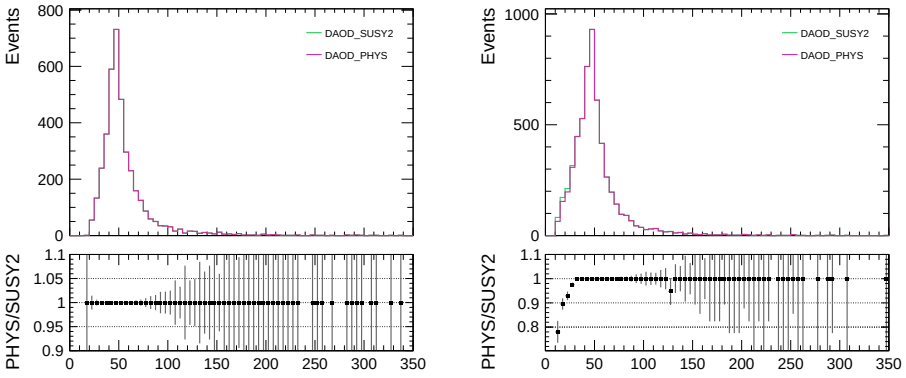

Figure 6.6: Comparison of $p_{\mathrm{T}}^{\ell_1}$ distributions for the PHYS and SUSY2 ntuples for period K of the 2018 data, after selecting exactly three baseline and exactly three signal leptons, for (a) electrons and (b) muons separately.

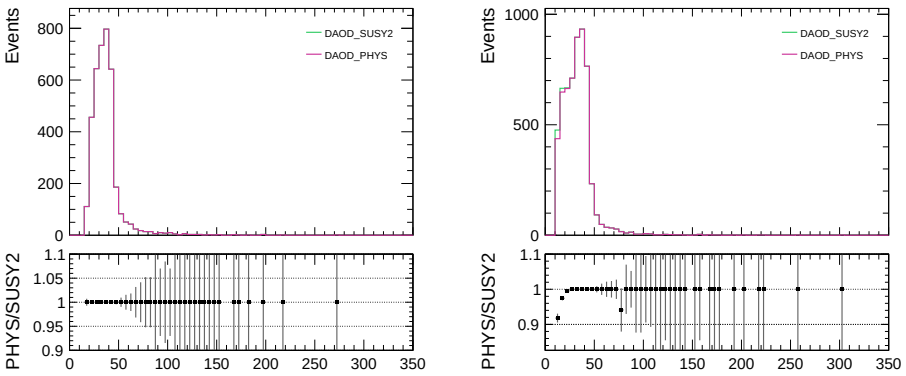

(a) (b)

Figure 6.7: Comparison of $p_{\mathrm{T}}^{\ell_2}$ distributions for the PHYS and SUSY2 ntuples for period K of the 2018 data, after selecting exactly three baseline and exactly three signal leptons, for (a) electrons and (b) muons separately.

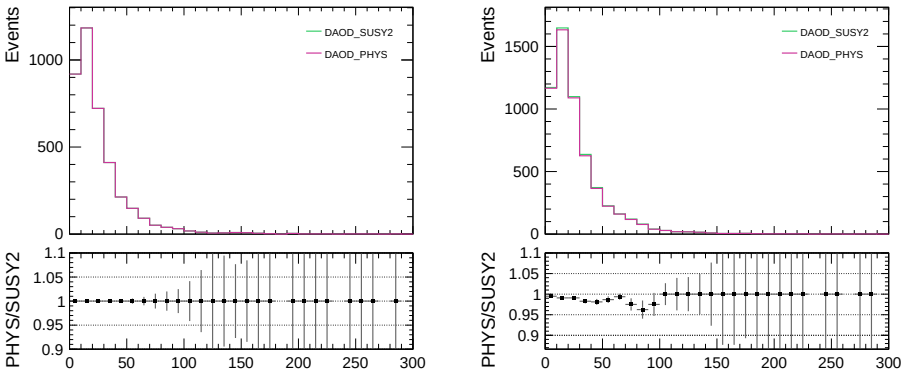

(a) (b)

Figure 6.8: Comparison of $E_{\mathrm{T}}^{\mathrm{miss}}$ distributions for the PHYS and SUSY2 ntuples for period K of the 2018 data, after selecting exactly three baseline and exactly three signal leptons, for (a) electrons and (b) muons separately.

particular event. For some purposes, however, it is necessary to know exactly which of the reconstruced objects fired the trigger.

In the Run 2 DAOD formats, the trigger objects are included. This means that the matching of trigger objects to the corresponding reconstructed objects can be performed with dedicated software at DAOD level. For the new PHYS format, the trigger objects are removed, reducing the file size by approximately

50 kB per event. Instead, this information is replaced by simple decorations on the reconstructed objects, indicating whether the object is matched to a given trigger. However, this means that the trigger-matching must be performed at an earlier stage, during DAOD production, introducing new software.

After bringing up our observations described in the previous section with the trigger software experts, they identified an inconsistency between the two trigger-matching procedures. In conclusion, they implemented changes to the central software to harmonize the two procedures to give consistent results.

6.3 Summary and outlook

This chapter presented two different studies for future LHC runs based on the three-lepton off-shell WZ analysis. The first study considered the choice between the L0-only and L0/L1 options for the ATLAS hardware trigger architecture for the High-Luminosity LHC. Although we found that the three-lepton off-shell WZ analysis would gain from lowering the $E_{\mathrm{T}}^{\mathrm{miss}}$ trigger threshold to 160 GeV, which would be possible with the L0/L1 option, the ATLAS Collaboration ultimately decided to go for the L0-only option.

The second study considered the new Run 3 DAOD format, DAOD_PHYS. By comparing distributions produced using this format to distributions produced using the Run 2 DAOD_SUSY2 format, we identified an inconsistency in the trigger-matching procedure between the old and the new derivation format, affecting low-p_{T} muons. This inconsistency was fixed for later releases of the derivation software. Note that a format targeting further reduced event sizes, of around 5 kB/event, is currently being prepared for Run 4. This format, named DAOD_PHYSLITE, will have improved handling of systematic uncertainties and facilitate columnar analysis.

Due to the delayed start of Run 3 by approximately one year, mainly due to the COVID-19 pandemic, my focus shifted from awaiting new data to summing up the status of supersymmetry searches after Run 2. My contributions to the electroweak SUSY combinations effort will be presented in the next chapter.

Chapter 7

Statistical combinations of Run 2 searches

At the end of Run 2, many separate electroweak SUSY analyses targeting common simplified models have been completed, including the ones presented in Ref. [22] and summarized in this thesis. The ATLAS Collaboration currently has a paper on statistical combinations of electroweak SUSY search results in the pipeline. The aim of these combinations is to extend and deepen the sensitivity offered by each analysis alone. This chapter summarizes my contribution to this combination effort, which has been to investigate and perform combinations for two different simplified models: higgsino $\tilde{\chi}_1^{\pm}\tilde{\chi}_2^0$ pair production decaying via W and Z bosons, and wino $\tilde{\chi}_1^{\pm}\tilde{\chi}_2^0$ pair production decaying via W and h bosons.

An introduction to statistical combinations will be given in Section 7.1, while Sections 7.2 and 7.3 present the work and results for the higgsino $\tilde{\chi}_1^{\pm}\tilde{\chi}_2^0$ via WZ and wino $\tilde{\chi}_1^{\pm}\tilde{\chi}_2^0$ via Wh simplified models, respectively.

7.1 Statistical combinations 101

The ATLAS Collaboration's rich program of Run 2 searches for electroweak SUSY cover multiple production modes, intermediate decay modes and final states. Some of the searches have unique sensitivity, while others have similar coverage. By statistically combining search results, both the breadth and the depth of ATLAS' sensitivity to supersymmetry can be extended. In the combination effort described in this chapter, results of searches targeting the same production and intermediate decay modes (i.e. the same simplified model) but different final states are combined. Only models conserving R-parity (introduced in Section 1.3.2) with promptly decaying supersymmetric particles (except the LSP) are considered.

7.1.1 Statistical independence

When combining analysis results, the analyses should be statistically independent, meaning that their event selections should not overlap, often referred to as the analyses being orthogonal. As this combination effort has been planned for many years, orthogonality has been built into the design of the different analyses as much as possible. One of the most efficient steps in this process is to require orthogonality in the lepton multiplicity of any analysis selection. That way, analyses with 0, 1, 2, etc., leptons are already independent before applying more complex selections. For this to work, all analyses must use the same baseline lepton recommendations.

Any remaining event-selection overlap must be carefully scrutinized. This is done by running all analyses over the same samples, to identify which of the analyses select the same events. To test the overlap across signal regions, the analyses are run over a large "supersample" of simulated simplified-model SUSY events. For the control regions, which are designed to have as little signal contamination as possible, the overlap is better tested by running over the real data sample. For analysis pairs showing an overlap and where a combination is intended, a detailed study of the overlap is performed to decide if it can be ignored (e.g. if there are only a few events overlapping between regions with very high statistics), or if it means that the analyses cannot be combined. In the latter case, the results for the analysis with the best, i.e. lowest, expected CL_s value of the pair is used for each signal point.

7.1.2 Signal grid harmonization

As indicated above, the combination of results for individual analyses is done per signal point $(m(\tilde{\chi}_2^0), m(\tilde{\chi}_1^0))$. This means that we would need results for the same signal points across analyses in order to perform a combination. However, the analyses to be combined do not necessarily consider the same signal points originally. Thus, some of the analyses are run over additional signal samples for the purpose of this combination effort. Both to harmonize the signal grids of the analyses to be combined, and to increase the density of points or extend to higher masses where needed. For analyses where the original analysis team has already moved on, results for additional signal points are obtained from the implementation of the analysis in the RECAST framework. This process will be explained in Section 7.3.3.

7.1.3 Tool and workflow

The statistical tool used to perform the combinations is PYHF [185, 186], which stands for "Python-based HistFactory". As explained in Section 5.5, HistFactory is a tool for creating parametric models by building parameterized probability density functions (PDFs). These PDFs are stored in so-called workspaces, which then contains a complete description of the likelihood function and model. With the model parameterized and stored like this, different statistical tests can easily be performed on the model.

Until 2018, the only implementation of HistFactory was based on ROOT [169, 170], a C++ library widely used in high energy physics. However, the HistFactory template is a pure mathematical representation, not limitied to any particular software specification. With PYHF, a new implementation of HistFactory in pure Python is introduced. By taking advantage of tensor calculations, PYHF outperforms the traditional C++ implementation of HistFactory on data from real LHC analyses [186]. In addition to the default NumPy [187] backend, PYHF also supports TensorFlow [188, 189], PyTorch [190] and JAX [191, 192] as alternative backend choices. By default, the fit optimization is performed with SciPy [193], with IMINUIT [194] as

an alternative.[1] Further, the declarative, plain-text JSON format is used for describing the likelihoods in pyhf, contrary to the XML format used in ROOT-based HistFactory. The move to this declarative format simplifies reinterpretation and long-term preservation in analysis data repositories such as HEPData (introduced in Section 5.7). In addition, pyhf introduces a toolkit that simplifies manipulating and interacting with the JSON workspaces, such as combining them.

Because when doing a statistical combination with pyhf, what is combined are workspaces, effectively combining the individual analysis likelihoods into a combined likelihood. Fits and statistical tests can then be performed on the combined workspace to get combined results. In the combination effort described in this chapter, we test for exclusion as described in Section 5.5.2 by calculating the combined CL_s value using the pyhf function hypotest. Combined 95% CL exclusion limits can then be derived.

For the original signal grids, workspaces per signal point have been provided by the individual analysis teams. As most original analysis results are obtained using HistFitter, careful checks are made to validate pyhf results for the individual analyses against the original results before combining. For additional signal points, workspaces are produced using the RECAST framework as will be described in Section 7.3.3.

Figure 7.1 shows a schematic overview of the usual HistFitter workflow (black) and the pyhf diversion (blue). Before combining workspaces for different analyses, some harmonization might be necessary. For instance, the name used for the signal sample across the analyses must be the same. Further, the treatment of systematic uncertainties across the analyses must be determined.

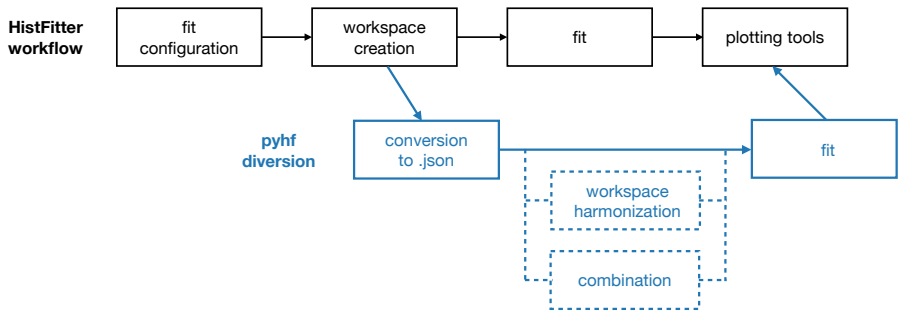

Figure 7.1: Schematic overview of the usual HistFitter workflow (black) and the relation with pyhf for the combination (blue). Figure made by Carlo Gottardo, member of the three-lepton analysis team.

[1] Unless stated otherwise, JAX+SciPy is used in the following.

Correlation of systematic uncertainties

When combining likelihoods from different analyses, parameters that cover the same systematic uncertainties should be correlated, such that they are not double-counted. In practice, this is achieved by naming them the same, as PYHF then treats them as correlated. The initial plan was to prepare a common naming scheme for systematic uncertainties, to be used by all Run 2 analyses intended to be included in the combination effort. However, no such naming scheme was ready in time. As a result, quite some effort has to go into figuring out which parameters cover the same systematic uncertainties despite having different names across the analyses. And vice versa, which parameters do not cover the same uncertainties despite having the same name.

7.2 Higgsino $\tilde{\chi}_1^{\pm}\tilde{\chi}_2^0$ production decaying via WZ

In the higgsino $\tilde{\chi}_1^{\pm}\tilde{\chi}_2^0$ via WZ simplified model discussed in this section, the $\tilde{\chi}_1^{\pm}$, $\tilde{\chi}_2^0$ and $\tilde{\chi}_1^0$ are purely higgsino states, and the mass of the $\tilde{\chi}_1^{\pm}$ is assumed to be exactly the mean of the $\tilde{\chi}_1^0$ and $\tilde{\chi}_2^0$ masses. The $\tilde{\chi}_1^{\pm}$ and $\tilde{\chi}_2^0$ decay to $\tilde{\chi}_1^0$ via Standard Model W and Z bosons, respectively, which in turn decay into different final states.

As explained in Section 5.6.2, an initial combination of the results of the three-lepton off-shell WZ analysis and the compressed two-lepton analysis presented in Ref. [173] has already been performed and published in Ref. [22]. Figure 5.11(d) shows the resulting combined 95% CL exclusion limit for the higgsino scenario. For the combination effort described in this chapter, the plan was to include a third analysis, but as this analysis progressed, it became clear that no significant improvement beyond the initial combination would be expected from it. The higgsino $\tilde{\chi}_1^{\pm}\tilde{\chi}_2^0$ via WZ simplified model is thus not included in the upcoming combinations paper. Instead, in this section, the results of the initial combination are reproduced to verify the setup, before moving to a novel combination for the wino $\tilde{\chi}_1^{\pm}\tilde{\chi}_2^0$ via Wh simplified model in Section 7.3.

The three-lepton off-shell WZ analysis was summarized in Chapter 5. The compressed two-lepton analysis targets, as the name indicates, production of supersymmetric particles in models with compressed mass spectra. The final state of interest contains missing transverse momentum and two same-flavor, oppositely charged leptons with low transverse momentum. The leptons originate from leptonic decay of the Z boson, while the W boson decays hadronically. Further, hadronic initial-state radiation is required to boost the system, to enhance the sensitivity of the search. A representative Feynman diagram for the targeted signal process is shown in Figure 7.2.

Figure 7.3 shows all signal points considered by the two analyses.

7.2.1 Reproducing original analysis results

Before combining, it is important to make sure that the original analysis results, provided by the respective analysis teams, can be reproduced. Figure 7.4 shows

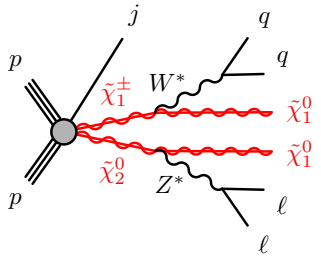

Figure 7.2: Feynman diagram representing the compressed two-lepton analysis [173].

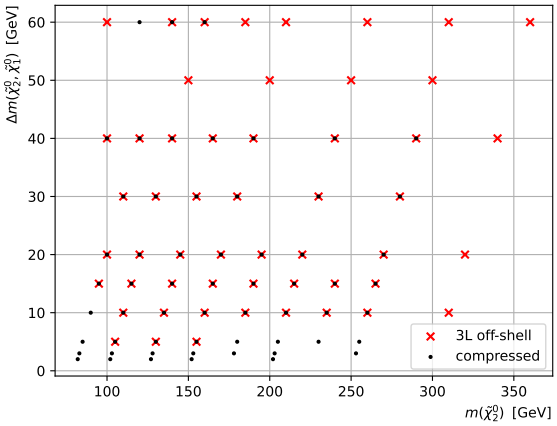

Figure 7.3: Signal points considered by the three-lepton off-shell WZ analysis (red crosses) and the compressed two-lepton analysis (black dots) for the higgsino $\tilde{\chi}_1^{\pm}\tilde{\chi}_2^0$ via WZ simplified model.

for the two analyses the expected CL_s values obtained using PYHF, together with their difference from the original CL_s values produced by the analysis teams. For the compressed two-lepton analysis, for which the original results are obtained using HISTFITTER, a difference of 0.01 is seen for a few signal points (b). For the three-lepton off-shell WZ analysis, both the original and reproduced results are obtained using PYHF (using the same backend and optimizer), and the agreement is consequently excellent (d).

Further, Figure 7.5 shows original and recreated 95% CL exclusion limits for both analyses. Note that the original limits are produced from the inputted original CL_s values, i.e. they are not the official limits produced by the analysis teams. The recreated and original limits agree nicely.

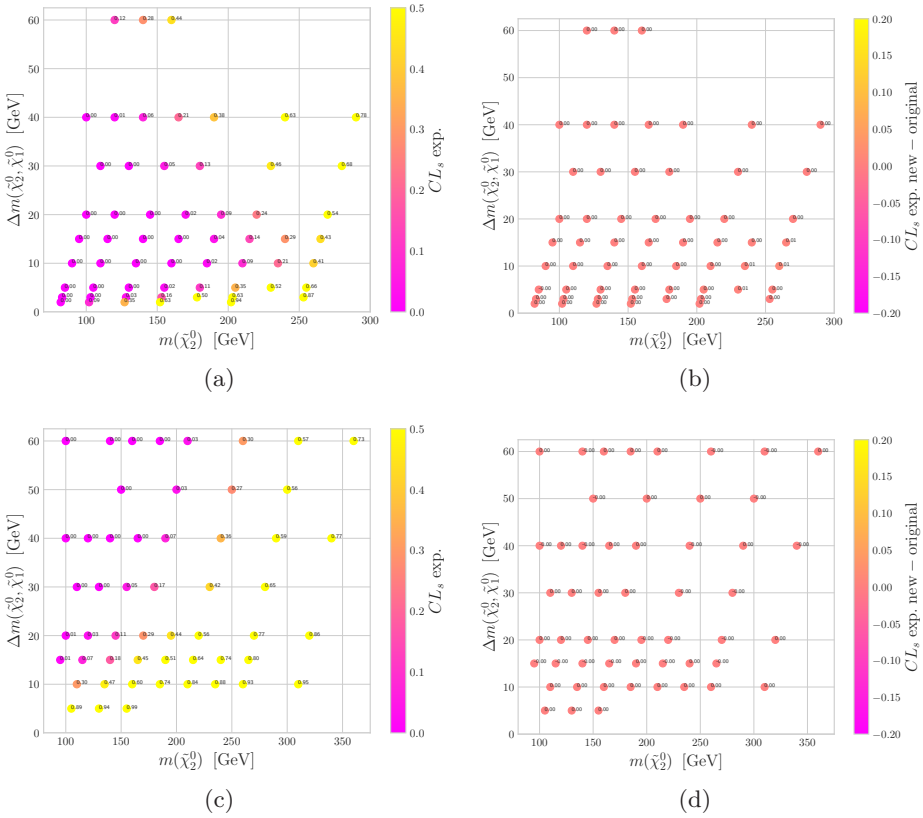

Figure 7.4: Expected CL_s values obtained using PYHF and their difference from the original CL_s values produced by the analysis teams, for (a-b) the compressed two-lepton analysis and (c-d) the three-lepton off-shell WZ analysis.

7.2.2 Reproducing initial combination results

Figure 7.3 shows all signal points for which workspaces (likelihoods) are available for the two analyses. Of the 59 and 53 signal points for the compressed two-lepton and three-lepton off-shell WZ analyses, respectively, 40 are common to both. Workspaces for the common points are combined using PYHF's COMBINE function. The combination is performed using the same correlation scheme for systematic uncertainties as in the initial combination: common experimental uncertainties are treated as correlated between regions and processes, theoretical uncertainties of the background and signal are treated as correlated between regions only, while statistical uncertainties are considered uncorrelated between regions and processes.

Figure 7.6 shows the expected CL_s values for the combination. The left plot shows the reproduced values, while the right plot shows their difference from the original values obtained in the initial combination published in Ref. [22]. Both

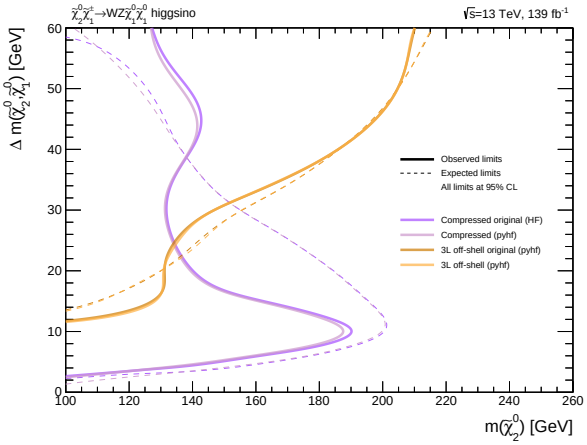

Figure 7.5: Original and recreated 95% CL exclusion limits for the three-lepton off-shell WZ (orange) and compressed two-lepton (purple) analyses, for the higgsino $\tilde{\chi}_1^{\pm}\tilde{\chi}_2^0$ via WZ simplified model.

the reproduced and the original values are obtained with PYHF, using the same backend and optimizer, and the agreement is excellent.

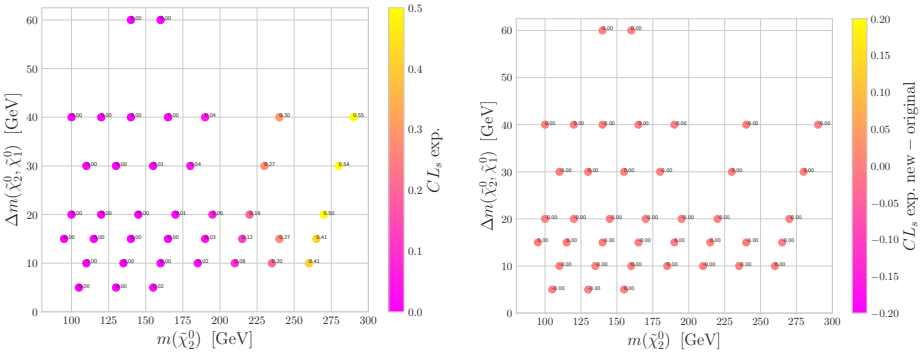

(a) (b)

Figure 7.6: Expected CL_s values for the combination of the three-lepton off-shell WZ and the compressed two-lepton analysis results: (a) reproduced values and (b) their difference from the values obtained in the initial combination published in Ref. [22].

Although there are relatively many common signal points between the two analyses, they are quite centered in $\Delta m(\tilde{\chi}_2^0, \tilde{\chi}_1^0)$. There are no common points below $\Delta m = 5$ GeV, and only a few above $\Delta m = 40$ GeV. In order to obtain sensible 95% CL exclusion contours, combination results are used for $\Delta m \in [8, 42]$ GeV, while compressed two-lepton and three-lepton off-shell

WZ results are used below and above this interval, respectively. The resulting exclusion limits are shown in Figure 7.7. The agreement with the official exclusion limits in Figure 5.11(d) is excellent.

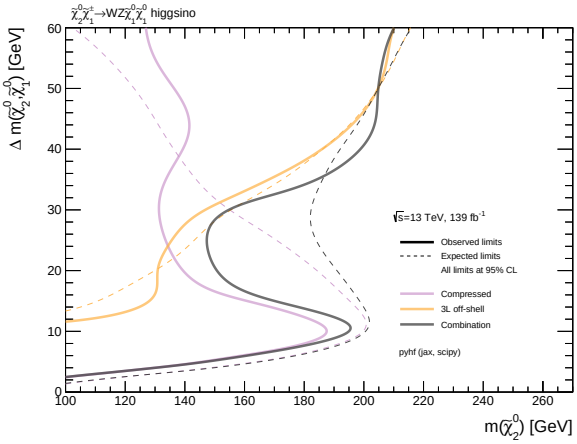

(a)

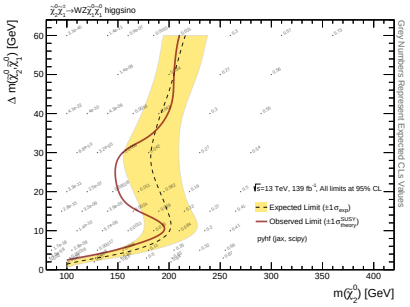

(b)

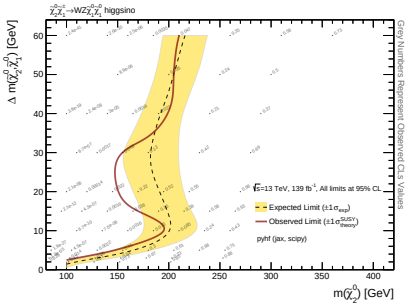

(c)

Figure 7.7: 95% CL exclusion limits for the combination of the three-lepton off-shell WZ and compressed two-lepton analysis results: (a) together with the exclusion limits for the individual analyses, (b) with the expected CL_s values for the combination overlaid, and (c) with the observed CL_s values for the combination overlaid. In all three plots, the combination limits are produced using combination results for $\Delta m \in [8, 42]$ GeV and compressed two-lepton (three-lepton off-shell WZ) results below (above) this interval.

7.2.3 Investigating 90% CL exclusion limits

As explained in Section 5.5.2, the standard in high energy physics is to set exclusion limits at 95% confidence level (CL). However, using this confidence

level is merely a choice and not a strict requirement. Some collaborations, e.g. the IceCube Collaboration, often set exclusion limits at 90% CL. Figure 7.8 shows the same exclusion limits as Figure 7.7, but at 90% CL instead of 95% CL, to illustrate how using a lower confidence level would exclude higher sparticle masses.

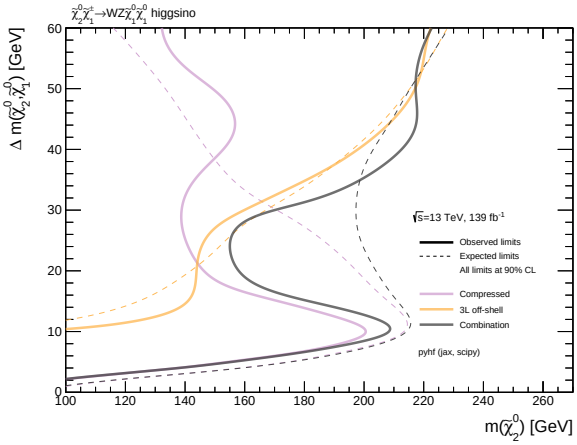

(a)

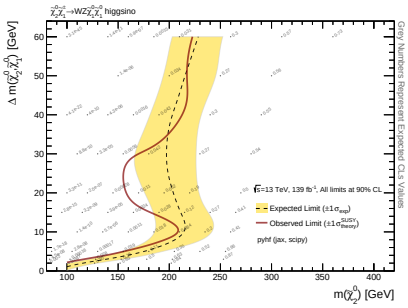

(b)

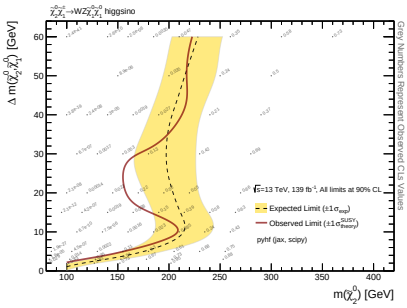

(c)

Figure 7.8: Same plots as in Figure 7.7, but using a 90% confidence level for the exclusion limits instead of the usual 95% confidence level, to illustrate how using a lower confidence level would exclude higher sparticle masses.

7.3 Wino $\tilde{\chi}_1^{\pm}\tilde{\chi}_2^0$ production decaying via Wh

In the wino $\tilde{\chi}_1^{\pm}\tilde{\chi}_2^0$ via Wh simplified model discussed in this section, the $\tilde{\chi}_1^{\pm}$ and $\tilde{\chi}_2^0$ are assumed to be purely wino and mass-degenerate states, while the $\tilde{\chi}_1^0$ is assumed to be purely bino. The $\tilde{\chi}_1^{\pm}$ and $\tilde{\chi}_2^0$ decay to $\tilde{\chi}_1^0$ via Standard Model W and Higgs bosons, respectively, which in turn decay into different final states.

For this model, results for five different analyses are considered for combination: the `all-hadronic` analysis [195], the `3L` analysis [22], the `1Lbb` analysis [196], the `2tau` analysis [197] and the `SS/3L` analysis [198]. A short description of each analysis is given below, and summarized in Table 7.1. Figure 7.9 shows representative Feynman diagrams for the different analyses. Note that for simplicity, the analysis labels used in this section are the labels used for different searches internally in the ATLAS SUSY working group. As some of the searches cover multiple simplified models (as was the case for the three-lepton search introduced in Chapter 3), the labels do not necessarily describe only the final state relevant for the wino $\tilde{\chi}_1^{\pm}\tilde{\chi}_2^0$ via Wh simplified model.

`3L` As part of the search presented in Ref. [22], the three-lepton Wh analysis was introduced in Section 3.3, and the resulting 95% CL exclusion limits were shown in Figure 5.12. In this analysis, both Standard Model bosons decay leptonically. The W boson decays into a lepton–neutrino pair directly, while the Higgs boson decays into two leptons+X (where X denotes additional decay products) indirectly, via WW, ZZ or $\tau\tau$. The resulting final state contains three light-flavored leptons. A representative Feynman diagram for the targeted signal process is shown in Figure 7.9(a).

`All-hadronic` In the `all-hadronic` analysis, only hadronic decay modes of the Standard Model bosons are considered. More specifically, the W boson decays into a pair of light quarks q, while the Higgs boson decays into a pair of bottom quarks b, leading to a $q\bar{q}b\bar{b}$ final state. To suppress Standard Model backgrounds, the Standard Model bosons are "boosted" by only considering mass-splittings $\Delta m(\tilde{\chi}_2^0, \tilde{\chi}_1^0)$ greater than 400 GeV. A representative Feynman diagram for the targeted signal process is shown in Figure 7.9(b).

`1Lbb` In the `1Lbb` analysis, the W boson decays leptonically, while the Higgs boson decays into a pair of botton quarks. The resulting final state contains one lepton and a $b\bar{b}$ pair. A representative Feynman diagram for the targeted signal process is shown in Figure 7.9(c).

`2tau` In the `2tau` analysis, the W boson decays into a lepton–neutrino pair, while the Higgs boson decays into a pair of tau leptons. The resulting final state contains one light-flavored lepton and two tau leptons. A representative Feynman diagram for the targeted signal process is shown in Figure 7.9(d).

`SS/3L` The `SS/3L` analysis considers a final state containing two light-flavored leptons with the same electric charge. The W boson decays into a lepton–neutrino pair, while all possible decays of the Higgs boson which ultimately result in one lepton and jets (mostly via intermediate states such as WW and $\tau\tau$) are taken into account. A representative Feynman diagram for the targeted signal process is shown in Figure 7.9(e).

Note that in the upcoming combinations paper, an additional analysis is considered for combination for the wino $\tilde{\chi}_1^{\pm}\tilde{\chi}_2^0$ via Wh simplified model. The `1L` analysis targets the same process as `1Lbb`, but uses machine-learning techniques to enhance sensitivity in the compressed region of the phase space, where signal kinematics are very close to the kinematics of the dominant backgrounds. This analysis was not completed when the work presented in this section was carried out, and has not yet been published at the time of writing.

Table 7.1: Analyses considered for combination for the wino $\tilde{\chi}_1^{\pm}\tilde{\chi}_2^0$ via Wh simplified model. In addition to the final-state descriptions below, all final states contain missing transverse momentum from the two LSPs and potential neutrinos.

Analysis label	Description	Reference
`3L`	$W \to \ell\nu$, $h \to 2\ell{+}X$ via WW, ZZ or $\tau\tau$. Final state with three light-flavored leptons.	[22]
`all-hadronic`	$W \to q\bar{q}$, $h \to b\bar{b}$. Fully hadronic final state.	[195]
`1Lbb`	$W \to \ell\nu$, $h \to b\bar{b}$. Final state with one light-flavored lepton and two bottom quarks.	[196]
`2tau`	$W \to \ell\nu$, $h \to \tau\tau$. Final state with one light-flavored lepton and two tau leptons.	[197]
`SS/3L`	$W \to \ell\nu$, $h \to \ell{+}$jets via all possible decay modes. Final state with two same-sign light-flavored leptons.	[198]

Figures 7.10 and 7.11 show the original 95% CL exclusion limits and signal grids, respectively, for all analyses. In order to get a meaningful overlap of signal points for the combination, additional points are considered for the `1Lbb`, `3L` and `all-hadronic` analyses. As the analysis teams for these analyses have moved on, workspaces for the additional signal points are produced using the RECAST framework, see Section 7.3.3. For the later `2tau` and `SS/3L` analyses, the original signal grids are already relatively harmonized, and only the original signal points are considered. For the `2tau` analysis, the two signal regions are not orthogonal, so the region with the lowest expected CL_s value is used for each signal point.

7.3.1 Orthogonality of analyses

As explained in Section 7.1.1, analyses to be combined should be statistically independent, meaning that they should not select the same events. The event-selection overlap across signal regions is studied using a large "supersample" of simulated SUSY events, while the overlap across control regions is studied using data. Figure 7.12 shows overviews of the overlap in events selected by the different analyses for the signal supersample and full Run 2 dataset. Note that all analyses considered in the overall combination effort are shown in these overviews, not only the ones combined for the wino $\tilde{\chi}_1^{\pm}\tilde{\chi}_2^0$ via Wh simplified model. In conclusion, one pair of analyses cannot be combined, namely `3L`

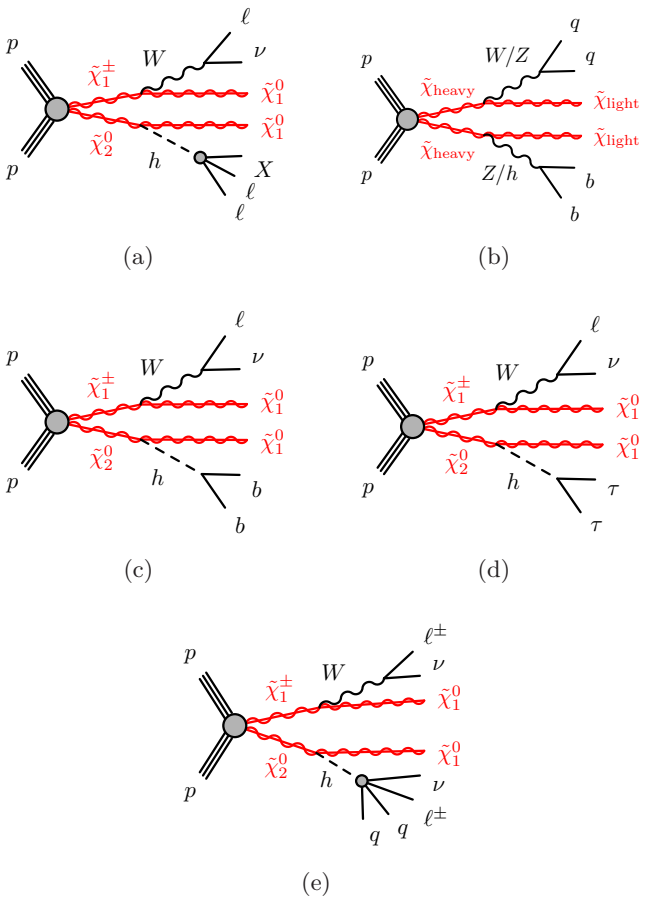

Figure 7.9: Representative Feynman diagrams for the analyses considered for combination for the wino $\tilde{\chi}_1^\pm\tilde{\chi}_2^0$ via Wh simplified model: (a) the `3L` analysis, (b) the `all-hadronic` analysis, (c) the `1Lbb` analysis, (d) the `2tau` analysis and (e) the `SS/3L` analysis.

and `SS/3L`.[2] These analyses have 22 and 411 events in common for the signal supersample and the Run 2 dataset, respectively. The analysis with the lowest expected CL_s value of the two is used for each signal point.

7.3.2 Reproducing original analysis results

Before combining, it is important to make sure that the original analysis results, all obtained using HistFitter, can be reproduced with pyhf. Figures 7.13 and 7.14 show for all analyses the expected CL_s values obtained using pyhf, together with their difference from the original CL_s values produced

[2]The same will be true for the `1Lbb` and `1L` analyses, when the latter is completed.

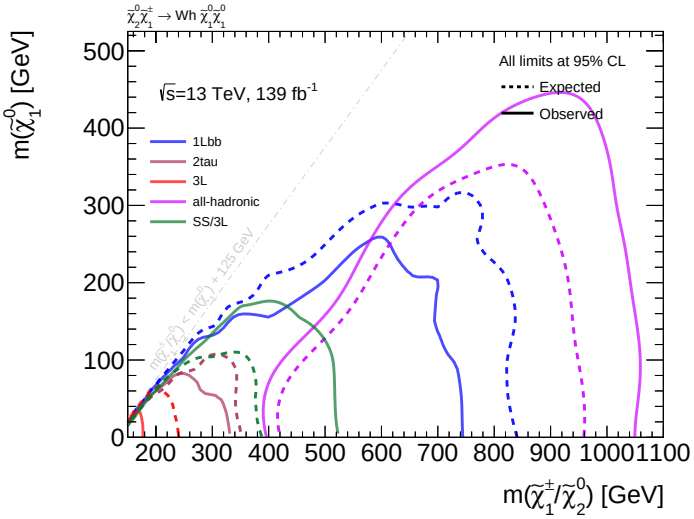

Figure 7.10: Original 95% CL exclusion limits for the analyses considered for combination for the wino $\tilde{\chi}_1^{\pm}\tilde{\chi}_2^0$ via Wh simplified model: `3L` (red), `all-hadronic` (purple), `1Lbb` (blue), `2tau` (mauve taupe) and `SS/3L` (green).

by the different analysis teams. Note that there is no difference plot for the `1Lbb` analysis, as original CL_s values were not provided for this analysis. Further, the two occurences of "not a number" (nan) in the `3L` difference plot (d) are due to original CL_s values not being available for these two signal points. As seen in the difference plots, the agreement with the original values is very good for all analyses.

Further, Figure 7.15 shows original and recreated 95% CL exclusion limits for all analyses. Note that the original limits are produced from the inputted original CL_s values, i.e. they are not the official limits produced by the analysis teams, except for the `1Lbb` analysis. The recreated and original limits mostly agree nicely. For the `SS/3L` analysis (which is still blinded in this figure), the discrepancy around $m(\tilde{\chi}_2^0) = 400$ GeV is due to the expected CL_s value for signal point $(m(\tilde{\chi}_2^0), m(\tilde{\chi}_1^0)) = (400, 50)$ GeV being 0.052 (not excluded) and 0.042 (excluded) for HistFitter and pyhf, respectively.

7.3.3 Producing workspaces for additional signal points

Although analyses like the one summarized in Chapter 5 are designed to target a specific beyond Standard Model (BSM) simplified-model scenario, they are often also sensitive to alternative models in the same or a similar phase space. This can be exploited by reinterpreting (or *recasting*) the analysis for such alternative models. As only the signal model is changing, the background estimates and observed data used in the original analysis can be reused. The only two necessary steps for reinterpretation are thus 1) generating simulated events for the new

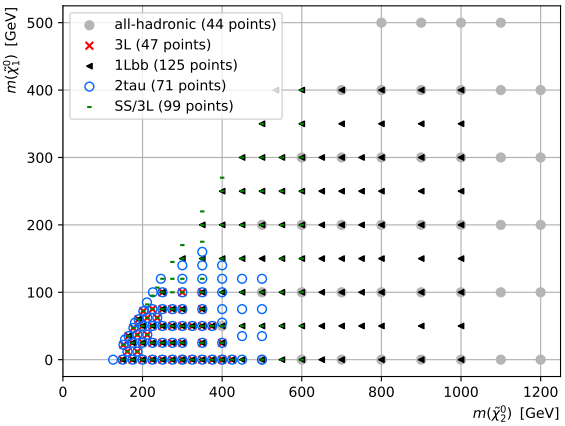

Figure 7.11: Original signal grids for the analyses considered for combination for the wino $\tilde{\chi}_1^{\pm}\tilde{\chi}_2^0$ via Wh simplified model: `all-hadronic` (gray filled circle), `3L` (red cross), `1Lbb` (black triangle), `2tau` (blue open circle) and `SS/3L` (green small rectangle).

candidate signal model and 2) re-executing the analysis (including event selection and statistical evaluation) for this new signal. In this particular case, however, we are not interested in re-executing the analysis for a new signal model, but rather for additional signal points for the same simplified-model scenario. The procedure is the same regardless.

A framework and tool for preserving and reinterpreting analyses is RECAST [199, 200], which stands for "Request Efficiency Computation for Alternative Signal Theories". It consists of three key components:

- **Analysis code preservation:** First, the analysis code framework used to perform the search for a particular physics model based on inputted data and MC samples must be preserved. In ATLAS, this is done using GitLab.
- **Environment preservation:** The analysis code framework above relies on having specific libraries, compilers and even operating systems in place, often with strict requirements on the exact versions of the dependencies. So the second part of analysis preservation is to capture the exact environment in which the code was run by the original analysts. This is done using Docker [201].
- **Automated reinterpretation:** The third and final part is to automate the steps in the analysis chain, i.e. the steps an analyst would go through from passing the new signal model to arriving at the new result. This is done using yadage [202].

Preparing a RECAST implementation of the analysis is an important step in the ATLAS SUSY analysis-approval procedure.

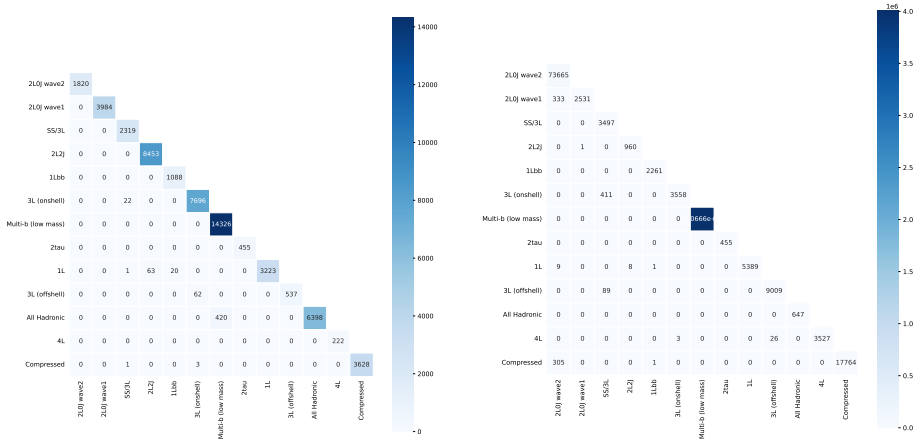

(a) (b)

Figure 7.12: Overview of the overlap in events selected by the different analyses for (a) the signal supersample and (b) the full Run 2 dataset.

Workspaces are produced for additional signal points for the `all-hadronic`, `3L` and `1Lbb` analyses using the RECAST implementations of them, as described in the following.

Investigating workspace and MC sample availability

Figure 7.16 shows all signal points (original signal grid plus extension) for all three analyses, while Figure 7.17 shows the points per analysis, also including workspace and MC sample availability. The input to RECAST are signal MC samples in DAOD format,[3] first introduced in Section 4.1.1.

For the `all-hadronic` and `1Lbb` analyses, not all original signal points have available workspaces. As these points might have been dropped with good reason in the original analysis, they might still be relevant to include in the combination. Therefore, workspaces are produced for all points in Figure 7.17 for which a workspace is not already available (indicated by a black dot). The only exceptions are the 22 original `1Lbb` points that in addition do not have available (D)AODs (points with only purple open marker "Original" in Figure 7.17(a)). In order to avoid having to produce additional AODs (which is quite CPU-intensive), these points are dropped as they are only considered by the `1Lbb` analysis anyway. For points with DAODs already available, all input to RECAST is ready. For points with only AODs available, DAODs are produced before running RECAST.

[3]One sample for each of the three "MC campaigns" corresponding to data samples for years 2015+2016, 2017 and 2018.

Running RECAST

Although the idea behind RECAST is clear, there is a lot of freedom in how to design the RECAST implementation of an analysis. For instance, there are no requirements on which steps the analysis chain should consist of (see "Automated reinterpretation" above), or which parameters should be hard-coded/configurable. This freedom is important as different analysis code frameworks can be set up very differently. However, it can complicate the usage, and careful considerations must be made to make sure that the treatment of relevant concepts such as cross-sections and theory uncertainties for the new signals are well-understood.

Some relevant details on running RECAST for the `3L`, `all-hadronic` and `1Lbb` analyses will be given below. Note that these comments are only valid for the time of running (fall of 2021), and that the RECAST implementations of these analyses might have been updated since then.

`3L` For the `3L` RECAST, signal cross-sections are not configurable, and only cross-sections for the original signal grid are hard-coded. Cross-sections for the extended signal grid thus have to be manually added to the preserved analysis code framework. Further, a hard-coded 10% flat (constant) theoretical uncertainty in the expected signal yield is used. Additionally, some changes are needed to produce and output workspaces in the desired JSON format, and not only fit-results directly.

`all-hadronic` A hard-coded 10% flat signal theory uncertainty is used also in the `all-hadronic` RECAST. And as for the `3L` RECAST, some changes are needed to output workspaces and not only fit-results directly. For some of the RECAST-produced `all-hadronic` workspaces close to the kinematic limit ($\Delta m(\tilde{\chi}_2^0, \tilde{\chi}_1^0) = m_h$), the subsequent CL_s calculation with PYHF either returns an expected CL_s value of 1.0 or fails, due to zero signal events in the SR or in both the SR and the CR, respectively. These 13 (expected CL_s 1.0) plus 6 (failed) signal points are not used in the combination.

`1Lbb` For the `1Lbb` RECAST, signal theory uncertainties are configurable, but only values for the original grid are available. As the signal points in the extension are mostly in between original points, interpolated values are obtained and used for these, for the three considered uncertainty sources separately.

Verifying the RECAST results

In order to verify the results, RECAST is also run for an original signal point for each analysis, so that the resulting CL_s values can be compared to the CL_s values provided by the original analysis team. In addition, the 95% CL exclusion limits are remade based on all signal points (original grid plus extension), to check that they do not change significantly. Figure 7.18 shows for all three analyses the exclusion limits based on the original grid only, together with the limits based on the original grid plus the extension. No significant differences are seen. The discrepancy for the `all-hadronic` limits (b) around $m(\tilde{\chi}_2^0) = 400$-$500$ GeV is due to many extension points in this area.

7.3.4 Points to combine

Figure 7.19 shows all workspaces available for combination. In order to avoid higher CL_s values for signal points considered by only one analysis in between lower CL_s values for points considered by multiple analyses, 9 `1Lbb` (black triangle) and 19 `2tau` (blue open circle) points are excluded. In addition, as discussed in Section 7.3.1, for signal points considered by both the `3L` (red cross) and `SS/3L` (green small rectangle) analyses, only the results for the analysis with the lowest expected CL_s value of the two is included in the combination.

Initially, the combination is performed with all systematic uncertainties set to be uncorrelated across the analyses. For this scenario, the expectation is that the lowest expected CL_s value for a given signal point is obtained by combining the results for all available analyses. Figure 7.20 shows the "combination scheme" used for this uncorrelated scenario.

7.3.5 Correlation of systematic uncertainties

As discussed in Section 7.1.3, parameters that cover the same systematic uncertainties should be correlated when combining likelihoods from different analyses. However, this process is not necessarily straightforward in practice.

As the analyses to be combined (mostly) consider different Standard Model backgrounds and/or group the background MC samples differently, correlating the related theoretical (modeling) uncertainties and normalization-factor uncertainties is not straightforward. All such uncertainties are therefore kept uncorrelated, resulting in more conservative results. Further, statistical uncertainties and (when relevant) uncertainties associated with shape fits are linked to the design of the different analyses, and are also kept uncorrelated in the combination. For experimental (instrumental) uncertainties, it is in principle possible to correlate uncertainties across the different analyses provided that they affect analogous objects. But if the analyses use different definitions for the same objects (e.g. different choice of working points), the overall efficiency for reconstructing and selecting the objects would differ between the analyses, and potential correlation becomes non-trivial. In that case, the uncertainties are kept uncorrelated.

Given these considerations, the analyses taking part in the combination for the wino $\tilde{\chi}_1^{\pm}\tilde{\chi}_2^0$ via Wh simplified model are scrutinized to assess which correlations can be introduced. An overview of the object definitions employed in each analysis is shown in Table 7.2. Note that in the `all-hadronic` analysis, light-flavored leptons are used to veto, not select, events. Considering correlations for uncertainties related to lepton objects is therefore not relevant for this analysis, indicated by "N/A" (not applicable) in the table. Based on this information, the correlation scheme reported in Table 7.3 is introduced. In the following, the effect of using this correlation scheme in the combination will be assessed by comparing the corresponding results to the results of the completely uncorrelated scenario. But before discussing the combination results, we must first scrutinize the nuisance-parameter behaviour in the combination fit.

Table 7.2: Overview of the object definitions employed in each analysis participating in the combination for the wino $\tilde{\chi}_1^{\pm}\tilde{\chi}_2^0$ via Wh simplified model.

		SS3ℓ	3ℓ-onShell	2tau	AllHadronic	1Lbb
Electrons	ID	Medium	Medium	Tight	N/A	Tight
	ISO	FCTight	FCTight	FCLoose+FCHighPtCaloOnly	N/A	FCLoose+FCHighPtCaloOnly
Muons	ID	Medium	Medium	Medium	N/A	Medium
	ISO	FCTightTrackOnly	FCTight	FCLoose	N/A	FCLoose
Jets	Type	AntiKt4EMPFlow	AntiKt4EMTopo	AntiKt4EMPFlow	AntiKt4EMPFlow	AntiKt4EMTopo
	Unc. scheme	CR_SJ	CR_SJ	SR_SJ	GR_SJ	CR_FJ
	JVT WP	tight	medium	tight	tight	medium
	W-tagging	N/A	N/A	N/A	✓	N/A
b-jets	Tagger	DL1r	MV2c10	DL1r	MV2c10	MV2c10
	Efficiency	70%	85%	77%	85%	77%
MET JET-term		tight	tight	tight	tight	tight
Trigger		Dilep+MET	Dilep	Ditau+MET	MET	MET

Table 7.3: Correlation scheme for systematic uncertainties considered in the combination for the wino $\tilde{\chi}_1^{\pm}\tilde{\chi}_2^0$ via Wh simplified model. For each row (parameter), the checkmarks indicate which analyses the corresponding systematic uncertainty is correlated across. For rows with both black and red checkmarks, correlations are made for two different subsets of analyses.

		SS3ℓ	3ℓ-onShell	2tau	AllHadronic	1Lbb
Electrons	RECO	✓	✓	✓		✓
	ID	✓	✓	✓		✓
	ISO	✓	✓	✓		✓
Muons	RECO	✓	✓	✓		✓
	ID	✓	✓	✓		✓
	ISO			✓		✓
Jets	JES		✓			✓
	JER	✓		✓		
	Other	✓	✓	✓		✓
	JVT	✓	✓	✓		✓
	b-tagging		✓		✓	
	Jet/W-tagging					
MET		✓	✓	✓		✓
Trigger					✓	✓
Pile-up		✓	✓	✓	✓	✓
Luminosity		✓	✓	✓	✓	✓
Theory						
Statistics/Shape						

7.3.6 Nuisance-parameter consistency

In statistical fits, a *pull* $(\theta - \hat{\theta})/\Delta\theta$ quantifies the standardized discrepancy between the observed value $\hat{\theta}$ and predicted value θ for a nuisance parameter. A large pull value indicates that the nuisance parameter is more influential in the fit than first anticipated. Ideally, the pull values for the combination fit should not differ (significantly) from the pull values for the individual analysis fits, as we do not want the combination itself to introduce any constraints amongst the nuisance parameters of each individual analysis. The combination-fit pulls for two representative signal points are considered in the following. To properly estimate the impact of each parameter in the fit, PYHF is run with the NUMPY

backend and the IMINIUT optimizer.

Figure 7.21 shows pull plots for signal point $(m(\tilde{\chi}_2^0), m(\tilde{\chi}_1^0)) = (400,100)$ GeV, for which results for the `3L`, `all-hadronic`, `1Lbb` and `2tau` analyses are combined. Only parameters whose combination-fit pulls (red) differ with more than two decimal points (2dp) from the pulls for the individual analysis fits (black) are shown, where the first part of the parameter label indicates which uncertainty it covers, and the second part indicates which analysis it stems from. The upper plot (a) show combination-fit pulls for the uncorrelated scenario, while the lower plot (b) show combination-fit pulls for the correlated scenario, applying the correlation scheme reported in Table 7.3. To also consider a combination including the `SS/3L` analysis, Figure 7.22 shows corresponding pull plots for signal point $(m(\tilde{\chi}_2^0), m(\tilde{\chi}_1^0)) = (190,60)$ GeV, for which results for the `1Lbb`, `2tau` and `SS/3L` analyses are combined. No significant differences are seen when comparing the combination-fit pulls to the pulls for the individual analysis fits.

To further test for unwanted constraints, we scrutinize the *correlation matrices* for the leading correlated uncertainties. No new strong correlations between nuisance parameters should be introduced when combining separate analyses. Figure 7.23 shows correlation matrices for the leading correlated uncertainties (only correlations larger than ± 0.15) for the two signal points discussed above. All relatively large correlations outside the diagonal are present also in the original analyses.

7.3.7 Improvement from the combination

Figure 7.24 shows 95% CL exclusion limits for the initial combination with all systematic uncertainties set to be uncorrelated across the analyses. Exclusion limits for the combination together with the limits for the individual analyses are shown in (a), while combination limits with the combined expected and observed CL_s values for each signal point overlaid are shown in (b) and (c), respectively. For large $\tilde{\chi}_2^0$ masses, the `all-hadronic` analysis (orange) excludes more than expected due to a deficit, while the `1Lbb` analysis (purple) excludes less than expected due to an excess. The combination (gray) smooths out these effects, with the expected limit for the combination being stronger than the `all-hadronic` one, and the observed limit being weaker.

Impact of correlating systematic uncertainties

Figure 7.25 compares the 95% CL exclusion limits for the combination for the uncorrelated and correlated scenarios, with corresponding observed CL_s values overlaid. Some minor differences in the observed CL_s values are seen, but the exclusion limits are effectively unaffected by applying the correlation scheme in Table 7.3 compared to keeping all systematic uncertainties uncorrelated. As the results are effectively the same, the simpler approach of keeping all systematic uncertainties uncorrelated is used in the upcoming combinations paper.

Upper limits on signal strength

The improvement in the level of exclusion that can be achieved by combining analysis results does not only refer to excluding a wider area of the sparticle mass plane, but also to the "depth" of the exclusion. The latter can be evaluated by comparing the 95% CL upper limit on the signal strength (μ_s^{UL}) from the combination with the upper limit from the best performing single analysis for each signal point. Figure 7.26 shows the relative difference in μ_s^{UL} for this comparison, for the expected (a) and observed (b) limits. Due to the deficit seen in the `all-hadronic` analysis, the observed upper limit worsens (increases) for the combination compared to the best performing single analysis in most of the mass plane. The best improvement, at the level of around 20–30%, is seen for $m(\tilde{\chi}_1^{\pm}/\tilde{\chi}_2^0) < 600$ GeV. For the expected upper limit, improvement is seen for almost the entire mass plane.

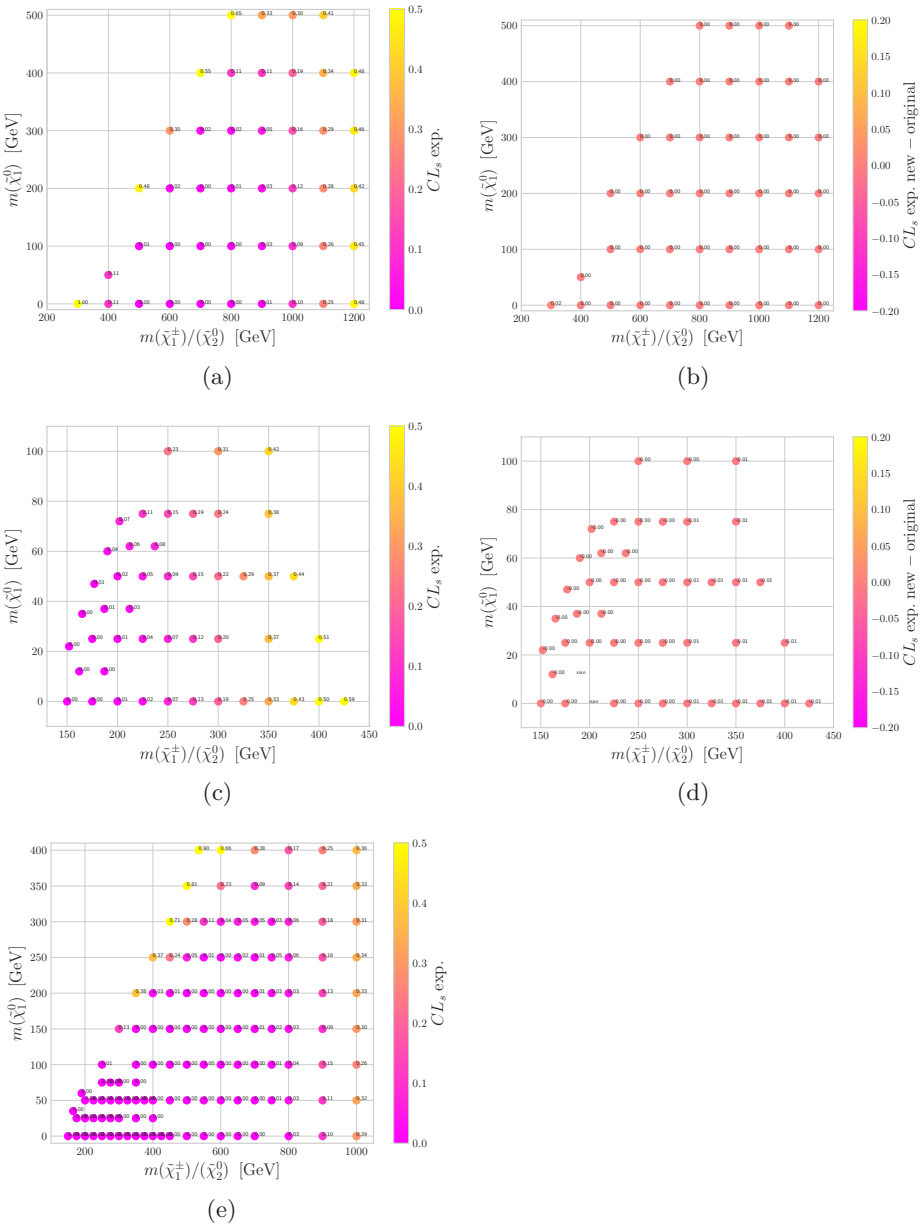

Figure 7.13: Expected CL_s values obtained using PYHF (left column), and their difference from the original CL_s values produced by the different analysis teams (right column), for all analyses considered for combination for the wino $\tilde{\chi}_1^{\pm}\tilde{\chi}_2^0$ via Wh simplified model. The top row (a-b) shows the results for the `all-hadronic` analysis, the middle row (c-d) shows the results for the `3L` analysis, while the bottom row (e) show the results for the `1Lbb` analysis. Continues in Figure 7.14.

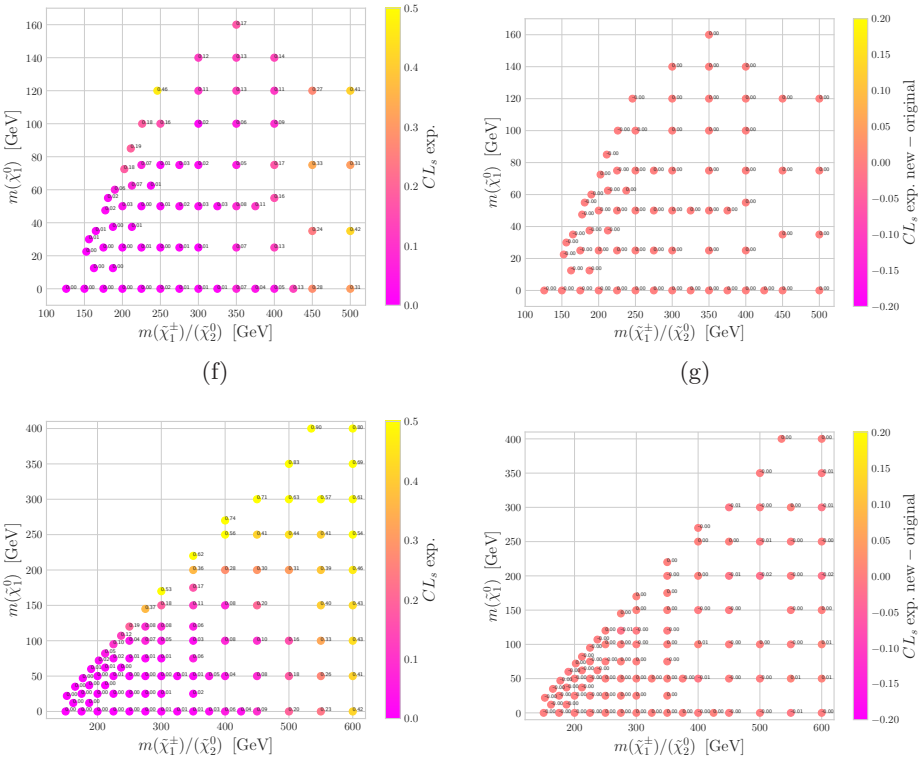

(f) (g)

(h) (i)

Figure 7.14: Continued from Figure 7.13. The top row (f-g) shows the results for the `2tau` analysis, while the bottom row (h-i) shows the results for the `SS/3L` analysis.

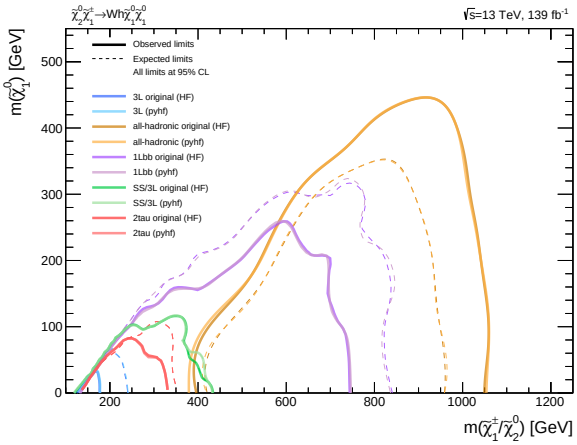

Figure 7.15: Recreated and original 95% CL exclusion limits for all analyses considered for combination for the wino $\tilde{\chi}_1^{\pm}\tilde{\chi}_2^0$ via Wh simplified model: `3L` (blue), `all-hadronic` (orange), `1Lbb` (purple), `SS/3L` (green) and `2tau` (red). Not that the `SS/3L` analysis is still blinded in this plot.

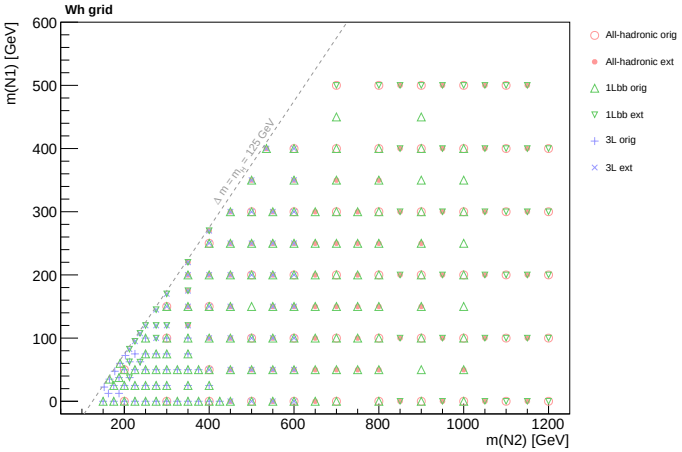

Figure 7.16: Original signal grids and extensions for the `1Lbb` (green), `3L` (purple) and `all-hadronic` (red) analyses for the wino $\tilde{\chi}_1^{\pm}\tilde{\chi}_2^0$ via Wh simplified model. The "mN2" and "mN1" axis labels refer to $m(\tilde{\chi}_2^0)$ and $m(\tilde{\chi}_1^0)$, respectively.

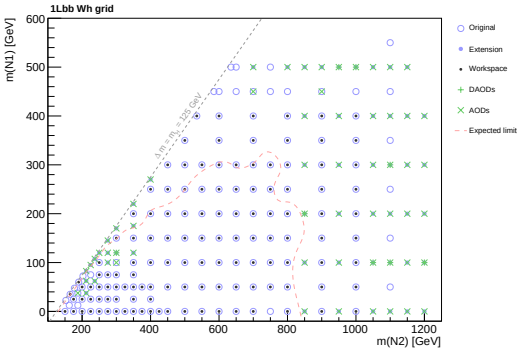

(a)

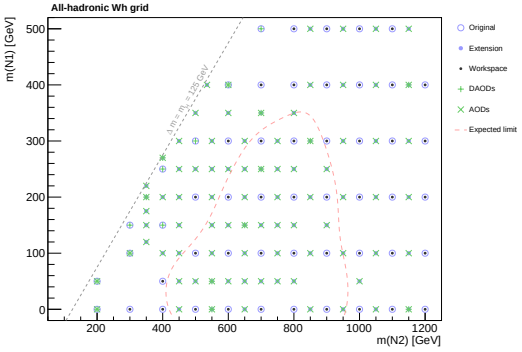

(b)

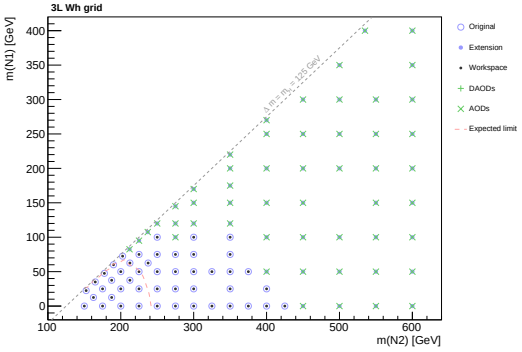

(c)

Figure 7.17: Original signal grid and its extension for the (a) `1Lbb`, (b) `all-hadronic` and (c) `3L` analyses, including workspace and (D)AOD availability. A black dot indicates that a workspace is already available for the signal point, while a green "+" ("x") for points without workspaces indicates that DAODs (AODs) are available. The red dashed line shows the expected 95% CL exclusion limit for the original analysis. The "mN2" and "mN1" axis labels refer to $m(\tilde{\chi}_2^0)$ and $m(\tilde{\chi}_1^0)$, respectively.

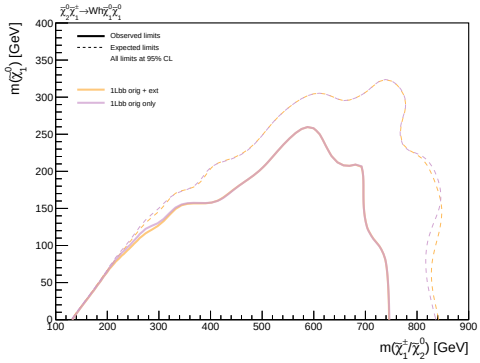

(a)

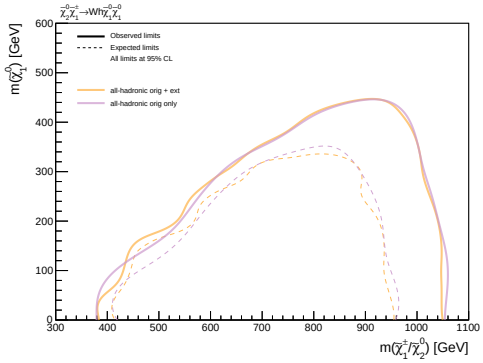

(b)

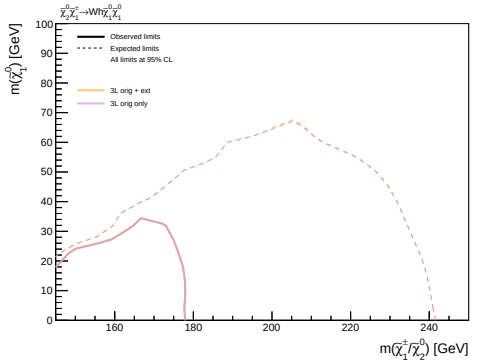

(c)

Figure 7.18: 95% CL exclusion limits based on the original signal grid only (purple), together with the limits based on the original grid plus the extension (orange), for (a) the `1Lbb` analysis, (b) the `all-hadronic` analysis, and (c) the `3L` analysis. To illustrate that the limits do not change significantly when also considering the additional signal points.

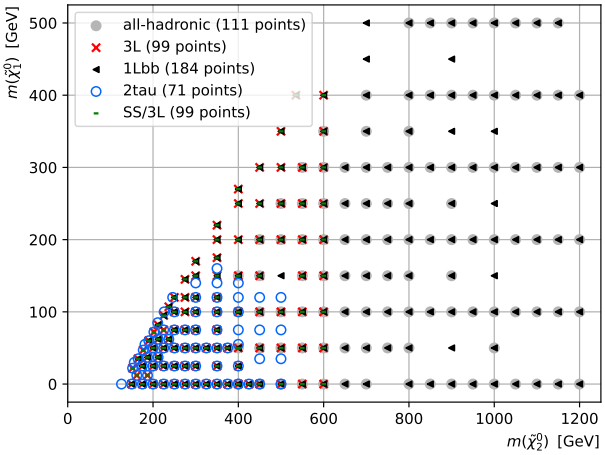

Figure 7.19: All workspaces available for combination for the wino $\tilde{\chi}_1^{\pm}\tilde{\chi}_2^0$ via *Wh* simplified model, for the `all-hadronic` (gray filled circle), `3L` (red cross), `1Lbb` (black triangle), `2tau` (blue open circle) and `SS/3L` (green small rectangle) analyses.

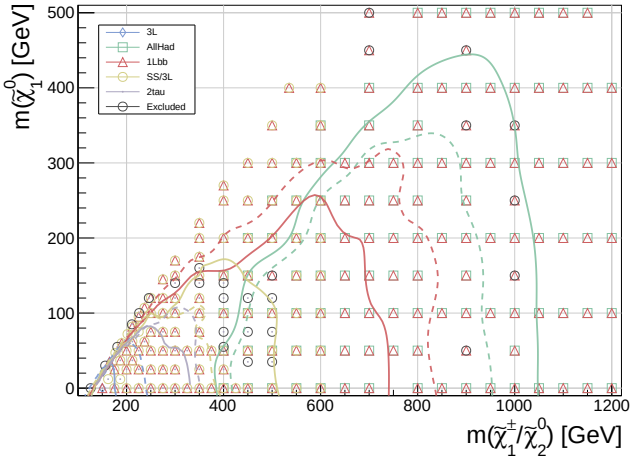

Figure 7.20: Combination scheme for the initial combination for the wino $\tilde{\chi}_1^{\pm}\tilde{\chi}_2^0$ via *Wh* simplified model, where all systematic uncertainties are set to be uncorrelated across the analyses. For each signal point, the analyses whose markers are shown are combined: `3L` (blue rhombus), `all-hadronic` (green square), `1Lbb` (red triangle), `SS/3L` (yellow circle) and `2tau` (purple dot). Signal points with a black circle are not used in the combination results. The dashed and solid lines show the expected and observed 95% CL exclusion limits, respectively, for the individual analyses.

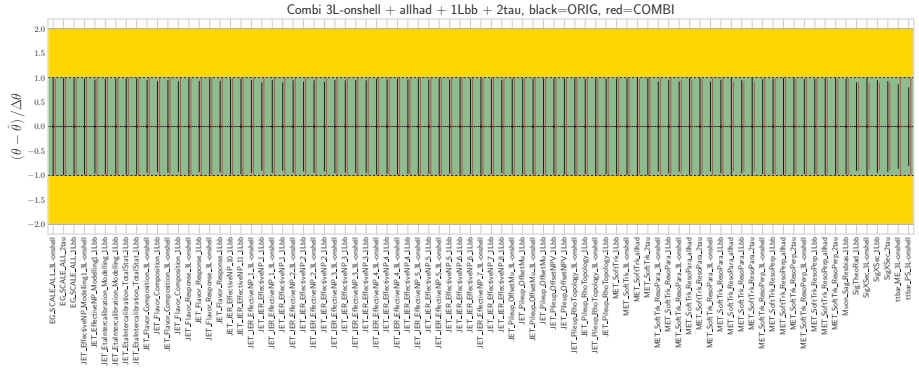

(a)

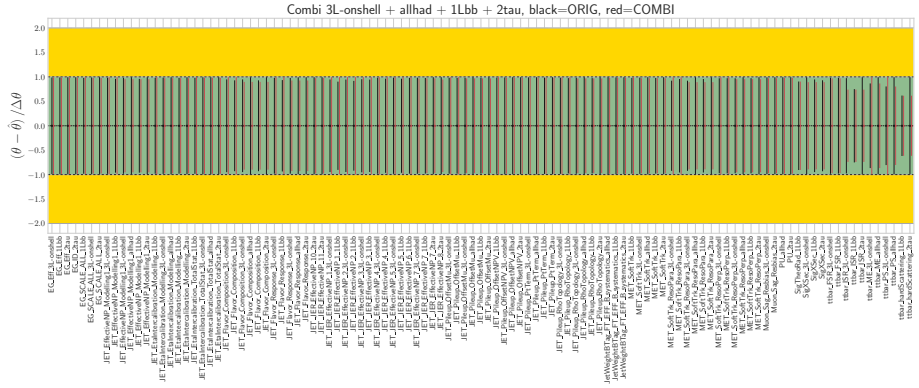

(b)

Figure 7.21: Pull plots for signal point $(m(\tilde{\chi}_2^0), m(\tilde{\chi}_1^0)) = (400,100)$ GeV, for which results for the `3L`, `all-hadronic`, `1Lbb` and `2tau` analyses are combined. Only parameters whose combination-fit pulls (red) differ with more than two decimal points (2dp) from the pulls for the individual analysis fits (black) are shown, where the first part of the parameter label indicates which uncertainty it covers, and the second part indicates which analysis it stems from. The upper plot (a) show combination-fit pulls for the uncorrelated scenario, while the lower plots (b) show combination-fit pulls for the correlated scenario, applying the correlation scheme reported in Table 7.3.

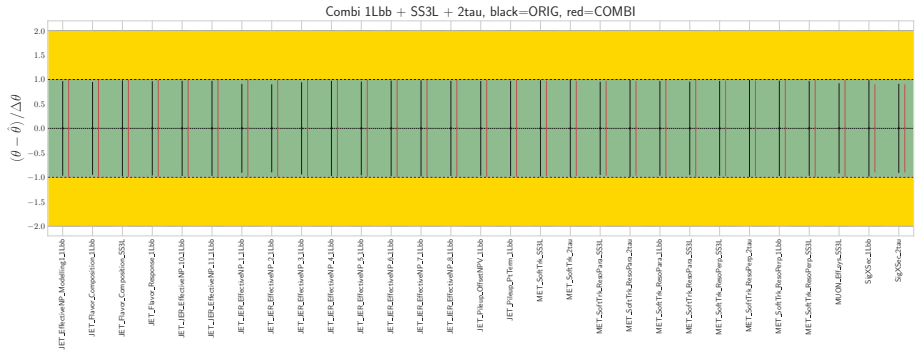

(a)

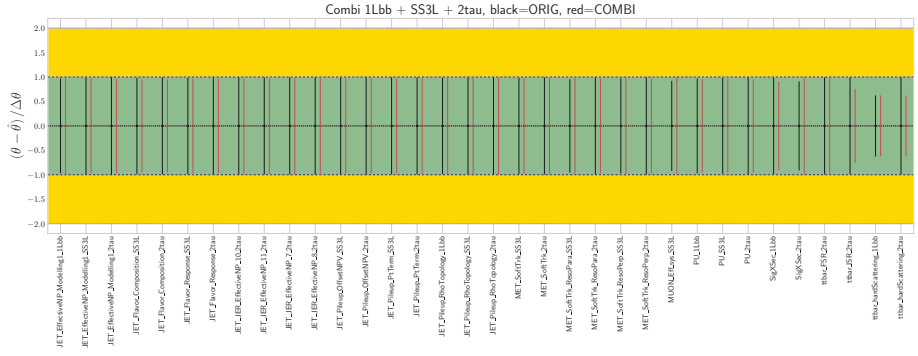

(b)

Figure 7.22: Pull plots for signal point $(m(\tilde{\chi}_2^0), m(\tilde{\chi}_1^0)) = (190,60)$ GeV, for which results for the `1Lbb`, `2tau` and `SS/3L` analyses are combined. Only parameters whose combination-fit pulls (red) differ with more than two decimal points (2dp) from the pulls for the individual analysis fits (black) are shown, where the first part of the parameter label indicates which uncertainty it covers, and the second part indicates which analysis it stems from. The upper plot (a) show combination-fit pulls for the uncorrelated scenario, while the lower plots (b) show combination-fit pulls for the correlated scenario, applying the correlation scheme reported in Table 7.3.

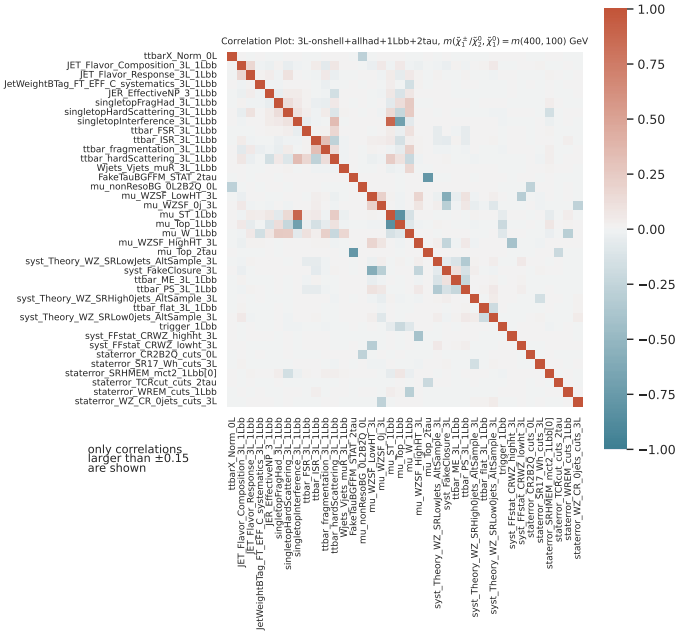

(a)

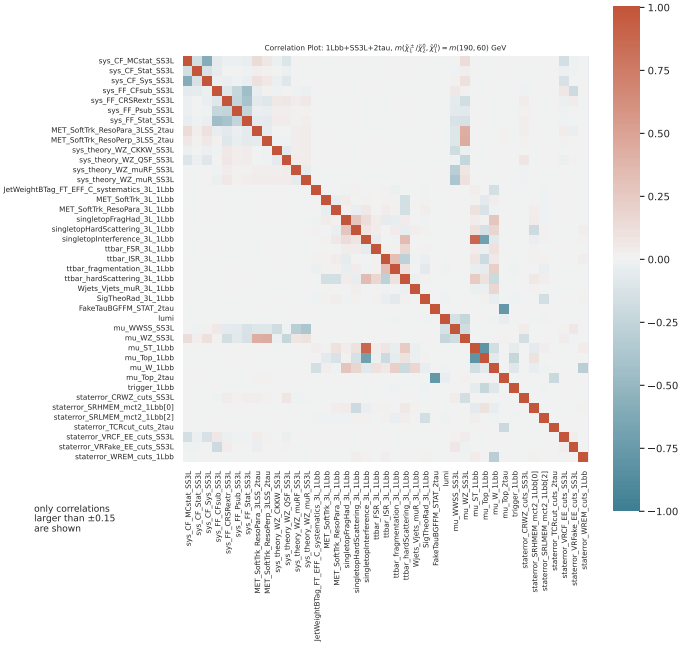

(b)

Figure 7.23: Correlation matrices for the leading correlated uncertainties for (a) the $(m(\tilde{\chi}_2^0), m(\tilde{\chi}_1^0)) = (400,100)$ GeV and (b) the $(m(\tilde{\chi}_2^0), m(\tilde{\chi}_1^0)) = (190,60)$ GeV signal points. Only nuisance parameters with at least one correlation larger than ± 0.15 are shown.

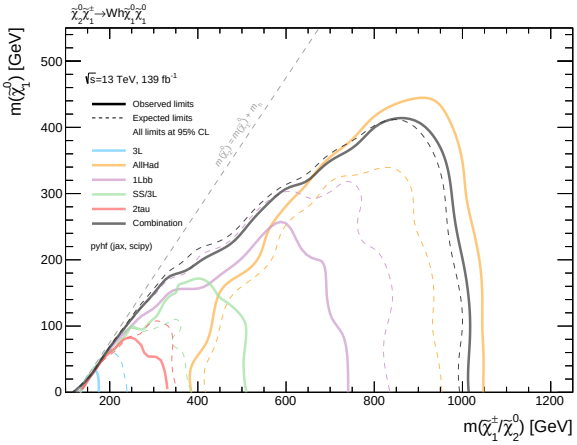

(a)

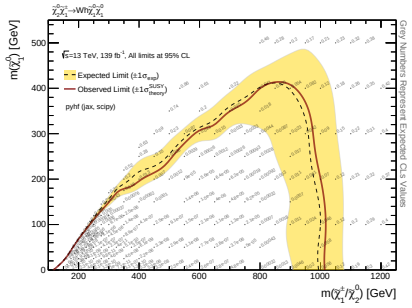

(b)

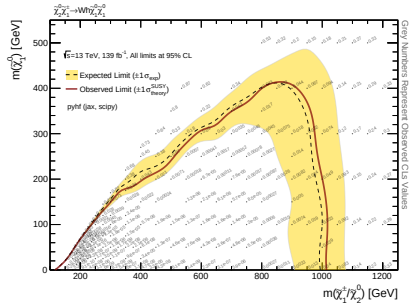

(c)

Figure 7.24: 95% CL exclusion limits for the initial combination with all systematic uncertainties set to be uncorrelated across the analyses, (a) with exclusion limits for the individual analyses overlaid, (b) with the combined expected CL_s value for each signal point overlaid, and (c) with the combined observed CL_s value for each signal point overlaid.

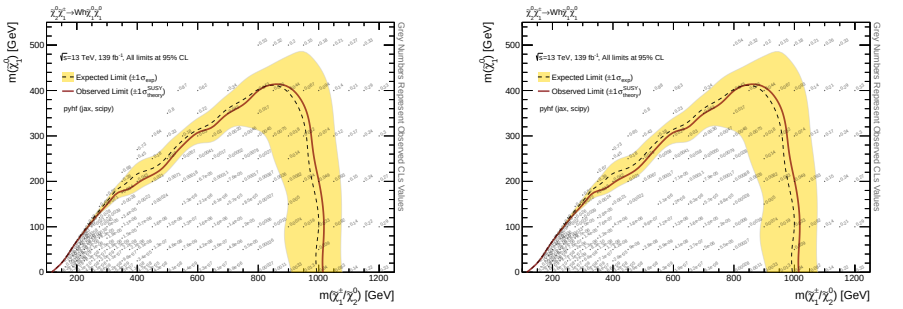

(a) (b)

Figure 7.25: 95% CL exclusion limits for the combination, with the combined observed CL_s value for each signal point overlaid, for (a) the uncorrelated scenario and (b) the correlated scenario, applying the correlation scheme reported in Table 7.3.

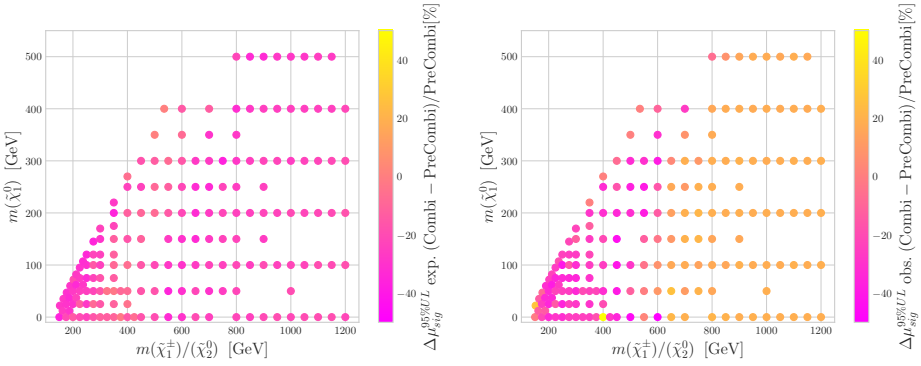

(a) (b)

Figure 7.26: Relative difference in the 95% CL upper limit on the signal strength (μ_s^{UL}) from the combination (uncorrelated scenario) with respect to the best performing single analysis for each signal point: (a) expected limits, (b) observed limits.

7.4 Summary and outlook

This chapter summarized my contribution to the ATLAS Collaboration's effort on statistically combining results of searches for electroweak SUSY using the full Run 2 dataset, for which a resulting paper is in the pipeline. Such combinations can extend and deepen the sensitivity offered by each analysis alone. I was in charge of investigating and performing combinations for two simplified models, namely higgsino $\tilde{\chi}_1^{\pm}\tilde{\chi}_2^0$ pair production decaying via W and Z bosons, and wino $\tilde{\chi}_1^{\pm}\tilde{\chi}_2^0$ pair production decaying via W and h bosons.

We began by giving an introduction to statistical combinations, covering statistical independence, signal grid harmonization, as well as tool and workflow. Then followed a summary of my work for the higgsino $\tilde{\chi}_1^{\pm}\tilde{\chi}_2^0$ via WZ simplified model. For this model, an initial combination of the results for two analyses had already been performed and published, and the plan for the combination effort described in this chapter was to include a third analysis in the combination. However, as this analysis progressed, it became clear that no improvement beyond the initial combination was expected from it. Instead, we reproduced the results of the initial combination to verify the setup, before moving to a novel combination for the wino $\tilde{\chi}_1^{\pm}\tilde{\chi}_2^0$ via Wh simplified model. After introducing the five analyses considered in the combination,[4] the orthogonality of the analyses was scrutinized, before reproducing the original analysis results. We then described how workspaces for additional signal points for some of the analyses were obtained using RECAST, in order to get a meaningful overlap of signal points for the combination. An initial combination was performed with all systematic uncertainties set to be uncorrelated across the analyses, before assessing the impact of correlating uncertainties. As the results were effectively the same, the uncorrelated scenario will be used in the upcoming paper.

Some lessons learned from this combination work will be summarized in the following. Not having a common naming scheme for systematic uncertainties ready in time for the commencement of the different analyses intended for combination resulted in a significant additional workload for the combination team. In total, close to 1,000 systematic uncertainties were involved in the combination fit for the wino $\tilde{\chi}_1^{\pm}\tilde{\chi}_2^0$ via Wh simplified model, and assessing which of these should and should not be correlated was a complicated task. Further, running RECAST to produce workspaces for additional signal points for some of the analyses ended up taking much longer than first anticipated. As described in Section 7.3.3, the idea behind RECAST is clear, but the necessary freedom in the design of the RECAST implementation of an analysis complicates the usage. However, maybe the designers could be reminded to think carefully about which parameters should be hard-coded/configurable, and encouraged to also provide workspaces and not only fit-results directly? Also, as most of the combination setup can be tested using preliminary workspaces, the different analysis teams should make workspaces available as soon as possible, even if they are not final.

[4] In the upcoming paper, an additional analysis will be included in the combination for the wino $\tilde{\chi}_1^{\pm}\tilde{\chi}_2^0$ via Wh simplified model. This analysis was not completed at the time the work described in this chapter was carried out.

This chapter concludes the part on searching for chargino–neutralino pair production. In the next chapter, the focus shifts from physics analysis to outreach and communication activities.

Part III

Outreach and communication

Chapter 8

ATLAS authorship qualification task on ATLAS@Home

In order to become an ATLAS author, meaning that one's name appears on the author list of all papers published by the ATLAS Collaboration, one has to fulfill a set of criteria. One of these criteria is to spend at least 80 working days on a so-called qualification task of technical work. Such tasks are typically work that is valuable to (or even necessary for) the collaboration, but not directly part of a physics analysis. I did my qualification task on the ATLAS@Home project [24–26], starting March 1, 2018, and finishing March 1, 2019. My local and technical supervisors were David Cameron and Andrej Filipčič, respectively.

This chapter will summarize my qualification task. In Section 8.1, the ATLAS@Home project will be introduced, including its software and architecture. In Section 8.2, the work I performed on this project to qualify as an ATLAS author will be described.

8.1 ATLAS@Home

ATLAS@Home was started in 2013, and has since 2017 been part of the larger LHC@Home project [27, 28]. As explained in Chapter 4, simulated data is an essential ingredient when doing physics analysis. Simulation of LHC physics is also important in other contexts, e.g. for improving the design of future accelerators. Most simulation is done using the Worldwide LHC Computing Grid (WLCG) [124, 125], which is a global collaboration of around 170 computing centres in more than 40 countries. However, as the WLCG has limited resources that are also used for other tasks, the idea behind LHC@Home is to allow volunteers to help out by running Monte Carlo simulation on their private computers. At the time of writing, LHC@Home consists of four different subprojects related to all aspects of LHC: beams, theory and experiments, including ATLAS@Home. For ATLAS@Home, the combined volunteers' resources actually make up a sizeable fraction of the overall resources for ATLAS detector simulation — 4.5% in 2018, when this qualification task was carried out.[1]

In addition to the "free" computing resources, LHC@Home also serves as an outreach project by letting the general public contribute to and feel part of

[1]This number actually includes ATLAS@Home being run in WLCG computing centres in addition to on private computers. In 2017, ATLAS@Home was further developed to enable running on grid worker nodes which for many reasons cannot be used to 100% of their CPU capacity. See Refs. [26, 203] for more information on this. However, the focus of the ATLAS@Home introduction given here will be on volunteers running ATLAS@Home on their private computers.

high energy physics experiments. As a means to the latter, a graphical interface has been developed for ATLAS@Home, showing some basic information on the physics relevant for ATLAS, in addition to personalized information on the volunteer's contribution. My qualification task regarded enhancing this graphical interface. Details will be given below, after the ATLAS@Home software and architecture have been introduced.

8.1.1 Software and architecture

As the majority of all volunteer computing projects, LHC@Home is using the free and open-source software BOINC (Berkeley Open Infrastructure for Network Computing) [204], which has a server–client architecture. The server hosts tasks or work units to be processed, while the client pulls and runs work units from the specified project (e.g. ATLAS@Home). Each work unit downloads a small set of input data and runs for several hours, depending on the computer and the number of cores used for the job. Once a work unit is processed, the client sends the result back to the server for validation. If the result is good, motivational credit is awarded to the volunteer. The BOINC client can be configured to run only when the volunteer's private computer is not in use, or to run at the lowest priority when the computer is in use.

In addition to BOINC, the virtualization software VirtualBox [205] is needed for ATLAS@Home, which is also free and open-source. VirtualBox allows for the creation of so-called virtual machines (VMs) inside the volunteer's private computer, which can run operating systems independently of the hardware-installed operating system. CERN software packages, like the detector simulation software used for ATLAS@Home, are often large with complex dependencies that cannot be easily ported to the volunteer's operating system. CERN has therefore developed the CERN Virtual Machine (CernVM) [206] for running such software. Additionally, using virtualization adds an extra layer of security: the volunteer's private computer will not be affected by any potential faults in the physics software. Figure 8.1 shows the basic ATLAS@Home architecture.

Graphical interface

The ATLAS@Home graphical interface is a web service running inside the virtual machine, accessed through the computer's web browser. It is built on JavaScript, mainly with the p5.js library [208]. Through visual and interactive animations, users can access information about high energy physics in general, the ATLAS experiment and the ATLAS@Home project itself. Since the interface runs inside the same virtual machine as the work unit/task, it can present task- and volunteer-specific information. Figure 8.2 shows screenshots of some example pages of the graphical interface.

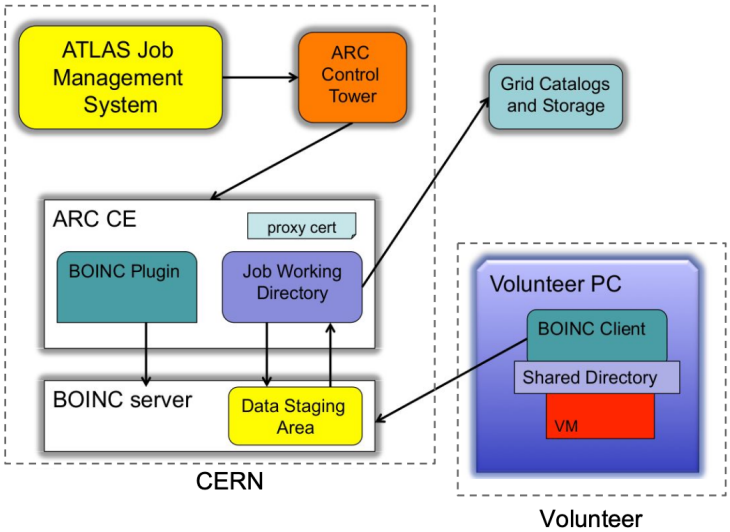

Figure 8.1: The basic ATLAS@Home architecture [207].

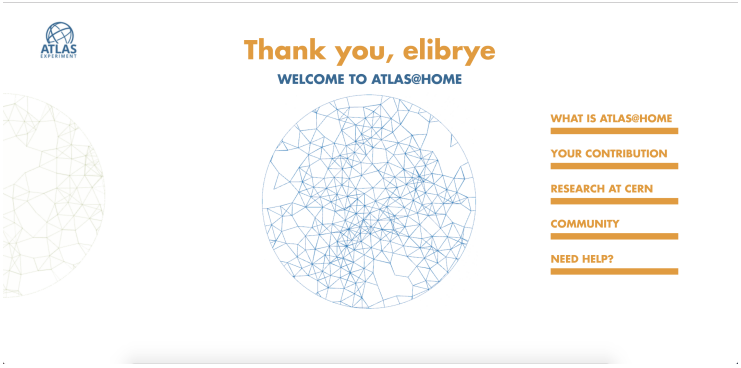

(a)

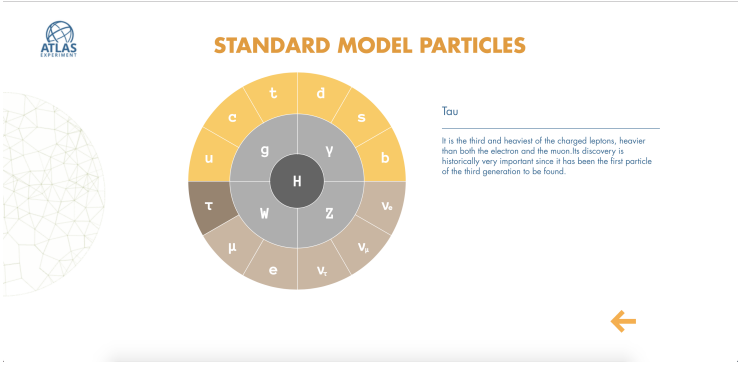

(b)

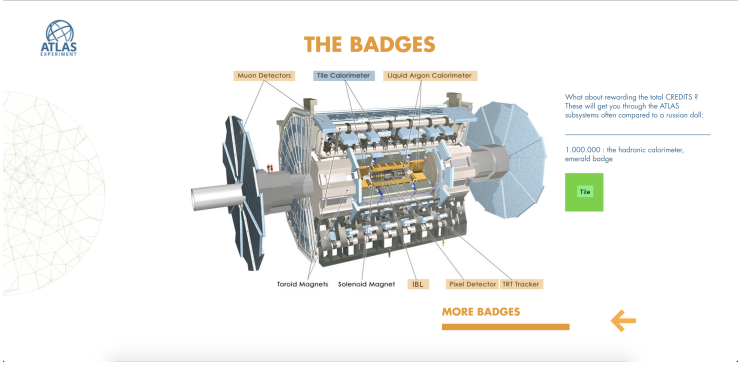

(c)

Figure 8.2: Screenshots of the ATLAS@Home graphical interface: (a) welcome page, (b) example of Standard Model information page and (c) example of "bagde" page for rewarding volunteers.

8.2 Enhancing the ATLAS@Home graphical interface

As stated above, my qualification task regarded enhancing the ATLAS@Home graphical interface. The task description is given below.

> **Enhanced graphical interface and workloads for ATLAS@Home**
> ATLAS@Home allows the general public to take part in ATLAS computing by allowing them to run Monte Carlo simulation on their home PCs. A key factor in attracting people and keeping them involved is visualization of the simulation tasks they are running. A graphics portal was recently developed which shows basic information on the physics behind ATLAS, the Standard Model, some sample visualizations and links to further information on ATLAS outreach pages.
>
> The proposed qualification task enhances this interface to provide live information on the events that are being simulated using the VP1 (Virtual Point 1) visualization framework, allowing people to see in real-time what their PCs are doing. This requires understanding what is necessary to integrate VP1 into the ATLAS@Home environment as well as how to modify the tasks to use it when necessary. Technical information on the running tasks such as CPU and memory usage should also be shown, as well as information on the overall status of ATLAS@Home tasks (e.g. rate of completion) and how each contributor matches up to others.
>
> ATLAS@Home runs MC simulation because it provides a reliable source of easy-to-run tasks (low memory and not data intensive). Event generation would also suit the requirements for ATLAS@Home but there is a large variation in the types of event generation run in ATLAS in terms of time per event and also in the supply of work. An extension to this task is to investigate ways of selecting suitable event generation tasks which could run on ATLAS@Home, testing these tasks and collecting feedback from the volunteers, to evaluate the potential of running event generation in the future.

To summarize, the plan was to add a couple of new features to the ATLAS@Home graphical interface:

1. Technical and task information in the form of run time and CPU and memory usage of the running task, as well as rate of completion.
2. Live event displays of events being simulated. (This part was not finalized, details below.)

Two important and time-consuming first steps was to learn JavaScript, which I did not know in advance, and to understand how the graphical interface code was set up so that I could add the desired features.

8.2.1 Adding technical and task information

For the technical and task information, I wrote a PYTHON script that extracts the relevant run time, CPU and memory information for the individual virtual machine cores running the task. This information is stored where the JAVASCRIPT code can access it, and is displayed in a table in the graphical interface. The script also extract information about the task completion, which is displayed as a progress bar in the graphical interface. The script is run in a cron job every minute, updating the table and the progress bar on the fly. Figure 8.3 shows screenshots of the table and the progress bar in the graphical interface.

8.2.2 Adding live event displays

The graphical interface was already showing some sample event displays, see Figure 8.4. The plan for the qualification task was to add *live* displays, showing events actually being simulated on the volunteer's computer. This was a more complicated exercise than adding the technical and task information described in Section 8.2.1, as it involved adding event display software to the workflow.

VIRTUAL POINT 1 (VP1) [209] is an interactive 3D event display software for the ATLAS experiment that is part of the main offline software framework for ATLAS called ATHENA [210]. All real and simulated events can thus be accessed and visualized with VP1. If run in so-called batch mode (no live graphics), which would be the case here, the desired "view" can be obtained using a configuration file with pre-saved settings. Further, a "random mode" was added to VP1 for the purpose of using this software with ATLAS@Home, where a random configuration file is chosen from a pool of files. The initial idea was to add a button in the graphical interface that the volunteers can press if they actually want live event displays. However, for simplicity, we decided to always run VP1. But to avoid consuming too many resources for the virtual machine, we decided to run VP1 only once, when a given number of events are ready (~ 10).

The output of ATLAS detector simulation are files in the so-called HITS-format, as shown in Figure 4.2. Such HITS files are the input to VP1. By default, each of the virtual machine cores produces a separate HITS file with the events it has simulated, which is updated on the fly. These files are later merged into one final HITS file. The initial plan was to run VP1 on the HITS file of one of the cores as soon as it has simulated the desired number of events. However, during testing, we found out that VP1 can not be run on a HITS file still being written to by the simulation software. After discussing our challenges with ATHENA experts, they suggested running the simulation software in a special mode where each event is written to a separate HITS file that is closed immediately, which can then be used for input to VP1 as soon as the event is finalized. As VP1 can run on multiple input files, this would still allow for running VP1 only once. I also checked that the run time of the simulation software did not change significantly for the default mode and this special mode. The only concern was that the merging into one final HITS file does not happen

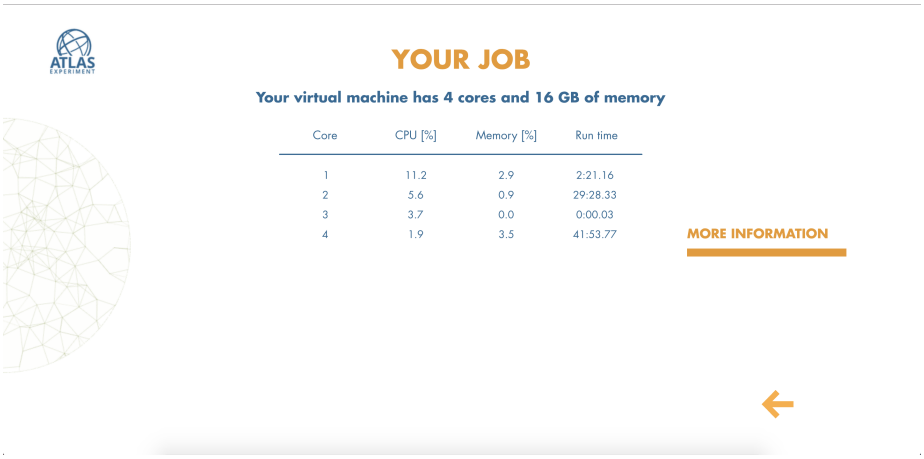

(a)

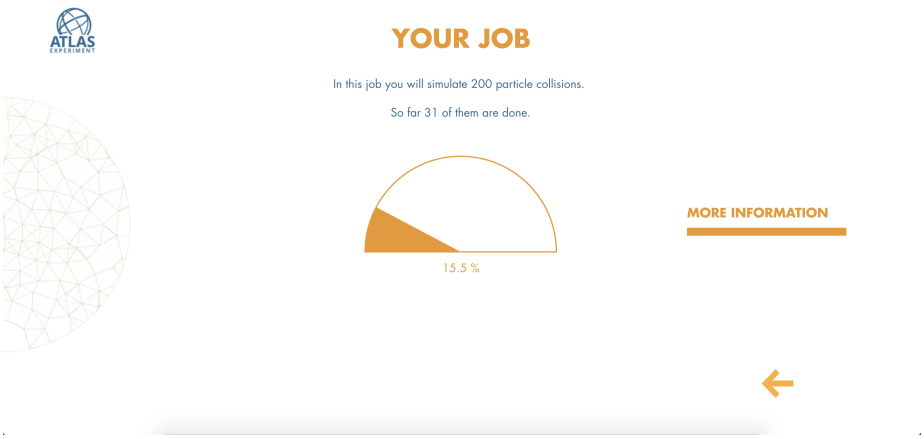

(b)

Figure 8.3: Screenshots of new features added to the ATLAS@Home graphical interface: (a) table with run time, CPU and memory information for the individual virtual machine cores running the task, and (b) progress bar indicating the task completion rate.

automatically when the simulation software is run in this special mode, so this has to be taken care of somehow.

For checking the number of finalized events and running VP1, I wrote a Bash script. The simulation software produces and updates a text file named "eventLoopHeartBeat.txt" for each core, containing the number of processed events. In the bash script, these files are checked every 30 seconds, to determine if the total number of simulated events for all cores is above the desired threshold.

Figure 8.4: Screenshot of graphical interface page showing sample event displays.

When the threshold is reached, VP1 is run, producing event displays for all finalized events. The displays are then renamed so that the JavaScript code can access them. Finally, the script fills a text file, indicating to the JavaScript code that the event displays are ready, so that they can be displayed in the graphical interface.

As my qualification period came to an end, this bash script was ready, but a few things still needed to be tested and validated. First, even though VP1 should be able to run on multiple input files, I did not get this to work at the time, as VP1 kept ignoring all input files except the first one. However, this was later solved by the VP1 developer working with us. Second, after running the simulation software in the special mode producing single-event HITS files, it was not straightforward how to merge all events into a final HITS file in a way that was satisfactory for all steps of the full workflow. At the time of writing, the live event display feature still has not been added to the graphical interface due to lack of personpower.

8.3 Summary

This chapter summarized my ATLAS authorship qualification task on the ATLAS@Home project, in which volunteers can run Monte Carlo simulation on their private computers. In addition to making use of "free" computing resources, ATLAS@Home serves as an outreach project by letting the general public contribute to and feel part of the experiment. My qualification task regarded enhancing the graphical interface developed for ATLAS@Home, which shows information about high energy physics in general, the ATLAS experiment and the ATLAS@Home project itself through visual and interactive animations. The plan was for me to add a couple of new features to this graphical interface:

(1) technical and task information in the form of run time and CPU and memory usage of the running task, as well as rate of completion, and (2) live event displays of events being simulated. I successfully implemented the former. The latter turned out to be more complicated than first anticipated, and I did not manage to finish it within my qualification period. Due to lack of personpower for the ATLAS@Home project, this feature has still not been added.

Chapter 9

Communicating physics

As described in the Introduction to this thesis, I have contributed to multiple communication, outreach and recruitment activities during the course of my Ph.D. In addition to believing that such activities are important, I truly enjoy them. When I started my Ph.D. research fellowship at the University of Oslo, I was asked by the communications adviser at the Department of Physics, Hilde Lynnebakken, if I wanted to work with her on recruitment and communicating physics instead of the usual 25% teaching duties required for a four-year fellowship.[1,2] Hilde was looking for some extra hands at the time and thought I would be a good fit. After settling this arrangement with the department's management, I ended up working with Hilde for the full 25% of mandatory duties, contributing to a variety of activities. As there is generally a big interest in universe-related topics among the general public, my particle-physics background came in handy. But I also found it very interesting to work with people and topics from other fields of physics.

This chapter will summarize the different communication, outreach and recruitment activities I have contributed to, starting with the 2019 Norwegian media visit to CERN in Section 9.1. Further, Sections 9.2 and 9.3 will give an overview of the different radio shows and podcasts I have visited and outreach talks I have given, respectively. In Section 9.4, the various social media series Hilde and I have created will be described. Finally, activities that do not fit any of the above-mentioned categories will be listed in Section 9.5.

9.1 Norwegian media visit to CERN

The probably most noteworthy activity directly related to particle physics was organizing a Norwegian two-day media visit to CERN in October 2019. Such national media visits were offered to all member states, candidate member states, associate member states and observer states during the long shutdown of the LHC after Run 2. They were arranged to ease the pressure on the CERN press office with handling individual requests, but also to maximize the amount of press to spike interest in CERN activities. The target media was print press and

[1] A Ph.D. research fellowship at the University of Oslo is usually of three years duration, but if the candidate has the necessary qualifications (e.g. speaking a Scandinavian language) and based on the teaching need of the department, the candidate can apply for an additional 25% teaching duty resulting in a total length of the fellowship of four years.

[2] During my bachelor's and master's studies, also at the University of Oslo, I had contributed to recruitment projects both for the Faculty of Mathematics and Natural Sciences in general and the Department of Physics in particular. See e.g. Youtube video "Studieprogrammet Fysikk, astronomi og meteorologi – FAM" from 2014, promoting the bachelor's program "Physics, Astronomy and Meteorology", and video "Universitetet i Oslo er ledende på databeregninger i utdanningen" from 2015, about computing in science education at the University of Oslo.

radio. For the Norwegian visit, I was in charge of inviting journalists, planning the program, and inviting and corresponding with contributors of all types. During the visit, I functioned as a tour guide. I also ended up being interviewed for some of the resulting articles and such myself.

A total of 10 journalists participated — a number we were quite happy with considering that they had to fund their own trip and money is tight in the media business these days. Most of them were science and/or research journalists from NRK[3] Viten, NRK Ekko, Khrono, forskning.no and Teknisk Ukeblad. Further, some of the journalists were affiliated with university media, such as Under Dusken, Apollon and titan.uio.no. A total of 17 people contributed during the visit, ranging from master students to professors, from the University of Oslo, the University of Bergen, the Norwegian University of Science and Technology, and CERN.

The program consisted of a mix of visits and talks. Underground, we visited the CMS experiment, the ALICE experiment and the LHC tunnel itself. Above ground, we visited the CERN Data Centre, the CERN Linear Electron Accelerator for Research (CLEAR) and the Antimatter Factory. The talks had a wide range of topics, such as "Hot or not — What's trendy in particle physics", "Big Data meets Big Science — How particle physicists do computing", "High-Luminosity LHC — How the machine that gave us the Higgs particle is becoming even more badass" and "What happens after the LHC?". The full program can be found here: https://indico.cern.ch/event/855625/.

The visit was a huge success, with happy participants and a lot of press resulting from it. A list of articles and such are given in Appendix B.

9.2 Radio and podcasts

Over the years, I have been invited to participate in a few popular science radio shows and podcasts. Although not directly related to my work with Hilde, these visits fit to be mentioned here.

9.2.1 Abels tårn and Abels forgård

"Abels tårn"[4] is a weekly hour-long live science radio show airing on NRK P2 every friday. It is recorded at the Science Library at the University of Oslo, with audience in the room. The concept is that a panel of three scientists answer questions sent in in advance by listeners, either by e-mail or to the Facebook page of the show. Each panelist prepares answers for three to four questions before the show.

[3] NRK is short for Norsk rikskringkasting AS, i.e. the Norwegian Broadcasting Corporation, the public service broadcaster in Norway.

[4] "Abel's tower", named after the Norwegian matematician Nils Henrik Abel and the mythical Tower of Babel.

I have been a panelist three times: June 14, 2019, November 7, 2020 and May 7, 2021,[5] where I answered questions about e.g. photons, antimatter and the Higgs boson, but also questions not related to particle physics. In addition, a special episode on only CERN-related topics was recorded during the media visit described in the Section 9.1,[6] in which I also participated.[7] In this episode, which aired on December 13, 2019, we answered questions such as "How can a particle without mass exist?" and "Where do the LHC protons come from?".

Further, I was the guest on "Abels forgård" on May 7, 2021.[8] This is a more in-depth interview with a scientist about a particular topic, airing the hour before "Abels tårn". I was interviewed about supersymmetry and visiting CERN as a researcher, but also about my summer job of the last 20 years as a milk maid ("budeie") at a summer farm in the mountains, where I have been milking cows and making brown cheese (a Norwegian speciality).[9]

9.2.2 Jøss!?

One of the most famous Norwegian physicists among the general public today is Andreas Wahl. His podcast "Jøss!?"[10] is a science fun-fact competition. In each episode, a few people in addition to Andreas himself present a fun fact each (fun or mind-blowing, preferably both), before there is a vote on which fact has the biggest wow-factor.

I have participated in three episodes. In the first episode, released October 1, 2021, I talked about the fact that microwave ovens were invented for the purpose of re-heating frozen hamsters in the laboratory in the 1950s.[11] In the second episode, released December 11, 2021, I talked about the infamous measurement of faster-than-light neutrinos by the OPERA experiment in 2011.[12] In the third episode, recorded live at the Science Library at the University of Oslo on May 3, 2023, I talked about the infamous 1896 "Crash at Crush" publicity stunt in Texas [211], in which two people died.[13]

[5] "Hvorfor håndballspillere er dårlige i håndball, og syklister har så store hoder", "Kan Torkild hypnotiseres til høne?" and "Tørste fisk, antimaterie og andre søte skapninger".

[6] The host of "Abels tårn" (part of NRK Ekko), Torkild Jemterud, participated in the media visit.

[7] "CERN spesial — Eksisterer vi, egentlig?".

[8] "Budeie og partikkelfysiker".

[9] After this interview I was invited to Norway's biggest morning TV show "God morgen Norge", to come talk about being both a particle physicist and a milk maid. But the focus of this TV interview, airing June 9, 2021, was mostly on my experience as a milk maid.

[10] "Jøss!?" can be translated into "Wow!?".

[11] "Rosa edderkopp, frosne hamstre og rullegardin for jorda".

[12] "Omelett med slegge og q-tips, Einstens fartsgrense, og Andreas ville veid mer om han ble født i Oslo".

[13] Løgn for å beskytte robotfølelser, regnefeil med døden til følge, frukthandler i 8 dimensjoner, og molekylvekten til promp.

9.2.3 God fysikk

A fellow Ph.D. student at the University of Oslo, Ida Storehaug, started a podcast named "God fysikk" ("Good physics") in 2022. In this podcast, Ida interviews young researchers on topics in particle physics, astrophysics and theoretical physics, in Norwegian. The target audience are people who know some physics in advance, i.e. the level is a bit higher than "regular" popular science. I was invited to come talk about supersymmetry, and the result was a 39 minute long episode released on February 17, 2022.[14]

9.3 Outreach talks

I have given many outreach talks on particle physics in different settings at the University of Oslo during the course of my Ph.D. Particle physics and the universe in general are very popular themes for such talks.

Every spring, the University of Oslo hosts an open day, aimed at everyone interested in studies at the university. The program consists of mini-lectures, stands, "speed dates" with students, and other activities. Several thousand high school students from the Oslo area attend this event each year. Both in 2018 and 2020, I was invited to hold a mini-lecture on particle physics and dark matter. Between 50 and 100 students attended these lectures, and I received many interesting questions afterwards.

Every semester, high-school students studying physics are invited to the department for a full-day physics seminar. The program consists of popular-science talks on topics relevant for the high-school physics curriculum, in addition to information on career opportunities for physicists and how it is like to study physics. I gave presentations on particle physics at such seminars in the fall of 2017, both spring and fall of 2018, and the spring of 2019.

In August every year, the new students at the department attend a "research safari", where they visit the different research groups to get an introduction to the research being performed there. I was involved in the presentation of the high energy physics group in both 2018 and 2019.

The International Physics Olympiad (IPhO) is an annual competition in physics for high-school students. The Norwegian final is hosted by the Department of Physics at the University of Oslo. Before the final, the candidates attend a week-long course at the department, where they among other things attend popular-science lectures. I gave a lecture on supersymmetry for the 2019 finalists.

The University of Oslo also hosts an open day for teachers every year, which is free and open for everyone working in the school system. Each department arranges a full day of lectures with relevant and engaging topics. I gave presentations on particle physics during this event in 2018 and 2020.

[14] "Sexy supersymmetri!".

9.4 Social media series

Over the years, Hilde and I have produced several series for social media, both to display the research taking place at the department, and to recruit students to the department's studies at all levels.

"Fysikkjærleik" ("Physics love") is a series of ten videos where different physicists at the department, ranging from early-year students to professors, explain why they love physics. This series was created for Instagram in the fall of 2018, and was also published on Facebook. The idea behind the series was to showcase different reasons for why physicists of all ages love their field.

"Eli besøker fysikere på jobben" ("Eli visits physicists at work") is a series of twelwe so-called stories (videos consisting of multiple slides of photos and short video clips) where physicists with different jobs explain what they do for a living, what their physics background is and how it is useful. This series was created for Instagram Stories in the spring of 2019, and was also published as videos on Facebook. The idea behind the series was to showcase a selection of the many interesting jobs one can get as a physicist.

"Min master" ("My master's") is a series of nine stories, where master students are interviewed about their master's project. This series was created for Instagram Stories in the spring of 2020, and was also published as videos on Facebook. The goal of the series was to recruit students to the master studies at our department.

"Fysikkfavoritt" ("Physics favorite") was a summer series during the pandemic in 2020. Eleven physicists recorded a minute-long video themselves, about their favorite topic in physics. The videos were published on Instagram and Facebook.

Finally, we created a series of nine stories where we interviewed scientists about a particular topic, such as fission, quantum technology, and shape-memory alloys. This series was published on Instagram Stories in the fall of 2020 and the spring of 2021. The idea behind the series was to give more in-depth introductions (but still popular science) to some interesting topics.

9.5 Other

"Fysikk på biblioteket" ("Physics at the Library") is a lecture series arranged at the Science Library at the University of Oslo. During my Ph.D., I was part of the team planning and arranging these lectures. In particular, I was in charge of inviting Dr. Ben Still, author of the popular science book "Particle Physics Brick by Brick", who came and gave a lecture on particle physics in 2019: "How to build a LEGO universe". Other lectures related to particle physics include "The journey to quantum gravity" by Carlo Rovelli, "How beauty leads physics astray" by Sabine Hossenfelder and "Emmy og symmetriene" ("Emmy and the symmetries") by Anders Kvellestad.

In March 2018, Hilde and I organized the event "Pitch your Ph.D." for the Ph.D. fellows at the department, led by presentation coach Torunn Meyer. During this event, the participants got tips and tricks on how to present their research

in different situations, focusing on tools such as storytelling, body language, variation and voice. They practiced presenting their own work and received group feedback. The event lasted a full day. Approximately 30 Ph.D. and postdoctoral fellows at the department participated, and gave the event good feedback.

At the time of writing, "Writing Science" is a mandatory course for all first-year master students at the department. In this course, the students learn how to write about physics, and the aim is to help them write their master thesis project plan before the December 1 deadline each year. When this course was arranged for the first time back in 2018, it was a pilot project. The sessions were then led by Åsmund Eikenes, who designed the concept. My role was to follow the sessions and write a report to the department summing up what worked well and what could be improved. The following year, I was in charge of the course from the department's side. I had regular meetings with the five second-year master students then leading the sessions, and also participated in some of the sessions myself.

Every year, more than 13,000 high school students in more than 50 countries take part in International Masterclasses [212], an initiative by the International Particle Physics Outreach Group (IPPOG). Here, the students get hands-on experience in particle physics by analyzing real data from different experiments, including the four large LHC experiments. The program begins with lectures on particle physics in general and on the methods used to analyze particle physics data, before the students get to analyze data themselves. In Norway, the students analyze open data from the ATLAS experiment [213], by following the so-called "Z-path" [214], which was developed at the University of Oslo. I helped out as a tutor in the hands-on sessions during the masterclasses at the University of Oslo in 2018 and 2019.

9.6 Summary and outlook

This final chapter summarized the various communication, outreach and recruitment activities I have taken part in during the course of this Ph.D. People with a background in the natural sciences are needed more than ever, but in Norway, the number of applications to science teacher education programs and physics bachelor's programs have been declining in recent years. Such activities are therefore important.

I began by summarizing the Norwegian media visit to CERN in 2019, before describing the different radio shows and podcasts I have visited. Then followed a summary of the different outreach talks I have given at various events over the years, as well as a description of the recruitment series Hilde and I have produced for social media. Finally, other activities not fitting any of the above-mentioned categories were listed, such as arranging the lecture series "Fysikk på biblioteket" ("Physics at the Library") and helping out as a tutor in the International Masterclasses.

Next year, in 2024, CERN celebrates 70 years. Many different events are

planned to celebrate this anniversary, both at CERN and in the member states. The goal is to ensure awareness of CERN and support for the organization's future. As CERN communication is part of my new job as administrative coordinator for the Norwegian center for CERN-related research (NorCC), I will be one of the contact persons for "CERN70" in Norway.[15]

Further, in the spring of 2022, before the start of LHC's Run 3, Hilde and I were planning a so-called virtual visit to the ATLAS experiment. This virtual visit was canceled due to the pandemic, but we might come back to this idea. If so, the visit will be organized in collaboration with the CERN press office. The plan would be to send live with the Instagram account of the department,[16] with Hilde filming and me in front of the camera. We would start outside by the Globe, explaining (in Norwegian) where we are and what the plan is, before moving inside to the ATLAS Visitor Center and then underground to look at the detector.

[15]Together with Hilde, who is Norway's representative in the European Particle Physics Communication Network (EPPCN).

[16]Instagram Live is a feature that lets you live stream or broadcast video to your Instagram followers in real-time.

Conclusions

Searching for chargino–neutralino pair production

The main topic of this thesis has been the search for supersymmetry, one of the most popular theories for physics beyond the Standard Model of particle physics. More specifically, the search for chargino–neutralino ($\tilde{\chi}_1^{\pm}\tilde{\chi}_2^0$) pair production using the full Run 2 dataset of $\sqrt{s} = 13$ TeV proton–proton collisions collected by the ATLAS detector at the Large Hadron Collider between 2015 and 2018. This dataset corresponds to an integrated luminosity of 139 fb^{-1}.

Work and results from two different analysis working groups within the ATLAS Collaboration have been presented. First, this thesis presented a search for chargino–neutralino pair production in final states with three leptons and missing transverse momentum, resulting in Ref. [22]. In this search, three simplified-model scenarios of $\tilde{\chi}_1^{\pm}\tilde{\chi}_2^0$ pair production were considered and analyzed separately, referred to as the on-shell WZ analysis, the off-shell WZ analysis and the Wh analysis. This thesis focused on the off-shell WZ analysis, for which three different physics interpretations of the $\tilde{\chi}_1^{\pm}\tilde{\chi}_2^0$ search were considered, referred to as the wino/bino (+) interpretation, the wino/bino (−) interpretation and the higgsino interpretation. No significant deviations from Standard Model predictions were seen for any of the interpretations, and the results were used to set limits. Exclusion limits at 95% confidence level were presented for the three-lepton off-shell WZ analysis alone, but also for statistical combinations of the results for the three-lepton off-shell WZ analysis, the on-shell WZ analysis and the compressed two-lepton analysis from Ref. [173]. The obtained results extend previous results by a large margin. For a pure higgsino $\tilde{\chi}_1^{\pm}\tilde{\chi}_2^0$ scenario, limits are set on $\tilde{\chi}_2^0$ masses up to 210 GeV. For a pure wino $\tilde{\chi}_1^{\pm}\tilde{\chi}_2^0$ scenario, limits are set on $\tilde{\chi}_2^0$ masses up to 640 GeV for decays via on-shell W and Z bosons, up to 300 GeV for decays via off-shell W and Z bosons, and up to 190 GeV for decays via W and Standard Model Higgs bosons.

Second, this thesis presented a statistical combination of results from multiple searches that all target production of a pure-wino $\tilde{\chi}_1^{\pm}\tilde{\chi}_2^0$ pair decaying via W and h bosons, but using different final states. Results from five different analyses were combined: the `3L` analysis (mentioned above as the Wh analysis), the `all-hadronic` analysis [195], the `1Lbb` analysis [196], the `2tau` analysis [197] and the `SS/3L` analysis [198]. The objective of such combinations is to extend the sensitivity offered by each analysis alone. Projected onto the $m(\tilde{\chi}_1^{\pm}/\tilde{\chi}_2^0)$ vs. $m(\tilde{\chi}_1^0)$ plane, the observed combined 95% CL exclusion contour extends the contours for the individual analyses in the area near the kinematic limit $\Delta m(\tilde{\chi}_2^0, \tilde{\chi}_1^0) = m_h$, but for large $\tilde{\chi}_2^0$ masses, it falls within the contour of the best performing single analysis (`all-hadronic`), due to one of the other analyses

experiencing an excess (`1Lbb`). This work is part of a larger effort on statistical combinations of searches for electroweak supersymmetry, which at the time of writing has a resulting paper in the pipeline.

Also two studies based on the three-lepton off-shell WZ analysis conducted in preparation for future runs of the LHC have been presented. The first study concerned the decision on the final ATLAS hardware trigger architecture for the High-Luminosity LHC, where one of the options would allow for lowering the offline $E_{\mathrm{T}}^{\mathrm{miss}}$ trigger threshold from 200–210 GeV to 160 GeV. The study, not taking into account the extra luminosity of the HL-LHC and without a dedicated reoptimization to make use of the additional low-$E_{\mathrm{T}}^{\mathrm{miss}}$ events, showed that the three-lepton off-shell WZ analysis would benefit materially from such a lowering. In the region with low $\Delta m(\tilde{\chi}_2^0, \tilde{\chi}_1^0)$, the significance was improved by up to 30%. This region is of particular interest, as it can predict the observed relic density of dark matter, and has not yet been excluded. In addition, this region covers the sensitivity gap in parameter space found between the three-lepton off-shell WZ analysis and the compressed two-lepton analysis. However, as the trigger-architecture decision relied on many other factors, such as cost and complexity, the ATLAS Collaboration ultimately decided to go for a different option.

The second study concerned the new ATLAS derivation data format, DAOD_PHYS. To save disk space, as many ATLAS analyses as possible should move to using this new baseline format from Run 3 onwards. The study, comparing distributions produced using the DAOD_PHYS format to distributions produced using the Run 2 DAOD_SUSY2 format, uncovered an inconsistency in the trigger-matching procedure between the two formats, affecting low-p_{T} muons. This inconsistency was reported to the relevant community within the collaboration.

In conclusion, no signs of electroweak supersymmetry have been observed in the work presented in this thesis. However, there are exciting times ahead, with the LHC experiments expecting more data and higher energies. Run 3 of the LHC is currently ongoing, with a record-breaking collision energy of 13.6 TeV, and the full Run 3 dataset is expected to be of similar size or larger than that of Run 2. Further, the era of the High-Luminosity LHC is quickly approaching. The HL-LHC is expected to operate at a collision energy up to 14 TeV and to produce more than ten times more data than Run 2 and Run 3 combined. With this new data we hope to extend the reach of supersymmetry searches in the three-lepton channel with ATLAS, and to probe important parts of the parameter space that have avoided current searches, such as the low $\Delta m(\tilde{\chi}_2^0, \tilde{\chi}_1^0)$ region, which can still accommodate a WIMP dark-matter candidate.

And telling people about it

This thesis has also summarized the various communication, outreach and recruitment activities I have taken part in during the course of this Ph.D. My ATLAS authorship qualification task was on the ATLAS@Home project, which

in addition to making use of "free" computing resources serves as an outreach project by letting the general public contribute to and feel part of the experiment. My qualification task regarded enhancing the graphical interface developed for ATLAS@Home. Other activities included organizing the Norwegian media visit to CERN in 2019, giving outreach talks at different events, and producing social-media series with the aim of recruiting students to the Department of Physics at the University of Oslo.

In Norway, the number of applicants to science teacher programs and physics bachelor's programs have been declining in recent years. At the same time, people with a background in the natural sciences are needed more than ever. Outreach and recruitment activities are therefore an important investment in the future.

Appendices

Appendix A

Acceptance and efficiency plots and cutflows for the wino/bino $(-)$ and higgsino interpretations

Acceptance and efficiency plots for the wino/bino (+) interpretation were shown in Figures 5.13 and 5.14 in Section 5.7. Corresponding plots for the wino/bino (−) and higgsino interpretations are shown in Figures A.1 and A.2, and Figures A.3 and A.4, respectively.

Further, cutflows for the wino/bino (+) interpretation were shown in Tables 5.9, 5.10 and 5.11 in Section 5.7. Corresponding cutflows for the wino/bino (−) and higgsino interpretations are shown in Tables A.1, A.2 and A.3, and Tables A.4, A.5 and A.6, respectively.

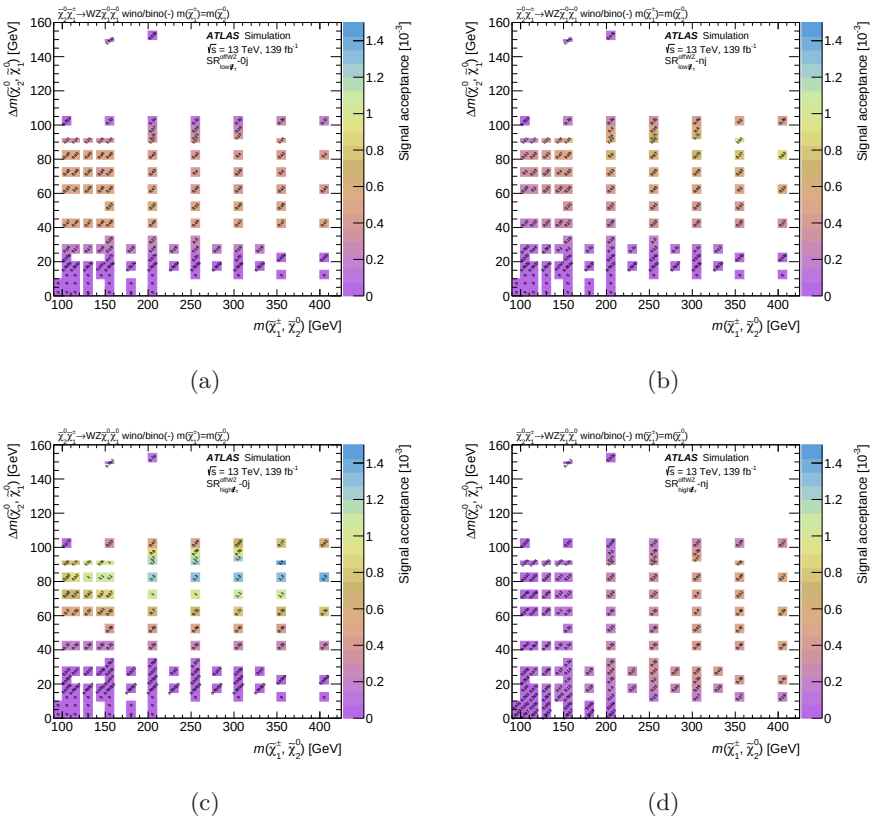

Figure A.1: Truth-level acceptances for the four inclusive off-shell WZ signal regions (a) $\mathtt{SR}^{\mathtt{offWZ}}_{\mathtt{low}E_{\mathrm{T}}^{\mathrm{miss}}}\mathtt{-0j}$, (b) $\mathtt{SR}^{\mathtt{offWZ}}_{\mathtt{low}E_{\mathrm{T}}^{\mathrm{miss}}}\mathtt{-nj}$, (c) $\mathtt{SR}^{\mathtt{offWZ}}_{\mathtt{high}E_{\mathrm{T}}^{\mathrm{miss}}}\mathtt{-0j}$ and (d) $\mathtt{SR}^{\mathtt{offWZ}}_{\mathtt{high}E_{\mathrm{T}}^{\mathrm{miss}}}\mathtt{-nj}$ for the wino/bino $(-)$ scenario.

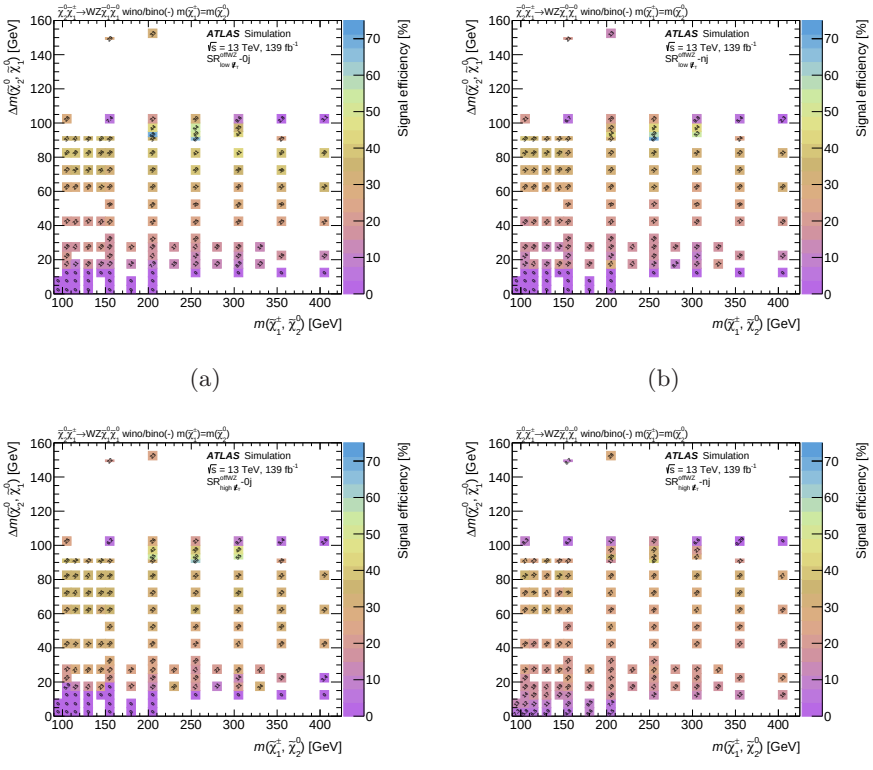

Figure A.2: Reconstruction efficiencies for the four inclusive off-shell WZ signal regions (a) $\mathtt{SR}^{\mathtt{offWZ}}_{\mathtt{low}E_{\mathrm{T}}}\mathtt{-0j}$, (b) $\mathtt{SR}^{\mathtt{offWZ}}_{\mathtt{low}E_{\mathrm{T}}}\mathtt{-nj}$, (c) $\mathtt{SR}^{\mathtt{offWZ}}_{\mathtt{high}E_{\mathrm{T}}}\mathtt{-0j}$ and (d) $\mathtt{SR}^{\mathtt{offWZ}}_{\mathtt{high}E_{\mathrm{T}}}\mathtt{-nj}$ for the wino/bino $(-)$ scenario.

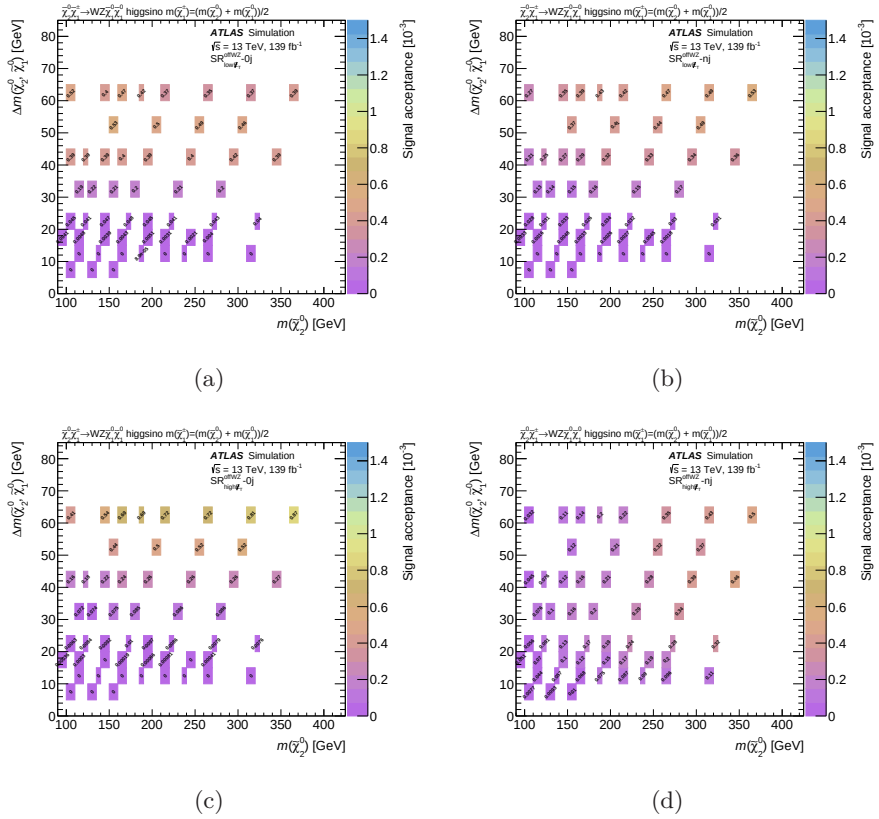

Figure A.3: Truth-level acceptances for the four inclusive off-shell WZ signal regions (a) $\mathtt{SR}^{\mathtt{offWZ}}_{\mathtt{low}E_{\mathrm{T}}^{\mathrm{miss}}}\mathtt{-0j}$, (b) $\mathtt{SR}^{\mathtt{offWZ}}_{\mathtt{low}E_{\mathrm{T}}^{\mathrm{miss}}}\mathtt{-nj}$, (c) $\mathtt{SR}^{\mathtt{offWZ}}_{\mathtt{high}E_{\mathrm{T}}^{\mathrm{miss}}}\mathtt{-0j}$ and (d) $\mathtt{SR}^{\mathtt{offWZ}}_{\mathtt{high}E_{\mathrm{T}}^{\mathrm{miss}}}\mathtt{-nj}$ for the higgsino scenario.

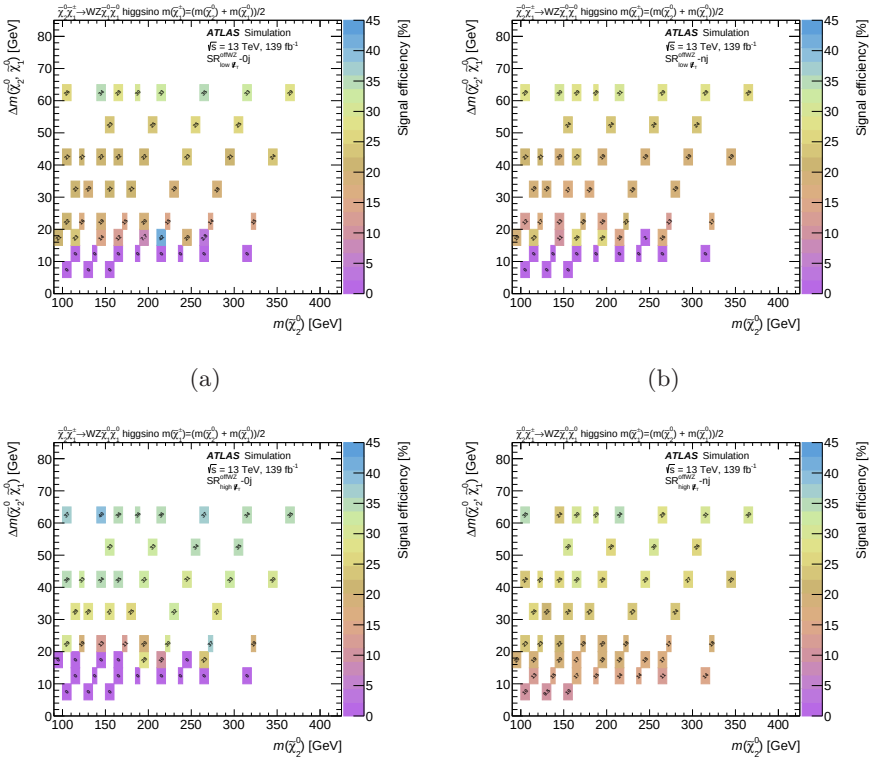

Figure A.4: Reconstruction efficiencies for the four inclusive off-shell WZ signal regions (a) $\mathtt{SR}^{\mathtt{offWZ}}_{\mathtt{low}E_{\mathrm{T}}^{\mathrm{miss}}}\mathtt{-0j}$, (b) $\mathtt{SR}^{\mathtt{offWZ}}_{\mathtt{low}E_{\mathrm{T}}^{\mathrm{miss}}}\mathtt{-nj}$, (c) $\mathtt{SR}^{\mathtt{offWZ}}_{\mathtt{high}E_{\mathrm{T}}^{\mathrm{miss}}}\mathtt{-0j}$ and (d) $\mathtt{SR}^{\mathtt{offWZ}}_{\mathtt{high}E_{\mathrm{T}}^{\mathrm{miss}}}\mathtt{-nj}$ for the higgsino scenario.

Table A.1: Cutflow for the off-shell WZ event selection for the $(m(\tilde{\chi}_2^0), m(\tilde{\chi}_1^0)) = (125{,}85)$ GeV signal point for the wino/bino $(-)$ scenario. The yields are normalized to a luminosity $\mathcal{L}$ of 139 fb^{-1}. MC-to-data efficiency weights from triggering and from the reconstruction and identification of individual physics objects are applied to the final yields in each signal region. After the initial selections, the table is split in row blocks for the inclusive $\mathrm{SR}^{\mathtt{offWZ}}_{\mathtt{low}\not{E}_{\mathrm{T}}}$-`0j`, $\mathrm{SR}^{\mathtt{offWZ}}_{\mathtt{low}\not{E}_{\mathrm{T}}}$-`nj`, $\mathrm{SR}^{\mathtt{offWZ}}_{\mathtt{high}\not{E}_{\mathrm{T}}}$-`0j`, $\mathrm{SR}^{\mathtt{offWZ}}_{\mathtt{high}\not{E}_{\mathrm{T}}}$-`nj` regions, with the individual signal region yields in columns. The inclusive OR of regions a through g2 is given in the last column. Selection details per bin are indicated in bracketed blue as relevant, and the final yields for each signal region is highlighted in bold green at the end of each block. The “3 isolated lepton selection” includes the preselection as described in Section 4.3 and the initial SFOS lepton pair selection.

$\tilde{\chi}_1^\pm\tilde{\chi}_2^0 \to WZ\tilde{\chi}_1^0\tilde{\chi}_1^0$ wino/bino (-)										m($\tilde{\chi}_2^0$,$\tilde{\chi}_1^0$) = (125, 85) GeV									
		a		**b**		**c**		**d**		**e**		**f1**		**f2**		**g1**		**g2**	**a through g2**
Common cuts																			
$\mathcal{L}\times\sigma$										1394866									1394866
$\mathcal{L}\times\sigma\times$BF										45634									45634
$\mathcal{L}\times\sigma\times$BF$\times$ filt. eff.										16811									16811
3 isolated lepton selection										2.25e+03									2.25e+03
b-veto										2.16e+03									2.16e+03
Trigger selection										1.52e+03									1.52e+03
$m_{\ell\ell}$, $m_{\ell\ell}^{\mathrm{max}}$ [GeV]									[< 75]	1.51e+03									1.51e+03
Common cuts $\mathrm{SR}^{\mathtt{offWZ}}_{\mathtt{low}\not{E}_{\mathrm{T}}}$																			
$m_{\ell\ell}^{\mathrm{min}}$ [GeV]		-	[∈ [12, 40]]	1.36e+03							[∈ [40, 75]]	1.37							1.36e+03
lepton $p_{\mathrm{T}}^{1,2,3}$ [GeV]		-	[> 10]	1.12e+03							[> 15]	0.690							1.13e+03
FNP lepton cleaning (conversions)		-		869								0.384							870
$m_{\ell\ell}^{\mathrm{max}}$ [GeV]		-	[< 60]	795								0.384							795
$m_{\ell\ell}^{\mathrm{min}}$ [GeV]		-	[∈ [12, 15]]	84.7	[∈ [15, 20]]	176	[∈ [20, 30]]	383	[∈ [30, 40]]	152	[∈ [40, 60]]	0.384			[∈ [60, 75]]	0			795
m_{T2}^{100} [GeV]		-	[< 115]	34.3	[< 120]	109	[< 130]	354		152		0.384				0			650
minΔR		-	[< 1.6]	34.3	[< 1.6]	108	[< 1.6]	295		152		0.384				0			591
Cuts $\mathrm{SR}^{\mathtt{offWZ}}_{\mathtt{low}\not{E}_{\mathrm{T}}}$-0j																			
$n_{\mathrm{jets}}^{p_{\mathrm{T}}>30\,\mathrm{GeV}}$		-	[= 0]	20.3	[= 0]	73.4	[= 0]	186	[= 0]	96.4	[= 0]	0.262			[= 0]	0			376
$E_{\mathrm{T}}^{\mathrm{miss}}$ [GeV]		-	[< 50]	18.3	[< 50]	62.6	[< 50]	144	[< 50]	78.6	[< 50]	0.183			[< 50]	0			304
$E_{\mathrm{T}}^{\mathrm{miss}}$ signif.		-	[> 1.5]	14.4	[> 1.5]	51.2	[> 1.5]	121	[> 1.5]	59.7	[> 1.5]	0.127			[> 1.5]	0			246
$m_{3\ell}$ [GeV]		-		14.4		51.2		121		59.7	[> 100]	5.50e-02			[> 100]	0			246
$m_{\mathrm{T}}^{\mathrm{minmll}}$ [GeV]		-	[< 50]	14.4	[< 50]	48.4	[< 50]	96.2	[< 60]	52.1	[< 60]	4.90e-02	[> 90]	0	[< 60]	0	[> 90]	0	211
$p_{\mathrm{T}}^{\mathrm{lep}}/E_{\mathrm{T}}^{\mathrm{miss}}$		-	[< 1.1]	9.42	[< 1.1]	32.4	[< 1.1]	62.2	[< 1.3]	45.2	[< 1.4]	4.90e-02	[< 1.4]	0	[< 1.4]	0	[< 1.4]	0	149
MC-to-data eff. weights		**-**		**8.72**		**28.8**		**57.5**		**41.4**		**4.40e-02**		**0**		**0**		**0**	**136**
Cuts $\mathrm{SR}^{\mathtt{offWZ}}_{\mathtt{low}\not{E}_{\mathrm{T}}}$-nj																			
$n_{\mathrm{jets}}^{p_{\mathrm{T}}>30\,\mathrm{GeV}}$		-	[> 0]	14.0	[> 0]	34.9	[> 0]	110	[> 0]	55.7	[> 0]	0.122			[> 0]	0			215
$E_{\mathrm{T}}^{\mathrm{miss}}$ [GeV]		-	[< 200]	12.9	[< 200]	31.3	[< 200]	102	[< 200]	51.9	[< 200]	0.122			[< 200]	0			198
$E_{\mathrm{T}}^{\mathrm{miss}}$ signif.		-	[> 3.0]	9.06	[> 3.0]	23.7	[> 3.0]	76.4	[> 3.0]	37.4	[> 3.0]	8.50e-02			[> 3.0]	0			147
$m_{\mathrm{T}}^{\mathrm{minmll}}$ [GeV]		-	[< 50]	5.79	[< 50]	16.7	[< 50]	43.6	[< 60]	22.6	[< 60]	5.80e-02	[> 90]	0	[< 60]	0	[> 90]	0	88.6
$p_{\mathrm{T}}^{\mathrm{lep}}/E_{\mathrm{T}}^{\mathrm{miss}}$		-	[< 1.0]	5.27	[< 1.0]	16.4	[< 1.0]	36.5	[< 1.0]	20.4	[< 1.2]	5.50e-02	[< 1.2]	0	[< 1.2]	0	[< 1.2]	0	78.6
MC-to-data eff. weights		**-**		**4.82**		**15.6**		**33.9**		**17.9**		**5.10e-02**		**0**		**0**		**0**	**72.3**
Cuts $\mathrm{SR}^{\mathtt{offWZ}}_{\mathtt{high}\not{E}_{\mathrm{T}}}$-0j																			
lepton $p_{\mathrm{T}}^{1,2,3}$ [GeV]									[> 25, 15, 10]	955									955
$m_{\ell\ell}^{\mathrm{min}}$ [GeV]		-	[∈ [12, 15]]	89.8	[∈ [15, 20]]	198	[∈ [20, 30]]	417	[∈ [30, 40]]	181	[∈ [40, 60]]	0.764			[∈ [60, 75]]	9.70e-02			887
m_{T2}^{100} [GeV]		-	[< 115]	38.7	[< 120]	129	[< 130]	386	[< 140]	181	[< 160]	0.764			[< 175]	9.70e-02			735
$n_{\mathrm{jets}}^{p_{\mathrm{T}}>30\,\mathrm{GeV}}$		-	[= 0]	23.4	[= 0]	84.4	[= 0]	239	[= 0]	114	[= 0]	0.556			[= 0]	9.70e-02			461
$E_{\mathrm{T}}^{\mathrm{miss}}$ [GeV]		-	[> 50]	4.68	[> 50]	18.0	[> 50]	54.7	[> 50]	25.2	[> 50]	0.104			[> 50]	0			103
$E_{\mathrm{T}}^{\mathrm{miss}}$ signif.		-	[> 3.0]	4.09	[> 3.0]	16.3	[> 3.0]	49.7	[> 3.0]	22.9	[> 3.0]	9.30e-02			[> 3.0]	0			93.1
$m_{\mathrm{T}}^{\mathrm{minmll}}$ [GeV]		-	[< 50]	3.95	[< 50]	15.4	[< 60]	46.4	[< 60]	19.7	[< 70]	9.30e-02	[> 90]	0	[< 70]	0	[> 90]	0	85.6
MC-to-data eff. weights		**-**		**4.18**		**14.2**		**43.0**		**18.4**		**8.80e-02**		**0**		**0**		**0**	**79.8**
Cuts $\mathrm{SR}^{\mathtt{offWZ}}_{\mathtt{high}\not{E}_{\mathrm{T}}}$-nj																			
lepton $p_{\mathrm{T}}^{1,2,3}$ [GeV]									[>4.5,3]	1.51e+03									1.51e+03
												f				**g**			
$m_{\ell\ell}^{\mathrm{min}}$ [GeV]	[∈ [1, 12]]	154	[∈ [12, 15]]	153	[∈ [15, 20]]	318	[∈ [20, 30]]	635	[∈ [30, 40]]	250	[∈ [40, 60]]	1.27			[∈ [60, 75]]	9.70e-02			1.51e+03
m_{T2}^{100} [GeV]	[< 112]	47.2	[< 115]	65.1	[< 120]	203	[< 130]	588	[< 140]	249	[< 160]	1.27			[< 175]	9.70e-02			1.15e+03
$n_{\mathrm{jets}}^{p_{\mathrm{T}}>30\,\mathrm{GeV}}$	[> 0]	17.6	[> 0]	30.3	[> 0]	79.9	[> 0]	243	[> 0]	97.8	[> 0]	0.433			[> 0]	0			470
$E_{\mathrm{T}}^{\mathrm{miss}}$ [GeV]	[> 200]	1.51	[> 200]	3.52	[> 200]	8.38	[> 200]	22.0	[> 200]	7.86	[> 200]	6.00e-03			[> 200]	0			43.3
$E_{\mathrm{T}}^{\mathrm{miss}}$ signif.	[> 3.0]	1.51	[> 3.0]	3.52	[> 3.0]	8.38	[> 3.0]	22.0	[> 3.0]	7.86	[> 3.0]	6.00e-03			[> 3.0]	0			43.3
$p_{\mathrm{T}}^{\mathrm{lep}}/E_{\mathrm{T}}^{\mathrm{miss}}$	[< 0.2]	1.25	[< 0.2]	3.36	[< 0.3]	7.85	[< 0.3]	14.4	[< 0.3]	4.64	[< 1.0]	6.00e-03			[< 1.0]	0			31.5
MC-to-data eff. weights		**1.24**		**3.18**		**7.44**		**13.4**		**4.23**		**6.00e-03**				**0**			**29.5**

Table A.2: Cutflow for the off-shell WZ event selection for the $(m(\tilde{\chi}_2^0), m(\tilde{\chi}_1^0)) = (250{,}170)$ GeV signal point for the wino/bino $(-)$ scenario. The yields are normalized to a luminosity $\mathcal{L}$ of 139 fb^{-1}. MC-to-data efficiency weights from triggering and from the reconstruction and identification of individual physics objects are applied to the final yields in each signal region. After the initial selections, the table is split in row blocks for the inclusive $\mathtt{SR}^{\mathtt{offWZ}}_{\mathtt{low}\not{E}_T}\mathtt{\text{-}0j}$, $\mathtt{SR}^{\mathtt{offWZ}}_{\mathtt{low}\not{E}_T}\mathtt{\text{-}nj}$, $\mathtt{SR}^{\mathtt{offWZ}}_{\mathtt{high}\not{E}_T}\mathtt{\text{-}0j}$, $\mathtt{SR}^{\mathtt{offWZ}}_{\mathtt{high}\not{E}_T}\mathtt{\text{-}nj}$ regions, with the individual signal region yields in columns. The inclusive OR of regions a through g2 is given in the last column. Selection details per bin are indicated in bracketed blue as relevant, and the final yields for each signal region is highlighted in bold green at the end of each block. The "3 isolated lepton selection" includes the preselection as described in Section 4.3 and the initial SFOS lepton pair selection.

$\tilde{\chi}_1^\pm\tilde{\chi}_2^0 \to WZ\tilde{\chi}_1^0\tilde{\chi}_1^0$ wino/bino (-)										m($\tilde{\chi}_2^0$,$\tilde{\chi}_1^0$) = (250, 170) GeV									
		a		**b**		**c**		**d**		**e**		**f1**		**f2**		**g1**		**g2**	**a through g2**
Common cuts																			
$\mathcal{L}\times\sigma$										108769									108769
$\mathcal{L}\times\sigma\times$BF										3559									3559
$\mathcal{L}\times\sigma\times$BF $\times$ filt. eff.										1638									1638
3 isolated lepton selection										422									422
b-veto										405									405
Trigger selection										338									338
$m_{\ell\ell}$, $m_{\ell\ell}^{\max}$ [GeV]									[< 75]	332									332
Common cuts $\mathrm{SR}^{\mathtt{offWZ}}_{\mathtt{low}\not{E}_T}$																			
$m_{\ell\ell}^{\min}$ [GeV]		-					[∈ [12, 40]]	116							[∈ [40, 75]]	212			328
lepton $p_T^{1,2,3}$ [GeV]		-					[> 10]	101							[> 15]	163			263
FNP lepton cleaning (conversions)		-						75.3								126			201
$m_{\ell\ell}^{\max}$ [GeV]		-					[< 60]	62.2								126			188
$m_{\ell\ell}^{\min}$ [GeV]		-	[∈ [12, 15]]	2.02	[∈ [15, 20]]	5.79	[∈ [20, 30]]	20.7	[∈ [30, 40]]	33.7	[∈ [40, 60]]	77.3			[∈ [60, 75]]	48.6			188
m_{T2}^{100} [GeV]		-	[< 115]	8.40e-02	[< 120]	1.34	[< 130]	8.17		33.7		77.3				48.6			169
minΔR		-	[< 1.6]	8.40e-02	[< 1.6]	1.33	[< 1.6]	7.70		33.7		77.3				48.6			169
Cuts $\mathrm{SR}^{\mathtt{offWZ}}_{\mathtt{low}\not{E}_T}\mathtt{\text{-}0j}$																			
$n_{\mathrm{jets}}^{p_T>30\,\mathrm{GeV}}$		-	[= 0]	6.30e-02	[= 0]	1.08	[= 0]	4.70	[= 0]	20.7	[= 0]	44.7			[= 0]	29.2			100
E_T^{miss} [GeV]		-	[< 50]	5.20e-02	[< 50]	0.692	[< 50]	2.85	[< 50]	8.15	[< 50]	18.9			[< 50]	14.2			44.9
E_T^{miss} signif.		-	[> 1.5]	2.70e-02	[> 1.5]	0.692	[> 1.5]	2.62	[> 1.5]	7.08	[> 1.5]	16.3			[> 1.5]	12.4			39.1
$m_{3\ell}$ [GeV]		-		2.70e-02		0.692		2.62		7.08	[> 100]	12.6			[> 100]	11.3			34.3
m_T^{minmll} [GeV]		-	[< 50]	2.70e-02	[< 50]	0.678	[< 50]	1.51	[< 60]	4.05	[< 60]	7.24	[> 90]	1.87	[< 60]	6.12	[> 90]	1.68	23.2
$p_T^{\mathrm{lep}}/E_T^{\mathrm{miss}}$		-	[< 1.1]	2.70e-02	[< 1.1]	0.530	[< 1.1]	0.804	[< 1.3]	3.20	[< 1.4]	6.22	[< 1.4]	1.68	[< 1.4]	5.33	[< 1.4]	1.60	19.4
MC-to-data eff. weights		**-**		**2.70e-02**		**0.623**		**0.711**		**3.16**		**5.73**		**1.64**		**5.00**		**1.52**	**18.4**
Cuts $\mathrm{SR}^{\mathtt{offWZ}}_{\mathtt{low}\not{E}_T}\mathtt{\text{-}nj}$																			
$n_{\mathrm{jets}}^{p_T>30\,\mathrm{GeV}}$		-	[> 0]	2.10e-02	[> 0]	0.243	[> 0]	3.00	[> 0]	13.0	[> 0]	32.6			[> 0]	19.4			68.3
E_T^{miss} [GeV]		-	[< 200]	2.10e-02	[< 200]	0.243	[< 200]	2.62	[< 200]	11.4	[< 200]	29.0			[< 200]	17.1			60.4
E_T^{miss} signif.		-	[> 3.0]	1.90e-02	[> 3.0]	0.243	[> 3.0]	2.31	[> 3.0]	9.53	[> 3.0]	24.4			[> 3.0]	14.0			50.5
m_T^{minmll} [GeV]		-	[< 50]	7.00e-03	[< 50]	0.193	[< 50]	1.40	[< 60]	2.88	[< 60]	8.61	[> 90]	9.19	[< 60]	4.74	[> 90]	5.79	32.8
$p_T^{\mathrm{lep}}/E_T^{\mathrm{miss}}$		-	[< 1.0]	7.00e-03	[< 1.0]	0.193	[< 1.0]	1.31	[< 1.0]	1.65	[< 1.2]	6.18	[< 1.2]	8.11	[< 1.2]	3.81	[< 1.2]	5.29	26.5
MC-to-data eff. weights		**-**		**6.00e-03**		**0.191**		**1.26**		**1.53**		**5.70**		**7.53**		**3.50**		**5.01**	**24.7**
Cuts $\mathrm{SR}^{\mathtt{offWZ}}_{\mathtt{high}\not{E}_T}\mathtt{\text{-}0j}$																			
lepton $p_T^{1,2,3}$ [GeV]									[> 25, 15, 10]	295									295
$m_{\ell\ell}^{\min}$ [GeV]		-	[∈ [12, 15]]	3.45	[∈ [15, 20]]	9.11	[∈ [20, 30]]	32.5	[∈ [30, 40]]	52.1	[∈ [40, 60]]	123			[∈ [60, 75]]	73.5			294
m_{T2}^{100} [GeV]		-	[< 115]	0.432	[< 120]	2.34	[< 130]	13.5	[< 140]	29.8	[< 160]	111			[< 175]	72.9			230
$n_{\mathrm{jets}}^{p_T>30\,\mathrm{GeV}}$		-	[= 0]	0.307	[= 0]	1.56	[= 0]	7.56	[= 0]	17.6	[= 0]	66.6			[= 0]	43.8			137
E_T^{miss} [GeV]		-	[> 50]	3.70e-02	[> 50]	0.505	[> 50]	2.88	[> 50]	6.67	[> 50]	35.3			[> 50]	22.0			67.4
E_T^{miss} signif.		-	[> 3.0]	3.70e-02	[> 3.0]	0.479	[> 3.0]	2.42	[> 3.0]	6.35	[> 3.0]	34.0			[> 3.0]	21.0			64.3
m_T^{minmll} [GeV]		-	[< 50]	7.00e-03	[< 50]	0.466	[< 60]	2.00	[< 60]	4.11	[< 70]	14.0	[> 90]	11.5	[< 70]	8.74	[> 90]	7.28	48.1
MC-to-data eff. weights		**-**		**6.00e-03**		**0.400**		**1.97**		**3.88**		**13.3**		**10.9**		**7.93**		**6.87**	**45.2**
Cuts $\mathrm{SR}^{\mathtt{offWZ}}_{\mathtt{high}\not{E}_T}\mathtt{\text{-}nj}$																			
lepton $p_T^{1,2,3}$ [GeV]									[>4.5,3]	332									332
												f				**g**			
$m_{\ell\ell}^{\min}$ [GeV]	[∈ [1, 12]]	3.97	[∈ [12, 15]]	5.27	[∈ [15, 20]]	12.4	[∈ [20, 30]]	39.9	[∈ [30, 40]]	58.8	[∈ [40, 60]]	134			[∈ [60, 75]]	77.5			332
m_{T2}^{100} [GeV]	[< 112]	0.660	[< 115]	0.611	[< 120]	3.06	[< 130]	15.9	[< 140]	33.6	[< 160]	121			[< 175]	76.9			252
$n_{\mathrm{jets}}^{p_T>30\,\mathrm{GeV}}$	[> 0]	0.529	[> 0]	0.288	[> 0]	1.14	[> 0]	7.21	[> 0]	14.3	[> 0]	49.3			[> 0]	31.4			104
E_T^{miss} [GeV]	[> 200]	0.231	[> 200]	4.00e-03	[> 200]	0.214	[> 200]	1.40	[> 200]	1.34	[> 200]	5.32			[> 200]	4.13			12.6
E_T^{miss} signif.	[> 3.0]	0.231	[> 3.0]	4.00e-03	[> 3.0]	0.214	[> 3.0]	1.40	[> 3.0]	1.34	[> 3.0]	5.32			[> 3.0]	4.07			12.6
$p_T^{\mathrm{lep}}/E_T^{\mathrm{miss}}$	[< 0.2]	1.50e-02	[< 0.2]	4.00e-03	[< 0.3]	0.214	[< 0.3]	1.05	[< 0.3]	0.866	[< 1.0]	5.17			[< 1.0]	3.95			11.3
MC-to-data eff. weights		**1.30e-02**		**4.00e-03**		**0.235**		**0.995**		**0.857**		**4.76**				**3.58**			**10.5**

Table A.3: Cutflow for the off-shell WZ event selection for the $(m(\tilde{\chi}_2^0), m(\tilde{\chi}_1^0)) = (250{,}235)$ GeV signal point for the wino/bino $(-)$ scenario. The yields are normalized to a luminosity $\mathcal{L}$ of 139 fb^{-1}. MC-to-data efficiency weights from triggering and from the reconstruction and identification of individual physics objects are applied to the final yields in each signal region. After the initial selections, the table is split in row blocks for the inclusive $\mathtt{SR}^{\mathtt{offWZ}}_{\mathtt{low}\not{E}_\mathrm{T}}\mathtt{\text{-}0j}$, $\mathtt{SR}^{\mathtt{offWZ}}_{\mathtt{low}\not{E}_\mathrm{T}}\mathtt{\text{-}nj}$, $\mathtt{SR}^{\mathtt{offWZ}}_{\mathtt{high}\not{E}_\mathrm{T}}\mathtt{\text{-}0j}$, $\mathtt{SR}^{\mathtt{offWZ}}_{\mathtt{high}\not{E}_\mathrm{T}}\mathtt{\text{-}nj}$ regions, with the individual signal region yields in columns. The inclusive OR of regions a through g2 is given in the last column. Selection details per bin are indicated in bracketed blue as relevant, and the final yields for each signal region is highlighted in bold green at the end of each block. The “3 isolated lepton selection” includes the preselection as described in Section 4.3 and the initial SFOS lepton pair selection.

$\tilde{\chi}_1^\pm\tilde{\chi}_2^0 \to WZ\tilde{\chi}_1^0\tilde{\chi}_1^0$ wino/bino (-)	m($\tilde{\chi}_2^0$,$\tilde{\chi}_1^0$) = (250, 235) GeV																			
		a		**b**		**c**		**d**		**e**		**f1**		**f2**		**g1**		**g2**		**a through g2**
Common cuts																				
$\mathcal{L}\times\sigma$		108769																		108769
$\mathcal{L}\times\sigma\times$BF		3559																		3559
$\mathcal{L}\times\sigma\times$BF$\times$filt. eff.		992																		992
3 isolated lepton selection		32.2																		32.2
b-veto		30.1																		30.1
Trigger selection		15.4																		15.4
$m_{\ell\ell}$, $m_{\ell\ell}^{\mathrm{max}}$ [GeV]	[< 75]	15.2																		15.2
Common cuts $\mathrm{SR}^{\mathtt{offWZ}}_{\mathtt{low}\not{E}_\mathrm{T}}$																				
$m_{\ell\ell}^{\mathrm{min}}$ [GeV]		-	[∈ [12, 40]]	1.85							[∈ [40, 75]]	0								1.85
lepton $p_\mathrm{T}^{1,2,3}$ [GeV]		-	[> 10]	0.626							[> 15]	0								0.626
FNP lepton cleaning (conversions)		-		0.566								0								0.566
$m_{\ell\ell}^{\mathrm{max}}$ [GeV]		-	[< 60]	0.529								0								0.529
$m_{\ell\ell}^{\mathrm{min}}$ [GeV]		-	[∈ [12, 15]]	0.528	[∈ [15, 20]]	1.00e-03	[∈ [20, 30]]	0	[∈ [30, 40]]	0	[∈ [40, 60]]	0			[∈ [60, 75]]	0				0.529
m_{T2}^{100} [GeV]		-	[< 115]	0.511	[< 120]	1.00e-03	[< 130]	0		0		0				0				0.512
minΔR		-	[< 1.6]	0.511	[< 1.6]	1.00e-03	[< 1.6]	0		0		0				0				0.512
Cuts $\mathrm{SR}^{\mathtt{offWZ}}_{\mathtt{low}\not{E}_\mathrm{T}}$-0j																				
$n_{\mathrm{jets}}^{p_\mathrm{T}>30\,\mathrm{GeV}}$		-	[= 0]	0.219	[= 0]	1.00e-03	[= 0]	0	[= 0]	0	[= 0]	0			[= 0]	0				0.220
$E_\mathrm{T}^{\mathrm{miss}}$ [GeV]		-	[< 50]	0.206	[< 50]	1.00e-03	[< 50]	0	[< 50]	0	[< 50]	0			[< 50]	0				0.207
$E_\mathrm{T}^{\mathrm{miss}}$ signif.		-	[> 1.5]	0.113	[> 1.5]	0	[> 1.5]	0	[> 1.5]	0	[> 1.5]	0			[> 1.5]	0				0.113
$m_{3\ell}$ [GeV]		-		0.113		0		0		0	[> 100]	0			[> 100]	0				0.113
$m_\mathrm{T}^{\mathrm{minmll}}$ [GeV]		-	[< 50]	0.113	[< 50]	0	[< 50]	0	[< 60]	0	[< 60]	0	[> 90]	0	[< 60]	0	[> 90]	0		0.113
$p_\mathrm{T}^{\mathrm{lep}}/E_\mathrm{T}^{\mathrm{miss}}$		-	[< 1.1]	9.40e-02	[< 1.1]	0	[< 1.1]	0	[< 1.3]	0	[< 1.4]	0	[< 1.4]	0	[< 1.4]	0	[< 1.4]	0		9.40e-02
MC-to-data eff. weights		**-**		**8.10e-02**		**0**		**0**		**0**		**0**		**0**		**0**		**0**		**8.10e-02**
Cuts $\mathrm{SR}^{\mathtt{offWZ}}_{\mathtt{low}\not{E}_\mathrm{T}}$-nj																				
$n_{\mathrm{jets}}^{p_\mathrm{T}>30\,\mathrm{GeV}}$		-	[> 0]	0.292	[> 0]	0	[> 0]	0	[> 0]	0	[> 0]	0			[> 0]	0				0.292
$E_\mathrm{T}^{\mathrm{miss}}$ [GeV]		-	[< 200]	0.225	[< 200]	0	[< 200]	0	[< 200]	0	[< 200]	0			[< 200]	0				0.225
$E_\mathrm{T}^{\mathrm{miss}}$ signif.		-	[> 3.0]	0.180	[> 3.0]	0	[> 3.0]	0	[> 3.0]	0	[> 3.0]	0			[> 3.0]	0				0.180
$m_\mathrm{T}^{\mathrm{minmll}}$ [GeV]		-	[< 50]	9.10e-02	[< 50]	0	[< 50]	0	[< 60]	0	[< 60]	0	[> 90]	0	[< 60]	0	[> 90]	0		9.10e-02
$p_\mathrm{T}^{\mathrm{lep}}/E_\mathrm{T}^{\mathrm{miss}}$		-	[< 1.0]	9.10e-02	[< 1.0]	0	[< 1.0]	0	[< 1.0]	0	[< 1.2]	0	[< 1.2]	0	[< 1.2]	0	[< 1.2]	0		9.10e-02
MC-to-data eff. weights		**-**		**7.90e-02**		**0**		**0**		**0**		**0**		**0**		**0**		**0**		**7.90e-02**
Cuts $\mathrm{SR}^{\mathtt{offWZ}}_{\mathtt{high}\not{E}_\mathrm{T}}$-0j																				
lepton $p_\mathrm{T}^{1,2,3}$ [GeV]	[> 25, 15, 10]	1.68																		1.68
$m_{\ell\ell}^{\mathrm{min}}$ [GeV]		-	[∈ [12, 15]]	0.317	[∈ [15, 20]]	1.00e-03	[∈ [20, 30]]	0	[∈ [30, 40]]	0	[∈ [40, 60]]	0			[∈ [60, 75]]	0				0.318
m_{T2}^{100} [GeV]		-	[< 115]	0.315	[< 120]	1.00e-03	[< 130]	0	[< 140]	0	[< 160]	0			[< 175]	0				0.316
$n_{\mathrm{jets}}^{p_\mathrm{T}>30\,\mathrm{GeV}}$		-	[= 0]	0.168	[= 0]	1.00e-03	[= 0]	0	[= 0]	0	[= 0]	0			[= 0]	0				0.169
$E_\mathrm{T}^{\mathrm{miss}}$ [GeV]		-	[> 50]	1.60e-02	[> 50]	0	[> 50]	0	[> 50]	0	[> 50]	0			[> 50]	0				1.60e-02
$E_\mathrm{T}^{\mathrm{miss}}$ signif.		-	[> 3.0]	1.20e-02	[> 3.0]	0	[> 3.0]	0	[> 3.0]	0	[> 3.0]	0			[> 3.0]	0				1.20e-02
$m_\mathrm{T}^{\mathrm{minmll}}$ [GeV]		-	[< 50]	1.20e-02	[< 50]	0	[< 60]	0	[< 60]	0	[< 70]	0	[> 90]	0	[< 70]	0	[> 90]	0		1.20e-02
MC-to-data eff. weights		**-**		**5.00e-03**		**0**		**0**		**0**		**0**		**0**		**0**		**0**		**5.00e-03**
Cuts $\mathrm{SR}^{\mathtt{offWZ}}_{\mathtt{high}\not{E}_\mathrm{T}}$-nj																				
lepton $p_\mathrm{T}^{1,2,3}$ [GeV]	[>4.5,3]	15.2																		15.2
											f				**g**					
$m_{\ell\ell}^{\mathrm{min}}$ [GeV]	[∈ [1, 12]]	13.4	[∈ [12, 15]]	1.84	[∈ [15, 20]]	7.00e-03	[∈ [20, 30]]	0	[∈ [30, 40]]	0	[∈ [40, 60]]	0			[∈ [60, 75]]	0				15.2
m_{T2}^{100} [GeV]	[< 112]	12.8	[< 115]	1.75	[< 120]	7.00e-03	[< 130]	0	[< 140]	0	[< 160]	0			[< 175]	0				14.5
$n_{\mathrm{jets}}^{p_\mathrm{T}>30\,\mathrm{GeV}}$	[> 0]	7.35	[> 0]	1.08	[> 0]	5.00e-03	[> 0]	0	[> 0]	0	[> 0]	0			[> 0]	0				8.44
$E_\mathrm{T}^{\mathrm{miss}}$ [GeV]	[> 200]	4.08	[> 200]	0.557	[> 200]	5.00e-03	[> 200]	0	[> 200]	0	[> 200]	0			[> 200]	0				4.64
$E_\mathrm{T}^{\mathrm{miss}}$ signif.	[> 3.0]	4.08	[> 3.0]	0.557	[> 3.0]	5.00e-03	[> 3.0]	0	[> 3.0]	0	[> 3.0]	0			[> 3.0]	0				4.64
$p_\mathrm{T}^{\mathrm{lep}}/E_\mathrm{T}^{\mathrm{miss}}$	[< 0.2]	4.05	[< 0.2]	0.542	[< 0.3]	5.00e-03	[< 0.3]	0	[< 0.3]	0	[< 1.0]	0			[< 1.0]	0				4.60
MC-to-data eff. weights		**4.07**		**0.551**		**5.00e-03**		**0**		**0**		**0**				**0**				**4.63**

Table A.4: Cutflow for the off-shell WZ event selection for the $(m(\tilde{\chi}_2^0), m(\tilde{\chi}_1^0)) = (120{,}100)$ GeV signal point for the higgsino scenario. The yields are normalized to a luminosity $\mathcal{L}$ of 139 fb^{-1}. MC-to-data efficiency weights from triggering and from the reconstruction and identification of individual physics objects are applied to the final yields in each signal region. After the initial selections, the table is split in row blocks for the inclusive $\text{SR}^{\mathtt{offWZ}}_{\mathtt{low}\not{E}_{\text{T}}}$-`0j`, $\text{SR}^{\mathtt{offWZ}}_{\mathtt{low}\not{E}_{\text{T}}}$-`nj`, $\text{SR}^{\mathtt{offWZ}}_{\mathtt{high}\not{E}_{\text{T}}}$-`0j`, $\text{SR}^{\mathtt{offWZ}}_{\mathtt{high}\not{E}_{\text{T}}}$-`nj` regions, with the individual signal region yields in columns. The inclusive OR of regions a through g2 is given in the last column. Selection details per bin are indicated in bracketed blue as relevant, and the final yields for each signal region is highlighted in bold green at the end of each block. The "3 isolated lepton selection" includes the preselection as described in Section 4.3 and the initial SFOS lepton pair selection.

$\tilde{\chi}_1^\pm\tilde{\chi}_2^0 \to WZ\tilde{\chi}_1^0\tilde{\chi}_1^0$ higgsino									m($\tilde{\chi}_2^0$,$\tilde{\chi}_1^0$) = (120, 100) GeV										
	a		**b**		**c**		**d**		**e**		**f1**		**f2**		**g1**		**g2**		**a through g2**
Common cuts																			
$\mathcal{L} \times \sigma$										466356									466356
$\mathcal{L} \times \sigma \times$ BF										17082									17082
$\mathcal{L} \times \sigma \times$ BF $\times$ filt. eff.										3949									3949
3 isolated lepton selection										164									164
b-veto										155									155
Trigger selection										73.2									73.2
$m_{\ell\ell}$, $m_{\ell\ell}^{\text{max}}$ [GeV]									[< 75]	72.3									72.3
Common cuts $\text{SR}^{\mathtt{offWZ}}_{\mathtt{low}\not{E}_{\text{T}}}$																			
$m_{\ell\ell}^{\text{min}}$ [GeV]		-				[∈ [12, 40]]	33.9							[∈ [40, 75]]	0				33.9
lepton $p_{\text{T}}^{1,2,3}$ [GeV]		-				[> 10]	15.2							[> 15]	0				15.2
FNP lepton cleaning (conversions)		-					12.1								0				12.1
$m_{\ell\ell}^{\text{max}}$ [GeV]		-				[< 60]	11.5								0				11.5
$m_{\ell\ell}^{\text{min}}$ [GeV]		-	[∈ [12, 15]]	6.33	[∈ [15, 20]]	5.12	[∈ [20, 30]]	0	[∈ [30, 40]]	0		[∈ [40, 60]]	0			[∈ [60, 75]]	0		11.5
m_{T2}^{100} [GeV]		-	[< 115]	6.29	[< 120]	5.12	[< 130]	0		0			0				0		11.4
minΔR		-	[< 1.6]	6.29	[< 1.6]	5.07	[< 1.6]	0		0			0				0		11.4
Cuts $\text{SR}^{\mathtt{offWZ}}_{\mathtt{low}\not{E}_{\text{T}}}$-`0j`																			
$n_{\text{jets}}^{p_{\text{T}}>30\,\text{GeV}}$		-	[= 0]	3.53	[= 0]	2.17	[= 0]	0	[= 0]	0		[= 0]	0			[= 0]	0		5.71
$E_{\text{T}}^{\text{miss}}$ [GeV]		-	[< 50]	3.25	[< 50]	2.14	[< 50]	0	[< 50]	0		[< 50]	0			[< 50]	0		5.39
$E_{\text{T}}^{\text{miss}}$ signif.		-	[> 1.5]	2.86	[> 1.5]	1.72	[> 1.5]	0	[> 1.5]	0		[> 1.5]	0			[> 1.5]	0		4.58
$m_{3\ell}$ [GeV]		-		2.86		1.72		0		0		[> 100]	0			[> 100]	0		4.58
$m_{\text{T}}^{\text{minmll}}$ [GeV]		-	[< 50]	2.86	[< 50]	1.72	[< 50]	0	[< 60]	0	[< 60]	0	[> 90]	0	[< 60]	0	[> 90]	0	4.58
$p_{\text{T}}^{\text{lep}}/E_{\text{T}}^{\text{miss}}$		-	[< 1.1]	2.16	[< 1.1]	1.20	[< 1.1]	0	[< 1.3]	0	[< 1.4]	0	[< 1.4]	0	[< 1.4]	0	[< 1.4]	0	3.36
MC-to-data eff. weights		**-**		**1.98**		**1.15**		**0**		**0**		**0**		**0**		**0**		**0**	**3.12**
Cuts $\text{SR}^{\mathtt{offWZ}}_{\mathtt{low}\not{E}_{\text{T}}}$-`nj`																			
$n_{\text{jets}}^{p_{\text{T}}>30\,\text{GeV}}$		-	[> 0]	2.76	[> 0]	2.90	[> 0]	0	[> 0]	0		[> 0]	0			[> 0]	0		5.66
$E_{\text{T}}^{\text{miss}}$ [GeV]		-	[< 200]	2.12	[< 200]	2.13	[< 200]	0	[< 200]	0		[< 200]	0			[< 200]	0		4.25
$E_{\text{T}}^{\text{miss}}$ signif.		-	[> 3.0]	1.46	[> 3.0]	1.71	[> 3.0]	0	[> 3.0]	0		[> 3.0]	0			[> 3.0]	0		3.17
$m_{\text{T}}^{\text{minmll}}$ [GeV]		-	[< 50]	1.23	[< 50]	1.18	[< 50]	0	[< 60]	0	[< 60]	0	[> 90]	0	[< 60]	0	[> 90]	0	2.41
$p_{\text{T}}^{\text{lep}}/E_{\text{T}}^{\text{miss}}$		-	[< 1.0]	1.23	[< 1.0]	1.18	[< 1.0]	0	[< 1.0]	0	[< 1.2]	0	[< 1.2]	0	[< 1.2]	0	[< 1.2]	0	2.41
MC-to-data eff. weights		**-**		**1.20**		**1.31**		**0**		**0**		**0**		**0**		**0**		**0**	**2.51**
Cuts $\text{SR}^{\mathtt{offWZ}}_{\mathtt{high}\not{E}_{\text{T}}}$-`0j`																			
lepton $p_{\text{T}}^{1,2,3}$ [GeV]									[> 25, 15, 10]	14.4									14.4
$m_{\ell\ell}^{\text{min}}$ [GeV]		-	[∈ [12, 15]]	5.07	[∈ [15, 20]]	3.84	[∈ [20, 30]]	0	[∈ [30, 40]]	0		[∈ [40, 60]]	0			[∈ [60, 75]]	0		8.92
m_{T2}^{100} [GeV]		-	[< 115]	5.07	[< 120]	3.84	[< 130]	0	[< 140]	0		[< 160]	0			[< 175]	0		8.92
$n_{\text{jets}}^{p_{\text{T}}>30\,\text{GeV}}$		-	[= 0]	3.01	[= 0]	1.45	[= 0]	0	[= 0]	0		[= 0]	0			[= 0]	0		4.47
$E_{\text{T}}^{\text{miss}}$ [GeV]		-	[> 50]	0.784	[> 50]	0.113	[> 50]	0	[> 50]	0		[> 50]	0			[> 50]	0		0.897
$E_{\text{T}}^{\text{miss}}$ signif.		-	[> 3.0]	0.705	[> 3.0]	0.113	[> 3.0]	0	[> 3.0]	0		[> 3.0]	0			[> 3.0]	0		0.818
$m_{\text{T}}^{\text{minmll}}$ [GeV]		-	[< 50]	0.705	[< 50]	0.113	[< 60]	0	[< 60]	0	[< 70]	0	[> 90]	0	[< 70]	0	[> 90]	0	0.818
MC-to-data eff. weights		**-**		**0.651**		**0.111**		**0**		**0**		**0**		**0**		**0**		**0**	**0.762**
Cuts $\text{SR}^{\mathtt{offWZ}}_{\mathtt{high}\not{E}_{\text{T}}}$-`nj`																			
lepton $p_{\text{T}}^{1,2,3}$ [GeV]									[>4.5,3]	72.3									72.3
												f				**g**			
$m_{\ell\ell}^{\text{min}}$ [GeV]	[∈ [1, 12]]	38.4	[∈ [12, 15]]	20.3	[∈ [15, 20]]	13.6	[∈ [20, 30]]	9.90e-02	[∈ [30, 40]]	0		[∈ [40, 60]]	0			[∈ [60, 75]]	0		72.3
m_{T2}^{100} [GeV]	[< 112]	37.1	[< 115]	20.0	[< 120]	13.6	[< 130]	9.90e-02	[< 140]	0		[< 160]	0			[< 175]	0		70.8
$n_{\text{jets}}^{p_{\text{T}}>30\,\text{GeV}}$	[> 0]	18.4	[> 0]	8.77	[> 0]	7.15	[> 0]	9.90e-02	[> 0]	0		[> 0]	0			[> 0]	0		34.4
$E_{\text{T}}^{\text{miss}}$ [GeV]	[> 200]	5.48	[> 200]	2.73	[> 200]	2.26	[> 200]	9.90e-02	[> 200]	0		[> 200]	0			[> 200]	0		10.6
$E_{\text{T}}^{\text{miss}}$ signif.	[> 3.0]	5.40	[> 3.0]	2.73	[> 3.0]	2.26	[> 3.0]	9.90e-02	[> 3.0]	0		[> 3.0]	0			[> 3.0]	0		10.5
$p_{\text{T}}^{\text{lep}}/E_{\text{T}}^{\text{miss}}$	[< 0.2]	5.05	[< 0.2]	2.50	[< 0.3]	2.26	[< 0.3]	9.90e-02	[< 0.3]	0		[< 1.0]	0			[< 1.0]	0		9.91
MC-to-data eff. weights		**4.83**		**2.42**		**2.32**		**0.101**		**0**			**0**				**0**		**9.67**

Table A.5: Cutflow for the off-shell WZ event selection for the $(m(\tilde{\chi}_2^0), m(\tilde{\chi}_1^0)) = (100{,}40)$ GeV signal point for the higgsino scenario. The yields are normalized to a luminosity $\mathcal{L}$ of 139 fb^{-1}. MC-to-data efficiency weights from triggering and from the reconstruction and identification of individual physics objects are applied to the final yields in each signal region. After the initial selections, the table is split in row blocks for the inclusive $\mathtt{SR}^{\mathtt{offWZ}}_{\mathtt{low}\not{E}_T}\mathtt{\text{-}0j}$, $\mathtt{SR}^{\mathtt{offWZ}}_{\mathtt{low}\not{E}_T}\mathtt{\text{-}nj}$, $\mathtt{SR}^{\mathtt{offWZ}}_{\mathtt{high}\not{E}_T}\mathtt{\text{-}0j}$, $\mathtt{SR}^{\mathtt{offWZ}}_{\mathtt{high}\not{E}_T}\mathtt{\text{-}nj}$ regions, with the individual signal region yields in columns. The inclusive OR of regions a through g2 is given in the last column. Selection details per bin are indicated in bracketed blue as relevant, and the final yields for each signal region is highlighted in bold green at the end of each block. The "3 isolated lepton selection" includes the preselection as described in Section 4.3 and the initial SFOS lepton pair selection.

$\tilde{\chi}_1^{\pm}\tilde{\chi}_2^0 \to WZ\tilde{\chi}_1^0\tilde{\chi}_1^0$ higgsino					$m(\tilde{\chi}_2^0,\tilde{\chi}_1^0) = (100, 40)$ GeV					
	a	**b**	**c**	**d**	**e**	**f1**	**f2**	**g1**	**g2**	**a through g2**
Common cuts										
$\mathcal{L}\times\sigma$					1384920					1384920
$\mathcal{L}\times\sigma\times$ BF					48276					48276
$\mathcal{L}\times\sigma\times$ BF $\times$ filt. eff.					16084					16084
3 isolated lepton selection					3.76e+03					3.76e+03
b-veto					3.62e+03					3.62e+03
Trigger selection					2.62e+03					2.62e+03
$m_{\ell\ell}, m_{\ell\ell}^{\mathrm{max}}$ [GeV]					[< 75] 2.38e+03					2.38e+03
Common cuts $\mathrm{SR}^{\mathtt{offWZ}}_{\mathtt{low}\not{E}_T}$										
$m_{\ell\ell}^{\mathrm{min}}$ [GeV]	-			[∈ [12, 40]] 1.59e+03			[∈ [40, 75]] 672			2.27e+03
lepton $p_T^{1,2,3}$ [GeV]	-			[> 10] 1.05e+03			[> 15] 327			1.38e+03
FNP lepton cleaning (conversions)	-			820			228			1.05e+03
$m_{\ell\ell}^{\mathrm{max}}$ [GeV]	-			[< 60] 770			228			998
$m_{\ell\ell}^{\mathrm{min}}$ [GeV]	-	[∈ [12, 15]] 36.6	[∈ [15, 20]] 101	[∈ [20, 30]] 302	[∈ [30, 40]] 331	[∈ [40, 60]] 228		[∈ [60, 75]] 0.362		998
m_{T2}^{100} [GeV]	-	[< 115] 15.6	[< 120] 59.1	[< 130] 262	331	228		0.362		895
minΔR	-	[< 1.6] 15.6	[< 1.6] 58.6	[< 1.6] 216	331	228		0.362		849
Cuts $\mathrm{SR}^{\mathtt{offWZ}}_{\mathtt{low}\not{E}_T}\mathtt{\text{-}0j}$										
$n_{\mathrm{jets}}^{p_T>30\,\mathrm{GeV}}$	-	[= 0] 11.5	[= 0] 43.7	[= 0] 149	[= 0] 216	[= 0] 150		[= 0] 0.191		570
E_T^{miss} [GeV]	-	[< 50] 10.1	[< 50] 32.9	[< 50] 103	[< 50] 161	[< 50] 102		[< 50] 8.10e-02		409
E_T^{miss} signif.	-	[> 1.5] 8.03	[> 1.5] 29.2	[> 1.5] 92.6	[> 1.5] 134	[> 1.5] 82.2		[> 1.5] 8.10e-02		346
$m_{3\ell}$ [GeV]	-	8.03	29.2	92.6	134	[> 100] 35.9		[> 100] 0		300
m_T^{minmll} [GeV]	-	[< 50] 7.41	[< 50] 26.8	[< 50] 80.2	[< 60] 118	[< 60] 30.9	[> 90] 1.69	[< 60] 0	[> 90] 0	265
$p_T^{\mathrm{lep}}/E_T^{\mathrm{miss}}$	-	[< 1.1] 5.94	[< 1.1] 18.0	[< 1.1] 50.4	[< 1.3] 100	[< 1.4] 27.1	[< 1.4] 1.69	[< 1.4] 0	[< 1.4] 0	203
MC-to-data eff. weights	**-**	**5.68**	**16.5**	**46.4**	**89.9**	**25.8**	**1.34**	**0**	**0**	**186**
Cuts $\mathrm{SR}^{\mathtt{offWZ}}_{\mathtt{low}\not{E}_T}\mathtt{\text{-}nj}$										
$n_{\mathrm{jets}}^{p_T>30\,\mathrm{GeV}}$	-	[> 0] 4.12	[> 0] 14.9	[> 0] 67.6	[> 0] 115	[> 0] 77.7		[> 0] 0.171		279
E_T^{miss} [GeV]	-	[< 200] 4.12	[< 200] 14.5	[< 200] 64.9	[< 200] 111	[< 200] 74.5		[< 200] 0.171		269
E_T^{miss} signif.	-	[> 3.0] 2.81	[> 3.0] 10.9	[> 3.0] 45.6	[> 3.0] 76.4	[> 3.0] 50.3		[> 3.0] 0.171		186
m_T^{minmll} [GeV]	-	[< 50] 1.96	[< 50] 9.16	[< 50] 34.2	[< 60] 60.9	[< 60] 41.4	[> 90] 3.28	[< 60] 0.171	[> 90] 0	151
$p_T^{\mathrm{lep}}/E_T^{\mathrm{miss}}$	-	[< 1.0] 1.68	[< 1.0] 7.34	[< 1.0] 27.6	[< 1.0] 44.4	[< 1.2] 30.8	[< 1.2] 3.28	[< 1.2] 0.171	[< 1.2] 0	115
MC-to-data eff. weights	**-**	**1.62**	**6.62**	**25.5**	**39.6**	**28.1**	**3.28**	**0.163**	**0**	**105**
Cuts $\mathrm{SR}^{\mathtt{offWZ}}_{\mathtt{high}\not{E}_T}\mathtt{\text{-}0j}$										
lepton $p_T^{1,2,3}$ [GeV]					[> 25, 15, 10] 1.35e+03					1.35e+03
$m_{\ell\ell}^{\mathrm{min}}$ [GeV]	-	[∈ [12, 15]] 37.1	[∈ [15, 20]] 102	[∈ [20, 30]] 313	[∈ [30, 40]] 396	[∈ [40, 60]] 476		[∈ [60, 75]] 1.26		1.33e+03
m_{T2}^{100} [GeV]	-	[< 115] 16.1	[< 120] 63.0	[< 130] 269	[< 140] 382	[< 160] 475		[< 175] 1.04		1.21e+03
$n_{\mathrm{jets}}^{p_T>30\,\mathrm{GeV}}$	-	[= 0] 11.8	[= 0] 46.6	[= 0] 184	[= 0] 252	[= 0] 315		[= 0] 0.630		810
E_T^{miss} [GeV]	-	[> 50] 1.23	[> 50] 16.7	[> 50] 68.2	[> 50] 75.9	[> 50] 84.7		[> 50] 0.110		247
E_T^{miss} signif.	-	[> 3.0] 1.13	[> 3.0] 16.2	[> 3.0] 65.0	[> 3.0] 72.5	[> 3.0] 79.7		[> 3.0] 0.110		235
m_T^{minmll} [GeV]	-	[< 50] 1.13	[< 50] 16.2	[< 60] 62.8	[< 60] 68.5	[< 70] 75.9	[> 90] 1.88	[< 70] 0.110	[> 90] 0	226
MC-to-data eff. weights	**-**	**1.13**	**15.0**	**57.1**	**64.8**	**71.6**	**1.44**	**2.40e-02**	**0**	**211**
Cuts $\mathrm{SR}^{\mathtt{offWZ}}_{\mathtt{high}\not{E}_T}\mathtt{\text{-}nj}$										
lepton $p_T^{1,2,3}$ [GeV]					[>4.5,3] 2.38e+03					2.38e+03
						f		**g**		
$m_{\ell\ell}^{\mathrm{min}}$ [GeV]	[∈ [1, 12]] 112	[∈ [12, 15]] 99.4	[∈ [15, 20]] 233	[∈ [20, 30]] 621	[∈ [30, 40]] 640	[∈ [40, 60]] 671		[∈ [60, 75]] 1.47		2.38e+03
m_{T2}^{100} [GeV]	[< 112] 35.3	[< 115] 42.4	[< 120] 140	[< 130] 537	[< 140] 617	[< 160] 670		[< 175] 1.25		2.04e+03
$n_{\mathrm{jets}}^{p_T>30\,\mathrm{GeV}}$	[> 0] 9.12	[> 0] 12.0	[> 0] 37.0	[> 0] 162	[> 0] 200	[> 0] 218		[> 0] 0.526		639
E_T^{miss} [GeV]	[> 200] 0.951	[> 200] 0.376	[> 200] 1.07	[> 200] 7.12	[> 200] 7.30	[> 200] 7.01		[> 200] 0		23.8
E_T^{miss} signif.	[> 3.0] 0.951	[> 3.0] 0.376	[> 3.0] 1.07	[> 3.0] 6.95	[> 3.0] 7.30	[> 3.0] 7.01		[> 3.0] 0		23.7
$p_T^{\mathrm{lep}}/E_T^{\mathrm{miss}}$	[< 0.2] 0.951	[< 0.2] 0.146	[< 0.3] 0.771	[< 0.3] 4.37	[< 0.3] 3.07	[< 1.0] 6.86		[< 1.0] 0		16.2
MC-to-data eff. weights	**0.878**	**0.152**	**0.944**	**4.24**	**2.75**	**6.70**		**0**		**15.7**

Table A.6: Cutflow for the off-shell WZ event selection for the $(m(\tilde{\chi}_2^0), m(\tilde{\chi}_1^0)) = (185{,}125)$ GeV signal point for the higgsino scenario. The yields are normalized to a luminosity $\mathcal{L}$ of 139 fb^{-1}. MC-to-data efficiency weights from triggering and from the reconstruction and identification of individual physics objects are applied to the final yields in each signal region. After the initial selections, the table is split in row blocks for the inclusive $\mathtt{SR}^{\mathtt{offWZ}}_{\mathtt{low}\not{E}_T}\mathtt{\text{-}0j}$, $\mathtt{SR}^{\mathtt{offWZ}}_{\mathtt{low}\not{E}_T}\mathtt{\text{-}nj}$, $\mathtt{SR}^{\mathtt{offWZ}}_{\mathtt{high}\not{E}_T}\mathtt{\text{-}0j}$, $\mathtt{SR}^{\mathtt{offWZ}}_{\mathtt{high}\not{E}_T}\mathtt{\text{-}nj}$ regions, with the individual signal region yields in columns. The inclusive OR of regions a through g2 is given in the last column. Selection details per bin are indicated in bracketed blue as relevant, and the final yields for each signal region is highlighted in bold green at the end of each block. The “3 isolated lepton selection” includes the preselection as described in Section 4.3 and the initial SFOS lepton pair selection.

$\tilde{\chi}_1^\pm\tilde{\chi}_2^0 \to WZ\tilde{\chi}_1^0\tilde{\chi}_1^0$ higgsino					m($\tilde{\chi}_2^0$,$\tilde{\chi}_1^0$) = (185, 125) GeV					
	a	**b**	**c**	**d**	**e**	**f1**	**f2**	**g1**	**g2**	**a through g2**
Common cuts										
$\mathcal{L}\times\sigma$					112226					112226
$\mathcal{L}\times\sigma\times$BF					3912					3912
$\mathcal{L}\times\sigma\times$BF$\times$ filt. eff.					1550					1550
3 isolated lepton selection					392					392
b-veto					374					374
Trigger selection					280					280
$m_{\ell\ell}, m_{\ell\ell}^{\mathrm{max}}$ [GeV]					[< 75] 253					253
Common cuts $\mathrm{SR}^{\mathtt{offWZ}}_{\mathtt{low}\not{E}_T}$										
$m_{\ell\ell}^{\mathrm{min}}$ [GeV]	-		[∈ [12, 40]] 165				[∈ [40, 75]] 76.8			242
lepton $p_T^{1,2,3}$ [GeV]	-		[> 10] 111				[> 15] 38.5			149
FNP lepton cleaning (conversions)	-		85.2				27.0			112
$m_{\ell\ell}^{\mathrm{max}}$ [GeV]	-		[< 60] 79.3				27.0			106
$m_{\ell\ell}^{\mathrm{min}}$ [GeV]	-	[∈ [12, 15]] 3.53	[∈ [15, 20]] 10.3	[∈ [20, 30]] 32.6	[∈ [30, 40]] 32.9	[∈ [40, 60]] 26.9		[∈ [60, 75]] 0.134		106
m_{T2}^{100} [GeV]	-	[< 115] 0.681	[< 120] 5.61	[< 130] 26.3	32.9	26.9		0.134		92.5
minΔR	-	[< 1.6] 0.681	[< 1.6] 5.55	[< 1.6] 23.2	32.9	26.9		0.134		89.4
Cuts $\mathrm{SR}^{\mathtt{offWZ}}_{\mathtt{low}\not{E}_T}\mathtt{\text{-}0j}$										
$n_{\mathrm{jets}}^{p_T>30\,\mathrm{GeV}}$	-	[= 0] 0.534	[= 0] 3.84	[= 0] 13.3	[= 0] 21.3	[= 0] 15.7		[= 0] 8.40e-02		54.8
E_T^{miss} [GeV]	-	[< 50] 0.465	[< 50] 2.70	[< 50] 7.47	[< 50] 12.8	[< 50] 9.78		[< 50] 3.50e-02		33.2
E_T^{miss} signif.	-	[> 1.5] 0.465	[> 1.5] 2.37	[> 1.5] 6.86	[> 1.5] 11.6	[> 1.5] 8.12		[> 1.5] 3.50e-02		29.4
$m_{3\ell}$ [GeV]	-	0.465	2.37	6.86	11.6	[> 100] 2.97		[> 100] 1.70e-02		24.3
m_T^{minmll} [GeV]	-	[< 50] 0.411	[< 50] 2.22	[< 50] 5.44	[< 60] 9.46	[< 60] 2.58	[> 90] 7.40e-02	[< 60] 1.70e-02	[> 90] 0	20.2
$p_T^{\mathrm{lep}}/E_T^{\mathrm{miss}}$	-	[< 1.1] 0.275	[< 1.1] 1.47	[< 1.1] 2.98	[< 1.3] 8.04	[< 1.4] 2.37	[< 1.4] 7.40e-02	[< 1.4] 1.70e-02	[< 1.4] 0	15.2
MC-to-data eff. weights	**-**	**0.241**	**1.39**	**2.78**	**7.33**	**2.27**	**6.10e-02**	**1.70e-02**	**0**	**14.1**
Cuts $\mathrm{SR}^{\mathtt{offWZ}}_{\mathtt{low}\not{E}_T}\mathtt{\text{-}nj}$										
$n_{\mathrm{jets}}^{p_T>30\,\mathrm{GeV}}$	-	[> 0] 0.147	[> 0] 1.71	[> 0] 9.91	[> 0] 11.7	[> 0] 11.2		[> 0] 5.10e-02		34.6
E_T^{miss} [GeV]	-	[< 200] 0.122	[< 200] 1.54	[< 200] 8.99	[< 200] 10.3	[< 200] 9.79		[< 200] 5.10e-02		30.8
E_T^{miss} signif.	-	[> 3.0] 8.30e-02	[> 3.0] 1.11	[> 3.0] 6.84	[> 3.0] 8.33	[> 3.0] 8.13		[> 3.0] 2.70e-02		24.5
m_T^{minmll} [GeV]	-	[< 50] 6.60e-02	[< 50] 0.886	[< 50] 4.62	[< 60] 5.97	[< 60] 5.85	[> 90] 1.03	[< 60] 2.70e-02	[> 90] 0	18.4
$p_T^{\mathrm{lep}}/E_T^{\mathrm{miss}}$	-	[< 1.0] 6.60e-02	[< 1.0] 0.783	[< 1.0] 3.64	[< 1.0] 4.53	[< 1.2] 5.04	[< 1.2] 0.939	[< 1.2] 2.70e-02	[< 1.2] 0	15.0
MC-to-data eff. weights	**-**	**6.50e-02**	**0.715**	**3.31**	**4.00**	**4.67**	**0.837**	**2.10e-02**	**0**	**13.6**
Cuts $\mathrm{SR}^{\mathtt{offWZ}}_{\mathtt{high}\not{E}_T}\mathtt{\text{-}0j}$										
lepton $p_T^{1,2,3}$ [GeV]					[> 25, 15, 10] 152					152
$m_{\ell\ell}^{\mathrm{min}}$ [GeV]	-	[∈ [12, 15]] 3.83	[∈ [15, 20]] 11.5	[∈ [20, 30]] 36.9	[∈ [30, 40]] 41.9	[∈ [40, 60]] 54.8		[∈ [60, 75]] 0.227		149
m_{T2}^{100} [GeV]	-	[< 115] 1.24	[< 120] 6.19	[< 130] 30.5	[< 140] 40.2	[< 160] 54.8		[< 175] 0.227		133
$n_{\mathrm{jets}}^{p_T>30\,\mathrm{GeV}}$	-	[= 0] 0.825	[= 0] 4.09	[= 0] 17.2	[= 0] 25.2	[= 0] 33.0		[= 0] 0.150		80.5
E_T^{miss} [GeV]	-	[> 50] 0.205	[> 50] 1.75	[> 50] 8.10	[> 50] 11.3	[> 50] 11.7		[> 50] 7.00e-02		33.1
E_T^{miss} signif.	-	[> 3.0] 0.205	[> 3.0] 1.64	[> 3.0] 7.79	[> 3.0] 11.0	[> 3.0] 10.5		[> 3.0] 7.00e-02		31.2
m_T^{minmll} [GeV]	-	[< 50] 0.205	[< 50] 1.54	[< 60] 7.39	[< 60] 10.1	[< 70] 9.79	[> 90] 0.474	[< 70] 4.80e-02	[> 90] 2.20e-02	29.6
MC-to-data eff. weights	**-**	**0.198**	**1.50**	**7.00**	**9.28**	**9.14**	**0.423**	**5.10e-02**	**7.00e-03**	**27.6**
Cuts $\mathrm{SR}^{\mathtt{offWZ}}_{\mathtt{high}\not{E}_T}\mathtt{\text{-}nj}$										
lepton $p_T^{1,2,3}$ [GeV]					[>4.5,3] 253					253
						f		**g**		
$m_{\ell\ell}^{\mathrm{min}}$ [GeV]	[∈ [1, 12]] 10.9	[∈ [12, 15]] 9.76	[∈ [15, 20]] 24.2	[∈ [20, 30]] 65.8	[∈ [30, 40]] 65.5	[∈ [40, 60]] 76.4		[∈ [60, 75]] 0.357		253
m_{T2}^{100} [GeV]	[< 112] 3.11	[< 115] 3.04	[< 120] 13.2	[< 130] 54.0	[< 140] 62.1	[< 160] 76.3		[< 175] 0.357		212
$n_{\mathrm{jets}}^{p_T>30\,\mathrm{GeV}}$	[> 0] 1.11	[> 0] 1.06	[> 0] 4.50	[> 0] 22.0	[> 0] 22.8	[> 0] 30.2		[> 0] 9.80e-02		81.8
E_T^{miss} [GeV]	[> 200] 0.149	[> 200] 8.60e-02	[> 200] 0.513	[> 200] 2.22	[> 200] 2.56	[> 200] 3.50		[> 200] 0		9.03
E_T^{miss} signif.	[> 3.0] 0.149	[> 3.0] 8.60e-02	[> 3.0] 0.513	[> 3.0] 2.22	[> 3.0] 2.56	[> 3.0] 3.47		[> 3.0] 0		9.00
$p_T^{\mathrm{lep}}/E_T^{\mathrm{miss}}$	[< 0.2] 0.107	[< 0.2] 8.60e-02	[< 0.3] 0.336	[< 0.3] 1.44	[< 0.3] 1.65	[< 1.0] 3.45		[< 1.0] 0		7.07
MC-to-data eff. weights	**0.121**	**8.10e-02**	**0.332**	**1.27**	**1.46**	**3.24**		**0**		**6.50**

Appendix B

Press resulting from the Norwegian media visit to CERN in 2019

Section 9.1 summarizes the two-day Norwegian media visit to CERN in October 2019. The below list summarizes the press resulting from the visit.

- titan.uio.no, “Jobben hans er å lage flest mulig kollisjoner i CERN”
- titan.uio.no, “Studenter holder hjulene i gang i partikkelfysikkens Mekka”
- titan.uio.no, “Slik angriper de universets minste mysterier fra hver sin kant”
- titan.uio.no, “‘Gudepartikkelen’ higgs er ikke lenger like mystisk”
- titan.uio.no, “Hvilken elementærpartikkel er du?”
- Under Dusken, “Studier ved CERN”
- Under Dusken, “Elementærpartiklenes fjerne slektninger”
- Under Dusken, “Som å kollidere to nåler på 10 kilometers avstand”
- Teknisk Ukeblad, “Cern forkaster nesten alle kollisjonsdataene sine. Dermed kan ny vitenskap gå tapt” (behind pay-wall)
- Teknisk Ukeblad, “Til daglig prøver Emma å forbedre kreftdiagnostikken. På fritiden bokser hun mot Cern-toppene”
- forskning.no, “Bli med på innsiden av CERN”
- Apollon, “De fant Guds partikkel. Nå jakter de noe enda større”
- Khrono, “De har den aller største maskina. Nå vil de bygge en som er fire ganger større. Bli med under bakken i Cern”
- NRK Ekko, Abels tårn (radio show), “CERN spesial — Eksisterer vi egentlig?”

Bibliography

[1] Glashow, S. L. "Partial Symmetries of Weak Interactions". *Nucl. Phys.* 22 (1961), 579–588. DOI: 10.1016/0029-5582(61)90469-2.

[2] Weinberg, S. "A Model of Leptons". *Phys. Rev. Lett.* 19 (1967), 1264–1266. DOI: 10.1103/PhysRevLett.19.1264.

[3] Salam, A. "Weak and Electromagnetic Interactions". *Conf. Proc. C* 680519 (1968), 367–377. DOI: 10.1142/9789812795915_0034.

[4] Fritzsch, H., Gell-Mann, M., and Leutwyler, H. "Advantages of the Color Octet Gluon Picture". *Phys. Lett. B* 47 (1973), 365–368. DOI: 10.1016/0370-2693(73)90625-4.

[5] Nambu, Y. and Han, M. Y. "Three triplets, paraquarks, and colored quarks". *Phys. Rev. D* 10 (1974), 674–683. DOI: 10.1103/PhysRevD.10.674.

[6] Gross, D. J. and Wilczek, F. "Asymptotically Free Gauge Theories - I". *Phys. Rev. D* 8 (1973), 3633–3652. DOI: 10.1103/PhysRevD.8.3633.

[7] Politzer, H. D. "Asymptotic Freedom: An Approach to Strong Interactions". *Phys. Rept.* 14 (1974), 129–180. DOI: 10.1016/0370-1573(74)90014-3.

[8] ATLAS Collaboration. "Observation of a new particle in the search for the Standard Model Higgs boson with the ATLAS detector at the LHC". *Phys. Lett. B* 716 (2012), 1–29. DOI: 10.1016/j.physletb.2012.08.020. arXiv: 1207.7214 [hep-ex].

[9] CMS Collaboration. "Observation of a New Boson at a Mass of 125 GeV with the CMS Experiment at the LHC". *Phys. Lett. B* 716 (2012), 30–61. DOI: 10.1016/j.physletb.2012.08.021. arXiv: 1207.7235 [hep-ex].

[10] Englert, F. and Brout, R. "Broken Symmetry and the Mass of Gauge Vector Mesons". *Phys. Rev. Lett.* 13 (1964), 321–323. DOI: 10.1103/PhysRevLett.13.321.

[11] Higgs, P. W. "Broken symmetries, massless particles and gauge fields". *Phys. Lett.* 12 (1964), 132–133. DOI: 10.1016/0031-9163(64)91136-9.

[12] Higgs, P. W. "Broken Symmetries and the Masses of Gauge Bosons". *Phys. Rev. Lett.* 13 (1964), 508–509. DOI: 10.1103/PhysRevLett.13.508.

[13] Guralnik, G. S., Hagen, C. R., and Kibble, T. W. B. "Global Conservation Laws and Massless Particles". *Phys. Rev. Lett.* 13 (1964), 585–587. DOI: 10.1103/PhysRevLett.13.585.

[14] Golfand, Y. and Likhtman, E. "Extension of the Algebra of Poincare Group Generators and Violation of P Invariance". *JETP Lett.* 13 (1971). [Pisma Zh. Eksp. Teor. Fiz. **13** (1971) 452], 323.

[15] Volkov, D. and Akulov, V. “Is the neutrino a goldstone particle?” *Phys. Lett. B* 46 (1973), 109. DOI: 10.1016/0370-2693(73)90490-5.

[16] Wess, J. and Zumino, B. “Supergauge transformations in four dimensions”. *Nucl. Phys. B* 70 (1974), 39. DOI: 10.1016/0550-3213(74)90355-1.

[17] Wess, J. and Zumino, B. “Supergauge invariant extension of quantum electrodynamics”. *Nucl. Phys. B* 78 (1974), 1. DOI: 10.1016/0550-3213(74)90112-6.

[18] Ferrara, S. and Zumino, B. “Supergauge invariant Yang-Mills theories”. *Nucl. Phys. B* 79 (1974), 413. DOI: 10.1016/0550-3213(74)90559-8.

[19] Salam, A. and Strathdee, J. “Super-symmetry and non-Abelian gauges”. *Phys. Lett. B* 51 (1974), 353. DOI: 10.1016/0370-2693(74)90226-3.

[20] Muon $g-2$ Collaboration. “Measurement of the Positive Muon Anomalous Magnetic Moment to 0.46 ppm”. *Phys. Rev. Lett.* 126 (14 Apr. 2021), 141801. DOI: 10.1103/PhysRevLett.126.141801.

[21] Aoyama, T. et al. “The anomalous magnetic moment of the muon in the Standard Model”. *Physics Reports* 887 (2020), 1–166. DOI: https://doi.org/10.1016/j.physrep.2020.07.006.

[22] ATLAS Collaboration. “Search for chargino–neutralino pair production in final states with three leptons and missing transverse momentum in $\sqrt{s} = 13$ TeV pp collisions with the ATLAS detector”. *Eur. Phys. J. C* 81 (2021), 1118. DOI: 10.1140/epjc/s10052-021-09749-7. arXiv: 2106.01676 [hep-ex].

[23] Maguire, E., Heinrich, L., and Watt, G. “HEPData: a repository for high energy physics data”. *J. Phys. Conf. Ser.* 898, no. 10 (2017), 102006. DOI: 10.1088/1742-6596/898/10/102006. arXiv: 1704.05473 [hep-ex].

[24] Adam-Bourdarios, C. et al. “ATLAS@Home: Harnessing Volunteer Computing for HEP”. *J. Phys. Conf. Ser.* 664, no. 2 (2015), 022009. DOI: 10.1088/1742-6596/664/2/022009.

[25] Adam-Bourdarios, C. et al. “Volunteer computing experience with ATLAS@Home”. *J. Phys. Conf. Ser.* 898, no. 5 (2017), 052009. DOI: 10.1088/1742-6596/898/5/052009.

[26] Cameron, David et al. “Advances in ATLAS@Home towards a major ATLAS computing resource”. *EPJ Web Conf.* 214 (2019), 03011. DOI: 10.1051/epjconf/201921403011.

[27] Barranco, J. et al. “LHC@Home: a BOINC-based volunteer computing infrastructure for physics studies at CERN”. *Open Eng.* 7, no. 1 (2017), 378–392. DOI: 10.1515/eng-2017-0042.

[28] Cameron, D. et al. “Extending CERN computing to volunteers - LHC@home consolidation and outlook”. *EPJ Web Conf.* 214 (2019), 03016. DOI: 10.1051/epjconf/201921403016.

[29] Henriksen, E. K. *The Education System in Norway*. https://indico.cern.ch/event/1211712/contributions/5279697/attachments/2637614/4563581/norwegian-educational-system-ekh-RECFA-meet-april2023.pdf. Accessed: 2023–06-23. 2023.

[30] Raklev, A. *Supersymmetry – Lecture notes for FYS5190/FYS9190 Supersymmetry*. https://www.uio.no/studier/emner/matnat/fys/FYS5190/h21/resurser/notes.pdf. Accessed: 2023–04-30. 2021.

[31] Martin, S. P. "A Supersymmetry primer". *Adv. Ser. Direct. High Energy Phys.* 18 (1998), 1–98. DOI: 10.1142/9789812839657_0001. arXiv: hep-ph/9709356.

[32] Purcell, A. "Go on a particle quest at the first CERN webfest. Le premier webfest du CERN se lance à la conquête des particules", no. 35/2012 (2012), 10. URL: https://cds.cern.ch/record/1473657.

[33] Particle Data Group. "Review of Particle Physics". *PTEP* 2022 (2022), 083C01. DOI: 10.1093/ptep/ptac097.

[34] Super-Kamiokande Collaboration. "Evidence for Oscillation of Atmospheric Neutrinos". *Physical Review Letters* 81, no. 8 (Aug. 1998), 1562–1567. DOI: 10.1103/physrevlett.81.1562.

[35] SNO Collaboration. "Measurement of the rate of $\nu_e + d \rightarrow p + p + e^-$ interactions produced by ^{8}B solar neutrinos at the Sudbury Neutrino Observatory". *Phys. Rev. Lett.* 87 (2001), 071301. DOI: 10.1103/PhysRevLett.87.071301. arXiv: nucl-ex/0106015.

[36] KATRIN Collaboration. "Direct neutrino-mass measurement with sub-electronvolt sensitivity". *Nature Physics* 18, no. 2 (2022), 160–166.

[37] Rubin, V. C., Ford, W. K. J., and Thonnard, N. "Rotational properties of 21 SC galaxies with a large range of luminosities and radii, from NGC 4605 (R = 4kpc) to UGC 2885 (R = 122 kpc)". *Astrophys. J.* 238 (June 1980), 471–487.

[38] Nanopoulos, D. V. "Protons are Not Forever". *Stud. Nat. Sci.* 16 (1979), 91–114. DOI: 10.1007/978-1-4613-3024-0_4.

[39] Georgi, H. and Glashow, S. L. "Unity of All Elementary Particle Forces". *Physical Review Letters* 32 (1974), 438–441.

[40] Pati, J. C. and Salam, A. "Lepton number as the fourth "color"". *Phys. Rev. D* 10 (1 July 1974), 275–289. DOI: 10.1103/PhysRevD.10.275.

[41] Buras, A. et al. "Aspects of the grand unification of strong, weak and electromagnetic interactions". *Nuclear Physics B* 135, no. 1 (1978), 66–92. DOI: https://doi.org/10.1016/0550-3213(78)90214-6.

[42] Coleman, S. R. and Mandula, J. "All Possible Symmetries of the S Matrix". *Phys. Rev.* 159 (1967), 1251–1256. DOI: 10.1103/PhysRev.159.1251.

[43] Haag, R., Lopuszanski, J. T., and Sohnius, M. "All Possible Generators of Supersymmetries of the s Matrix". *Nucl. Phys. B* 88 (1975), 257. DOI: 10.1016/0550-3213(75)90279-5.

[44] Goldberg, H. "Constraint on the Photino Mass from Cosmology". *Phys. Rev. Lett.* 50 (1983), 1419. DOI: 10.1103/PhysRevLett.50.1419. Erratum: *Phys. Rev. Lett.* 103 (2009), 099905. DOI: 10.1103/PhysRevLett.103.099905.

[45] Ellis, J. et al. "Supersymmetric relics from the big bang". *Nucl. Phys. B* 238 (1984), 453. DOI: 10.1016/0550-3213(84)90461-9.

[46] Fayet, P. "Supersymmetry and weak, electromagnetic and strong interactions". *Phys. Lett. B* 64 (1976), 159. DOI: 10.1016/0370-2693(76)90319-1.

[47] Fayet, P. "Spontaneously broken supersymmetric theories of weak, electromagnetic and strong interactions". *Phys. Lett. B* 69 (1977), 489. DOI: 10.1016/0370-2693(77)90852-8.

[48] Ibáñez, L. E. and Ross, G. G. "$SU(2)_L \times U(1)$ Symmetry Breaking as a Radiative Effect of Supersymmetry Breaking in Guts". *Phys. Lett. B* 110 (1982), 215. DOI: 10.1016/0370-2693(82)91239-4.

[49] Inoue, K. et al. "Aspects of Grand Unified Models with Softly Broken Supersymmetry". *Prog. Theor. Phys.* 68 (1982), 927. DOI: 10.1143/PTP.68.927. Erratum: *Prog. Theor. Phys.* 70 (1983), 330. DOI: 10.1143/PTP.70.330.

[50] Farrar, G. R. and Fayet, P. "Phenomenology of the production, decay, and detection of new hadronic states associated with supersymmetry". *Phys. Lett. B* 76 (1978), 575. DOI: 10.1016/0370-2693(78)90858-4.

[51] Chamseddine, A. H., Arnowitt, R. L., and Nath, P. "Locally Supersymmetric Grand Unification". *Phys. Rev. Lett.* 49 (1982), 970. DOI: 10.1103/PhysRevLett.49.970.

[52] Barbieri, R., Ferrara, S., and Savoy, C. A. "Gauge Models with Spontaneously Broken Local Supersymmetry". *Phys. Lett. B* 119 (1982), 343. DOI: 10.1016/0370-2693(82)90685-2.

[53] Kane, G. L. et al. "Study of constrained minimal supersymmetry". *Phys. Rev. D* 49 (1994), 6173. DOI: 10.1103/PhysRevD.49.6173. arXiv: hep-ph/9312272.

[54] Brust, C. et al. "SUSY, the Third Generation and the LHC". *Journal of High Energy Physics* 2012, no. 3 (Mar. 2012). DOI: 10.1007/jhep03(2012)103.

[55] Papucci, M., Ruderman, J. T., and Weiler, A. "Natural SUSY endures". *Journal of High Energy Physics* 2012, no. 9 (Sept. 2012). DOI: 10.1007/jhep09(2012)035.

[56] CERN. *CERN Annual report 2021*. Tech. rep. 2022. DOI: 10.17181/AnnualReport2021.

[57] CERN. "Member states" (2012). URL: https://cds.cern.ch/record/1997223.

[58] Evans, L. and Bryant, P. "LHC Machine". *Journal of Instrumentation* 3, no. 08 (Aug. 2008), S08001. DOI: 10.1088/1748-0221/3/08/S08001.

[59] *The Large Hadron Collider*. https://home.cern/science/accelerators/large-hadron-collider. Accessed: 2023-01-29.

[60] Thomson, M. *Modern Particle Physics*. Cambridge University Press, 2013. DOI: 10.1017/CBO9781139525367.

[61] Mobs, E. "The CERN accelerator complex in 2019." (2019). URL: https://cds.cern.ch/record/2684277.

[62] Brüning, O. S. et al. *LHC Design Report*. CERN Yellow Reports: Monographs. CERN, 2004. DOI: 10.5170/CERN-2004-003-V-1.

[63] ATLAS Collaboration. *Standard Model Summary Plots February 2022*. Tech. rep. 2022. URL: https://cds.cern.ch/record/2804061.

[64] LHC SUSY Cross Section Working Group. *SUSY cross-sections*. https://twiki.cern.ch/twiki/bin/view/LHCPhysics/SUSYCrossSections. Accessed: 2022-01-31.

[65] ATLAS Collaboration. "The ATLAS Experiment at the CERN Large Hadron Collider". *Journal of Instrumentation* 3, no. 08 (Aug. 2008), S08003. DOI: 10.1088/1748-0221/3/08/S08003.

[66] ATLAS Collaboration. "ATLAS: Detector and physics performance technical design report. Volume 1" (May 1999).

[67] *ATLAS Experiment*. https://atlas.cern. Accessed: 2023-01-15.

[68] Pequenao, J. "Computer generated image of the whole ATLAS detector". 2008. URL: https://cds.cern.ch/record/1095924.

[69] Mehlhase, S. "ATLAS detector slice (and particle visualisations)" (2021). URL: https://cds.cern.ch/record/2770815.

[70] Pequenao, J. "Computer generated image of the ATLAS inner detector". 2008. URL: https://cds.cern.ch/record/1095926.

[71] Rodriguez Vera, A. M. and Antunes Pequenao, J. "ATLAS Detector Magnet System". General Photo. 2021. URL: https://cds.cern.ch/record/2770604.

[72] Fabjan, C. W. and Gianotti, F. "Calorimetry for particle physics". *Rev. Mod. Phys.* 75 (2003), 1243–1286. DOI: 10.1103/RevModPhys.75.1243.

[73] Pequenao, J. "Computer Generated image of the ATLAS calorimeter". 2008. URL: https://cds.cern.ch/record/1095927.

[74] Pequenao, J. "Computer generated image of the ATLAS Muons subsystem". 2008. URL: https://cds.cern.ch/record/1095929.

[75] ATLAS Collaboration. "Operation of the ATLAS trigger system in Run 2". *JINST* 15, no. 10 (2020), P10004. DOI: 10.1088/1748-0221/15/10/P10004. arXiv: 2007.12539 [physics.ins-det].

[76] Mehlhase, S. "ATLAS detector slice (and particle visualisations)" (2021). URL: https://cds.cern.ch/record/2770815.

[77] ATLAS Collaboration. "Electron reconstruction and identification in the ATLAS experiment using the 2015 and 2016 LHC proton-proton collision data at $\sqrt{s} = 13$ TeV". *Eur. Phys. J. C* 79, no. 8 (2019), 639. DOI: 10.1140/epjc/s10052-019-7140-6. arXiv: 1902.04655 [physics.ins-det].

[78] ATLAS Collaboration. "Muon reconstruction and identification efficiency in ATLAS using the full Run 2 *pp* collision data set at $\sqrt{s} = 13$ TeV". *Eur. Phys. J. C* 81, no. 7 (2021), 578. DOI: 10.1140/epjc/s10052-021-09233-2. arXiv: 2012.00578 [hep-ex].

[79] ATLAS Collaboration. "Muon reconstruction performance of the ATLAS detector in proton–proton collision data at $\sqrt{s}$ =13 TeV". *Eur. Phys. J. C* 76, no. 5 (2016), 292. DOI: 10.1140/epjc/s10052-016-4120-y. arXiv: 1603.05598 [hep-ex].

[80] ATLAS Collaboration. "Topological cell clustering in the ATLAS calorimeters and its performance in LHC Run 1". *Eur. Phys. J. C* 77 (2017), 490. DOI: 10.1140/epjc/s10052-017-5004-5. arXiv: 1603.02934 [hep-ex].

[81] Cacciari, M., Salam, G. P., and Soyez, G. "The anti-k_t jet clustering algorithm". *JHEP* 04 (2008), 063. DOI: 10.1088/1126-6708/2008/04/063. arXiv: 0802.1189 [hep-ph].

[82] Cacciari, M., Salam, G. P., and Soyez, G. "FastJet User Manual". *Eur. Phys. J. C* 72 (2012), 1896. DOI: 10.1140/epjc/s10052-012-1896-2. arXiv: 1111.6097 [hep-ph].

[83] ATLAS Collaboration. "Jet reconstruction and performance using particle flow with the ATLAS Detector". *Eur. Phys. J. C* 77, no. 7 (2017), 466. DOI: 10.1140/epjc/s10052-017-5031-2. arXiv: 1703.10485 [hep-ex].

[84] ATLAS Collaboration. "Performance of missing transverse momentum reconstruction with the ATLAS detector using proton-proton collisions at $\sqrt{s} = 13$ TeV". *Eur. Phys. J. C* 78, no. 11 (2018), 903. DOI: 10.1140/epjc/s10052-018-6288-9. arXiv: 1802.08168 [hep-ex].

[85] Zurbano Fernandez, I. et al. "High-Luminosity Large Hadron Collider (HL-LHC): Technical design report". 10/2020 (Dec. 2020). DOI: 10.23731/CYRM-2020-0010.

[86] *LHC/HL-LHC Plan updated in February 2022*. https://hilumilhc.web.cern.ch/article/ls3-schedule-change. Accessed: 2022-09-03.

[87] *European Strategy for Partile Physics*. https://europeanstrategy.cern/home. Accessed: 2023-06-08.

[88] *Future Circular Collider study*. https://fcc.web.cern.ch. Accessed: 2023-06-08.

[89] Moroi, T. "The Muon anomalous magnetic dipole moment in the minimal supersymmetric standard model". *Phys. Rev. D* 53 (1996). [Erratum: Phys.Rev.D 56, 4424 (1997)], 6565–6575. DOI: 10.1103/PhysRevD.53.6565. arXiv: hep-ph/9512396.

[90] Feng, J. L. and Moroi, T. "Supernatural supersymmetry: Phenomenological implications of anomaly mediated supersymmetry breaking". *Phys. Rev. D* 61 (2000), 095004. DOI: 10.1103/PhysRevD.61.095004. arXiv: hep-ph/9907319.

[91] Endo, M. et al. "Muon $g-2$ vs LHC Run 2 in supersymmetric models". *JHEP* 04 (2020), 165. DOI: 10.1007/JHEP04(2020)165. arXiv: 2001.11025 [hep-ph].

[92] Alwall, J. et al. "Searching for directly decaying gluinos at the Tevatron". *Phys. Lett. B* 666 (2008), 34. DOI: 10.1016/j.physletb.2008.06.065. arXiv: 0803.0019 [hep-ph].

[93] Alwall, J., Schuster, P., and Toro, N. "Simplified models for a first characterization of new physics at the LHC". *Phys. Rev. D* 79 (2009), 075020. DOI: 10.1103/PhysRevD.79.075020. arXiv: 0810.3921 [hep-ph].

[94] Alves, D. et al. "Simplified models for LHC new physics searches". *J. Phys. G* 39 (2012), 105005. DOI: 10.1088/0954-3899/39/10/105005. arXiv: 1105.2838 [hep-ph].

[95] CMS Collaboration. "Combined search for electroweak production of charginos and neutralinos in proton-proton collisions at $\sqrt{s} = 13$ TeV". *JHEP* 03 (2018), 160. DOI: 10.1007/JHEP03(2018)160. arXiv: 1801.03957 [hep-ex].

[96] ATLAS Collaboration. "Searches for electroweak production of supersymmetric particles with compressed mass spectra in $\sqrt{s} = 13$ TeV pp collisions with the ATLAS detector". *Phys. Rev. D* 101, no. 5 (2020), 052005. DOI: 10.1103/PhysRevD.101.052005. arXiv: 1911.12606 [hep-ex].

[97] ATLAS Collaboration. "Search for direct production of charginos and neutralinos in events with three leptons and missing transverse momentum in $\sqrt{s} = 8$TeV pp collisions with the ATLAS detector". *JHEP* 04 (2014), 169. DOI: 10.1007/JHEP04(2014)169. arXiv: 1402.7029 [hep-ex].

[98] ALEPH, DELPHI, L3, OPAL Experiments. *Combined LEP Chargino Results, up to 208 GeV for low DM*. 2002. URL: http://lepsusy.web.cern.ch/lepsusy/www/inoslowdmsummer02/charginolowdm_pub.html.

[99] ALEPH Collaboration. "Search for scalar leptons in e^+e^- collisions at center-of-mass energies up to 209 GeV". *Phys. Lett. B* 526 (2002), 206–220. DOI: 10.1016/S0370-2693(01)01494-0. arXiv: hep-ex/0112011.

[100] ALEPH Collaboration. "Search for charginos nearly mass degenerate with the lightest neutralino in e^+e^- collisions at center-of-mass energies up to 209 GeV". *Phys. Lett. B* 533 (2002), 223–236. DOI: 10.1016/S0370-2693(02)01584-8. arXiv: hep-ex/0203020.

[101] ALEPH Collaboration. "Absolute lower limits on the masses of selectrons and sneutrinos in the MSSM". *Phys. Lett. B* 544 (2002), 73–88. DOI: 10.1016/S0370-2693(02)02471-1. arXiv: hep-ex/0207056.

[102] ALEPH Collaboration. "Absolute mass lower limit for the lightest neutralino of the MSSM from e^+e^- data at $\sqrt{s}$ up to 209 GeV". *Phys. Lett. B* 583 (2004), 247–263. DOI: 10.1016/j.physletb.2003.12.066.

[103] DELPHI Collaboration. "Searches for supersymmetric particles in e^+e^- collisions up to 208 GeV and interpretation of the results within the MSSM". *Eur. Phys. J. C* 31 (2003), 421–479. DOI: 10.1140/epjc/s2003-01355-5. arXiv: hep-ex/0311019.

[104] L3 Collaboration. "Search for charginos with a small mass difference with the lightest supersymmetric particle at $\sqrt{s} = 189$ GeV". *Phys. Lett. B* 482 (2000), 31–42. DOI: 10.1016/S0370-2693(00)00488-3. arXiv: hep-ex/0002043.

[105] L3 Collaboration. "Search for scalar leptons and scalar quarks at LEP". *Phys. Lett. B* 580 (2004), 37–49. DOI: 10.1016/j.physletb.2003.10.010. arXiv: hep-ex/0310007.

[106] OPAL Collaboration. "Search for anomalous production of di-lepton events with missing transverse momentum in e^+e^- collisions at $\sqrt{s} = 183$–209 GeV". *Eur. Phys. J. C* 32 (2004), 453–473. DOI: 10.1140/epjc/s2003-01466-y. arXiv: hep-ex/0309014.

[107] OPAL Collaboration. "Search for nearly mass-degenerate charginos and neutralinos at LEP". *Eur. Phys. J. C* 29 (2003), 479–489. DOI: 10.1140/epjc/s2003-01237-x. arXiv: hep-ex/0210043.

[108] Buckley, A. et al. "General-purpose event generators for LHC physics". *Phys. Rept.* 504 (2011), 145–233. DOI: 10.1016/j.physrep.2011.03.005. arXiv: 1101.2599 [hep-ph].

[109] Dobbs, M. A. et al. "Les Houches guidebook to Monte Carlo generators for hadron collider physics". *3rd Les Houches Workshop on Physics at TeV Colliders*. Mar. 2004, 411–459. arXiv: hep-ph/0403045.

[110] ATLAS Collaboration. "The ATLAS Simulation Infrastructure". *Eur. Phys. J. C* 70 (2010), 823–874. DOI: 10.1140/epjc/s10052-010-1429-9. arXiv: 1005.4568 [physics.ins-det].

[111] Lukas, W. "Fast Simulation for ATLAS: Atlfast-II and ISF". *J. Phys. Conf. Ser.* 396 (2012), 022031. DOI: 10.1088/1742-6596/396/2/022031.

[112] Höche, S. "Introduction to parton-shower event generators". *Theoretical Advanced Study Institute in Elementary Particle Physics: Journeys Through the Precision Frontier: Amplitudes for Colliders*. 2015, 235–295. DOI: 10.1142/9789814678766_0005. arXiv: 1411.4085 [hep-ph].

[113] Sjostrand, T., Mrenna, S., and Skands, P. Z. "A Brief Introduction to PYTHIA 8.1". *Comput. Phys. Commun.* 178 (2008), 852–867. DOI: 10.1016/j.cpc.2008.01.036. arXiv: 0710.3820 [hep-ph].

[114] Bahr, M. et al. "Herwig++ Physics and Manual". *Eur. Phys. J. C* 58 (2008), 639–707. DOI: 10.1140/epjc/s10052-008-0798-9. arXiv: 0803.0883 [hep-ph].

[115] Bellm, J. et al. "Herwig 7.0/Herwig++ 3.0 release note". *Eur. Phys. J. C* 76, no. 4 (2016), 196. DOI: 10.1140/epjc/s10052-016-4018-8. arXiv: 1512.01178 [hep-ph].

[116] Gleisberg, T. et al. "Event generation with SHERPA 1.1". *JHEP* 02 (2009), 007. DOI: 10.1088/1126-6708/2009/02/007. arXiv: 0811.4622 [hep-ph].

[117] Alwall, J. et al. "The automated computation of tree-level and next-to-leading order differential cross sections, and their matching to parton shower simulations". *JHEP* 07 (2014), 079. DOI: 10.1007/JHEP07(2014)079. arXiv: 1405.0301 [hep-ph].

[118] Lange, D. J. "The EvtGen particle decay simulation package". *Nucl. Instrum. Meth. A* 462 (2001), 152–155. DOI: 10.1016/S0168-9002(01)00089-4.

[119] Agostinelli, S. et al. "Geant4—a simulation toolkit". *Nuclear Instruments and Methods in Physics Research Section A: Accelerators, Spectrometers, Detectors and Associated Equipment* 506, no. 3 (2003), 250–303. DOI: https://doi.org/10.1016/S0168-9002(03)01368-8.

[120] Allison, J. et al. "Geant4 developments and applications". *IEEE Transactions on Nuclear Science* 53, no. 1 (2006), 270–278. DOI: 10.1109/TNS.2006.869826.

[121] Allison, J. et al. "Recent developments in Geant4". *Nuclear Instruments and Methods in Physics Research Section A: Accelerators, Spectrometers, Detectors and Associated Equipment* 835 (2016), 186–225. DOI: https://doi.org/10.1016/j.nima.2016.06.125.

[122] ATLAS, C. et al. *The simulation principle and performance of the ATLAS fast calorimeter simulation FastCaloSim*. Tech. rep. 2010. URL: https://cds.cern.ch/record/1300517.

[123] Catmore, J. *The ATLAS data processing chain: from collisions to papers*. https://indico.cern.ch/event/472469/contributions/1982677/attachments/1220934/1785823/intro_slides.pdf. Accessed: 2022–08-15. 2016.

[124] Bos, K. et al. *LHC computing Grid: Technical Design Report. Version 1.06 (20 Jun 2005)*. Technical design report. LCG. 2005. URL: https://cds.cern.ch/record/840543.

[125] Bird, I. et al. *Update of the Computing Models of the WLCG and the LHC Experiments*. Tech. rep. 2014. URL: https://cds.cern.ch/record/1695401.

[126] Artoisenet, P. et al. "Automatic spin-entangled decays of heavy resonances in Monte Carlo simulations". *JHEP* 03 (2013), 015. DOI: 10.1007/JHEP03(2013)015. arXiv: 1212.3460 [hep-ph].

[127] De Sanctis, U. et al. "Perspectives for the detection and measurement of Supersymmetry in the focus point region of mSUGRA models with the ATLAS detector at LHC". *Eur. Phys. J. C* 52 (2007), 743–758. DOI: 10.1140/epjc/s10052-007-0415-3. arXiv: 0704.2515 [hep-ex].

[128] Beenakker, W. et al. "The Production of charginos / neutralinos and sleptons at hadron colliders". *Phys. Rev. Lett.* 83 (1999). [Erratum: Phys.Rev.Lett. 100, 029901 (2008)], 3780–3783. DOI: 10.1103/PhysRevLett.100.029901. arXiv: hep-ph/9906298.

[129] Debove, J., Fuks, B., and Klasen, M. "Threshold resummation for gaugino pair production at hadron colliders". *Nucl. Phys. B* 842 (2011), 51–85. DOI: 10.1016/j.nuclphysb.2010.08.016. arXiv: 1005.2909 [hep-ph].

[130] Fuks, B. et al. "Gaugino production in proton-proton collisions at a center-of-mass energy of 8 TeV". *JHEP* 10 (2012), 081. DOI: 10.1007/JHEP10(2012)081. arXiv: 1207.2159 [hep-ph].

[131] Fuks, B. et al. "Precision predictions for electroweak superpartner production at hadron colliders with Resummino". *Eur. Phys. J. C* 73 (2013), 2480. DOI: 10.1140/epjc/s10052-013-2480-0. arXiv: 1304.0790 [hep-ph].

[132] Fiaschi, J. and Klasen, M. "Neutralino-chargino pair production at NLO+NLL with resummation-improved parton density functions for LHC Run II". *Phys. Rev. D* 98, no. 5 (2018), 055014. DOI: 10.1103/PhysRevD.98.055014. arXiv: 1805.11322 [hep-ph].

[133] Borschensky, C. et al. "Squark and gluino production cross sections in pp collisions at $\sqrt{s} = 13$, 14, 33 and 100 TeV". *Eur. Phys. J. C* 74, no. 12 (2014), 3174. DOI: 10.1140/epjc/s10052-014-3174-y. arXiv: 1407.5066 [hep-ph].

[134] ATLAS Collaboration. *Multi-Boson Simulation for 13 TeV ATLAS Analyses*. Tech. rep. 2016. URL: https://cds.cern.ch/record/2119986.

[135] ATLAS Collaboration. *ATLAS simulation of boson plus jets processes in Run 2*. Tech. rep. 2017. URL: https://cds.cern.ch/record/2261937.

[136] Frixione, S., Nason, P., and Ridolfi, G. "A Positive-weight next-to-leading-order Monte Carlo for heavy flavour hadroproduction". *JHEP* 09 (2007), 126. DOI: 10.1088/1126-6708/2007/09/126. arXiv: 0707.3088 [hep-ph].

[137] Re, E. "Single-top Wt-channel production matched with parton showers using the POWHEG method". *Eur. Phys. J. C* 71 (2011), 1547. DOI: 10.1140/epjc/s10052-011-1547-z. arXiv: 1009.2450 [hep-ph].

[138] Frederix, R., Re, E., and Torrielli, P. "Single-top t-channel hadroproduction in the four-flavour scheme with POWHEG and aMC@NLO". *JHEP* 09 (2012), 130. DOI: 10.1007/JHEP09(2012)130. arXiv: 1207.5391 [hep-ph].

[139] Alioli, S. et al. "NLO single-top production matched with shower in POWHEG: s- and t-channel contributions". *JHEP* 09 (2009). [Erratum: JHEP 02, 011 (2010)], 111. DOI: 10.1088/1126-6708/2009/09/111. arXiv: 0907.4076 [hep-ph].

[140] Hartanto, H. B. et al. "Higgs boson production in association with top quarks in the POWHEG BOX". *Phys. Rev. D* 91, no. 9 (2015), 094003. DOI: 10.1103/PhysRevD.91.094003. arXiv: 1501.04498 [hep-ph].

[141] Quintero, N., Diaz-Cruz, J. L., and Lopez Castro, G. "Lepton pair emission in the top quark decay $t \to bW^+\ell^-\ell^+$". *Phys. Rev. D* 89, no. 9 (2014), 093014. DOI: 10.1103/PhysRevD.89.093014. arXiv: 1403.3044 [hep-ph].

[142] Avoni, G. et al. "The new LUCID-2 detector for luminosity measurement and monitoring in ATLAS". *Journal of Instrumentation* 13, no. 07 (July 2018), P07017–P07017. DOI: 10.1088/1748-0221/13/07/p07017.

[143] ATLAS Collaboration. "ATLAS data quality operations and performance for 2015–2018 data-taking". *JINST* 15, no. 04 (2020), P04003. DOI: 10.1088/1748-0221/15/04/P04003. arXiv: 1911.04632 [physics.ins-det].

[144] ATLAS Collaboration. *Luminosity determination in pp collisions at $\sqrt{s} = 13$ TeV using the ATLAS detector at the LHC*. Tech. rep. 2019. URL: https://cds.cern.ch/record/2677054.

[145] ATLAS Collaboration. "Performance of the ATLAS muon triggers in Run 2". *JINST* 15 (2020), P09015. DOI: 10.1088/1748-0221/15/09/p09015. arXiv: 2004.13447 [hep-ex].

[146] ATLAS Collaboration. "Performance of electron and photon triggers in ATLAS during LHC Run 2". *Eur. Phys. J. C* 80 (2020), 47. DOI: 10.1140/epjc/s10052-019-7500-2. arXiv: 1909.00761 [hep-ex].

[147] ATLAS Collaboration. "Performance of the missing transverse momentum triggers for the ATLAS detector during Run-2 data taking". *JHEP* 08 (2020), 080. DOI: 10.1007/JHEP08(2020)080. arXiv: 2005.09554 [hep-ex].

[148] ATLAS Collaboration. "Electron and photon performance measurements with the ATLAS detector using the 2015–2017 LHC proton-proton collision data". *Journal of Instrumentation* 14, no. 12 (Dec. 2019), P12006–P12006. DOI: 10.1088/1748-0221/14/12/p12006.

[149] ATLAS Collaboration. "Muon reconstruction and identification efficiency in ATLAS using the full Run 2 *pp* collision data set at $\sqrt{s} = 13$ TeV". *Eur. Phys. J. C* 81, no. 7 (2021), 578. DOI: 10.1140/epjc/s10052-021-09233-2. arXiv: 2012.00578 [hep-ex].

[150] ATLAS Collaboration. "Evidence for the associated production of the Higgs boson and a top quark pair with the ATLAS detector". *Phys. Rev. D* 97, no. 7 (2018), 072003. DOI: 10.1103/PhysRevD.97.072003. arXiv: 1712.08891 [hep-ex].

[151] ATLAS Collaboration. *Selection of jets produced in 13TeV proton-proton collisions with the ATLAS detector*. Tech. rep. 2015. URL: https://cds.cern.ch/record/2037702.

[152] ATLAS Collaboration. "Performance of pile-up mitigation techniques for jets in pp collisions at $\sqrt{s} = 8$ TeV using the ATLAS detector". *Eur. Phys. J. C* 76, no. 11 (2016), 581. DOI: 10.1140/epjc/s10052-016-4395-z. arXiv: 1510.03823 [hep-ex].

[153] ATLAS Collaboration. *Tagging and suppression of pileup jets with the ATLAS detector*. Tech. rep. 2014. URL: https://cds.cern.ch/record/1700870.

[154] ATLAS Collaboration. *Optimisation and performance studies of the ATLAS b-tagging algorithms for the 2017-18 LHC run*. Tech. rep. 2017. URL: https://cds.cern.ch/record/2273281.

[155] ATLAS Collaboration. "AtlFast3: the next generation of fast simulation in ATLAS". *Comput. Softw. Big Sci.* 6 (2022), 7. DOI: 10.1007/s41781-021-00079-7. arXiv: 2109.02551 [hep-ex].

[156] Lester, C. G. and Summers, D. J. "Measuring masses of semiinvisibly decaying particles pair produced at hadron colliders". *Phys. Lett. B* 463 (1999), 99–103. DOI: 10.1016/S0370-2693(99)00945-4. arXiv: hep-ph/9906349.

[157] Barr, A., Lester, C., and Stephens, P. "m(T2): The Truth behind the glamour". *J. Phys. G* 29 (2003), 2343–2363. DOI: 10.1088/0954-3899/29/10/304. arXiv: hep-ph/0304226.

[158] ATLAS Collaboration. *Object-based missing transverse momentum significance in the ATLAS detector*. Tech. rep. 2018. URL: https://cds.cern.ch/record/2630948.

[159] Kyle Cranmer. *namespace RooStats::NumberCountingUtils*. Accessed: 2023-08-18. URL: https://root.cern/root/html534/RooStats__NumberCountingUtils.html#RooStats__NumberCountingUtils:BinomialExpZ.

[160] *ROOT Reference Guide 6.07/01 – NumberCountingUtils.cxx*. Accessed: 2023-08-18. URL: https://root.cern/doc/v606/NumberCountingUtils_8cxx_source.html#l00029.

[161] Moneta, L. et al. *The RooStats Project*. 2010. URL: https://arxiv.org/abs/1009.1003.

[162] *Formulae for Estimating Significance*. Tech. rep. 2020. URL: https://cds.cern.ch/record/2736148.

[163] ATLAS Collaboration. "Measurement of the WW cross section in $\sqrt{s} = 7$ TeV pp collisions with the ATLAS detector and limits on anomalous gauge couplings". *Phys. Lett. B* 712 (2012), 289–308. DOI: 10.1016/j.physletb.2012.05.003. arXiv: 1203.6232 [hep-ex].

[164] ATLAS Collaboration. *Prospects for Higgs Boson Searches using the $H \to WW^{(*)} \to \ell\nu\ell\nu$ Decay Mode with the ATLAS Detector for 10 TeV*. Tech. rep. 2010. URL: https://cds.cern.ch/record/1270568.

[165] Cousins, R. D., Linnemann, J. T., and Tucker, J. "Evaluation of three methods for calculating statistical significance when incorporating a systematic uncertainty into a test of the background-only hypothesis for a Poisson process". *Nuclear Instruments and Methods in Physics Research Section A: Accelerators, Spectrometers, Detectors and Associated Equipment* 595, no. 2 (Oct. 2008), 480–501. DOI: 10.1016/j.nima.2008.07.086.

[166] Baak, M. et al. "HistFitter software framework for statistical data analysis". *Eur. Phys. J. C* 75 (2015), 153. DOI: 10.1140/epjc/s10052-015-3327-7. arXiv: 1410.1280 [hep-ex].

[167] Cranmer, K. et al. *HistFactory: A tool for creating statistical models for use with RooFit and RooStats*. Tech. rep. 2012. URL: https://cds.cern.ch/record/1456844.

[168] Verkerke, W. and Kirkby, D. *The RooFit toolkit for data modeling*. 2003. DOI: 10.48550/ARXIV.PHYSICS/0306116.

[169] Brun, R. and Rademakers, F. "ROOT: An object oriented data analysis framework". *Nucl. Instrum. Meth. A* 389 (1997), 81–86. DOI: 10.1016/S0168-9002(97)00048-X.

[170] Antcheva, I. et al. "ROOT: A C++ framework for petabyte data storage, statistical analysis and visualization". *Comput. Phys. Commun.* 180 (2009), 2499–2512. DOI: 10.1016/j.cpc.2009.08.005. arXiv: 1508.07749 [physics.data-an].

[171] Cowan, G. et al. "Asymptotic formulae for likelihood-based tests of new physics". *Eur. Phys. J. C* 71 (2011). [Erratum: Eur.Phys.J.C 73, 2501 (2013)], 1554. DOI: 10.1140/epjc/s10052-011-1554-0. arXiv: 1007.1727 [physics.data-an].

[172] Read, A. L. "Presentation of search results: The CL(s) technique". *J. Phys. G* 28 (2002), 2693–2704. DOI: 10.1088/0954-3899/28/10/313.

[173] ATLAS Collaboration. "Searches for electroweak production of supersymmetric particles with compressed mass spectra in $\sqrt{s} = 13$ TeV pp collisions with the ATLAS detector". *Phys. Rev. D* 101, no. 5 (2020), 052005. DOI: 10.1103/PhysRevD.101.052005. arXiv: 1911.12606 [hep-ex].

[174] Aghanim, N. et al. "Planck 2015 results. XI. CMB power spectra, likelihoods, and robustness of parameters". *Astron. Astrophys.* 594 (2016), A11. DOI: 10.1051/0004-6361/201526926. arXiv: 1507.02704 [astro-ph.CO].

[175] Duan, G. H. et al. "Probing bino-wino coannihilation dark matter below the neutrino floor at the LHC". *Phys. Rev. D* 98, no. 1 (2018), 015010. DOI: 10.1103/PhysRevD.98.015010. arXiv: 1804.05238 [hep-ph].

[176] ATLAS Collaboration. *SimpleAnalysis: Truth-level Analysis Framework*. Tech. rep. 2022. URL: https://cds.cern.ch/record/2805991.

[177] Petersen, B. and Stark, G. *SimpleAnalysis, v1.1.0*. DOI: 10.5281/zenodo.6328570. URL: https://simpleanalysis.docs.cern.ch/.

[178] Bierlich, C. et al. "Robust Independent Validation of Experiment and Theory: Rivet version 3". *SciPost Phys.* 8 (2020), 026. DOI: 10.21468/SciPostPhys.8.2.026. arXiv: 1912.05451 [hep-ph].

[179] Djouadi, A., Muhlleitner, M. M., and Spira, M. "Decays of supersymmetric particles: The Program SUSY-HIT (SUspect-SdecaY-Hdecay-InTerface)". *Acta Phys. Polon. B* 38 (2007), 635–644. arXiv: hep-ph/0609292.

[180] Kraml, S. et al. "SModelS: a tool for interpreting simplified-model results from the LHC and its application to supersymmetry". *Eur.Phys.J.* C74 (2014), 2868. DOI: 10.1140/epjc/s10052-014-2868-5. arXiv: 1312.4175 [hep-ph].

[181] Alguero, G. et al. "Constraining new physics with SModelS version 2" (Dec. 2021). arXiv: 2112.00769 [hep-ph].

[182] *SModelS User Manual*. https://smodels.readthedocs.io/en/stable/. Accessed: 2023-06-17.

[183] GAMBIT Collaboration. "GAMBIT: The Global and Modular Beyond-the-Standard-Model Inference Tool". *Eur. Phys. J. C* 77, no. 11 (2017). [Addendum: Eur.Phys.J.C 78, 98 (2018)], 784. DOI: 10.1140/epjc/s10052-017-5321-8. arXiv: 1705.07908 [hep-ph].

[184] Lanni, F. et al. *Decision on the Phase-II Trigger architecture: ATLAS Trigger Architecture Decision Process*. Tech. rep. INTERNAL. 2020. URL: https://cds.cern.ch/record/2740489.

[185] Heinrich, L., Feickert, M., and Stark, G. *pyhf: v0.6.3*. Version 0.6.3. DOI: 10.5281/zenodo.1169739.

[186] Heinrich, L. et al. "pyhf: pure-Python implementation of HistFactory statistical models". *Journal of Open Source Software* 6, no. 58 (2021), 2823. DOI: 10.21105/joss.02823.

[187] Harris, C. R. et al. "Array programming with NumPy". *Nature* 585, no. 7825 (Sept. 2020), 357–362. DOI: 10.1038/s41586-020-2649-2.

[188] Abadi, M. et al. *TensorFlow: A system for large-scale machine learning*. 2016. arXiv: 1605.08695 [cs.DC].

[189] Abadi, M. et al. *TensorFlow: Large-Scale Machine Learning on Heterogeneous Systems*. Software available from tensorflow.org. 2015. URL: https://www.tensorflow.org/.

[190] Paszke, A. et al. "PyTorch: An Imperative Style, High-Performance Deep Learning Library". *Advances in Neural Information Processing Systems 32*. Curran Associates, Inc., 2019, 8024–8035. URL: http://papers.neurips.cc/paper/9015-pytorch-an-imperative-style-high-performance-deep-learning-library.pdf.

[191] Frostig, R., Johnson, M., and Leary, C. "Compiling machine learning programs via high-level tracing". 2018. URL: https://mlsys.org/Conferences/doc/2018/146.pdf.

[192] Bradbury, J. et al. *JAX: composable transformations of Python+NumPy programs*. Version 0.3.13. 2018. URL: http://github.com/google/jax.

[193] Virtanen, P. et al. "SciPy 1.0: Fundamental Algorithms for Scientific Computing in Python". *Nature Methods* 17 (2020), 261–272. DOI: 10.1038/s41592-019-0686-2.

[194] Ongmongkolkul, P. et al. *iminuit - A Python interface to MINUIT*. Accessed: 2022-12-12. URL: https://github.com/iminuit/iminuit.

[195] ATLAS Collaboration. "Search for charginos and neutralinos in final states with two boosted hadronically decaying bosons and missing transverse momentum in pp collisions at $\sqrt{s} = 13$ TeV with the ATLAS detector". *Phys. Rev. D* 104, no. 11 (2021), 112010. DOI: 10.1103/PhysRevD.104.112010. arXiv: 2108.07586 [hep-ex].

[196] ATLAS Collaboration. "Search for direct production of electroweakinos in final states with one lepton, missing transverse momentum and a Higgs boson decaying into two b-jets in pp collisions at $\sqrt{s} = 13$ TeV with the ATLAS detector". *Eur. Phys. J. C* 80, no. 8 (2020), 691. DOI: 10.1140/epjc/s10052-020-8050-3. arXiv: 1909.09226 [hep-ex].

[197] ATLAS Collaboration. *Search for the direct production of charginos and neutralinos in final states with tau leptons in $\sqrt{s} = 13$ TeV pp collisions with the ATLAS detector*. Tech. rep. 2022. URL: https://cds.cern.ch/record/2815678.

[198] ATLAS Collaboration. *Search for direct production of winos and higgsinos in events with two same-charge leptons or three leptons in pp collision data at $\sqrt{s} = 13$ TeV with the ATLAS detector*. 2023. arXiv: 2305.09322 [hep-ex].

[199] Cranmer, K. and Yavin, I. "RECAST: Extending the Impact of Existing Analyses". *JHEP* 04 (2011), 038. DOI: 10.1007/JHEP04(2011)038. arXiv: 1010.2506 [hep-ex].

[200] Cranmer, K. and Heinrich, L. "Analysis Preservation and Systematic Reinterpretation within the ATLAS experiment". *J. Phys. Conf. Ser.* 1085, no. 4 (2018), 042011. DOI: 10.1088/1742-6596/1085/4/042011.

[201] Merkel, D. "Docker: lightweight linux containers for consistent development and deployment". *Linux journal* 2014, no. 239 (2014), 2.

[202] Cranmer, K. and Heinrich, L. "Yadage and Packtivity - analysis preservation using parametrized workflows". *J. Phys. Conf. Ser.* 898, no. 10 (2017), 102019. DOI: 10.1088/1742-6596/898/10/102019. arXiv: 1706.01878 [physics.data-an].

[203] Wu, W., Cameron, D., and Qing, D. “Using ATLAS@Home to exploit extra CPU from busy grid sites”. *Comput. Softw. Big Sci.* 3, no. 1 (2019). [Erratum: Comput.Softw.Big Sci. 3, 8 (2019)], 14. DOI: 10.1007/s41781-019-0023-6. arXiv: 1811.12578 [physics.comp-ph].

[204] Anderson, D. “BOINC: A System for Public-Resource Computing and Storage”. Dec. 2004, 4–10. ISBN: 0-7695-2256-4. DOI: 10.1109/GRID.2004.14.

[205] Watson, J. “VirtualBox: Bits and Bytes Masquerading as Machines”. *Linux J.* 2008, no. 166 (Feb. 2008).

[206] Buncic, P. et al. “CernVM – a virtual software appliance for LHC applications”. *Journal of Physics: Conference Series* 219, no. 4 (Apr. 2010), 042003. DOI: 10.1088/1742-6596/219/4/042003.

[207] Cameron, D. et al. “Advances in ATLAS@Home towards a major ATLAS computing resource” (June 2018). URL: https://cds.cern.ch/record/2626282.

[208] *p5.js website*. https://p5js.org. Accessed: 2022-05-15.

[209] Kittelmann, T. H. et al. “The virtual point 1 event display for the ATLAS experiment”. *J. Phys. Conf. Ser.* 219 (2010), 032012. DOI: 10.1088/1742-6596/219/3/032012.

[210] *ATLAS Software Documentation*. https://atlassoftwaredocs.web.cern.ch. Accessed: 2023-05-28.

[211] Crash at Crush. *Crash at Crush — Wikipedia, The Free Encyclopedia*. Accessed: 2023-06-25. URL: https://en.wikipedia.org/wiki/Crash_at_Crush.

[212] *International Masterclasses — hands on particle physics*. https://physicsmasterclasses.org/index.php. Accessed: 2023-05-29.

[213] *ATLAS Open Data*. https://atlas.cern/Resources/Opendata. Accessed: 2023-05-29.

[214] *Z-Path*. https://atlas.physicsmasterclasses.org/en/zpath.htm. Accessed: 2023-05-29.